UNIVERSITA' DEGLI STUDI DI PARMA

Dottorato di ricerca in FISICA

Ciclo XXVIII

Quantum Information Processing with spin systems:

from modeling to possible implementations

Coordinatore:
Chiar.mo Prof. Cristiano Viappiani

Tutor:
Chiar.mo Prof. Stefano Carretta

Dottorando: Alessandro Chiesa

Quantum Information Processing with spin systems:

from modeling to possible implementations

PhD thesis by

ALESSANDRO CHIESA

UNIPR MOLECULAR MAGNETISM group

SUPERVISOR: prof. Stefano Carretta

COSUPERVISOR: prof. Paolo Santini

UNIVERSITÀ DEGLI STUDI DI PARMA
il mondo che ti aspetta
PhD in Physics
DiFeST
DIPARTIMENTO DI FISICA E SCIENZE DELLA TERRA

January 2016

Commission of the final examination:

External Members:
Prof. Marco Affronte
Prof. Joris van Slageren

Internal Member:
Prof. Mauro Riccò

Final examination:

March 2016,

Università degli Studi di Parma, Dipartimento di Fisica e Scienze della Terra, Parma, Italy

"Computers are incredibly fast, accurate and stupid;
humans are incredibly slow, inaccurate and brilliant;
together they are powerful beyond imagination."

To my parents,
who paved me the way till the bottom of the hill

Design:

This document was typeset by the author using LaTeXmarkup language, with MikTeX2.9 software and WinEdt editor. The file in Portable Document Format was generated with pdfLaTeX.

MIUR subjects:

FIS/03

PACS:

75.50.Xx, 31.15.aq, 31.15.E-, 31.15.V-, 03.67.Lx, 42.50.Pq, 85.25.-j, 75.10.Jm, 71.70.Gm, 78.70.Nx, 76.30.-v

---

Abstract

The physical implementation of quantum information processing is one of the major challenges of current research. In the last few years, several theoretical proposals and experimental demonstrations on a small number of qubits have been carried out, but a quantum computing architecture that is straightforwardly scalable, universal, and realizable with state-of-the-art technology is still lacking. In particular, a major ultimate objective is the construction of quantum simulators, yielding massively increased computational power in simulating quantum systems.

Here we investigate promising routes towards the actual realization of a quantum computer, based on spin systems. The first one employs molecular nanomagnets with a doublet ground state to encode each qubit and exploits the wide chemical tunability of these systems to obtain the proper topology of inter-qubit interactions. Indeed, recent advances in coordination chemistry allow us to arrange these qubits in chains, with tailored interactions mediated by magnetic linkers. These act as switches of the effective qubit-qubit coupling, thus enabling the implementation of one- and two-qubit gates. Molecular qubits can be controlled either by uniform magnetic pulses, either by local electric fields. We introduce here two different schemes for quantum information processing with either global or local control of the inter-qubit interaction and demonstrate the high performance of these platforms by simulating the system time evolution with state-of-the-art parameters.

The second architecture we propose is based on a hybrid spin-photon qubit encoding, which exploits the best characteristic of photons, whose mobility is exploited to efficiently establish long-range entanglement, and spin systems, which ensure long coherence times. The setup consists of spin ensembles coherently coupled to single photons within superconducting coplanar waveguide resonators. The tunability of the resonators frequency is exploited as the only manipulation tool to implement a universal set of quantum gates, by bringing the photons into/out of resonance with the spin transition. The time evolution of the system subject to the pulse sequence used to implement complex quantum algorithms has been simulated by numerically integrating the master equation for the system density matrix, thus including the harmful effects of decoherence. Finally a scheme to overcome the leakage of information due to inhomogeneous broadening of the spin ensemble is pointed out.

Both the proposed setups are based on state-of-the-art technological achievements. By extensive numerical experiments we show that their performance is remarkably good, even for the implementation of long sequences of gates used to simulate interesting physical models. Therefore, the here examined systems are really promising building-blocks of future scalable architectures and can be used for proof-of-principle experiments of quantum information processing and quantum simulation.

Contents

List of Figures

List of Tables

Notations

Abbreviations:

QIP	Quantum Information Processing
QC	Quantum Computer/Computation
QS	Quantum Simulator/Simulation
CNOT	Controlled-NOT
Cφ, CZ	Controlled-phase, Controlled-Z
QEC	Quantum Error Correction
MNM	Molecular Nanomagnet
SH	spin Hamiltonian
ZFS	Zero-field splitting
DM	Dzyaloshinskii-Moriya
INS	Inelastic Neutron Scattering
EPR	Electron Paramagnetic Resonance
SQUID	Superconducting QUantum Interference Device
QED	Quantum Electro-dynamics
cQED	circuit Quantum Electro-dynamics
CWR	Coplanar Waveguide Resonator
SE	Spin Ensemble
IB	Inhomogeneous Broadening
TLS	Three-level system
CPB	Cooper-pair box
FM	Ferromagnetic
AFM	Anti-ferromagnetic
SE	Super-exchange
CE	Coulomb exchange
CF	Crystal Field
DFT	Density Functional Theory
LDA	Local Density Approximation
cLDA	constrained Local Density Approximation

Symbols:

$\hat{O}$	Operator
$\hat{H}$	System Hamiltonian
$\hat{\rho}$	System density matrix
$\hat{\mathcal{H}}$	Target Hamiltonian to be simulated
$\mathbf{a}$	Classical vector
$\hat{\mathbf{a}}$	Vector quantum-mechanical operator
$\underline{\mathbf{A}}$	Tensor
$\mathcal{L}[.]$	Lindblad super-operator
$\mathcal{D}[.]$	Dissipator
Tr[.]	Trace
$\mathscr{L}$	System Langrangian
$\hat{\mathbf{s}}$	Spin operator
$\hat{s}_\alpha$	Spin operator (α component)
$\hat{\sigma}_\alpha$	Pauli matrices ($\alpha = x, y, z$)
$\hat{c}^\dagger_{im\sigma}$, $\hat{c}_{im\sigma}$	Fermionic creation, annihilation operators
$\hat{a}^\dagger_\mu$, $\hat{a}_\mu$	Bosonic creation, annihilation operators
$\hat{T}^{(k)}_q$	q-th component of a rank-k tensor operator.
J_{ij}	Isotropic exchange interaction between ions i and j
$J^{\alpha\beta}_{ij}$	Anisotropic exchange interaction ($\alpha\beta$ component) between ions i and j
$\underline{\mathbf{D}}$	Zero-field splitting Tensor
$\underline{\mathbf{g}}$	Spectroscopic g-tensor
$U^{i,i}$, $\mathcal{J}^{i,i}$	Coulomb Hubbard interactions on site i.
$t^{i,i'}_{m,m'}$	Hopping integrals of the generalized Hubbard model.
$\bar{G}_m$	Spin ensemble(transition m)-resonator coupling
G_μ	Transmon-resonator(μ) coupling
κ	Photon-hopping coupling
Γ_j	Damping rate for mode j
γ_j	Pure-dephasing rate for mode j
T_1	Relaxation time
T_1	Pure-dephasing time
Q	Resonator quality factor
ω_μ	Resonator μ frequency
$\hat{R}_\alpha(\varphi)$	Single-qubit rotation of an angle φ about α axis of the Bloch sphere

Introduction

CHAPTER 0

Unveiling the counter-intuitive aspects of quantum physics is one of the major challenges of current research. In this perspective, simulating and predicting the behaviour of matter at the nano-scale is as crucial as difficult to be obtained with classical means. Quantum computers promise to solve this issue. By performing calculations based on the laws of quantum mechanics, these machines could solve many outstanding problems which are prohibitive for a classical device. Recent progresses in the control and manipulation of molecules and atoms give us direct access to the strange features of the quantum [1], but a computer based on a fully quantum technology is still lacking. Therefore, great efforts are now devoted to identify suitable physical systems for the implementation of quantum information processing. The present work aims to explore some of these routes towards the actual realization of a quantum computer. Since future technological developments are unpredictable, we emphasize the importance of pursuing several parallel roads. Moreover, the final quantum computer will probably be a hybrid device, exploiting the best characteristic of distinct physical systems.

A variety of quantum systems have been so far proposed as qubits, ranging from photons to cold atoms, trapped ions, nuclear and electron spins, superconducting circuits [2]. Among these, electron spins in solids are particularly promising. In fact, they are relatively decoupled from the environment and do not need to be trapped optically or electromagnetically, being integrated in the solid-state. Quantum dots in semiconductors have shown excellent properties as single-qubit units [3], which can be controlled with very high fidelity, but the scalability of these architectures to multi-qubits registers remains a hard task.

Conversely, the use of collective spin degrees of freedom (resulting from coupled electron spins) to encode the qubits in magnetic molecules offers several advantages [4]. Indeed, qubits can be manipulated with magnetic pulses resonant with specific energy gaps; they provide many auxiliary states (besides the computational basis) which can be exploited to design schemes for quantum information which do not require a local control; collective degrees of freedom (such as spin chirality) can protect quantum information from decoherence; qubits can be arranged into arrays or deposited onto surfaces, thus enabling local control with electric tips [5, 6, 7, 8, 9]. Moreover, striking progresses in coordination chemistry allow the synthesis of molecular nanomagnets in which the structure, the number and type of spins, as well as the topology and hierarchy of interactions fit the requirements of specific quantum information schemes.

Molecular spin qubits constitute the first category of systems we propose as a promising quantum computer architectures. The second one is based on the strong coupling between spin systems and photons within superconducting resonators. This allows us to exploit the photonic degree of freedom to establish long-distance entanglement and to obtain multi-qubit interactions, while a hybrid spin-photon encoding is introduced to increase the qubits lifetime.

0.1 Quantum Information Processing

A quantum computer is a machine which performs calculations according to the laws of quantum mechanics. It consists of many quantum bits (*qubits*), i.e. quantum systems which behave, to a good level of approximation, as spins $S = 1/2$, having two distinct (orthogonal) states. These are usually labeled as $|0\rangle$ and $|1\rangle$. Clearly a qubit can encode one bit of information, because it is possible to prepare it in either of these states. However, a qubit differs from its classical counterpart because it can be prepared in any superposition $|\psi\rangle = \alpha|0\rangle + \beta|1\rangle$. Quantum algorithms can be decomposed into a sequence of elementary logical gates, similarly to what is usually done in classical computation. Each of these gates is represented by a unitary operator acting on the qubits wave-function. Quantum and classical computers differ in another important aspect: while we can stop a classical computer at any stage, examine the result and restart the calculation, the same cannot be done with a quantum computer. Indeed, any such intervention would modify the state of the qubits and then it would be not possible to resume the computation.

In principle, any quantum system with two quantum states can be used to provide a physical implementation of a qubit (e.g., the orientation of a spin-half particle, the two orthogonal polarization states of a photon, a pair of electronic energy levels in an atom, ion, or quantum dot). However, in his pioneering work [10], DiVincenzo pointed out five (plus two) essential requirements that any working laboratory device should meet for the physical implementation of Quantum Computation (QC). We recall them in the following list:

1. *A scalable physical system with well characterized qubits.* The system should have well-defined qubits. It is necessary to be able to access the state space of each of these, to realize any desired unitary transformation. We need to be able to upgrade the processor by adding further qubits (scalability).

2. *The ability to initialize the state of the qubits to a simple fiducial state, such as* $|00...0\rangle$. This must be a pure state. For instance, if we can prepare our set of qubits in a product state, then the application of suitable quantum gates will allow us to generate any desired state.

3. *Long relevant decoherence times, much longer than the gate operation time.* The interaction of qubits with the environment can rapidly and uncontrollably modify our quantum state and ruin the computation. Even with efficient quantum error correction, decoherence times have to be very long compared with gate operation times. This is probably the greatest challenge: on the one hand, we would like our

qubits to interact strongly with controlling external influences and with each other, on the other hand we want the qubits to be decoupled from anything else.

4. *A "universal" set of quantum gates*, i.e. a small set of gates which can be used to compute any unitary operation on the N qubits register. Many universal sets exist. It can be shown [11] that an arbitrary unitary operator may be expressed as the product of unitary operators each acting non-trivially only on a subspace spanned by two computational basis states. Starting from this result, one finds that the simplest universal sets consist of single qubit gates about two distinct axes of the Bloch sphere plus one two-qubit entangling gate, such as the controlled-NOT, the controlled-phase shift or the $\sqrt{\text{SWAP}}$ (see subsection 0.1.2 below).

5. *A qubit-specific measurement capability*. We need the capability to perform projective measurements of each of the qubits.

In addition to these fundamental criteria, DiVincenzo also enumerated a pair of desiderata for quantum communication (the ability to interconvert stationary and flying qubits and the ability faithfully to transmit flying qubits between specified locations).

0.1.1 Single-qubit rotations

Since the norm of the vector describing the qubit must be preserved, any gate is expressed by a unitary operator. We quickly summarize here single-qubit operations. Among the most common single qubit operators are the Pauli matrices $\sigma_x = \begin{pmatrix} 0 & 1 \\ 1 & 0 \end{pmatrix}$, $\sigma_y = \begin{pmatrix} 0 & -i \\ i & 0 \end{pmatrix}$, $\sigma_z = \begin{pmatrix} 1 & 0 \\ 0 & -1 \end{pmatrix}$, and the Hadamard gate

$$H_1 = \frac{1}{\sqrt{2}} \begin{pmatrix} 1 & 1 \\ 1 & -1 \end{pmatrix}, \tag{0.1}$$

which transforms the computational basis state $|0\rangle$ ($|1\rangle$) into a symmetric, $\frac{|0\rangle+|1\rangle}{\sqrt{2}}$, (antisymmetric, $\frac{|0\rangle-|1\rangle}{\sqrt{2}}$) superposition. The generic state of a single qubit $|\psi\rangle = a|0\rangle + b|1\rangle$ can also be visualized as a point (θ, φ) on a unitary (Bloch) sphere, with $a = \cos\,\theta/2$, $b = e^{i\varphi}\sin\,\theta/2$ and a can be taken to be real because the overall phase of the state is unobservable. Rotations about x, y and z axis of the Bloch sphere can be expressed in terms of the Pauli matrices as follows:

$$R_x(\theta) \equiv e^{-i\theta\sigma_x/2} = \cos\frac{\theta}{2} - i\sin\frac{\theta}{2}\sigma_x = \begin{pmatrix} \cos\frac{\theta}{2} & -i\sin\frac{\theta}{2} \\ -i\sin\frac{\theta}{2} & \cos\frac{\theta}{2} \end{pmatrix}, \tag{0.2}$$

$$R_y(\theta) \equiv e^{-i\theta\sigma_y/2} = \cos\frac{\theta}{2} - i\sin\frac{\theta}{2}\sigma_y = \begin{pmatrix} \cos\frac{\theta}{2} & -\sin\frac{\theta}{2} \\ \sin\frac{\theta}{2} & \cos\frac{\theta}{2} \end{pmatrix}, \tag{0.3}$$

$$R_z(\theta) \equiv e^{-i\theta\sigma_z/2} = \cos\frac{\theta}{2} - i\sin\frac{\theta}{2}\sigma_z = \begin{pmatrix} e^{-i\frac{\theta}{2}} & 0 \\ 0 & e^{i\frac{\theta}{2}} \end{pmatrix}. \tag{0.4}$$

In general, if $\mathbf{n} = (n_x, n_y, n_z)$ is a real unit vector in three dimensions, a rotation by θ about $\mathbf{n}$ is defined by the matrix:

$$R_{\mathbf{n}}(\theta) \equiv e^{-i\theta\mathbf{n}\cdot\boldsymbol{\sigma}/2} = \cos\frac{\theta}{2} - i\sin\frac{\theta}{2}(n_x\sigma_x + n_y\sigma_y + n_z\sigma_z). \tag{0.5}$$

Finally, it can be proved that, given two non-parallel axes of the Bloch sphere $\mathbf{n}$ and $\mathbf{m}$, any unitary single-qubit operator $\hat{U}$ can be decomposed as

$$\hat{U} = e^{i\alpha} \hat{R}_{\mathbf{n}}(\beta) \hat{R}_{\mathbf{m}}(\gamma) \hat{R}_{\mathbf{n}}(\delta) \tag{0.6}$$

for a proper choice of α, β, γ and δ.

0.1.2 Entangling gates

A universal set of gates includes at least one two-qubit gate. The most common are probably controlled-$\hat{V}$ operations. These are characterized by two input qubits, known as *control* and *target* qubit, respectively. If the control qubit is set to $|1\rangle$, then $\hat{V}$ is applied to the target qubit, otherwise the target qubit is left alone; that is, $|c\rangle|t\rangle \rightarrow |c\rangle\hat{V}^c|t\rangle$.
Particular choices of $\hat{V}$ give rise to the controlled-phase shift (Cφ) and to the controlled-not (CNOT) gates. These are represented, on the two-qubit basis $\{|00\rangle, |01\rangle, |10\rangle, |11\rangle\}$ by the unitary matrices:

$$U_{C\varphi} = \begin{pmatrix} 1 & 0 & 0 & 0 \\ 0 & 1 & 0 & 0 \\ 0 & 0 & 1 & 0 \\ 0 & 0 & 0 & e^{-i\varphi} \end{pmatrix}. \tag{0.7}$$

and

$$U_{CNOT} = \begin{pmatrix} 1 & 0 & 0 & 0 \\ 0 & 1 & 0 & 0 \\ 0 & 0 & 0 & 1 \\ 0 & 0 & 1 & 0 \end{pmatrix}. \tag{0.8}$$

For $\varphi = \pi$, Cφ is a controlled-$\hat{\sigma}_z$ operation (CZ), while CNOT is an alias of a controlled-$\hat{\sigma}_x$. Notice that, while controlled-gates generally require to distinguish control and target qubit, this is not the case for Cφ, which is symmetric (indeed expressed by a diagonal matrix) in the computational basis.
We finally mention a widely used class of two-qubit gates which originates from exchange interactions between the qubit. This happens in many physical implementations of quantum computation. Imagine that the hardware consists of a couple of qubits interacting via the Hamiltonian: $\hat{H}_{12}/\hbar = J_x \hat{S}_{x,1}\hat{S}_{x,2} + J_y \hat{S}_{y,1}\hat{S}_{y,2} + J_z \hat{S}_{z,1}\hat{S}_{z,2}$ and that we are able to turn on and off this interaction at will. Then, the two qubits undergo the unitary evolution $e^{-i\hat{H}_{12}t}$, represented by the matrix

$$U_J = \begin{pmatrix} e^{iJ_z t/2}\cos\frac{J_x - J_y}{4}t & 0 & 0 & i\, e^{iJ_z t/2}\sin\frac{J_x - J_y}{4}t \\ 0 & \cos\frac{J_x + J_y}{4}t & i\sin\frac{J_x + J_y}{4}t & 0 \\ 0 & i\sin\frac{J_x + J_y}{4}t & \cos\frac{J_x + J_y}{4}t & 0 \\ i\, e^{iJ_z t/2}\sin\frac{J_x - J_y}{4}t & 0 & 0 & e^{iJ_z t/2}\cos\frac{J_x - J_y}{4}t \end{pmatrix}. \tag{0.9}$$

for the amount of time t the interaction was on. The gating capabilities derive from its entangling properties [12]. The operators known as *perfect entanglers* are able to generate a maximally entangled state (such as a Bell state) from a separable state. The two-qubit entanglement can be quantified by means of the *concurrence* ($\mathcal{C}$) [13]. For a mixed state of two qubits, the concurrence is defined as

$$\mathcal{C} \equiv \max\ (0, \lambda_1 - \lambda_2 - \lambda_3 - \lambda_4)\,, \tag{0.10}$$

where $\lambda_1, ..., \lambda_4$ are the eigenvalues, in decreasing order, of the Hermitian operator $\hat{R} = \sqrt{\sqrt{\hat{\rho}}\hat{\tilde{\rho}}\sqrt{\hat{\rho}}}$, with $\hat{\tilde{\rho}} = (\hat{\sigma}_y \otimes \hat{\sigma}_y)\,\hat{\rho}^*\,(\hat{\sigma}_y \otimes \hat{\sigma}_y)$. The concurrence is an entanglement monotone: a separable state exhibits no entanglement at all ($\mathcal{C} = 0$), while, e.g., a Bell state exhibits maximal entanglement ($\mathcal{C} = 1$). CNOT and Cφ are perfect entanglers, while the performance of U_J varies depending on t. For instance, if we consider an XY interaction between the two qubits ($J_x = J_y = \tilde{J}$, $J_z = 0$) and we choose $t = \pi/2\tilde{J}$, we get the $\sqrt{\text{iSWAP}}$ gate (SQiSW):

$$U_{SQiSW} = \begin{pmatrix} 1 & 0 & 0 & 1 \\ 0 & 1/\sqrt{2} & i/\sqrt{2} & 0 \\ 0 & i/\sqrt{2} & 1/\sqrt{2} & 0 \\ 1 & 0 & 0 & 1 \end{pmatrix}, \tag{0.11}$$

which is a perfect entangler. This form of the qubit-qubit interaction is common to many implementation, ranging from spin-qubits to the superconducting qubits dispersively coupled via a photon bus. Several other two-qubit gates exist, but often they are not perfect-entanglers, thus increasing the overall depth of quantum circuits.

It is worth including in this overview also an important three-qubit gate: the Toffoli gate, which flips the third qubit, the target qubit, conditioned on the first two qubits, the control qubits, being set to $|1\rangle$. It is, indeed, a controlled-controlled-NOT gate. Its importance originates from its role in many quantum error correction algorithms. While it is always possible, in principle, to build any N-qubit gate starting from single- and two-qubit operations, this can be sometimes cumbersome. For instance, decomposing the Toffoli gate requires five two-qubit gates. Hence, the possibility of directly implementing it within a quantum computing architecture makes the whole computation much more efficient, as illustrated in the case of our hybrid spin-photon device in Section 10.3. Moreover, the Toffoli gate constitutes a universal set by itself, without requiring single-qubit rotations.

0.1.3 Principles of quantum computation

Our aim now is to use our quantum processor to compute the result of a given function f, acting on a given string of qubits a. Ideally, this would produce the unitary transformation:

$$|a\rangle \rightarrow \hat{U}|a\rangle = |f(a)\rangle, \tag{0.12}$$

where a is any desired binary number. The final measurement of each qubit would give the desired value of $f(a)$. We note, however, that this is not allowed for all possible functions. Indeed, since unitary transformations preserve the overlap between any pair of states, not-injective functions are such that $\hat{U}|a\rangle \neq |f(a)\rangle$, and hence cannot be implemented [1]. In order to be able to compute any function, we introduce an auxiliary qubit string prepared in a state $|b\rangle$:

$$|a\rangle \otimes |b\rangle \rightarrow \hat{U}|a\rangle \otimes |b\rangle = |a\rangle \otimes |b \oplus f(a)\rangle. \tag{0.13}$$

Here $b \oplus f(a)$ represents a string where each bit is given by the modulo 2 addition of the corresponding bit in the strings b and $f(a)$. We can easily verify that the states $|a_1\rangle \otimes |b \oplus f(a_1)\rangle$ and $|a_2\rangle \otimes |b \oplus f(a_2)\rangle$ are now orthogonal even if $f(a_1) = f(a_2)$. By

---

[1] If $|a_1\rangle \neq |a_2\rangle$, then $0 = \langle a_1|a_2\rangle = \langle a_1\hat{U}^\dagger\hat{U}|a_2\rangle$. However, for not-injective functions there exist $|a_1\rangle \neq |a_2\rangle$ such that $|f(a_1)\rangle = |f(a_2)\rangle \Rightarrow |\langle f(a_1)|f(a_2)\rangle| = 1$. Hence, at least for some a, $\hat{U}|a\rangle \neq |f(a)\rangle$.

choosing $b = 0$ a measurement of the final state of the second string of qubits directly reveals the required function $f(a)$.
The power of a quantum computer originates from its intrinsic *quantum parallelism*. This can be exploited by considering an input state given by the superposition of many numbers a. For instance, we can obtain it by initializing the computer with all the qubits in $|0\rangle$ and then applying Hadamard gates to bring each of them into $(|0\rangle + |1\rangle)/\sqrt{2}$:

$$|0\rangle^{\otimes N} \rightarrow \frac{1}{2^{N/2}}(|0\rangle + |1\rangle) \otimes (|0\rangle + |1\rangle) \otimes \cdots \otimes (|0\rangle + |1\rangle) = \frac{1}{2^{N/2}} \sum_{a=0}^{2^N-1} |a\rangle. \tag{0.14}$$

Then the quantum processor calculates simultaneously the values of $f(a)$ for all a, meaning that states corresponding to all of these values are present in the final state:

$$\frac{1}{2^{N/2}} \sum_{a=0}^{2^N-1} |a\rangle \otimes |0\rangle \rightarrow \frac{1}{2^{N/2}} \sum_{a=0}^{2^N-1} |a\rangle \otimes |f(a)\rangle. \tag{0.15}$$

Here the auxiliary qubit has been prepared in $|0\rangle$. Performing the unitary transformation with an array of quantum gates requires a time that is polynomial in N. However, the prepared state contains a superposition of 2^N computed values, so our processor has performed an exponential (in N) number of calculations in a polynomial time.
Useful quantum algorithms are known which exploit the *quantum parallelism* to solve problems that are intractable for classical devices. Among these, the most famous is probably Shor's factoring algorithm. Its power relies on the capability of a quantum computer of determining the period of a periodic function in a polynomial time, by means of the quantum Fourier transform. This can be implemented on N qubits by a total of N Hadamard gates plus $N(N-1)/2$ controlled-phase gates. We refer to [11] for a detailed treatment. Here we only recall the effect of the quantum Fourier transform ($\hat{U}_{QFT}$) on a given string of qubits $|b\rangle$:

$$|b\rangle \rightarrow \hat{U}_{QFT}|b\rangle = \frac{1}{2^{N/2}} \sum_{a=0}^{2^N-1} e^{i\frac{2\pi}{2^N}ab}|a\rangle. \tag{0.16}$$

As above, $|a\rangle \equiv |a_1 a_2 \dots a_N\rangle$ and $|b\rangle \equiv |b_1 b_2 \dots b_N\rangle$ represent a binary string of qubits. The sequence of gates corresponding to the quantum Fourier transform will be simulated in Section 11.5 on a chain of three hybrid spin-photon qubits.

0.1.4 Distance measures for quantum information

We introduce here two important functionals which can be used as figures of merit for the accuracy of the implemented quantum gates: the fidelity and the trace distance. They are quantum operations quantifying the proximity and the distance between quantum states, respectively [11]. They can be used to test the performance of the quantum computing architecture by comparing the target state and the final density matrix obtained in the implementation of quantum algorithms. Errors can arise from gate imperfection or from decoherence.
The most widely used figure of merit is the fidelity, defined as:

$$\mathcal{F}(\hat{\rho}, |\psi\rangle\langle\psi|) \equiv \sqrt{\langle\psi|\hat{\rho}|\psi\rangle}, \tag{0.17}$$

where $\hat{\rho}$ is the final density matrix induced by the implementation of quantum gates and $|\psi\rangle$ is the target state. With the same notation, the trace distance is given by

$$\mathcal{T}(\hat{\rho}, |\psi\rangle\langle\psi|) \equiv \frac{1}{2}\text{tr}||\,\hat{\rho} - |\psi\rangle\langle\psi|\,||, \tag{0.18}$$

where $||\hat{A}|| \equiv \sqrt{\hat{A}^\dagger \hat{A}}$ is the positive square root of $\hat{A}^\dagger \hat{A}$. Both $\mathcal{T}$ and $\mathcal{F}$ are positively defined and ≤ 1. A perfect gate is the one maximizing the fidelity, while leading to vanishing values of the trace distance. In the definitions above we have measured the distance between a real (mixed) state, represented by the density operator $\hat{\rho}$ and a pure state (the target), represented by the ket $|\psi\rangle$, or, equivalently, by the density operator $|\psi\rangle\langle\psi|$.

For two given quantum states $\hat{\rho}$ and $\hat{\sigma}$, fidelity and trace distance are related by the inequalities:

$$1 - \mathcal{F}(\hat{\rho}, \hat{\sigma}) \leq \mathcal{T}(\hat{\rho}, \hat{\sigma}) \leq \sqrt{1 - \mathcal{F}(\hat{\rho}, \hat{\sigma})^2}. \tag{0.19}$$

0.1.5 Quantum Simulation

If our target is not a *general purpose*, but a *dedicated* Quantum Computer (QC), oriented to the solution of a specific problem, the requirements for the physical system are less demanding. One of the most appealing dedicated QCs is a quantum simulator. It is also probably one of the few applications of a quantum processor within the reach of present technology. Indeed, while several thousands or even millions of qubits are needed for the non-trivial implementation of quantum algorithms such as Shor's code for factoring large numbers in primes or Grover's search code, thus requiring an amazing degree of control on the hardware, only a few dozens of qubits would outperform a classical computer in simulating quantum systems. As suggested by Feynman in the early 80s *"Nature isn't classical, dammit, and if you want to make a simulation of nature, you'd better make it quantum mechanical, and by golly it's a wonderful problem, because it doesn't look so easy"*. The simulation of quantum systems by a classical computer is intrinsically inefficient because the required number of bits grows exponentially with the system size. This makes many important problems in physics and chemistry intractable with standard computational approaches and resources. Such a limitation might be overcome by quantum simulators (QSs), whose dynamics can be controlled so as to mimic the evolution of the target system [14]. The implementations of quantum simulators so far proposed essentially fall into one of two categories. In analog simulators a certain quantum system directly emulates another one, whereas in digital simulators the state of the target system is encoded in qubits and the time evolution of any target system can be discretized into a sequence of logical gates. Digital architectures are small, general purpose quantum computers. They are usually able to simulate broad classes of Hamiltonians, whereas analog ones are restricted to specific target problems. For a recent review on these different approaches, we refer to [15] and references therein.

The aim of this work is to propose architectures and efficient schemes for the implementation of a digital quantum simulator. Therefore, we now focus on the general problem of how to decompose the time evolution induced by any target Hamiltonian into a sequence of elementary steps, controlled by the experimenter, i.e., a sequence of one- and two-qubit gates. To this goal, we exploit the mathematical formalization introduced by Lloyd [16], who translated into quantum information perspectives Feynman's intuition. Most Hamiltonian of physical interest can be written as the sum of L local terms, $\hat{\mathcal{H}} = \sum_k^L \hat{\mathcal{H}}_k$. Hence, the system dynamics can be approximated by a sequence of local unitary operators according to the Trotter-Suzuki formula ($\hbar = 1$):

$$\hat{U}(t) = e^{-i\hat{\mathcal{H}}t} \approx (e^{-i\hat{\mathcal{H}}_1\tau} \cdots e^{-i\hat{\mathcal{H}}_L\tau})^n, \tag{0.20}$$

where $\tau = t/n$ and the total *digital* error of this approximation can be made as small as desired by choosing n sufficiently large [16]. Commuting terms in the Hamiltonian do not require any Trotter decomposition. In this way the simulation reduces to the sequential implementation of local unitary operators, each one corresponding to a small time interval t/n. This can be implemented by a proper sequence of single- and two-qubit gates. The problem then reduces to finding a suitable mapping between the physical hardware (consisting of many qubits, described by means of Pauli algebra) and the target Hamiltonian.

The mapping of $s = 1/2$ models onto an array of qubits is straightforward. Let's consider here two kinds of significant local terms in the target Hamiltonian, namely one- ($\hat{\mathcal{H}}^{(1)}_\alpha$) and two-body ($\hat{\mathcal{H}}^{(2)}_{\alpha\beta}$) terms, with $\alpha, \beta = x, y, z$. The unitary time evolution corresponding to one-body terms $\hat{\mathcal{H}}^{(1)}_\alpha = b\hat{s}_\alpha$ is directly implemented by single-qubit rotations $\hat{R}_\alpha(b\tau)$. Conversely, two-body terms describe a generic spin-spin interaction of the form $\hat{\mathcal{H}}^{(2)}_{\alpha\beta} = \lambda\hat{s}_{1\alpha}\hat{s}_{2\beta}$, for any choice of $\alpha, \beta = x, y, z$. The evolution operator, $e^{-i\hat{\mathcal{H}}^{(2)}_{\alpha\beta}\tau}$, can be decomposed as [17]

$$e^{-i\lambda\hat{s}_{1\alpha}\hat{s}_{2\beta}\tau} = [\hat{u}_{1\alpha} \otimes \hat{u}_{2\beta}]\, e^{-i\hat{\Lambda}\tau}\, [\hat{u}_{1\alpha} \otimes \hat{u}_{2\beta}]^\dagger\,, \tag{0.21}$$

with $\hat{\Lambda} = \lambda\hat{s}_{1z}\hat{s}_{2z}$, $\hat{u}_x = \hat{R}_y(\pi/2)$, $\hat{u}_y = \hat{R}_x(3\pi/2)$, $\hat{u}_z = \hat{I}$. The Ising evolution operator, $e^{-i\lambda\hat{s}_{1z}\hat{s}_{2z}\tau}$, can be obtained starting from the two-qubit Cφ gate and exploiting the identity (apart from an overall phase)

$$e^{-i\lambda\hat{s}_{1z}\hat{s}_{2z}\tau} = [\hat{R}_{\varphi/2,1} \otimes \hat{I}_2]\, \hat{U}_{C\varphi}\, [\hat{I}_1 \otimes \hat{R}_{\varphi/2,2}], \tag{0.22}$$

where $\varphi = \lambda\tau$. Here $\hat{R}_\varphi = e^{i\varphi/2}\hat{R}_z(\varphi)$ are phase gates, which can be simultaneously implemented on both the involved qubits [2].

Besides the trivial case of spin-1/2 Hamiltonians, most models of physical interest can be re-written in terms of spin-1/2 operators. For instance, the simulation of Hamiltonians involving $S > 1/2$ spins can be performed by encoding the state of each spin-S onto that of $2S$ qubits (as an example, see Sec. 10.2.1 for an implementation with hybrid spin-photon qubits).

Furthermore, fermionic creation and annihilation operators $\hat{c}^\dagger_j$, $\hat{c}_j$, can be expressed in terms of Pauli matrices by exploiting the Jordan-Wigner transformation:

$$\begin{aligned} \hat{c}^\dagger_j &= e^{i\pi\sum_{k=1}^{j-1}\hat{c}^\dagger_k\hat{c}_k}\hat{\sigma}^+_j \\ \hat{c}_j &= e^{-i\pi\sum_{k=1}^{j-1}\hat{c}^\dagger_k\hat{c}_k}\hat{\sigma}^-_j \\ \hat{c}^\dagger_j\hat{c}_j &= \frac{1}{2}\left(\hat{\sigma}^z_j + 1\right). \end{aligned} \tag{0.23}$$

Here $\hat{\sigma}^\pm_j = \left(\hat{\sigma}^x_j \pm \hat{\sigma}^y_j\right)/2$, with σ^α_j the Pauli matrices. This mapping ensures the correct fermionic anti-commutation relationships, $\left\{\hat{c}_j, \hat{c}^\dagger_k\right\} = \delta_{jk}$, $\{\hat{c}_j, \hat{c}_k\} = \left\{\hat{c}^\dagger_j, \hat{c}^\dagger_k\right\} = 0$.

---

[2] Being diagonal on the computational basis, all the unitary operators in the decomposition 0.22 commute. Therefore, rotations can be implemented simultaneously, without requiring a local control on each qubit.

The above transformation massively increases the class of addressable problems, including many-body electron Hamiltonians in Chemical Physics, as well as Hubbard, Kondo or Anderson models. The spin index of fermionic operators can also be accounted for by doubling the number of qubits. This mapping has, however, a serious drawback: the two-body interaction between fermions is transformed into a many-spin interaction, whose efficient implementation in a quantum simulation scheme is far from being trivial. We will show how this can be embedded in our hybrid spin-photon setup in Section 10.2.2.

0.2 Physical implementations

Up to now, most efficient protocols for QS have been proposed and experimentally realized with trapped ions [18, 19]. In this thesis we consider two promising architectures for quantum information processing and quantum simulation, which are based on available technology. We fully characterize the dynamics of these quantum systems by detailed numerical experiments, which include the most important sources of decoherence in a master equation formalism and, in some cases, envision possible ways to overcome them. The first one (introduced in Sec. 0.2.1 and discussed in detail in Part 1) is based on a family of molecular nanomagnets, which shows long coherence times and allows for a detailed physical characterization, as well as an extraordinary chemical control. The qubit-qubit coupling in these compounds can be manipulated either by local electric (in presence of a redox active unit which acts as a switch) or by global magnetic fields, exploiting the excitations of a magnetic linker to turn on and off the interaction. The second one (Sec. 0.2.2 and Part 2) is based on spin ensembles strongly coupled to single-photons within coplanar superconducting waveguide resonators. The striking technological advances in this field allow for high fidelity gates and a local control at the single-qubit level, thus increasing the amount of Hamiltonians which can be simulated.

0.2.1 Molecular Nanomagnets

Molecular nanomagnets (MNMs) [20] have been proposed as promising candidates for both spintronics [21, 22, 23] and quantum information processing (QIP) [4, 5, 6, 7, 8, 24, 9]. These are clusters containing a finite number of paramagnetic (typically $3d$) ions, whose spins are strongly coupled by Heisenberg exchange interactions. Magnetic cores of adjacent molecules are well separated from each other by a surrounding of organic ligands, so that inter-molecular interactions are negligible. Therefore, molecular crystals formed by these kind of metallorganic clusters behave like an ensemble of non-interacting identical molecules and it is possible to address the magnetic properties of a single molecule by bulk measurements. The attractiveness of MNMs stems from their wide tunability, both at the intermolecular and at the intramolecular level, and from the possibility of providing a detailed microscopic description in terms of a quantum spin Hamiltonian. Since exact precise calculations are often possible, MNMs constitute tunable model systems to study fundamental issues related to quantum phenomena, such as quantum tunneling, coherence, quantum-classical crossover. Moreover, many classes of MNMs have interesting technological applications. Among these, we recall the high-density storage of information in single-molecule magnets [25], the magnetocaloric refrigeration in high-spin isotropic systems [26], as well as quantum computation in effective $S = 1/2$ molecules [6, 27].

Among the most widely investigated systems for quantum information processing are even-numbered antiferromagnetic (AF) rings. Heterometallic rings with $S \neq 0$ can be obtained from an $S = 0$ homonuclear ring by chemical substitution of some magnetic centers. For instance, Cr_7M rings (M = Zn, Cd, Mn, Ni) are derived from the homometallic Cr_8 ring [28] by substitution of one divalent cation M = Zn, Cd, Mn, Ni for a trivalent Cr ion [29]. Cr_7Ni AF ring has been proposed as a good candidate qubit, since it is characterised by a $S = 1/2$ doublet ground state. Moreover, it is possible to enhance its decoherence time by proper chemical substitutions [30], reaching values above 10 μs. One-qubit operations have already been performed on ensembles of MNMs [31, 32, 33], in times much shorter than the observed coherence times, thus allowing the implementation of more complex algorithmic sequences.

In order to implement such sequences, the most direct way would be to use external fields varying in time and from qubit to qubit and an external tool to switch on and off the qubit-qubit couplings locally for two-qubit gates. This represents an extremely tough experimental challenge [7], which can be obtained by employing redox-active metal unit as a switch of the qubit-qubit interaction. Then molecules should be grafted onto surfaces without significantly modifying their properties (which has already been shown in some cases [34, 35]) and individually addressed by an electric TIP.

A less demanding approach is to use uniform magnetic fields to induce the required time evolution of the register, by exploiting auxiliary states and the structure of intermolecular interactions [27, 36, 17]. This quantum computation scheme [17] is based on two classes of MNMs that play two distinct roles: effective $S = 1/2$ spins are used to encode the qubits, whereas interposed complexes with a singlet ground state are used as switches of the effective qubit-qubit interaction. In particular, by an appropriate topology and hierarchy of exchange couplings between different molecular units, it would be possible to use uniform pulses to switch on and off intermolecular interactions, thus implementing two-qubit gates and quantum simulation algorithms. However, the engineering of potentially scalable supramolecular complexes fitting these requisites has proven a very hard chemical task.

In the present work we explore both these challenging routes towards the actual implementation of quantum computation with molecular nanomagnets, in which the qubit-qubit interaction is controlled either locally (with electric field gradients) either globally (with uniform magnetic fields). We propose different schemes that can implement a universal set of quantum gates on specific molecular systems, which have been properly synthesized to fit specific requirements. These systems are characterized with detailed measurements and ab-initio calculations and their performance as quantum information units has been tested with numerical experiments which include the harmful effect of decoherence.

0.2.2 Circuit Quantum-Electrodynamics

The second part of the work concerns the investigation of a hybrid architecture consisting of spin ensembles (notably, MNMs) coupled to superconducting resonators. Circuit quantum electrodynamics (cQED) systems are engineered, macroscopic quantum systems in which (artificial) atoms or molecules interact with quanta of the electromagnetic field. Conceived in 2004 by Blais et al. [37] and Wallraff et al. [38], circuit QED has already proved to be a versatile testbed for fundamental quantum physics and a promising platform for processing quantum information. The tremendous progress of the experimental technology has led to circuit QED architectures with multiple components and steadily increasing coherence times, as well as a high level of control provided by microwave fields. These solid-state approaches attempt to define and address the qubits on a chip, similarly to the transistors which are now packed into an integrated circuit on

a silicon microprocessor.
Large lattices of superconducting resonators have already been realized and demonstrated as quantum simulators [39, 40]. Quantum gates operating with superconducting qubits such as transmons or Cooper-pair boxes have been experimentally realized either in the dispersive [41] or in the semi-resonant regime [42]. Classical microwave fields, together with the tunability of the qubit transition frequencies, are used as manipulation tools. However, the scalability of these architectures and the implementation of complex quantum algorithms is still limited by the coherence time of superconducting qubits, which do not exceeds tens of μs.
To overcome this problem, in this work we introduce a hybrid spin-photon qubit encoding, which exploits the best characteristics of distinct physical systems. Indeed, as a classical computer is made of a variety of physical components specialized for different tasks, a quantum computer will probably be a similarly hybrid device. In this spirit, much work has recently been done to achieve strong coupling of high-quality factor coplanar-waveguide resonators with superconducting qubits, such as Cooper-pair boxes (CPBs) [38, 41, 43] and transmons [44] and/or spin ensembles (SEs) [45, 46]. In our hybrid encoding, spin ensembles are not used only as a memory for information storage. Conversely, spins and photons enter on an equal footing in the definition of the qubits. This allows us to exploit the best characteristics of the different components, namely the long coherence times of the spins, which can encode quantum information and protect it from decoherence, the nonlinearity and fast control ensured by the transmon devices and the mobility of photons entering this hybrid encoding. As shown throughout this work, on-site tunability and scalability make this architecture extremely promising.
Hybrid setups consisting of ensembles of MNMs coupled to photons into superconducting resonators can also be envisaged. Indeed, by employing properly designed MNMs instead of single spins (such as rare-earth ions or nitrogen vacancies) one could reach the strong coupling with the resonator with a reduced number of spins in the ensemble (ideally with a single molecule). Moreover, combining the strong spin-resonator coupling with the use of degrees of freedom protected from the environment would allow us to overcome both spin dephasing and inhomogeneous broadening of the molecular ensemble.

0.3 Thesis overview

The work is divided in two parts, joined by the common aim of finding a physical implementation of quantum computation. The first one is devoted to Molecular Nanomagnets. The theoretical framework and the experimental techniques used to characterize these systems are introduced in Chapter 1 and 2, respectively. In the following Chapters 3 and 4 two schemes for quantum information processing with MNMs are proposed. The former employs uniform magnetic pulses to control the qubit-qubit interaction, while the latter uses local electric fields. Both these schemes are applied to existing MNMs, which have been extensively characterized by ab-inito calculations and by EPR spectroscopy. A detailed first-principle investigation of a family of anti-ferromagnetic molecular wheels, containing also some promising qubits, is reported in Chapter 5. This study employs a novel ab-initio approach to build many-body models for MNMs, explicitly including strong electron-electron correlations and deriving the full spin Hamiltonian without any assumption on its form. Modeling the interaction of MNMs with the environmental degrees of freedom is of crucial importance for their use as quantum devices. This is the topic of Chapter 6, where the anti-ferromagnetic ring Cr_8Zn is characterized by thermo-

dynamic and EPR measurements and the behaviour of its coherence time is modeled by taking into account dipolar, hyperfine and spin-phonon interactions. MNMs are also attractive for studying fundamental magnetic phenomena, such as frustration. In Chapter 7 we present a study of two newly-synthesized anti-ferromagnetic odd-numbered rings which manifest a somewhat frustrated behaviour: Cr_8Mn and Cr_9.
In the second part of the thesis we present a hybrid setup, which is based on spin ensembles coupled to superconducting resonators. The basics of circuit Quantum Electrodynamics, as well as the state of the art of quantum computation with superconducting circuits are overviewed in Chapter 8. The novel hybrid spin-photon encoding is introduced in the following Chapter 9. Here we also simulate one- and two-qubit gates with state-of-the-art parameters, thus demonstrating the performance of the proposed setup. In Chapter 10 this platform is used as a digital quantum simulator of interesting physical models. Finally, Chapter 11 presents a scheme to overcome the detrimental effect of inhomogeneous broadening of the spin ensemble, thus enhancing the spin ensemble coherence times of orders of magnitude and enabling the implementation of long sequences of gates.

Part I

Molecular Nanomagnets

Theoretical Framework

CHAPTER 1

In this chapter we introduce the theoretical methods which have been used throughout the work to study Molecular Nanomagnets. The approach is twofold: on the one hand, the spin Hamiltonian description provides in most cases a good, simple and effective picture of the investigated systems. On the other hand, it is sometimes crucial to understand the origin and hierarchy of the dominant magnetic interactions starting from a more fundamental perspective. To this aim we have introduced a flexible and efficient scheme which allows us to deduce from first principles the model spin Hamiltonian, no matter the complexity of the system. This approach could become essential for modeling MNMs whose spin Hamiltonian contains many anisotropic terms, which cannot be directly inferred from experiments.

1.1 Many-Body Models

We present here a flexible and effective *ab-initio* scheme to build many-body models for molecular nanomagnets, and to calculate the magnetic couplings entering the spin Hamiltonian [47]. If the form of the spin Hamiltonian is known, the magnetic couplings can be in principle extracted from total-energy density-functional theory calculations for different spin configurations [48, 49, 50, 51, 52, 53]. This approach can become unpractical if many parameters have to be determined, as, e.g., in heterometallic compounds or anisotropic MNMs; furthermore, subtle interactions, which could greatly influence, e.g., the relaxation dynamics, can be easily overlooked. An alternative consists in computing the couplings via energy variations at small spin rotations [54]. However, at a more fundamental level, a common problem of all these approaches is that the most used density-functional theory functionals (the local-density approximation (LDA) and its simple extensions), do not properly describe strong correlation effects in open d or f shells, while LDA + U or hybrid functionals include them only at the static mean-field level [55].

Conversely, we use localized Foster-Boys orbitals [56] as a one-electron basis to construct

molecule-specific generalized Hubbard models, in which strong electron-electron correlation effects are explicitly included. We use the constrained local-density approximation (cLDA) scheme [57] to calculate the screened Coulomb interactions in such a Foster-Boys basis. In a second step, we obtain the spin Hamiltonian systematically by using a canonical transformation [58] to eliminate charge fluctuations, without any a priori assumption on its form. A similar scheme is followed in the solid state, using Wannier orbitals to describe local correlations in periodic structures [59].
We adopt the following procedure. First we perform LDA calculations using a triple-zeta valence basis set of Gaussians. We employ the experimental structures determined by X-ray diffraction, without geometry optimization. Then we identify the transition metal $d-$like orbitals and we localize them by means of the Foster-Boys method [56]. This minimizes the spatial extent of the orbitals by maximizing the function $\sum_{i>j} |\langle\psi_i|\mathbf{r}|\psi_i\rangle - \langle\psi_j|\mathbf{r}|\psi_j\rangle|^2$, expressed in terms of the Kohn-Sham orbitals $|\psi_i\rangle$. In this way we obtain a set of localized orbitals, centered on the metal ions and describing the low energy $d-$subspace. Using these orbitals we construct the corresponding generalized Hubbard model:

$$\begin{aligned} \hat{H} &= -\sum_{ii'\sigma}\sum_{mm'} t^{i,i'}_{m,m'} \hat{c}^{\dagger}_{im\sigma}\hat{c}_{i'm'\sigma} \\ &+ \frac{1}{2}\sum_{ii'\sigma\sigma'}\sum_{mm'}\sum_{pp'} U^{i,i'}_{mpm'p'} \hat{c}^{\dagger}_{im\sigma}\hat{c}^{\dagger}_{i'p\sigma'}\hat{c}_{ip'\sigma'}\hat{c}_{i'm'\sigma} \\ &+ \sum_i \lambda_i \sum_m \hat{\mathbf{s}}_{im}\cdot\hat{\boldsymbol{\ell}}_{im} - \hat{H}_{DC}. \end{aligned} \tag{1.1}$$

Here $\hat{c}^{\dagger}_{im\sigma}$ ($\hat{c}_{im\sigma}$) creates (annihilates) an electron with spin σ in the Boys orbital m at site i. The parameters $t^{i,i'}_{m,m'}$ are the hopping integrals ($i \neq i'$) or the crystal-field matrix ($i = i'$), while $U^{i,i'}_{mpm'p'}$ are the screened Coulomb integrals. The term $\hat{H}_{DC}$ is the double counting correction, which removes the part of the Coulomb interaction already included and well accounted for in the LDA; λ_i is the spin-orbit coupling, assumed to be the same for all the electrons within the same ion. The results presented in this work are obtained, for simplicity, neglecting Coulomb anisotropy and terms in $U^{i,i'}_{mpm'p'}$ with more than two orbital indices. In this case (for d electrons) all parameters can be expressed as a function of the averaged screened Coulomb couplings $U^{i,i}$ and $\mathcal{J}^{i,i}$, which, in turn, depend only on the Slater integrals F_0, F_2 and F_4 [60]; the average screened direct Coulomb integral for site i is $U^{i,i} = F_0$ and the average screened exchange integral is defined as $\mathcal{J}^{i,i} = (F_2 + F_4)/14$. Finally, we use the rotational invariant form of the Coulomb vertex, including spin-flip and pair hopping terms. Then the Hamiltonian (1.1) reduces to

$$\begin{aligned} \hat{H} &= -\sum_{ii'\sigma}\sum_{mm'} t^{i,i'}_{m,m'} \hat{c}^{\dagger}_{im\sigma}\hat{c}_{i'm'\sigma} + \sum_{i,m} U^{i,i}\hat{n}_{im\uparrow}\hat{n}_{im\downarrow} \\ &+ \frac{1}{2}\sum_{i\sigma\sigma'}\sum_{m\neq m'} (U^{i,i} - 2\mathcal{J}^{i,i} - \mathcal{J}^{i,i}\delta_{\sigma,\sigma'})\hat{n}_{im\sigma}\hat{n}_{im'\sigma'} \\ &- \sum_{i,m\neq m'} \mathcal{J}^{i,i}\left[\hat{c}^{\dagger}_{im\uparrow}\hat{c}^{\dagger}_{im\downarrow}\hat{c}_{im'\uparrow}\hat{c}_{im'\downarrow} + \hat{c}^{\dagger}_{im\uparrow}\hat{c}_{im\downarrow}\hat{c}^{\dagger}_{im'\downarrow}\hat{c}_{im'\uparrow}\right] \\ &+ \sum_i \lambda_i \sum_m \hat{\mathbf{s}}_{im}\cdot\hat{\boldsymbol{\ell}}_{im} - \hat{H}_{DC}. \end{aligned} \tag{1.2}$$

Here $\hat{n}_{im\sigma} = \hat{c}^{\dagger}_{im\sigma}\hat{c}_{im\sigma}$ is the fermionic number operator. The terms on the third line describe the pair hopping and spin-flip processes and are essential to determine the correct structure of the spin multiplets. The screened Coulomb couplings are calculated by using the cLDA [57] approach in the Foster-Boys basis (see below). For $\hat{H}_{DC}$ we adopt the common expression for the paramagnetic case [60], $H_{DC} = \frac{1}{2}\sum_i U^{i,i} n_d^i(n_d^i - 1) - \frac{1}{2}\sum_i \mathcal{J}^{i,i} n_d^i(\frac{1}{2}n_d^i - 1)$, where n_d^i is the number of d electrons at site i. Finally, we extract the spin-orbit coupling λ_i by comparing the one-electron part of Hamiltonian (1.2) obtained with and without spin-orbit interaction.

Once we have obtained the parameters of the Hubbard model, by using a canonical transformation, we eliminate charge fluctuations and derive the corresponding low-energy spin model. This is possible in the limit $|t^{i,i'}_{m,m'}| \ll U^{i,i}$, which is usually the case for MNMs containing transition metal ions ($|t^{i,i'}_{m,m'}| \approx 10 - 100$ meV, while $U^{i,i} \approx$ several eV).

1.1.1 Determination of hopping and Coulomb integrals from first principles

We illustrate here the procedure we apply to calculate the hopping and Coulomb integrals of the generalized Hubbard model 1.2 from first principles. The method is based on DFT (see Appendix A) self-consistent runs in local density approximation (LDA) and constrained local density approximation (cLDA). Self-consistent calculations for these big molecules (from two to several hundreds of atoms) are very time consuming. We employ the NWChem quantum chemistry code [61], which is optimized to exploit the power of modern massively parallel supercomputers. Calculations are performed in direct space, using a linear superposition of Gaussians as a one electron basis to approximate the atomic orbitals.

First, a self-consistent closed-shell DFT run is performed in LDA, based on the following steps [62]:

- Specify a molecule (a set of nuclear coordinates, atomic numbers and number of electrons).
- Choose an *atomic* basis set, $\{|\phi_\mu\rangle\}$. In this step we use as basis a triple-zeta valence set of Gaussians.
- Calculate the many-body wave-function, as the Slater determinant obtained from the product of the doubly-occupied one-electron orbitals, and the initial electron density.
- Calculate also all required one-electron and two-electron integrals, starting from the initial guess for the density.
- The atomic orbitals do not form an orthonormal set. Hence, we orthogonalize the basis by computing the overlap matrix $S_{\mu\nu} = \langle\phi_\mu|\phi_\nu\rangle$ and the orthogonalization matrix $X = S^{-1/2}$.
- Calculate the system Hamiltonian (whose potential depends on the electron density) and rotate it in the orthogonal basis.
- Diagonalize the Hamiltonian.
- Form the new density from the eigenvectors of the Hamiltonian and the new potential.

- Repeat until convergence.

Starting from the Kohn-Sham orbitals obtained from the converged DFT run, we identify the subset of correlated states (typically d-states, close to the Fermi level) and we apply the Foster-Boys localization onto this subspace in order to get a localized one-electron basis $\{|\beta_{im}\rangle\}$ to construct molecule-specific generalized Hubbard models (Eq. 1.1). The hopping integrals are calculated as $t^{i,i'}_{m,m'} = \langle\beta_{im}|\hat{h}|\beta_{i'm'}\rangle$, where $|\beta_{im}\rangle$ is the m Boys orbital on atom i and $\hat{h}$ is the one-body Hamiltonian obtained at the end of the self-consistent LDA calculation. In the following, it is convenient to work in the basis of crystal-field (CF) one-electron states $|\xi_{ik}\rangle$. These are obtained as the eigenstates of the on-site hopping matrices $t^{i,i}_{m,m'}$. The corresponding splitting of the crystal-field eigenvalues ε^i_k reflect the symmetry of the ligand field on the examined site.
$U^{i,i}$ and $\mathcal{J}^{i,i}$ (appearing in Eq. 1.2) are deduced ab-initio by perfoming analogous LDA calculations with different occupancies $n_{im\sigma}$ of the CF states, a procedure known as constrained LDA. This gives a contribution to the total energy that is occupancy-dependent: $E_{\{n_{im\sigma}\}} \propto \sum_{i,m} U^{i,i} n_{im\sigma} n_{im-\sigma} + \sum_{i\sigma\sigma'}\sum_{m\neq m'}(U^{i,i} - 2\mathcal{J}^{i,i} - \mathcal{J}^{i,i}\delta_{\sigma,\sigma'}) n_{im\sigma} n_{im'\sigma'}$. Here we are including only density-density terms of the Coulomb tensor. Therefore, once the hoppings have been cut, the Hamiltonian (1.2) is diagonal and the energy is computed straightforwardly. By performing various total energy calculations with different sets of $\{n_{im\sigma}\}$ we can extract $U^{i,i}$ and $\mathcal{J}^{i,i}$. In the code the procedure is the following:

1. Start from a previously converged LDA run and from a set of already determined CF orbitals. Suppose that $\hat{D}$ is the transformation from the atomic basis $\{|\phi_\mu\rangle\}$ to the localized CF one $\{|\xi_{im}\rangle\}$.

2. Calculate the Hamiltonian $\hat{H}$ in the atomic basis set $\{|\phi_\mu\rangle\}$.

3. Rotate it to the localized basis, getting $\hat{H}' = \hat{D}^\dagger \hat{H} \hat{D}$.

4. Cut all the inter-site hoppings, setting by hand $(\hat{H}')_{ij} = 0$ for (i, j) belonging to the subspace of correlated electrons. In this way the hopping term is excluded from the calculation of the total energy, which is not renormalized by the motion of correlated electrons.

5. Now we need to fix the occupancy of the CF states. This is done by changing the occupancy n^d_{im} of the $|\xi_{im}\rangle$ orbitals. The superscript d is introduced to emphasize the $d-$character of the correlated electrons.

6. With the modified occupations of the correlated electrons we can calculate the density:
$$n(\mathbf{r}) = 2\sum_k |\psi_k(\mathbf{r})|^2 + \sum_{im} n^d_{im} |\xi_{im}(\mathbf{r})|^2 , \tag{1.3}$$
where the first sum is over the core, doubly occupied orbitals, while the second is on the correlated, localized ones, with occupancies modified by hand.

7. Finally we rotate back the eigenvectors from the CF states to the Kohn-Sham orbitals and go on with the self-consistent calculation. In this way the new Hamiltonian and its expectation value on the ground many-body state (total energy) are calculated according to the new modified density 1.3.

We stress that the procedure is implemented self-consistently, so that the core electron density can readjust due to the change of the occupancies of the correlated electrons, belonging to the localized orbitals, which are kept fixed during the calculation. At the end of the self-consistent cycle, the total energy is obtained as a function of the occupancies of the CF states.

Long-range correlations, which are already included in the LDA calculation, need to be subtracted from the generalized Hubbard model, in order to avoid double counting. LDA accounts for such long-range correlation at a static, mean-field level. Hence, here we adopt the common mean-field expression for $H_{DC} = \frac{1}{2}\sum_i U^{i,i} n_d^i (n_d^i - 1) - \frac{1}{2}\sum_i \mathcal{J}^{i,i} n_d^i (\frac{1}{2} n_d^i - 1)$. Here n_d^i is the LDA occupancy of site i. For homonuclear systems such correction amounts to a shift of the d levels $\varepsilon_n^i \to \varepsilon_n^i + \Delta\varepsilon_n^i$, where $\Delta\varepsilon_n^i = -U^{i,i}(n_d^i - \frac{1}{2}) + \mathcal{J}^{i,i}(\frac{1}{2} n_d^i - \frac{1}{2})$ which is the same for all sites and orbitals, and and can be incorporated in the chemical potential. In the case of heteronuclear compounds, instead, the shift is different for d levels of different sites (due to different LDA occupancy and/or different Coulomb integrals) and H_{DC} has to be taken into account explicitly.

Spin-orbit calculations are somewhat cumbersome and very time consuming, due to the doubling of the basis set required to include the spin index. We use the Zeroth Order Relativistic Approximation (ZORA) of the Dirac equation [63] to account for spin-orbit coupling. We model it as an on-site effect acting on the Kohn-Sham orbitals: $\hat{H}_{SO}^i = \lambda_i \sum_m \hat{\boldsymbol{\ell}}_{im} \cdot \hat{\boldsymbol{s}}_{im}$. We deduce the spin orbit coupling by comparing the CF one-electron energy levels ε_m obtained in the non relativistic and relativistic calculations. To do this, we employ a generalization of the Boys localization to deal with complex matrices [1]. Due to the computational complexity of the self-consistent relativistic calculations, in some cases we use the typical values for λ_i reported in Ref. [64] for single ions in a proper crystal-field cage. Otherwise, we employ the value we previously obtained self-consistently for the same ion in a similar environment.

1.1.2 Derivation of the spin Hamiltonian

In $3d$ molecular nanomagnets, one usually finds that the essential spin interactions are described by the spin Hamiltonian

$$H = \sum_{i,j} \hat{\mathbf{s}}_i \cdot \underline{\mathbf{J}}_{ij} \cdot \hat{\mathbf{s}}_j + \sum_i \hat{\mathbf{s}}_i \cdot \underline{\mathbf{D}}_i \cdot \hat{\mathbf{s}}_i \tag{1.4}$$

where $\underline{\mathbf{J}}_{ij}$ is the exchange coupling tensor between ions i and j and $\underline{\mathbf{D}}_i$ is the local zero-field splitting (ZFS) tensor. For molecules containing transition metal ions, the leading interaction is usually the isotropic exchange, J_{ij}. Other terms appearing in $\underline{\mathbf{J}}_{ij}$, such as anisotropic or antisymmetric exchange interactions, originate from spin-orbit interactions and can also be extracted by the present method (see Chapter 5).

The coupling $J_{ij} = J_{ij}^{CE} + J_{ij}^{SE}$ is the sum of a ferromagnetic (FM) screened Coulomb exchange term, J_{ij}^{CE}, which we obtain via cLDA calculations, and a super-exchange term J_{ij}^{SE}, which can be FM or antiferromagnetic (AFM). The ZFS local tensor $\underline{\mathbf{D}}_i$ originates from the combined action of crystal-field and spin-orbit interactions. The full tensor can be determined by considering the action of the spin-orbit term in the ground spin multiplet, obtained by diagonalizing the local Coulomb part of Hamiltonian (1.2). Then we

---

[1] The Foster-Boys localization is based on an algorithm which proceeds iteratively over pair of states (applying the so-called two-by-two Jacobi-sweeps) and is written for real matrices. Indeed, in the absence of spin-orbit interaction, the eigenvectors of the molecular system can always be recast in real form.

project the spin-orbit term onto Stevens spin operators, which for $3d$ ions reduce to second order terms $\hat{s}_{i,\alpha}\hat{s}_{i,\beta}$ $(\alpha, \beta = x, y, z)$. The calculated $D_i^{\alpha,\beta} \sim \lambda_i^2/(n\mathcal{J}^{i,i} + \Delta\varepsilon)$, where $\Delta\varepsilon$ is a difference between single-electron crystal-field eigenvalues and n is a system-specific integer number.

In the reference frame which diagonalizes $\underline{\mathbf{D}}_i$ the zero-field splitting interaction can be expressed as a function of an axial and a rhombic term:

$$\hat{\mathbf{s}}_i \cdot \underline{\mathbf{D}}^i \cdot \hat{\mathbf{s}}_i = d_i \left[\hat{s}_{i,z}^2 - \frac{1}{3}s_i(s_i+1)\right] + e_i \left[\hat{s}_{i,x}^2 - \hat{s}_{i,y}^2\right]. \tag{1.5}$$

Notice that d_i is negative if z is an easy axis (see Sec. 1.2.1 below).

Our approach allows us to derive also the $\underline{\mathbf{g}}_i$ tensor on each magnetic ion (see application of this method in Chapter 5). To obtain it we need to evaluate the matrix elements of the orbital angular momentum onto the ground spin multiplet states $|S, M\rangle$, corrected to first order in the spin-orbit interaction. Then we compare them with the spin matrices of rank S and we extract the correction $\Delta\mathbf{g}$ to the isotropic $\mathbf{g} = 2I$. Notice that $\underline{\mathbf{g}}_i$ is diagonal in the reference frame which diagonalizes $\underline{\mathbf{D}}_i$.

Differently than spin-configurations based approaches, the method outlined above allows us to determine the spin model without a priori assumptions on the form and the range of the Hamiltonian. Furthermore, since it yields the parameters of the Hubbard model, it works also when charge fluctuations are sizeable and the spin is not well defined, like for molecules with metal-metal bonds, or when electrons are less localized, such as in $4d$ and $5d$ systems, and can be used to calculate spectral functions. This scheme is flexible, its complexity does not increase when the symmetry is low, and it does not rely on the B3LYP or LDA + U approximation to correlation effects. It could become essential for modeling MNMs whose spin Hamiltonian contains many anisotropic terms, in particular if the principal-axis directions and relative magnitude cannot be inferred simply by inspecting the molecular structure, as is often the case for Co or f-electrons systems. In such situations, a more systematic approach is needed to deduce the final low-energy Hamiltonian from the generalized Hubbard model 1.1. Molecules containing $4d$ or Co ions often cannot be described as spin-only due to the absence of quenching of the orbital angular momentum and/or sizeable spin-orbit interaction. If the hopping term is still small, the general form of the exchange tensor can be obtained by considering its effect as a perturbation on many-body single-ion states obtained by diagonalizing the on-site part of Hamiltonian 1.1 (including spin-orbit). This procedure will be described in detail in Chapter 5.

1.2 Spin Hamiltonian

The ab-initio approach introduced above is important to obtain an initial guess of the hierarchy of the magnetic interactions. Once we have a system-specific model, the spin Hamiltonian (SH) description offers an accurate, simple and effective way to directly compare with experiments, thus obtaining a fit of the leading couplings. This formalism is based on the assumption that each magnetic ion in the molecule can be represented by an effective spin and it allows us to express all the contributions to the energy of the system (exchange or dipolar interactions and local zero-field splittings) in terms of spin operators only [65, 20]. As we will show below, the irreducible tensor operators (ITOs) technique and the Wigner-Eckart theorem [66] simplify the calculation of the Hamiltonian matrix elements on the total-spin basis. The formalism of ITOs is summarized in Appendix B. In the subsections below we will show how to apply it to the study of

molecular spin systems. First we express the SH in terms of ITOs. Then we outline an efficient technique for the calculation of the matrix elements of the SH and for its diagonalization, by writing it in the total spin basis.
Each molecule is described by an effective spin Hamiltonian, consisting usually of three main contributions:

$$\hat{H}_s = \hat{H}_{ex} + \hat{H}_{ZFS} + \hat{H}_B. \tag{1.6}$$

The first term represents the two-body exchange interaction between couples of spins within the molecule. It includes the isotropic (super-)exchange interaction (which is usually the leading term term), as well as anisotropic and anti-symmetric contributions to the exchange (which usually provide only small corrections to the energy spectrum). Dipole-dipole interactions are also included in the form of anisotropic-exchange couplings. The second term represents the zero-field splitting single-ion anisotropy, produced by the combined action of the spin-orbit interaction and of the local crystal electric field of the ligands surrounding each magnetic ion. The last term models the Zeeman interaction with an external magnetic field.

1.2.1 Main contributions to the SH

Here we analyze in detail the terms of the spin Hamiltonian 1.6. We first review the fundamental interactions characterizing molecular nanomagnets and their physical meaning; then we express them in terms of irreducible tensor operators.

Exchange interactions

The two-body exchange interaction between the magnetic ions is expressed in the most general form as

$$\hat{H}_{ex} = \sum_{i>j} \hat{\mathbf{s}}_i \cdot \underline{\mathbf{J}}_{ij} \cdot \hat{\mathbf{s}}_j. \tag{1.7}$$

It is useful to decompose it in three different contributions:

$$\hat{H}_{ex} = \hat{H}_{iso} + \hat{H}_{an} + \hat{H}_{DM}, \tag{1.8}$$

where $\hat{H}_{iso}$ is the Heisenberg-Dirac isotropic-exchange Hamiltonian, $\hat{H}_{an}$ represents the anisotropic-exchange and $\hat{H}_{DM}$ the anti-symmetric Dzyaloshinskii-Moriya (DM) interaction. These terms are expressed as a function of spin operators as follows:

$$\begin{aligned} \hat{H}_{iso} &= \sum_{i>j} J_{ij} \hat{\mathbf{s}}_i \cdot \hat{\mathbf{s}}_j && (1.9) \\ \hat{H}_{an} &= \sum_{i>j} \sum_{\alpha,\beta} J_{ij}^{\alpha\beta} \hat{s}_{i,\alpha} \hat{s}_{j,\beta} && (1.10) \\ \hat{H}_{DM} &= \sum_{i>j} \mathbf{G}_{ij} \cdot \hat{\mathbf{s}}_i \times \hat{\mathbf{s}}_j, && (1.11) \end{aligned}$$

where $\hat{\mathbf{s}}_i$ are the spin operators acting on the i-th magnetic ion of the molecule and $\alpha, \beta = x, y, z$. J_{ij} and $J_{ij}^{\alpha\beta}$ are isotropic and anisotropic exchange couplings, whereas $\mathbf{G}_{ij}$ are the antisymmetric parameters, i.e., antisymmetric vectors ($\mathbf{G}_{ij} = -\mathbf{G}_{ji}$).
The dipolar intra-molecular interactions can also be included in $\hat{H}_{ex}$, since both dipolar and exchange interactions contain the same dependence on spin operators, given

by Eq. 1.7. Being a long-range interaction, the dipole coupling is present also for couples of spins sufficiently far to suppress all the other, short-range exchange interactions. Usually this is evaluated within the point-dipole approximation [67]. The coefficients of 1.7 accounting for the dipolar contribution to the exchange between magnetic moments $\hat{\mathbf{m}}_i = -\mu_B \underline{\mathbf{g}}_i \cdot \hat{\mathbf{s}}_i$ are given by:

$$\left(J_{ij}^{\alpha\beta}\right)^{dip} = \frac{\mu_B^2}{R_{ij}^3}\left[\sum_{\xi} g_1^{\alpha\xi} g_2^{\xi\beta} - 3\frac{\left(\sum_{\xi} g_1^{\alpha\xi} R_{\xi}\right)\left(\sum_{\zeta} R_{\zeta} g_2^{\zeta\beta}\right)}{R_{ij}^2}\right], \tag{1.12}$$

where $\xi, \zeta = x, y, z$. It is important to note that in the general case, when $\underline{\mathbf{g}}_1 \neq \underline{\mathbf{g}}_2$, the coupling tensor $\underline{\mathbf{J}}_{ij}^{dip}$ is not symmetric. In fact, it consists of an isotropic, anisotropic and antisymmetric part.

We now express the exchange terms of the Hamiltonian in terms of ITOs, by exploiting the formalism reported in Appendix B. Each term results from the composition of two tensor operators of rank $k_i = k_j = 1$, acting on two different spins i and j. In particular, isotropic exchange is expressed by a scalar product and is rotationally invariant. Therefore, it behaves as a compound operator with rank $k = 0$ and $q = 0$, whose explicit representation becomes:

$$\hat{H}_{iso} = -\sqrt{3}\sum_{i>j} J_{ij}\left\{\hat{T}^{(1)}(s_i)\otimes\hat{T}^{(1)}(s_j)\right\}_0^{(0)} = -\sqrt{3}\sum_{i>j}\hat{T}_0^{(0)}(11|ij). \tag{1.13}$$

We notice that the isotropic exchange interaction, being represented by a tensor operator with rank $k = 0$, is block-diagonal in the total spin. Indeed, it does not connect states with different S and its matrix element do not depend on M.

Anisotropic and antisymmetric terms can also be recast in terms of ITOs [68]:

$$\begin{aligned} \hat{H}_{an} &= \sum_{i>j} J_{ij}^{a}\hat{T}_0^{(0)} + J_{ij}^{v}\hat{T}_0^{(2)} + J_{ij}^{u}\left[\hat{T}_2^{(2)}(11|ij) + \hat{T}_{-2}^{(2)}(11|ij)\right] && (1.14)\\ \hat{H}_{DM} &= -i\sqrt{2}\sum_{i>j}\sum_{q}(-1)^q G_{ij}^{q}\hat{T}_{-q}^{(1)}(11|ij). && (1.15) \end{aligned}$$

Here

$$G_{ij}^{q} = \begin{cases} \mp\left(G_{ij}^{x} \pm iG_{ij}^{y}\right)/\sqrt{2}, & \text{if } q = \pm 1\\ G_{ij}^{z}, & \text{if } q = 0 \end{cases} \tag{1.16}$$

$$\begin{aligned} J_{ij}^{a} &= -\frac{1}{\sqrt{3}}\left(J_{ij}^{x} + J_{ij}^{y} + J_{ij}^{z}\right)\\ J_{ij}^{u} &= \frac{1}{2}\left(J_{ij}^{x} - J_{ij}^{y}\right)\\ J_{ij}^{v} &= \frac{1}{\sqrt{6}}\left(2J_{ij}^{z} - J_{ij}^{x} - J_{ij}^{y}\right) \end{aligned} \tag{1.17}$$

and we have assumed a diagonal exchange tensor $J_{ij}^{\alpha\beta}\delta_{\alpha\beta} \equiv J_{ij}^{\alpha}$. The scalar contribution ($k = 0$) appearing in $\hat{H}_{an}$ can be incorporated in the isotropic exchange term.

Notice that tensor operators of rank k shall mix states with different total spin, according to the selection rule $\Delta S = 0, ..., \pm k$. Hence, $\Delta S = 0, \pm 1$ for DM interaction, while $\Delta S = 0, \pm 1, \pm 2$ for anisotropic exchange.

Zero-Field Splitting

The interaction of each magnetic ion with the surrounding ligand charges is described by the one-body zero-field splitting (ZFS) term of the spin Hamiltonian. This term describes the influence of the electric field produced by the neighboring ions on the electronic structure of the magnetic site. Such an anisotropic electric field acts on the spin multiplets due to the presence of spin-orbit interaction. See Section 1.1 for a discussion about the microscopic origin of the single-ion anisotropy. The ZFS Hamiltonian can be decomposed in terms of *Stevens equivalent operators* $\hat{O}_k^q(\mathbf{s}_i)$ [65]; these are effective spin operators acting on a given total-spin multiplet:

$$\hat{H}_{ZFS} = \sum_i \sum_{k \leq 2s_i} \sum_{q=-k}^{k} b_k^q(i) \hat{O}_k^q(\hat{\mathbf{s}}_i) . \tag{1.18}$$

It can be shown that k must be even. Hamiltonian 1.18 can be easily written in terms of ITOs, since it consists of only one-body operators acting on a single site. For instance, the widely used second-order Hamiltonian $\sum_i [d_i \hat{s}_{z,i}^2 + e_i(\hat{s}_{x,i}^2 - \hat{s}_{y,i}^2)]$ (Eq. 1.5) becomes

$$\hat{H}_{ZFS} = \sum_i d_i \sqrt{\frac{2}{3}} \hat{T}_0^{(2)}(2|i) + e_i \left[\hat{T}_2^{(2)}(2|i) + \hat{T}_{-2}^{(2)}(2|i) \right] . \tag{1.19}$$

In a molecule containing several magnetic centres, as for the exchange interaction, the operators $\hat{T}_q^{(2)}$ of Eq. 1.19 are compound tensor operators. However, they are particularly simple, since they are obtained by the composition of a tensor operator of rank 2 on the examined site with the identity on all the other ions. Since these operators have $k = 2$, the ZFS interaction will mix states with different total spin, according to the selection rules $\Delta S = 0, \pm 1, \pm 2$ and $\Delta M = 0, \pm 1, \pm 2$ (similarly to anisotropic-exchange).
If the isotropic exchange interaction is largely dominant over all the other contributions (*strong-exchange limit*), the splitting within each total-spin multiplet will be much smaller than the energy difference between two multiplets with different total-spin S. Therefore to describe the behavior of the system we can reduce to the ground state multiplet, describing the whole molecule as a giant spin S, experiencing an effective ZFS and a Zeeman interaction with an external field. This particular SH is called single-Spin Hamiltonian and it is easier to manage, since the Hilbert space associated to the molecule is reduced to the dimension of the ground state total-spin multiplet, $2S + 1$. The ZFS Hamiltonian acting on such multiplet takes the form [20]:

$$\hat{H}_{ZFS} = \hat{\mathbf{S}} \cdot \underline{\mathbf{D}} \cdot \hat{\mathbf{S}}, \tag{1.20}$$

where $\underline{\mathbf{D}}$ is the symmetric ZFS tensor. In the absence of an external field, Hamiltonian 1.20 induces a splitting of the $(2S + 1)-$fold degenerate ground multiplet. If we choose the reference frame to be coincident with the three principal axes of $\underline{\mathbf{D}}$, the ZFS tensor is diagonal and Eq. 1.20 can be recast in the form:

$$\hat{H}_{ZFS} = D \left[\hat{S}_z^2 - S(S+1)/3 \right] + E \left(\hat{S}_x^2 - \hat{S}_y^2 \right) , \tag{1.21}$$

where $D = D_{zz} - (D_{xx} + D_{yy})/2$, $E = (D_{xx} - D_{yy})/2$, $E \leq D/3$ and we have subtracted the constant $DS(S+1)/3$ to make the tensor traceless. The values of D and E are determined by the symmetry of the cage surrounding the magnetic ion. In cubic symmetry

$D = E = 0$ (only $k = 4$ Stevens operators enter in the ZFS expression), in axial symmetry only $D \neq 0$, while both $D, E \neq 0$ in case of rhombic symmetry.
In systems with axial symmetry, if $D < 0$ the lowest energy states are those maximizing $|M|$ (M being the eigenvalues of $\hat{S}_z$), giving rise to the so-called *easy axis* anisotropy. Conversely, if $D > 0$ we get *easy plane* anisotropy and the most stable state shows the minimum $|M|$. When also $E \neq 0$, if S is an integer the degeneracy between the $|M\rangle$ and the $|-M\rangle$ states is removed, while they remain degenerate in pairs if S is an half integer. This is a consequence of time reversal symmetry and the pairs of degenerate levels are called *Kramers doublet* [65].
The parameters D and E can be related to the microscopic crystal field parameters d_i and e_i (see Eq. 1.5) by the relations:

$$D = \sum_i \Gamma_i d_i \tag{1.22}$$

$$E = \sum_i \Gamma_i e_i \tag{1.23}$$

where Γ_i are projection coefficients [69]. In a similar way, also the dipolar and other anisotropic exchange interactions can be projected onto the effective ground multiplet parameters D and E.

Zeeman interaction

The interaction of each metal ion with an external magnetic field **B** is expressed by the Zeeman Hamiltonian:

$$\hat{H}_B = \mu_B \sum_i \mathbf{B} \cdot \underline{\mathbf{g}}_i \cdot \hat{\mathbf{s}}_i, \tag{1.24}$$

where μ_B is the Bohr magneton and $\underline{\mathbf{g}}_i$ is the spectroscopic splitting tensor on ion i. The magnetic field breaks the $(2S+1)$ degeneracy within each total-spin multiplet.
This term can be easily expressed in terms of rank-1 ITOs, by recalling the irreducible representation of spin operators (Eq. B.7). Hence, for a generic orientation of **B**, it mixes states according to the selection rules $\Delta S = 0, \pm 1$ and $\Delta M = 0, \pm 1$.

1.2.2 Basis choice and recoupling

The dimension of the whole Hilbert space spanned by the SH of MNMs is often huge, since it blows up with the number of magnetic ions: $d = \prod_i (2s_i + 1)$. Hence, it is crucial to reduce the dimension of the examined Hilbert space, in order to make the SH diagonalization feasible with available computational techniques. This can be done by addressing the problem starting from the leading interaction, which is usually represented by the isotropic exchange.
A natural choice for the basis set is represented by the product states:

$$|s_1 m_1\rangle |s_2 m_2\rangle \dots |s_N m_N\rangle. \tag{1.25}$$

However, since the isotropic-exchange Hamiltonian is block-diagonal in the total spin, a smarter choice for the basis set is represented by the eigenstates of the total spin $\hat{\mathbf{S}} = \sum_i \hat{\mathbf{s}}_i$. To obtain the total spin S we also have to choose an appropriate coupling scheme of the single-ion spins s_i. In a $N-$ion cluster a successive coupling scheme yields the following basis vectors:

$$|s_1 s_2 (\tilde{S}_{12}) s_3 (\tilde{S}_{123}) \dots s_N S M\rangle \equiv |(\tilde{S}) S M\rangle, \tag{1.26}$$

where $(\tilde{S})$ denotes the set of intermediate quantum numbers $(\tilde{S}_{12}), (\tilde{S}_{123}), \dots, (\tilde{S}_{12\dots N-1})$, obtained by the coupling of spins s_1 and s_2 to get $(\tilde{S}_{12})$, $(\tilde{S}_{12})$ and s_3 to get $(\tilde{S}_{123})$ and so on. The best choice for the coupling scheme is the one which reflects the symmetry of the molecular system. Nonetheless, all the possible coupling schemes are equivalent, since the corresponding representative vectors are connected to each other by a given unitary transformation.
The same coupling scheme should be followed in the composition of tensor operators:

$$\hat{T}_q^{(k)} = \left\{ \left\{ \left\{ \hat{T}^{(k_1)}(1) \otimes \hat{T}^{(k_2)}(2) \right\}^{(k_{12})} \otimes \hat{T}^{(k_3)}(3) \right\}^{(k_{123})} \otimes \cdots \right\}_q^{(k)}, \tag{1.27}$$

where $\hat{T}^{(k_j)}(i)$ are tensor operators of rank k_j acting on ion i. The Wigner-Eckart theorem simplifies the calculation of matrix elements, by expressing them as the product of Wigner-$3j$ symbols (Appendix C) and reduced matrix elements. These are computed by means of the rules outlined in Appendix B for a couple of spins (*recoupling* technique). For molecules containing many spins, we apply iteratively Eq. B.12 as long as we reduce (a part from a product of a pre-factor and of some $9j$ symbols) to the computation of single-ion spin operators, whose reduced matrix elements are tabulated. We report here the values they take for $k = 0, 1, 2$.

$$\begin{aligned} \langle S||\hat{S}^{(0)}||S\rangle &= \sqrt{2S+1} \\ \langle S||\hat{S}^{(1)}||S\rangle &= \sqrt{S(S+1)(2S+1)} \\ \langle S||\hat{S}^{(2)}||S\rangle &= \frac{1}{2\sqrt{6}}\sqrt{(2S+3)(2S+2)(2S+1)2S(2S-1)} \end{aligned} \tag{1.28}$$

1.2.3 Spin Hamiltonian diagonalization

As stated in the previous section, the dramatic increase of the dimension of the Hilbert space with the number of magnetic centers requires advanced numerical techniques to calculate the matrix elements and diagonalize the Hamiltonian. For molecules exhibiting high symmetry, this problem can be attacked more efficiently by taking advantage of the point group symmetry of the cluster, which results in an additional reduction of the dimension of the matrices. For isotropic systems, the Hamiltonian matrix is block-factorized according to the value of the total-spin S, its projection M and the irreducible representation of the point group of the molecule.
The calculation of matrix elements of anisotropic terms, mixing states with different total-spin is performed according to the procedure outlined above. Diagonalization of the full SH would be possible only for relatively small systems. However, this massive effort is often useless, since observable quantities are usually influenced only by levels thermally occupied at very low temperatures. Therefore, we adopt a perturbative approach, which solves the problem by a two-steps procedure. First, only the Heisenberg-Dirac Hamiltonian $\hat{H}_{iso}$ (block-diagonal in S) is considered. The eigenvalues and eigenvectors $|\alpha SM\rangle$ of the cluster are thus determined; the energy spectrum consists of several spin multiplets separated by the isotropic exchange:

$$|\alpha SM\rangle = \sum_{(\tilde{S})} \langle(\tilde{S})SM|\alpha SM\rangle |(\tilde{S})SM\rangle = \sum_{(\tilde{S})} c_{(\tilde{S})\alpha} |(\tilde{S})SM\rangle, \tag{1.29}$$

here expressed in terms of the total-spin basis 1.26. It is worth noting that, since the matrix elements of $\hat{H}_{iso}$ are independent of M, also the coefficients $c_{(\tilde{S})\alpha}$ do not depend on M. Then we express the matrix element of each compound tensor operator of the SH in the basis of the eigenstates of the isotropic Hamiltonian $|\alpha S M\rangle$:

$$\begin{aligned} &\langle \alpha S M|\hat{T}^{(k)}|\alpha' S' M'\rangle = \\ &= (-1)^{S-M} \sum_{(\tilde{S}),(\tilde{S}')} c^{*}_{(\tilde{S})\alpha} c_{(\tilde{S}')\alpha'} \langle (\tilde{S})S||\hat{T}^{(k)}||(\tilde{S}')S'\rangle \begin{pmatrix} S & k & S' \\ -M & q & M' \end{pmatrix}. \end{aligned} \tag{1.30}$$

Thanks to Wigner-Eckart theorem the geometric dependence on M, M' and q is limited to the Wigner-$3j$ symbol.

The calculation is done by retaining only the low-lying energy multiplets: we fix an energy threshold and limit the expansion 1.29 to the isotropic exchange eigenvectors corresponding to eigenvalues below that threshold. Within this reduced spin subspace all magnetic interactions can be evaluated, with $\hat{T}^{(k)}$ corresponding to any of the anisotropic terms listed in the previous section. Finally, the here determined SH is diagonalized into the reduced spin subspace. This procedure includes S-mixing effects within the examined subspace [69], and only neglects mixing of the states belonging to the truncated subspace with higher ones, not included in the computation of anisotropic terms of the Hamiltonian. This approximation can be checked to produce a negligible error with respect to experimental data, by a little increase of the dimension of the reduced spin subspace.

System-specific Fortran codes have been written for the calculation of matrix elements and for the Hamiltonian diagonalization of each examined system.

Experimental techniques

CHAPTER 2

In this chapter we give an overview of the main experimental techniques employed to investigate static and dynamical properties of Molecular Nanomagnets [20, 70]. Our aim is to highlight what kind of information can be obtained from the different techniques and how the experimental data can be analyzed and interpreted within the theoretical framework outlined in the previous chapter. In this thesis, our interest focuses on the characterization of the static properties and of the coherent dynamics of MNMs. This is achieved by means of bulk magnetometry, Inelastic Neutron Scattering and Electron Paramagnetic Resonance measurements. A detailed investigation of the incoherent magnetization dynamics would require Nuclear Magnetic Resonance, as well as AC susceptibility techniques, which are beyond the scope of this thesis. See, e.g., Ref. [70].

2.1 Thermodynamic measurements

2.1.1 Magnetization and DC-susceptibility

Magnetization measurements on MNMs are usually performed by means of SQUID magnetometers. A SQUID (superconducting quantum interference device) is a very sensitive magnetometer used to measure extremely small magnetic fields, and it is based on superconducting loops containing Josephson junctions. By moving the sample inside the loop, a superconducting current is induced across the junction and the flux threading the loop is varied in units of the flux quantum. Then the variation of flux (induced by the magnetic moment of the sample) is converted in voltage and read as an output.
Starting from the spin model Hamiltonian of the examined system, the magnetization can be calculated as follows:

$$\mathbf{M}(T) = \frac{\mu_B}{Z} \sum_m \langle \psi_m | \boldsymbol{\mu} | \psi_m \rangle e^{-\beta E_m}, \tag{2.1}$$

where μ_B is the Bohr magneton, $|\psi_m\rangle$ are the system eigenstates, E_m the corresponding eigenvalues, $\beta = 1/k_B T$, T is the temperature, $Z = \sum_m e^{-\beta E_m}$ the partition function and $\boldsymbol{\mu} = -\sum_i \underline{\mathbf{g}}_i \cdot \hat{\mathbf{S}}_i$ the magnetic moment of the molecule. Here the sum runs over the magnetic ions i.

The magnetic susceptibility can be easily computed as the limit for small applied magnetic field ($\mathbf{B}$) of the M/B ratio. In general, for not collinear $\mathbf{M}$ and $\mathbf{B}$, we define the susceptibility tensor (per single molecule) as

$$\chi_{\alpha\beta} = \mu_B \frac{\partial \langle \mu_\alpha \rangle}{\partial B_\beta}, \tag{2.2}$$

where $\alpha, \beta = x, y, z$ and $\langle \boldsymbol{\mu} \rangle$ is the thermal average of the magnetic moment.

For isotropic and homonuclear systems, a simplified expression can be used [71]:

$$\chi T = \frac{N_A g^2 \mu_B^2}{3k_B} \frac{\sum_i S_i(S_i+1)(2S_i+1)e^{-\beta E(S_i)}}{\sum_i (2S_i+1)e^{-\beta E(S_i)}}. \tag{2.3}$$

Here $E(S_i)$ are the isotropic exchange eigenvalues of the molecule. Since anisotropic contributions usually lead only to small corrections, Eq. 2.3 can be used to easily evaluate the susceptibility of MNMs, in which the leading interaction is the Heisenberg exchange. One only needs to know the eigenvalues and the total spin S_i of the spin multiplets.

Finally, for an atomic system in presence of crystal field interactions, characterized by a set of partially degenerate states $\{\Gamma_n\}$ with energies E_n, the Van Vleck expression holds [65]:

$$\chi(T) = \frac{\mu_B^2}{Z} \sum_n \left[\beta A_{nn}^2 + 2 \sum_{n' \neq n} \frac{A_{nn'}^2}{E_{n'} - E_n} \right], \tag{2.4}$$

where $A_{nn}^2 = \sum_{\nu_n, \nu'_n} |\langle \Gamma_{n\nu_n} | \mu | \Gamma_{n\nu'_n} \rangle|^2$ and $A_{nn'}^2 = \sum_{\nu_n, \nu_{n'}} |\langle \Gamma_{n\nu_n} | \mu | \Gamma_{n'\nu_{n'}} \rangle|^2$. The indices n, n' run over states $\{\Gamma_n\}$, while the indices $\nu_n, \nu_{n'}$ run within the respective multiplets $\{\Gamma_n\}$ and $\{\Gamma_{n'}\}$. The second sum leads to a temperature-independent contribution to the susceptibility, also known as TIP (temperature independent paramagnetism).

2.1.2 Torque magnetometry

Cantilever devices allow the high sensitivity investigation of single crystals with torque magnetometry. A cantilever consists of a thin slab of a non-magnetic metallic alloy (typically CuBe) fixed at one end and hanging free at the other end, parallel to a fixed metal platform. This results in a parallel-plane capacitor, with capacitance $C = \epsilon A/d$ [see Figure 2.1-(a)]. Here ϵ is the dielectric constant, A is the area of the plates, and d is their separation ($< 100\ \mu m$). The sample is positioned on the slab, close to the free end and the presence of a mechanical couple induces a flexion of the cantilever and a consequent change in C. For small deflections the linear-response approximation is valid and (in the reference frame sketched in Fig. 2.1) the capacitance variation ΔC is proportional to the t_y component of the magnetic torque [72]:

$$\mathbf{t} = \mathbf{M} \times \mathbf{B}, \tag{2.5}$$

where $\mathbf{M}$ is the magnetization of the sample and $\mathbf{B}$ the applied magnetic field. With this technique it is possible to measure the torque experienced by an anisotropic molecular sample under the influence of a homogeneous magnetic field. If we choose [Figure

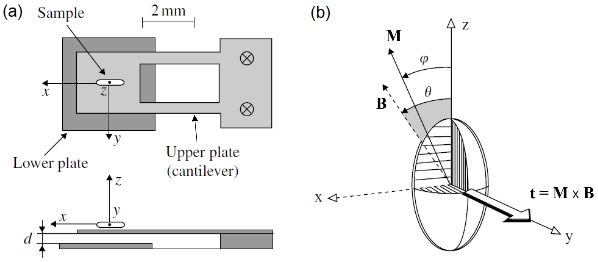

Figure 2.1: (a) Schematic front (top) and side (bottom) view of the cantilever device for magnetic torque measurements. (b) Geometrical arrangement of the magnetic field, the magnetization and the magnetic torque. (Figure used with permission from Ref. [72].)

2.1-(b)] a reference frame so that **M** and **B** lie in the xz plane, the magnetic torque **t** is necessarily parallel to y (i.e. $t_x = t_z = 0$) and is given by

$$t_y = M_z B_x - M_x B_z = B^2 \left(\frac{M_z}{B_z} - \frac{M_x}{B_x} \right) \sin\theta\cos\theta, \tag{2.6}$$

where θ is the angle between the magnetic field and the z axis. It is clear from Eq. 2.6 that the magnetic torque originates from the non-collinearity between the magnetization and the applied field. Therefore, torque measurements are particularly useful to gain information about the magnetic anisotropy of the sample.

Finally, it was shown [73, 74] that low-temperature torque measurements at variable magnetic field can be used to identify the presence of anti-crossing in the spin level diagram, induced by S-mixing between different total-spin multiplets. Indeed, while in absence of S-mixing the torque signal as a function of B is characterized by steps at the crossing fields, the oscillations of the total spin produce an additional sizeable peaklike contribution. From the above definition (Eq. 2.5) and choosing the magnetic field along z axis, $t_y \propto B\langle \hat{S}_x \rangle$. Quantum fluctuations of $|\mathbf{\hat{S}}|$ near the (anti)crossing field are accompanied by fluctuations of $\hat{S}_z$ and the latter are connected with $\langle \hat{S}_x \rangle$. Indeed, near the anti-crossings,

$$(\Delta S_z)^2 = \langle \hat{S}_z^2 \rangle - \langle \hat{S}_z \rangle^2 \simeq 0.25 \langle \hat{S}_x \rangle^2, \tag{2.7}$$

leading to $t_y \propto 2B\Delta S_z$. Accordingly, $\langle \hat{S}_x \rangle$ traces the increase and decrease of these fluctuations while sweeping over the anti-crossing, leading to a peak in the torque. In case of crossing ΔS_z is always zero and the torque does not peak.

2.1.3 Specific Heat

The behaviour of the specific heat (C_v) of a magnetic system can be calculated just from the knowledge of its eigenvalues E_n. We define

$$C_v = \frac{\partial \langle E \rangle}{\partial T} = \frac{1}{k_B T^2} \frac{\partial^2 \ln Z}{\partial \beta^2}, \tag{2.8}$$

with k_B the Boltzmann constant, Z the partition function, $\beta = 1/k_BT$ and T the temperature. From this definition, an explicit expression of the specific heat per unit mole can be deduced:

$$\frac{C_v}{R} = \frac{n_a\beta^2}{Z^2}\sum_{m>n} g_n g_m \left(E_n - E_m\right)^2 e^{-\beta(E_n+E_m)}, \tag{2.9}$$

where n_a represents the number of magnetic atoms per molecule and g_n is the degeneracy of level n.

It is particulary instructive to consider the expression of the specific heat for a two level system. In that case Eq. 2.9 reduces to

$$\frac{C_v}{R} = n_a(\Delta\beta)^2\frac{g_1}{g_2}\frac{e^{\beta\Delta}}{\left(1+\frac{g_1}{g_2}e^{\beta\Delta}\right)^2}, \tag{2.10}$$

where Δ is the gap between the two levels. By increasing T the respective population of the two levels varies: we start from a situation in which only the lowest is populated, and we end up with the populations of the two levels approximately the same. At temperatures of the order of Δ a steep variation of the internal energy is observed, corresponding to a high number of transitions between the two levels. At those temperatures the magnetic contribution to the specific heat abruptly increases (*Schottky effect*), whereas for temperatures away from Δ it goes to zero. The Schottky peak is found at a temperature $T_{SP} \sim \Delta/2$, given by the solution of the equation: $\frac{g_1}{g_2}e^{\Delta\beta_{SP}} = \frac{\Delta\beta_{SP}+2}{\Delta\beta_{SP}-2}$.

This analysis can be applied also to systems consisting of more than two levels, provided that the lowest doublet is well separated in energy from the excited states. Moreover, sometimes it is useful to study the specific heat as a function of the applied field. This technique can be used to identify the presence of anti-crossings between energy eigenstates. Indeed, in presence of a level crossing one should observe two peaks in the specific heat plotted vs. external magnetic field with a dip in the middle centered at the crossing field, as a result of a double Schottky anomaly. In particular, in presence of a pure level crossing the dip between the two Schottky peaks should go down to zero, while in presence of a level repulsion the dip can be much less pronounced and it gives a direct measurement of the gap at the anti-crossing.

A final remarks concerns the difficulty that usually is found in isolating the magnetic contribution to the specific heat from other sources which can dominate the signal of interest. In particular, the phonon contribution (which is expected to dominate magnetic effects above 3-4 K) can be estimated as:

$$\frac{C_v^{ph}}{R} = \frac{234rT^3}{(\Theta+\delta T^2)^3}, \tag{2.11}$$

where r is the number of atoms per molecule and $\Theta + \delta T^2$ is the Debye temperature.

2.2 Electron Paramagnetic Resonance

Electron Paramagnetic Resonance (EPR) is a spectroscopic technique for studying atoms or molecules with unpaired electrons (such as transition metal ions, lanthanides or radicals) [64]. In an EPR experiment, the sample is placed inside a cavity, subject to an external magnetic field which can be varied in a controlled way. In addition to this static field a controlled, but smaller oscillating magnetic field is superimposed on the cavity.

Thus the signal response from the cavity is modulated at the frequency of the oscillating field, and transitions between energy states resonant with that frequency are recorded. These are in the micro-wave frequency range. The ideal way to perform the experiment would be to apply a fixed magnetic field and vary the microwave frequency. However, microwave generators are only tunable over very limited ranges. Hence, the frequency ω of the incident radiation is fixed and the applied magnetic field is varied in order to match the resonance condition [75].
In single spin S paramagnetic centers, EPR spectroscopy studies transitions between $|SM\rangle$ states which are split by the static magnetic field. It provides information about the chemical environment of the magnetic ion, associated with the spectroscopic splitting tensor $\underline{\mathbf{g}}$ and the zero-field splitting tensor $\underline{\mathbf{D}}$. In MNMs this technique is used to probe transitions occurring within total-spin multiplets, thus allowing to extract the effective $\underline{\mathbf{g}}$ and $\underline{\mathbf{D}}$ tensors. In case of MNMs showing sizeable S-mixing effects induced by strong anisotropic terms in the Hamiltonian, *forbidden* EPR transitions can be observed between states belonging to different total-spin multiplets.

2.2.1 Interpretation of EPR spectra

The interpretation of EPR spectra is based on linear-response theory [76]. As reported in Appendix D, the absorption of a system in a resonance experiment, resulting from the response to an applied time-dependent perturbation $\hat{H}_1(t) = -\hat{A}f(t)$, is proportional to the imaginary part of the susceptibility:

$$\chi''_{AA}(\omega) = \pi \sum_{\alpha\alpha'} \langle\alpha|\hat{A}^\dagger|\alpha'\rangle\langle\alpha'|\hat{A}|\alpha\rangle \left(n_\alpha - n_{\alpha'}\right) \delta\left(\hbar\omega - (E_{\alpha'} - E_\alpha)\right). \tag{2.12}$$

Here E_α and $|\alpha\rangle$ are the eigenvalues and eigenvectors of the unperturbed Hamiltonian, $n_\alpha = e^{-\beta E_\alpha}/Z$ and Z is the partition function $Z = \sum_{\alpha'} e^{-\beta E_{\alpha'}}$. In an EPR experiment, the term $\langle\alpha|\hat{A}^\dagger|\alpha'\rangle\langle\alpha'|\hat{A}|\alpha\rangle$ in Eq. 2.12 represents the transition intensity between $|\alpha\rangle$ and $|\alpha'\rangle$, while the time-dependent perturbation $\hat{H}_1$ is the microwave oscillating field, perpendicular to the applied static field $\mathbf{B}$.
EPR experiments are often performed on polycrystalline powder samples. Hence, the powder spectrum results from the spherical average of the spectra calculated for each orientation $\{\theta, \phi\}$ of the applied static field with respect to the principal coordinate system of the magnetic center. For homo-metallic molecules (with all the ions characterized by the same $\underline{\mathbf{g}}$), transition intensities between states $|\alpha\rangle$ and $|\alpha'\rangle$ are calculated with the following angular dependence [77, 78]:

$$\begin{aligned}
I_{\alpha\alpha'}(\theta,\phi) \;&=\; \left(1-\sin^2\theta\,\cos^2\phi\right)\; S^*_{x,\alpha\alpha'}S_{x,\alpha\alpha'} \,+\\
&-\; \sin^2\theta\,\sin\phi\,\cos\phi\;\left[S^*_{x,\alpha\alpha'}S_{y,\alpha\alpha'} + S^*_{y,\alpha\alpha'}S_{x,\alpha\alpha'}\right] +\\
&-\; \cos\theta\,\sin\theta\,\cos\phi\;\left[S^*_{x,\alpha\alpha'}S_{z,\alpha\alpha'} + S^*_{z,\alpha\alpha'}S_{x,\alpha\alpha'}\right] +\\
&+\; \left(1-\sin^2\theta\,\sin^2\phi\right)\; S^*_{y,\alpha\alpha'}S_{y,\alpha\alpha'} \,+\\
&-\; \cos\theta\,\sin\theta\,\sin\phi\;\left[S^*_{y,\alpha\alpha'}S_{z,\alpha\alpha'} + S^*_{z,\alpha\alpha'}S_{y,\alpha\alpha'}\right] +\\
&+\; \left(\sin^2\theta\right)\; S^*_{z,\alpha\alpha'}S_{z,\alpha\alpha'},
\end{aligned} \tag{2.13}$$

where $S_{\gamma,\alpha\alpha'} = \langle\alpha|\hat{S}_\gamma|\alpha'\rangle$ and $\hat{S}_\gamma$ is the total-spin operator ($\gamma = x, y, z$). In order to simulate the EPR powder spectrum we proceed as follows: first we calculate the zero-field system Hamiltonian, as well as the spin operators in the total-spin basis. Then, for each magnitude (B) and orientation $\{\theta, \phi\}$ of the static field we add the Zeeman contribution to the zero-field Hamiltonian and we diagonalize it. Having retained eigenvalues and corresponding eigenvectors up to a fixed energy threshold, we calculate $I_{\alpha\alpha'}(\theta, \phi)$ and the corresponding imaginary susceptibility $\chi''_{AA}(\omega, \theta, \phi)$. As a next step, we compute the spherical average by $\frac{\sum_{\theta,\phi} \chi''_{AA}(\omega,\theta,\phi)\sin\theta}{\sum_{\theta,\phi}\sin\theta}$. By sweeping the magnetic field while keeping ω fixed, we obtain the field-dependence of the absorbance. Experimental data are usually reported as $\frac{d\chi''}{dB}$, so that resonance fields correspond to a zero in the derivative of the absorbance (equivalent to a peak in χ'').

The two most-commonly considered functions to model the line-shape are the Lorentzian and the Gaussian, replacing the $\delta-$function to account for homogeneous or inhomogeneous broadening, respectively [79]. Homogeneous broadening arises from the finite lifetimes of the initial and final states of the transitions, induced by relaxation mechanisms. In diluted samples, where dipolar inter-molecular interactions are substantially suppressed, relaxation is mainly due to spin-phonon and hyperfine interactions of electronic spins with the neighboring nuclei. This last mechanism dominates at low temperature, where the average phonon number is very low (see discussion on decoherence mechanisms in Chapter 6). Inhomogeneous broadening results from a distribution of the Hamiltonian parameters, induced, e.g., by local disorder. In this case the resonance field results from a distribution of the slightly different transition frequencies of the different magnetic centers. Assuming a random distribution of these frequencies gives rise to a Gaussian line-shape. More complex line-shapes can also be employed, to account for both homogeneous and inhomogeneous broadening.

2.3 Inelastic Neutron Scattering

The starting point to investigate molecular nanomagnets is to determine their spin Hamiltonian. Inelastic Neutron Scattering (INS) is the ideal technique to find isotropic-exchange and zero-field splitting parameters. Moreover, high resolution INS experiments allow us to extract the energy splitting induced by anisotropic interactions, as well as the parameters related to spin operators with $k > 2$ [80].

Indeed, the typical INS spectrum consists of a series of peaks whose positions directly give the differences between the system eigenvalues, while the intensities are related to the composition of the eigenvectors. If compared to EPR spectroscopy, INS shows some remarkable advantages: a detailed picture of the low lying energy levels from an analysis of spectra taken with zero magnetic field, the possibility to observe not only intra-multiplet but also inter-multiplets (with $\Delta S = 1$) transitions and the information about the composition of the eigenfunctions, given by the dependence of the cross-section on the transferred wave-vector.

Recently developed INS instruments also yield the four-dimensional inelastic-neutron scattering function in vast portions of reciprocal space and enables the spin dynamics to be determined directly [81].

2.3.1 INS Cross-section

The magnetic scattering is induced by the interaction of the magnetic moment of the neutron with the magnetic field **B** generated by the unpaired electrons of the examined magnetic ions:

$$\hat{H} = -\hat{\boldsymbol{\mu}}_n \cdot \mathbf{B}. \tag{2.14}$$

Here $\hat{\boldsymbol{\mu}}_n$ is the magnetic moment of the neutron. We recall that the magnetic moment of the electron (neutron) is related to its spin by $\hat{\boldsymbol{\mu}}_e = -\gamma_e \mu_B \hat{\mathbf{s}}$ ($\hat{\boldsymbol{\mu}}_n = -\gamma_n \mu_n \hat{\boldsymbol{\sigma}}$)[1]. μ_B (μ_n) are electronic (nuclear) Bohr magnetons and $\gamma_e = -2$ ($\gamma_n = -1.91$) are the respective gyromagnetic factors. From now on, we consider spin-only magnetic scattering events, neglecting the contribution of the orbital angular momentum of the ion to the magnetic moment. This is a reasonable assumption in all the MNMs investigated in this work, since they consist of $3d$ ions whose orbital angular momentum is nearly completely quenched by the crystal field interaction. Furthermore, we usually consider atoms where the unpaired electrons have strongly localized wave-functions.
The magnetic field generated by the electron moving with $\mathbf{v}_e$ is given by:

$$\mathbf{B} = \nabla \times \left(\frac{\hat{\boldsymbol{\mu}}_e \times \mathbf{R}}{|\mathbf{R}|^3} \right) - \frac{e}{c} \frac{\mathbf{v}_e \times \mathbf{R}}{|\mathbf{R}|^3}, \tag{2.15}$$

where $\mathbf{R}$ is the distance between the electron and the neutron. Consequently, the magnetic contribution in Eq. 2.14 becomes:

$$-\gamma_n \mu_n \hat{\boldsymbol{\sigma}} \cdot \mathbf{B} = \gamma_n \mu_n \left[2\mu_B \hat{\boldsymbol{\sigma}} \cdot \nabla \times \left(\frac{\hat{\mathbf{s}} \times \mathbf{R}}{|\mathbf{R}|^3} \right) - \frac{e}{2 m_e c} \left(\hat{\mathbf{p}}_e \cdot \frac{\hat{\boldsymbol{\sigma}} \times \mathbf{R}}{|\mathbf{R}|^3} + \frac{\hat{\boldsymbol{\sigma}} \times \mathbf{R}}{|\mathbf{R}|^3} \cdot \hat{\mathbf{p}}_e \right) \right], \tag{2.16}$$

where the first part is a dipolar term, while the second one represents the electron-neutron interaction, due to the motion of the electron. $\hat{\mathbf{p}}_e$ represents the linear momentum of the electron.
Then, if we consider an INS experiment in which the magnetic ions of the sample interact with a neutron beam, the differential cross-section may be expressed as:

$$\begin{aligned} \frac{d^2\sigma}{d\Omega dE'} = (2\gamma_n \mu_n \mu_B)^2 \frac{k'}{k} \sum_{\lambda\lambda'} \sum_{\sigma\sigma'} \Bigg[& p_\lambda p_\sigma \\ |\langle \mathbf{k}' \lambda' \sigma' \,|\, \sum_i \boldsymbol{\sigma} \cdot \nabla \times \frac{\hat{\mathbf{s}}_i \times \mathbf{R}}{|\mathbf{R}|^3} - \frac{1}{2\hbar} \left(\hat{\mathbf{p}}_i \cdot \frac{\hat{\boldsymbol{\sigma}} \times \mathbf{R}}{|\mathbf{R}|^3} + \frac{\hat{\boldsymbol{\sigma}} \times \mathbf{R}}{|\mathbf{R}|^3} \cdot \hat{\mathbf{p}}_i \right) |\mathbf{k} \lambda \sigma \rangle|^2 & \\ \delta\left(\hbar\omega + E_\lambda - E_{\lambda'} \right) \Bigg]. & \end{aligned} \tag{2.17}$$

Here the index i labels the magnetic ions. $\mathbf{k}$ and $\mathbf{k}'$ are, respectively, the initial and final wave-vectors of the neutron, $|\lambda\rangle$ and $|\lambda'\rangle$ the initial and final state of the system with energies E_λ and $E_{\lambda'}$, $|\sigma\rangle$ and $|\sigma'\rangle$ the initial and final polarization state of the neutron. The occupation probability of the initial state is $p_\lambda = e^{-\beta E_\lambda}/Z$, with $Z = \sum_\nu e^{-\beta E_\nu}$. Finally, the Dirac delta function guarantees the energy conservation, being $\hbar\omega$ the energy exchanged by the neutron in the interaction with the system.
The matrix element of the magnetic interaction potential can be recast in the form:

$$\begin{aligned} \frac{2\pi\hbar^2}{m_n} \left\langle \mathbf{k}' \left| \hat{\boldsymbol{\sigma}} \cdot \nabla \times \frac{\hat{\mathbf{s}}_i \times \mathbf{R}}{|\mathbf{R}|^3} \right| \mathbf{k} \right\rangle &= 4\pi e^{i\mathbf{Q}\cdot\mathbf{r}_i} \hat{\boldsymbol{\sigma}} \cdot \left[\tilde{\mathbf{Q}} \times \left(\hat{\mathbf{s}}_i \times \tilde{\mathbf{Q}} \right) \right] \\ \frac{2\pi\hbar^2}{m_n} \left\langle \mathbf{k}' \left| \hat{\mathbf{p}}_i \cdot \frac{\hat{\boldsymbol{\sigma}} \times \mathbf{R}}{|\mathbf{R}|^3} \right| \mathbf{k} \right\rangle &= -\frac{4\pi i}{|\mathbf{Q}|} e^{i\mathbf{Q}\cdot\mathbf{r}_i} \hat{\boldsymbol{\sigma}} \cdot \left(\tilde{\mathbf{Q}} \times \hat{\mathbf{p}}_i \right), \end{aligned} \tag{2.18}$$

---

[1] Here $\hat{\mathbf{s}} = \hat{\boldsymbol{\sigma}}/2$ and $\mu_n = \frac{m_e}{m_n}\mu_B$, m_e and m_n being the electron and neutron mass, respectively.

where $\mathbf{r}_i$ is the position vector of the i^{th} electron, $\mathbf{Q} = \mathbf{k} - \mathbf{k}'$ and $\tilde{\mathbf{Q}} = \mathbf{Q}/|\mathbf{Q}|$. By introducing the operator

$$\hat{\mathbf{Q}}_\perp = \sum_i e^{i\mathbf{Q}\cdot\mathbf{r}_i} \left[\tilde{\mathbf{Q}} \times \left(\hat{\mathbf{s}}_i \times \tilde{\mathbf{Q}} \right) - \frac{i}{\hbar|\mathbf{Q}|} \tilde{\mathbf{Q}} \times \hat{\mathbf{p}}_i \right], \tag{2.19}$$

we see that neutrons are only sensitive to the perpendicular component of the exchanged wave-vector. Indeed, the cross-section can be rewritten as:

$$\begin{aligned} \frac{d^2\sigma}{d\Omega dE'} = \left(\frac{m_n}{2\pi\hbar^2}\right)^2 \left(8\pi\gamma_n\mu_n\mu_B\right)^2 \frac{k'}{k} \sum_{\lambda\lambda'} \sum_{\sigma\sigma'} \Bigg[p_\lambda p_\sigma \times \\ \times \langle\lambda\sigma| \left(\hat{\boldsymbol{\sigma}} \cdot \hat{\mathbf{Q}}_\perp\right)^\dagger |\lambda'\sigma'\rangle\langle\lambda'\sigma'|\hat{\mathbf{Q}}_\perp \cdot \hat{\boldsymbol{\sigma}}|\lambda\sigma\rangle \delta\left(\hbar\omega + E_\lambda - E_{\lambda'}\right) \Bigg]. \end{aligned} \tag{2.20}$$

Since, for unpolarized neutrons, $\sum_\sigma p_\sigma \langle\sigma|\hat{\sigma}_\alpha\hat{\sigma}_\beta|\sigma\rangle = \delta_{\alpha\beta}$, the differential cross-section simplifies into:

$$\frac{d^2\sigma}{d\Omega dE'} = r_0^2 \frac{k'}{k} \sum_{\alpha\beta} \left(\delta_{\alpha\beta} - \tilde{Q}_\alpha\tilde{Q}_\beta\right) \sum_{\lambda\lambda'} p_\lambda \langle\lambda|\hat{Q}_\alpha^\dagger|\lambda'\rangle\langle\lambda'|\hat{Q}_\beta|\lambda\rangle\delta\left(\hbar\omega + E_\lambda - E_{\lambda'}\right). \tag{2.21}$$

Here $r_0 = \frac{\gamma_n e^2}{m_e c^2}$, $\alpha, \beta = x, y, z$ and we have skipped some boring mathematical passages. For *spin-only* scattering events, as it is often the case in MNMs containing transition metal ions, the operator $\hat{\boldsymbol{Q}}$ is given by:

$$\hat{\boldsymbol{Q}} = \sum_d e^{i\mathbf{Q}\cdot\mathbf{R}_d} \sum_\nu e^{i\mathbf{Q}\cdot\mathbf{r}_\nu} \hat{\mathbf{s}}_\nu, \tag{2.22}$$

where the sum over d runs over all the atomic sites with position $\mathbf{R}_d$ and the sum over ν runs over the unpaired electrons within each magnetic ion, with position $\mathbf{r}_\nu$. By introducing the total spin of each magnetic ion at position d, $\hat{\mathbf{s}}_d$, we find

$$\langle\lambda|\hat{\boldsymbol{Q}}|\lambda'\rangle = \sum_d e^{i\mathbf{Q}\cdot\mathbf{R}_d} F_d(\mathbf{Q}) \langle\lambda|\hat{\mathbf{s}}_d|\lambda'\rangle, \tag{2.23}$$

i.e. the matrix elements of the operator $\hat{\boldsymbol{Q}}$ are proportional to that of the total-spin operator, with coefficients related to the *form factor* of the ion, $F_d(\mathbf{Q}) = \int e^{i\mathbf{Q}\cdot\mathbf{r}} \rho_s(\mathbf{r}) d\mathbf{r}$. This is the Fourier transform of the normalized spin density $\rho_s(\mathbf{r})$ associated to the d^{th} ion of the system.
We finally get the following expression for the differential cross-section for spin-only magnetic scattering:

$$\begin{aligned} \frac{d^2\sigma}{d\Omega dE'} = r_0^2 \frac{k'}{k} \sum_{\alpha\beta} \left(\delta_{\alpha\beta} - \tilde{Q}_\alpha\tilde{Q}_\beta\right) \times \\ \times \sum_{\lambda\lambda'} p_\lambda \sum_{d,d'} F_d^*(\mathbf{Q}) F_{d'}(\mathbf{Q}) e^{i\mathbf{Q}\cdot(\mathbf{R}_{d'} - \mathbf{R}_d)} \times \\ \times \langle\lambda|\hat{s}_{\alpha,d}|\lambda'\rangle\langle\lambda'|\hat{s}_{\beta,d'}|\lambda\rangle\delta\left(\hbar\omega + E_\lambda - E_{\lambda'}\right). \end{aligned} \tag{2.24}$$

It is customary to write it as $\frac{d^2\sigma}{d\Omega dE'} = r_0^2 \frac{k'}{k} S(\mathbf{Q},\omega)$, where $S(\mathbf{Q},\omega)$ is the scattering function. The differential cross-section can also be rewritten as

$$\frac{d^2\sigma}{d\Omega dE'} = \frac{A}{N_m}\frac{k'}{k} e^{-2W} \sum_{\lambda\lambda'} \frac{e^{-\beta E_\lambda}}{Z} I_{\lambda,\lambda'}(\mathbf{Q}) \delta\left(\hbar\omega + E_\lambda - E_{\lambda'}\right), \tag{2.25}$$

where we have included the Debye-Waller factor e^{-2W}, the number of magnetic ions, N_m, and incorporated all the constants into $A = 0.29$ barn and the transition intensity into $I_{\lambda,\lambda'}(\mathbf{Q})$.

2.3.2 Cross-section for powder samples

Due to the difficulty of synthesizing sufficiently large single crystals, INS experiments are often performed on powder polycrystalline samples. The cross-section for a powder sample is obtained by averaging Eq. 2.25 over all the possible directions of $\mathbf{Q}$. In other words, we need to replace $I_{\lambda,\lambda'}(\mathbf{Q})$ with [82]

$$\bar{I}_{\lambda,\lambda'}(Q) = \sum_{d,d'} \int \frac{d\Omega}{4\pi} e^{i\mathbf{Q}\cdot\mathbf{R}_{dd'}} \sum_{\alpha\beta} \left(\delta_{\alpha\beta} - \tilde{Q}_\alpha\tilde{Q}_\beta\right) \langle\lambda|\hat{s}_{\alpha,d}|\lambda'\rangle\langle\lambda'|\hat{s}_{\beta,d'}|\lambda\rangle. \tag{2.26}$$

The numerical evaluation of this integral is a computationally long task. However, it was shown that it can be analytically determined [83]. With some algebra, one finds the following expression:

$$\begin{aligned}
\bar{I}_{\lambda,\lambda'}(Q) \;&= \sum_{d,d'} F_d^*(Q)F_{d'}(Q)\Big\{\frac{2}{3}\Big[j_0(QR_{dd'}) + C_0^2 j_2(QR_{dd'})\Big]\tilde{s}_{z_d}\tilde{s}_{z_{d'}} \\
&+ \frac{2}{3}\Big[j_0(QR_{dd'}) - \frac{1}{2}C_0^2 j_2(QR_{dd'})\Big]\left(\tilde{s}_{x_d}\tilde{s}_{x_{d'}} + \tilde{s}_{y_d}\tilde{s}_{y_{d'}}\right) \\
&+ \frac{1}{2}j_2(QR_{dd'})\Big[C_2^2\left(\tilde{s}_{x_d}\tilde{s}_{x_{d'}} - \tilde{s}_{y_d}\tilde{s}_{y_{d'}}\right) + C_{-2}^2\left(\tilde{s}_{x_d}\tilde{s}_{y_{d'}} + \tilde{s}_{y_d}\tilde{s}_{x_{d'}}\right)\Big] \\
&+ j_2(QR_{dd'})\Big[C_1^2\left(\tilde{s}_{z_d}\tilde{s}_{x_{d'}} + \tilde{s}_{x_d}\tilde{s}_{z_{d'}}\right) + C_{-1}^2\left(\tilde{s}_{z_d}\tilde{s}_{y_{d'}} + \tilde{s}_{y_d}\tilde{s}_{z_{d'}}\right)\Big]\Big\}
\end{aligned} \tag{2.27}$$

where $R_{dd'}$ gives the relative position of ions d and d', $j_{0,2}(QR_{dd'})$ are spherical Bessel functions and

$$\begin{aligned}
C_0^2 &= \frac{1}{2}\left[3\left(\frac{R_{dd',z}}{R_{dd'}}\right)^2 - 1\right] \\
C_2^2 &= \frac{R_{dd',x}^2 - R_{dd',y}^2}{R_{dd'}^2} \\
C_{-2}^2 &= \frac{R_{dd',x}R_{dd',y}}{R_{dd'}^2} \\
C_1^2 &= \frac{R_{dd',x}R_{dd',z}}{R_{dd'}^2} \\
C_{-1}^2 &= \frac{R_{dd',y}R_{dd',z}}{R_{dd'}^2}
\end{aligned} \tag{2.28}$$

and $\tilde{s}_{\alpha_d}\tilde{s}_{\beta_{d'}} = \langle\lambda|s_{\alpha_d}|\lambda'\rangle\langle\lambda'|s_{\beta_{d'}}|\lambda\rangle$, $\alpha,\beta = x,y,z$. Since spin operators appearing in the expression of the scattered intensity are rank 1 tensor operators, the allowed magnetic transitions obey the selection rules $\Delta S = 0, \pm 1$ and $\Delta M = 0, \pm 1$. Eq. 2.27 represents a general form of the formula reported in [82] and it can be used whatever the symmetry and the anisotropy of the investigated system. In molecules showing axial symmetry, only products of terms with $\alpha = \beta$ survive.

To account for the finite experimental resolution, the delta-function in the expression of the cross-section should be replaced by a peak function, usually a gaussian. Furthermore, peaks can result larger than the experimental resolution due to local disorder (as in the case of EPR).

Together with the inelastic peaks, INS data also contain an elastic and a quasi-elastic contribution. The elastic contribution arises from neutron diffraction ($k = k'$). Conversely, quasi-elastic neutron scattering is characterized by small energy transfers, if compared to the incident energy of the neutrons. In order to reproduce the experimental curves, it is therefore necessary to add to the inelastic cross-section a gaussian and a lorentzian function, accounting respectively for the elastic and quasi-elastic scattering, whose width depend on the instrumental resolution and on the temperature. Moreover, the contribution arising from phonon-scattering gives rise to a non-trivial background which must be carefully subtracted in order to focus on magnetic transitions.

2.3.3 Unravelling the spin dynamics

The implementation of large arrays of position-sensitive detectors in cold-neutron time-of-flight spectrometers, together with the advances in software, has recently opened unprecedented possibilities in single-crystal INS experiments on MNMs, allowing the determination of the four-dimensional scattering function $S(\mathbf{Q}, \omega)$ in a vast portion of the reciprocal space. On the one hand, this provides a much more selective characterization of the MNMs when different candidate models can be discriminated only by the vectorial **Q**-dependence of $S(\mathbf{Q}, \omega)$. On the other hand, the amount of available information is so large that the full pattern of real-space dynamical two-spin correlations can be determined, without using any model Hamiltonian [81]. For a MNM with uniaxial anisotropy and $T \to 0$

$$S(\mathbf{Q}, \omega) \propto \sum_{\alpha=x,y,z} \left(1 - \frac{Q_\alpha^2}{Q^2}\right) \sum_\lambda \sum_{d \geq d'} F_d(Q) F_{d'}(Q) \cos(\mathbf{Q} \cdot \mathbf{R}_{dd'}) \times \\ \times \langle 0 | \hat{s}_{\alpha,d} | \lambda \rangle \langle \lambda | \hat{s}_{\alpha,d'} | 0 \rangle \delta(\omega - \omega_\lambda), \tag{2.29}$$

where $|0\rangle$ is the ground eigenstate, $\omega_\lambda = E_\lambda / \hbar$ and we have fixed $E_0 = 0$. This formula can be recast in terms of $T = 0$ dynamical correlation functions:

$$\langle \hat{s}_{\alpha,d}(t) \hat{s}_{\alpha,d'}(0) \rangle = \sum_\lambda \langle 0 | \hat{s}_{\alpha,d} | \lambda \rangle \langle \lambda | \hat{s}_{\alpha,d'} | 0 \rangle e^{-i\omega_\lambda t}. \tag{2.30}$$

In fact, the Fourier coefficients $c^\alpha_{dd'}(\omega_\lambda) = \langle 0 | \hat{s}_{\alpha,d} | \lambda \rangle \langle \lambda | \hat{s}_{\alpha,d'} | 0 \rangle$ in Eq. 2.30 coincide with those in Eq. 2.29. Whereas the values of ω_λ are directly read out from the energies of the peaks in the INS spectrum, the $c^\alpha_{dd'}(\omega_\lambda)$ can be extracted from the data by fitting Eq. 2.29 to the observed **Q**-dependence of each peak. Indeed, for each value of ω_λ these coefficients are the only unknown quantities in equation Eq. 2.29.

The information on the low-temperature spin dynamics embedded in the dynamical correlation functions can be visualized by exploiting the link between these correlations and linear response functions (see Appendix D). The building blocks of such functions are the set of susceptibilities $\chi^{\alpha',d'}_{\alpha,d}(t)$, which provide the response of $\hat{s}_{\alpha,d}$ at time t to a

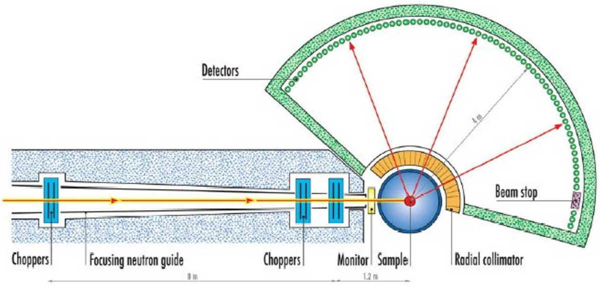

Figure 2.2: Scheme of a IN5 direct time-of-flight neutron spectrometer at the Institute Laue-Langevin. Figure from http://www.ill.eu/instruments-support/instruments-groups/instruments/in5.

delta-pulse perturbation produced by a field b of direction α' applied on spin d' at time zero:

$$\delta\hat{H}(t) = -b\hat{s}_{\alpha',d'}\delta(t) \to \langle\hat{s}_{\alpha,d}\rangle(t) - \langle\hat{s}_{\alpha,d}\rangle_{eq} = b\chi_{\alpha,d}^{\alpha',d'}(t) \tag{2.31}$$

with

$$\chi_{\alpha,d}^{\alpha',d'}(t) = \frac{i}{\hbar}\Theta(t)\langle[\hat{s}_{\alpha,d}(t), \hat{s}_{\alpha',d'}(0)]\rangle \equiv \delta_{\alpha\alpha'}\frac{2}{\hbar}\Theta(t)\sum_{\lambda} c_{dd'}^{\alpha}(\omega_\lambda)\sin(\omega_\lambda t), \tag{2.32}$$

where $\Theta(t)$ is the Heaviside step-function and $\langle\hat{s}_{\alpha,d}\rangle_{eq}$ is the equilibrium average. Here the response is diagonal because of axial symmetry. This framework allows us to extract, for instance, the propagation through the molecule of a fluctuation on a given site at time $t = 0$.

2.3.4 Time-of-flight spectrometers

Neutrons can be produced either by continuous (reactors) or by pulsed (spallation) sources. The former exploit a controlled chain reaction of nuclear fission (typically on Uranium), while the latter use a particle accelerator to produce a beam of neutrons. A mercury, tantalum, lead or other heavy metal target is used, and 20 to 30 neutrons are expelled after each impact of the proton beam. Although this is a far more expensive way of producing neutron beams than by a fission reaction in a nuclear reactor, it has the advantage that the beam can be pulsed with relative ease, without needing a monochromator (as in the case of continuous sources). In both cases the final state of the neutrons is analyzed either by a crystal analyzer or by the time-of-flight technique.

The Time-of-flight (TOF) technique is a general method for determining the kinetic energy of a traveling neutron, by measuring the time it takes to fly between two fixed points whose distance is known. It is particularly useful in the case of the neutron spectroscopy, where the energy of the scattered neutrons has to be determined. Furthermore, the TOF technique can also be used for fixing the energy of the neutron beam before the interaction with the sample, i.e. for filtering a particular velocity, by means of a complex system of rotating disc choppers. This kind of choppers system acts as a monochromator, since it selects just a wavelength out of the incoming white beam, by means of the

De Broglie's relationship $\lambda = h/mv$, v being the neutron velocity.
TOF spectrometers may be divided into two classes:

- Direct geometry spectrometers: in which the incident energy is defined before the sample by a device such as a monocrystal (Bragg diffraction principle) or a choppers system (TOF method), and the final energy is determined by time-of-flight between the sample and the detectors.
- Indirect (inverted) geometry spectrometers: in which the sample is illuminated by a white incident beam, the incident energy is determined at the sample position by the measurement of the time-of-flight, and the final energy is measured by a monocrystal.

By recording the time of arrival t_f of each analysed neutron in a detector relative to the emission time t_0, we can investigate the energy gain/loss occurring within the sample. A scheme of a direct-geometry time-of-flight spectrometer (the IN5 spectrometer at the Institute Laue Langevin in Grenoble) is shown in Fig. 2.2. The primary flight-path, L_1, as well as the secondary path L_2 (from the sample to the bank of detectors) are accurately known. Hence, the loss/gain in neutron energy can be calculated as a result of a distribution of arrival times:

$$\Delta E = E_{in} - E_{out} = \frac{1}{2} m_n \left[\left(\frac{L_1}{\tau_1} \right)^2 - \left(\frac{L_2}{\tau - \tau_1} \right)^2 \right]. \tag{2.33}$$

Here $\tau = t_f - t_0$ is the total time-of-flight, while τ_1 is the time it takes for a detected neutron to travel a distance L_1.

MNMs controlled by uniform pulses for QIP

CHAPTER 3

We report here a scheme for quantum information processing with molecular nanomagnets, manipulated by uniform magnetic pulses. These are used to implement a set of one- and two-qubit gates, which can lead, on a properly-engineered molecular register, to universal quantum computation. As first proposed in Refs. [27, 36, 17], uniform magnetic fields can be used to induce the required time evolution of the register, by exploiting auxiliary states and the structure of intermolecular interactions. In particular, by an appropriate topology and hierarchy of exchange couplings between different molecular units, it would be possible to use uniform pulses to effectively switch on and off intermolecular interactions, thus implementing two-qubit gates and quantum simulation algorithms [17]. These ideas [4] are outlined in section 3.1. So far, however, the engineering of potentially scalable supramolecular complexes fitting these requisites has proven a very hard chemical task.

We show that the here-reported Cr_7Ni-Ni-Cr_7Ni and Cr_7Ni-Co-Cr_7Ni families of complexes have the right characteristics to implement one- and two-qubit gates with uniform magnetic fields, i.e., with no need of local control [84]. The magnetic couplings are engineered by coordination chemistry and several variants with different geometry are obtained, with either Ni^{2+} or Co^{2+} ions acting as a switch of the effective inter-molecular interaction. These two-qubit units are optimal for proof-of-principle experiments and can be exploited as building blocks of scalable architectures for quantum simulation.

We first focus on the Ni-switch compounds. We carry out an *ab-initio* study of this newly synthesized family of complexes by means of the approach introduced in Sec. 1.1. Using the calculated parameters, we numerically simulate one- and two-qubit gates, finding high fidelity ($\geq 99\%$) on all compounds. As an example of quantum simulation, we theoretically demonstrate how a simple pulse sequence can be used to mimic the time-evolution of the transverse-field Ising model. The robustness of the scheme is demonstrated by including the effect of decoherence in a master equation formalism. For reasonable values of the qubits dephasing time, we still achieve high fidelity on the quantum simulation.

The Co-switch complex is characterized by EPR spectroscopy. The combination of the

perpendicular arrangement of the rings and of the anisotropy of their $\underline{\mathbf{g}}$ tensors allows us to selectively address each of them, thus implementing CNOT gates and simulating anti-symmetric Hamiltonians with very high fidelity.
Finally, we provide an estimate of the residual qubit-qubit effective interaction which is still present when the switch is in the off state. We also suggest possible strategies to minimize it in order to improve the performance of the setup, in view of scaling it to a sizeable number of qubits.

3.1 Quantum gates in permanently coupled molecular qubits: state of the art

In order to be good candidate qubits, MNMs should have an effective $S = 1/2$ ground state well separated in energy from the excited multiplets. The two states of the doublet can be split by means of a static magnetic field and microwave pulses resonant with this gap can be used to perform rotations. The low-lying gap should be spectroscopically resolved from all the others (in terms of pulse spectral-width), in order to implement rotations with negligible leakage to other states, outside from the computational basis. This condition is easily fulfilled with attainable pulse durations. Typical *Rabi* oscillations between logical $|0\rangle$ and $|1\rangle$ occur on a time-scale of a few ns for technologically achievable values of the oscillating field ($\sim$ 10 G) and matrix elements of about 1 μ_B.
Rabi oscillations have been demonstrated in several molecular systems, such as the high-spin Fe_4 [33] or the low-spin V_{15} [85, 86], besides the Cr_7Ni anti-ferromagnetic ring [6, 87]. To date, this is probably one of the most promising molecular qubits. Indeed, the intra-ring interactions result in a nearly isotropic doublet ground state, with remarkably long decoherence times [30], which could be further increased by chemically engineering the molecular structure. Furthermore, it can be grafted onto surfaces without significantly modifying its magnetic properties [35].
Besides single-qubit rotations, the implementation of quantum algorithms requires two-qubit entangling gates. So far, these have been experimentally demonstrated only in permanently coupled molecular nanomagnets. For instance, Nakazawa et al. [88] designed a two-qubit assembly consisting of two radicals, made inequivalent by the $\underline{\mathbf{g}}$ tensors pointing along different directions. The distinguishability of the qubits is a necessary condition for the implementation of the CNOT. The dipolar interaction between the qubits produces a splitting in the lowest two-qubit states which allows to selectively address the $|10\rangle \leftrightarrow |11\rangle$ transition by means of resonant pulses, while keeping the other components of the wave-function frozen. In other words, the excitation of the target qubit depends on the state of the control. The coherent oscillation of the target qubit was achieved on a time-scale of about 200 ns (determined by the qubit-qubit interaction), below the measured decoherence time ($\sim \mu s$). A similar approach was followed in Ref. [89], by using a dimer of rare-earth ions (CeEr). One spin belonging to a MNM dimer is selectively excited depending on the state of the other, by addressing a single transition among the transitions of the dimer. Two-qubit units consisting of permanently coupled Cr_7Ni rings have been recently employed to implement a conditional dynamics by double electron–electron resonance techniques [90], in the line of proposals [88, 89]. The drawback of this approach is that the two qubits are permanently coupled, thus making the implementation of single-qubit rotations tricky. In principle, this could be done by simultaneously irradiating the sample with two pulses of slightly different frequencies, matching the pertinent gaps. However, in a many-qubit register, spectroscopically resolving the relevant gaps would be challenging, thus hindering the scalability of such

architecture. Finally, the inability of turning off the inter-qubit interaction leads to an unwanted spontaneous evolution of the system, which should be corrected for a reliable computation.

Here we focus on an alternative approach, which exploits non-computational states to switch on and off the inter-qubit coupling [27, 36]. This is possible by properly choosing the linkers between the qubits and the pattern of the exchange interactions among them. In particular, this scheme requires molecular qubits to be permanently coupled to non-computational magnetic units interposed between them, which act as a switch of the inter-qubit coupling. The interaction between qubits and switches should be such that the effective qubit-qubit coupling vanishes as long as the switches are in their ground state, thus allowing the implementation of single-qubit rotations. Because of the qubit-unit interaction, the energy required to bring the qubit-switch-qubit trimer into the state in which the switch is excited depends on the initial state of the qubits. Therefore, a conditional excitation of, e.g., the $|11\rangle$ component of the two-qubit wave-function is possible. The application of two subsequent pulses with proper delay to excite and de-excite the switch implements a controlled-phase gate.

A scheme for quantum information processing and quantum simulation based on these ideas is described in detail in Ref. [17]. It relies on using effective $S = 1/2$ spins (Cr_7Ni) to encode the qubits, while interposed complexes with a $S = 0$ ground state are used as switches of the effective qubit-qubit interaction. The register consists of an ABAB chain of qubits, in which A and B transitions are spectroscopically distinguishable. In the idle configuration, the qubits are decoupled. Hence, single qubit gates can be implemented simultaneously on all A (B) qubits of the chain by resonant magnetic pulses. Conversely, conditional gates between neighboring pairs of qubits are performed by temporarily bringing the switch to an excited $S = 1$ state by a microwave pulse of suitable phase and duration.

Beyond enabling to switch on and off the qubit-qubit interaction, the presence of non-computational states would also allow to bypass the lack of local control. This could be done, in an ABAB chain of qubits, by using A qubits to encode quantum information, while adjacent B qubits are ancillary units [91, 27]. All the B qubits are set to $|0\rangle$, except for a *control unit* that is prepared in $|1\rangle$. Then, the control unit is moved along the chain via a series of SWAP gates, thus bringing it close to the qubit (qubit-pair) which we aim to manipulate. This allows one to individually address single (or single pairs) of qubits with uniform pulses, thus making the ABAB register universal. We note, however, that in a real system the large number of required SWAP gates would result in very long computational times (possibly exceeding the decoherence time). In fact, this approach implies a sequential implementation of the gates. In general, the capabilities of the device (e.g. the class of Hamiltonians that could be simulated) are enlarged by reducing the degree of parallelization. We stress that the physical implementation of a dedicated quantum computer (e.g. oriented to the digital simulation of some interesting quantum models) would already be a great achievement. Many translationally invariant Hamiltonians could be, for instance, simulated even in the lack of local control and in a completely parallel implementation, as we will show below.

An ideal switch fitting the scheme of Ref. [17] is represented by antiferromagnetically coupled homo-metallic dimers (showing an $S = 0$ ground state), symmetrically linked to the two neighboring Cr_7Ni qubits. However, the dimer can be excited to the $S = 1$ state (thus turning on the inter-qubit coupling) only if the spectroscopic $\underline{\mathbf{g}}$ tensors of the two ions of the dimer are significantly different. Otherwise the matrix element of the transition vanishes and the excitation becomes too slow, or forbidden at all. Due to the difficulty of chemically engineering a pair of symmetrically-coupled homometallic

ions with sufficiently different ligand cages (and hence different $\underline{\mathbf{g}}$), this ideal approach (which guarantees a perfect decoupling of the qubits in the idle phase) is not straightforward.
In this work we propose a different and easier implementation of that scheme, which can be exploited for proof-of-principle experiments of quantum simulation algorithms on dimers or short chains of molecular qubits. Here the qubit-qubit coupling is switched by a single interposed ion (M). Even if less efficient, this approach can be implemented with the newly synthesized family of complexes here reported, namely Cr_7Ni-M-Cr_7Ni. A necessary condition is that as long as the switch is in the ground state, the effective qubit-qubit interaction (resulting from virtual excitations of the switch) is small enough that the associated unwanted evolution is very slow on the timescale of the quantum gates. This condition is fulfilled if the energy of the excited state of the switch is much larger than the qubit-switch coupling. However, this coupling must be large-enough to ensure that the excitation energy of the switch is sufficiently dependent on the state of the qubits to enable conditional dynamics. This requires a suitable chemical engineering of the qubit-switch bond. In particular, the feasibility of the scheme relies on a weak M-ring coupling, if compared to the other energy-scales, namely the central-ion zero-field splitting and the Zeeman interaction with an applied field. In this respect, the $(Cr_7Ni)_2Ni$ and $(Cr_7Ni)_2Co$ classes of compounds are particularly promising, as we demonstrate below. Indeed, on the one hand, Ni^{2+} ions typically show sizeable zero-field splittings; on the other hand, the highly anisotropic behavior of Co^{2+} leads to a significant splitting of the $|01\rangle$-$|10\rangle$ states, thus effectively suppressing the residual inter-qubit interaction.

3.2 Ni switch

A sketch of the here-proposed systems is shown in Fig. 3.1, consisting of two Cr_7Ni qubits, linked through a central Ni^{2+} ion. This acts as a switch in the Cr_7Ni-Ni-Cr_7Ni complex and can be described as an $S = 1$ spin with axial anisotropy $\mathscr{D}S_z^2$. To match the schematic structure of Figure 3.1 in a supramolecule our chemists coworkers (prof. Winpenny's group) have introduced an N-donor ligand onto the backbone of the Cr_7Ni ring, thus functionalizing it to be linked to a suitable ion. The five synthesized compounds all contain two Cr_7Ni rings disposed about a central Ni^{2+} switch (Figure 3.2). The structural parameters within the individual Cr_7Ni rings are unchanged between the compounds, however the coordination geometries at the central Ni-site varies between them. The chemistry allows us to modify the crystal environment of the Ni-switch moving from *cis* to *trans* geometries, and this influences the Ni anisotropy and the Ni-ring coupling. Compounds CIS-**1** and CIS-**2** contain a cis arrangement of the N-donors derived from the

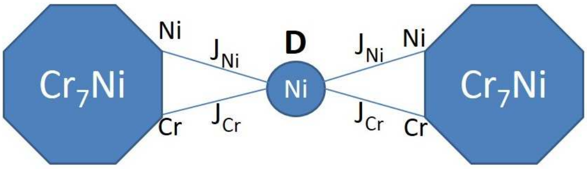

Figure 3.1: Scheme of a pair of Cr_7Ni rings, linked by a Ni^{2+} ion. The effective isotropic and axial Ni-ring couplings are given by $J_{iso} = 1.13J_{Cr} - 0.63J_{Ni}$ and $J_{an} = 0.14J_{Cr} - 0.10J_{Ni}$, respectively (see Eqs. 3.1 and 3.2).

substituted rings and in both cases the central Ni site lies on a two-fold rotation axis. In TRANS-**3**, TRANS-**4** and TRANS-**5** the pyridine donors are arranged trans; for TRANS-**4** and TRANS-**5** the Ni site sits on an inversion centre, while for TRANS-**3** the Ni is not on any symmetry element. In each case the Ni site is six-coordinate, with four sites occupied by O-donors and two by N-donors. If we consider the two cis-compounds, the Ni-N distance is noticeable longer in CIS-**2** than in CIS-**1**, suggesting the strength of the Ni-ring coupling will be weaker in CIS-**2** than in CIS-**1**. The variation in the trans-compounds is perhaps more subtle; the Ni-N bond length is very slightly longer in TRANS-**3**. The bond angles are all close to those expected for a regular octahedral coordination geometry, with the greatest variation found for compound TRANS-**3**, which is the only molecule where the Ni is not on a symmetry element. Within each family of compounds, the Ni-ring coupling is also controlled by the chemical substitution $CF_3 \to CH_3$ close to the Ni-ring bond. In addition, we can envisage connecting some of these elementary units in order to obtain chains of qubits.
We first investigate this newly synthesized family of compounds by means of the ab-initio approach introduced in Sec. 1.1. In this way we determine the low-energy spin Hamiltonian and the relevant parameters describing the system.

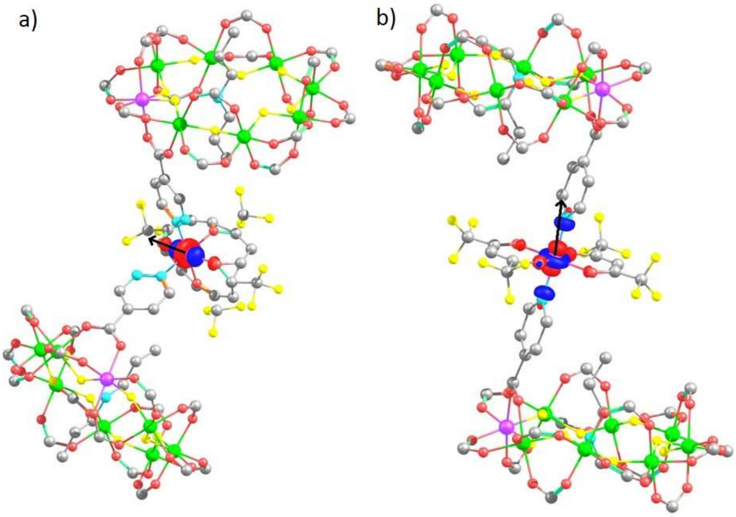

Figure 3.2: Molecular structures determined from x-ray data for CIS-**2**, a), and TRANS-**4**, b). The plane of the two rings are parallel in b), while they are not in a). The localized highest energy $3d$ orbital on the central ion obtained by *ab-initio* calculations is also shown. The black arrows indicate the z direction in Eq. 3.1, determined by diagonalization of the zero-field-splitting tensor calculated *ab-initio*. In the figure, H atoms and CH_3 groups on the rings are not shown for clarity, O are red, F are yellow, C are grey, N blue, Cr green and Ni violet.

3.2.1 Ab-initio calculations

Ab-initio calculations are based on a novel and flexible approach (see Section 1.1 and Chapter 5) which has already been successfully applied to determine the spin Hamiltonians of three prototype MNMs, including Cr_7Ni [47]. Differently from other schemes, strong correlation effects are not accounted for at a static mean field level by means of

hybrid exchange-correlation functionals [53, 52, 92]. They are explicitly included in a generalized Hubbard model [60], which is constructed using localized Boys orbitals [56] to describe the $3d$ electrons of the transition metal ions. The model accounts for both the electron-transfer effect, by means of the so-called hopping integrals, and the strong electron-electron correlations, controlled by the screened Coulomb integrals. The hopping integrals are obtained at the end of a self-consistent DFT run, performed in the Local Density Approximation (LDA). In a subsequent step, the screened Coulomb integrals are also calculated self-consistently by means of the constrained LDA method [57]. This leads to a molecule-specific generalized Hubbard model (Eq. 1.1). Finally, the spin Hamiltonian is obtained by means of a canonical transformation [58] applied to such a Hubbard model. In this way, no assumption on the form of this spin Hamiltonian is needed and all the interactions are deduced systematically, including subtle anisotropic terms. In order to reduce the computational effort, calculations are performed by substituting CH_3 groups with H on the rings, according to the hydrogen termination technique [53]. However, we did not modify the neighborhood of the central Ni ion. We have checked that this approximation leads only to slight modifications in the extracted single-ring parameters.
To derive the low-energy spin model, it is convenient to work in the basis of crystal-field states, obtained by diagonalizing the on-site matrices $t^{i,i}_{m,m'}$ (see Eq. 1.1). The different geometry of the CIS and TRANS compounds leads to significantly different one-electron crystal-field eigenstates. At all sites the environment of the magnetic ion is approximatively octahedral; thus the crystal-field orbitals split into a lower energy t_{2g}-like quasitriplet and a 1-2 eV higher energy e_g-like quasidoublet. The highest-energy crystal field orbital is shown, for the central Ni^{2+} ion of (CIS-**2**) and (TRANS-**4**), in Fig. 3.2: it clearly shows a $3d_{3z^2-1}$ shape, with significant tails on the neighboring ligands. These tails are involved in electron-hopping and consequent super-exchange processes.
For the present class of compounds, we find that the relevant interactions are described by the following microscopic spin Hamiltonian:

$$\hat{H}_{micro} = \sum_{i=1}^{2} \left(J_{Ni} \hat{\mathbf{S}} \cdot \hat{\mathbf{s}}^i_{Ni} + J_{Cr} \hat{\mathbf{S}} \cdot \hat{\mathbf{s}}^i_{Cr} \right) + \hat{\mathbf{S}} \cdot \underline{\mathbf{D}} \cdot \hat{\mathbf{S}} \\ + \mu_B \mathbf{B} \cdot \underline{\mathbf{g}}^{Ni} \cdot \hat{\mathbf{S}} + \sum_{i=1}^{2} \hat{H}_{ring}(i), \tag{3.1}$$

where the first term describes the exchange coupling between the two Cr_7Ni rings and the central Ni^{2+} ion, and $\underline{\mathbf{D}}$ is the zero field splitting tensor of the Ni ion (see Fig. 3.1). We indicate with capital letters (S) the spin of the central Ni^{2+} ion and with lowercase letters those belonging to the rings ($s^{1,2}_{Ni}$, $s^{1,2}_{Cr}$). The last term describes the intra-ring Hamiltonian which has been determined from neutron spectroscopy [87], torque magnetometry [73] and electron paramagnetic resonance [9]. The parameters of $\hat{H}_{ring}$ inferred from experiments are in good agreement with those calculated from first principles by means of the present approach [47].
The exchange constants J_{Ni} and J_{Cr} are the sum of a ferromagnetic (FM) screened Coulomb exchange contribution J^{CE} and a super-exchange term J^{SE}, which contains both FM and AFM contributions. Table 3.1 reports the values of the super- and screened Coulomb-exchange parameters obtained *ab-initio*. We find a small resulting exchange interaction in all compounds. While compounds (CIS-**2**), (TRANS-**3**) and (TRANS-**5**) show a competition between J^{SE} and J^{CE}, in (CIS-**1**) and (TRANS-**4**) the Coulomb part dominates. It is important to note that the resulting Ni-ring superexchange coupling,

Table 3.1: Calculated super-exchange and Coulomb-exchange couplings (in μeV) for CIS and TRANS variants of Cr$_7$Ni-Ni-Cr$_7$Ni. The Coulomb-exchange coupling is estimated starting by its bare value and introducing a factor of screening comparable with the one obtained in analogous calculations.

	J^{SE}_{Ni}	J^{CE}_{Ni}	J^{SE}_{Cr}	J^{CE}_{Cr}
(CIS-**1**)	27	-69	-2	-7
(CIS-**2**)	0.6	-1.4	3.5	-2.5
(TRANS-**3**)	2	-1	2	-1
(TRANS-**4**)	14	-28	-8	-24
(TRANS-**5**)	2	-12	9	-2

although very small ($J^{SE} \sim 10$ μeV), can be reliably obtained by means of the present approach. Indeed, the value of J^{SE} depends on the ratio between the square of the hopping integrals (of the order of meV) and the screened Coulomb terms ($\sim$ eV) which are well beyond our numerical accuracy. The screened value of J^{CE} is in this case too small to be reliably determined with the constrained LDA approach. Nevertheless, a reasonable estimate can be obtained by assuming that the bare Coulomb exchange integrals are screened with the same screening-factor determined *ab-initio* for Cr$_7$Ni in Ref. [47]. Finally, $\underline{\mathbf{D}}$ and the small anisotropy of the $\underline{\mathbf{g}}^{Ni}$ tensor originate from the combined action of crystal-field and spin-orbit interactions. We determine the full tensors and we diagonalize them in order to find the principal anisotropy axes.

3.2.2 Effective low-energy Hamiltonian

Since the interactions of each ring with the central Ni^{2+} ion are much weaker than the intra-ring couplings, the microscopic Hamiltonian $\hat{H}_{micro}$ (Eq. 3.1) can be projected in the subspace in which the two rings are in the ground doublets $T = 1/2$, thus obtaining:

$$\begin{aligned}\hat{H}_s &= J_{iso}\sum_{i=1}^{2}\left(\hat{S}_x\hat{T}^i_{x_i}+\hat{S}_y\hat{T}^i_{y_i}+\hat{S}_z\hat{T}^i_{z_i}\right)+J_{an}\sum_{i=1}^{2}\left(2\hat{S}_z\hat{T}^i_{z_i}-\hat{S}_x\hat{T}^i_{x_i}-\hat{S}_y\hat{T}^i_{y_i}\right)\\ &+ \mathscr{D}\left[\hat{S}_z^2-S(S+1)/3\right]+\mathcal{E}(\hat{S}_x^2-\hat{S}_y^2)+\mu_B\mathbf{B}\cdot\underline{\mathbf{g}}^{Ni}\cdot\hat{\mathbf{S}}+\mu_B\mathbf{B}\cdot\sum_{i=1}^{2}\underline{\mathbf{g}}^{i}\cdot\hat{\mathbf{T}}^{i},\end{aligned} \tag{3.2}$$

where $\hat{S}_\alpha$ and $\hat{T}^i_\alpha$ indicate, respectively, the components of the spin of the central Ni^{2+} ion and of each ring, z, x, y are the principal anisotropy axes of the Ni^{2+} ion and z_i, x_i, y_i are the principal axes of the two rings. $\mathscr{D}$ and $\mathcal{E}$ are axial and rhombic zero-field-splitting parameters. The last terms describe the Zeeman interaction with an external field **B**. The effective exchange parameters can be then deduced from the microscopic parameters calculated *ab-initio*: $J_{iso} = 1.13\ J_{Cr} - 0.63\ J_{Ni}$ and $J_{an} = 0.14\ J_{Cr} - 0.10\ J_{Ni}$.
Table 3.2 reports the resulting parameters for the effective Hamiltonian 3.2. We find a small Ni-ring exchange interaction in all compounds. In particular, J_{iso} is AFM for the two CIS compounds, but significantly stronger in CIS-**1** than in CIS-**2**, due to the substitution between pyridine and pyridazine groups in the super-exchange path. AFM couplings of the same order are found in the TRANS-**5** and TRANS-**3** variants, while TRANS-**4** shows a FM and significantly larger value of J_{iso}. This difference reflects the complete substitution CH$_3$ → CF$_3$ in the cage of the central Ni^{2+} ion in TRANS-**4**. Indeed, Figure 3.3 shows that the overlap between the calculated d-like orbitals of the Ni^{2+}

Table 3.2: Parameters of the Spin Hamiltonian deduced ab-initio. Calculated exchange (in μeV) and zero field splitting (in meV) parameters of the effective Hamiltonian (3.2).

	J_{iso} (μeV)	J_{an} (μeV)	$\mathscr{D}$ (meV)	$\mathcal{E}$ (meV)
CIS-**1**	16.1	3.00	-0.32	-0.01
CIS-**2**	1.7	0.23	-0.27	-0.03
TRANS-**3**	0.5	0.03	-0.47	-0.06
TRANS-**4**	-27.4	-3.00	-0.72	-0.05
TRANS-**5**	14.2	2.00	-0.44	-0.02

ion and of the ring is significantly larger in this case, because the $CH_3 \rightarrow CF_3$ substitution leads to a larger delocalization of the orbitals belonging to the central Ni-switch. This also explains the intermediate value of J_{iso} found in TRANS-**5**, in which the substitution has been carried out on only half of the CH_3 groups. These results demonstrate the sophisticated level of chemical control of the magnetic coupling between the Ni-switch and the rings in this family.

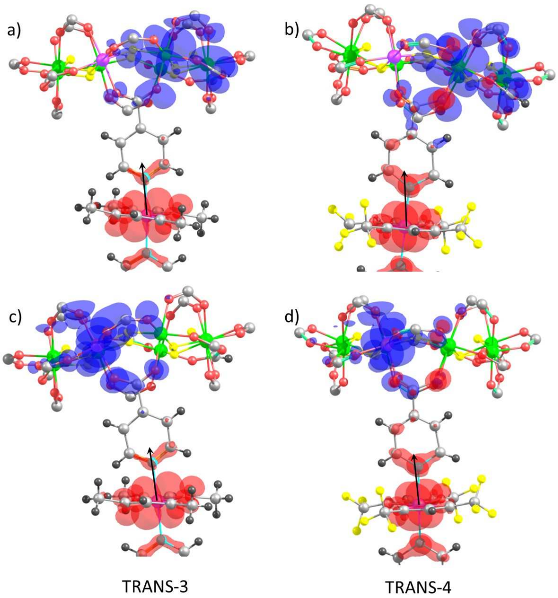

Figure 3.3: Chemical control of the ring-Ni coupling. The substitution of CF_3 groups close to the central Ni^{2+} ion increases the delocalization of its d-like orbitals, resulting in a larger overlap with the d-like orbitals of Cr_7Ni rings. This effect is visible in these pictures where only the upper half molecule of Fig. 3.2 is shown. The surface plots map the modulus of exemplary orbitals providing large contributions to the ring-Ni^{2+} exchange (red surface: central Ni^{2+} ion, blue surface: Cr^{3+} (a,b) and Ni^{2+} (c,d) ions belonging to the upper Cr_7Ni ring). (a) and (c) panels refer to the TRANS-**3** compound, whereas (b) and (d) panels refer to TRANS-**4**, which displays the largest Ni-ring exchange interaction. In TRANS-**3** $Ni(hfac)_2$ is the central switch, rather than $Ni(acac)_2$ in TRANS-**4** (H: dark grey, F: yellow).

Figures 3.2 and 3.3 also show (black arrows) the z axis direction, obtained by diagonalization of the on-site zero field splitting tensor $\underline{\mathbf{D}}$. We note that this direction is nearly orthogonal to the planes of the two rings for the TRANS variants, and nearly parallel for the CIS ones, reflecting the different ligand cages of the Ni^{2+} ion. The diagonal form of the $\underline{\mathbf{D}}$ tensor gives direct access to the axial and rhombic parameters, $\mathscr{D}$ and $\mathcal{E}$, appearing in the effective Hamiltonian 3.2: we find negative values of $\mathscr{D}$ for all the examined compounds, indicating an easy-axis magnetic anisotropy along the black arrows of Fig. 3.2. By comparing the crystalline environment of the central Ni^{2+} in the different variants, we note a higher rhombicity in CIS-**2** and TRANS-**3** which results in a larger value of $\mathcal{E}/\mathscr{D}$ calculated for these compounds (see Table 3.2). In the reference frame diagonalizing $\underline{\mathbf{D}}$, also $\underline{\mathbf{g}}^{Ni}$ is diagonal. We find nearly isotropic g-tensors for all the examined compounds, with $2.11 < g^{Ni}_{\alpha\alpha} < 2.19$, $\alpha = x, y, z$.

3.2.3 Quantum gates with always on magnetic coupling

Since J_{iso} and J_{an} are much smaller than the other terms, the eigenstates of 3.2 are practically factorized states $|\text{qubits}\rangle \otimes |M_{Ni}\rangle$ and to first order the coupling with the Ni^{2+} ion merely renormalizes the external field felt by the qubits. If $\mathbf{B}$ is along z and neglecting for simplicity the small rhombic term (i.e., assuming $\mathcal{E} = 0$), second-order corrections lead to a small xy residual qubit-qubit interaction quadratic in the exchange couplings and inversely proportional to $\mathscr{D} + \mu_B \Delta g B$:

$$\hat{H}_{res} = \frac{\lambda}{2}\left(\hat{\sigma}^1_z + \hat{\sigma}^2_z\right) + \frac{\Gamma}{4}\left(\hat{\sigma}^1_x\hat{\sigma}^2_x + \hat{\sigma}^1_y\hat{\sigma}^2_y\right), \tag{3.3}$$

where $\hat{\sigma}^{1,2}_\alpha$ are Pauli matrices referred to each qubit, $\Gamma = (J_{iso} - J_{an})^2/(\mathscr{D} + \mu_B \Delta g B)$, $\lambda = \Gamma/2 - (J_{iso} + 2J_{an})$ and $\Delta g = g^{ring}_z - g^{Ni}_z$. Hence, sufficiently large values of $\mathscr{D}$ and $\mu_B \Delta g B$ with respect to J_{iso} result in a very slow unwanted evolution of the qubits, thus allowing us to implement gates without significant errors. This conclusion also holds for $\mathbf{B}$ along a generic direction and $\mathcal{E} \neq 0$.

To illustrate the way gates are implemented, we consider here two representative examples of CIS and TRANS compounds. Fig. 3.4-(a) shows the calculated level diagram of (CIS-**2**) as a function of the static field. The four low-energy levels labeled $|\alpha, \beta\rangle$ $(\alpha, \beta = 0, 1)$ in Fig. 3.4-(a) practically correspond to $|M_1\rangle \otimes |M_2\rangle \otimes |M_{Ni} = -1\rangle$, where $|M_i\rangle$ is the eigenstate of the component of spin i along $\mathbf{B}$. Hence, in these states the two rings are effectively decoupled and we can straightforwardly define the computational basis. Single-qubit gates can thus be implemented by means of uniform resonant magnetic pulses whose duration is chosen in order to obtain a rotation of the desired angle. Since in the CIS variants the two rings lie in non-parallel planes, the anisotropy of the $\underline{\mathbf{g}}^i$ tensors of the rings can be exploited to independently rotate each qubit. As an example, Fig. 3.5-(a) reports the calculated time-dependence of the components of the wavefunction $|c_j(t)|^2 = |\langle j|\psi(t)\rangle|^2$ of compound CIS-**2** in a π rotation of the first qubit around the x axis. In the previous expression, $|j\rangle$ are the two-qubit states belonging to the computational basis and $|\psi(t)\rangle$ is the wave-function at time t. In the simulations, we employed an oscillating field with a gaussian envelope, $\mathbf{B}(t) = \mathbf{B}_0 \cos(\omega t + \phi) e^{-\frac{(t-t_0)^2}{2\tau^2}}$, perpendicular to the static field. In an ideal scenario, the rotation of each qubit is completely independent from the state of the other qubit. Consequently, for instance, transitions $|00\rangle \rightarrow |01\rangle$ and $|10\rangle \rightarrow |11\rangle$ should be induced by the same pulse. In the case of a δ-like pulse, this would mean that the pulse frequency should match $E_{11} - E_{10} = E_{01} - E_{00}$. However, the small residual coupling between the qubits causes an energy-shift $\delta E \equiv (E_{11} - E_{10}) - (E_{01} - E_{00})$, which could prevent

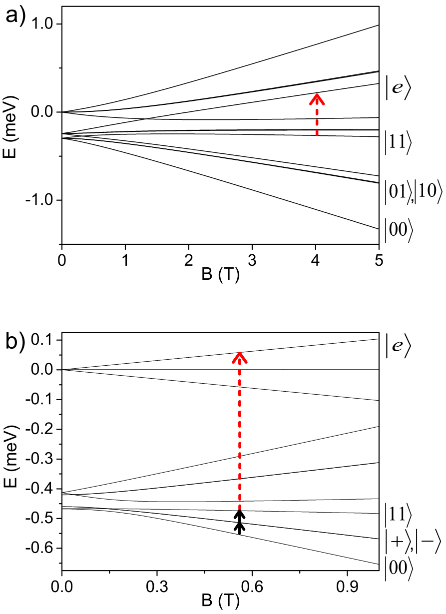

Figure 3.4: Level diagram for two representative compounds. (a) Level diagram of (CIS-**2**) as a function of the external magnetic field. The parameters of the spin Hamiltonian 3.2 are deduced *ab-initio*. Quantum gates are simulated with a static field of $B = 4\ T$, choosing the direction ($\theta = 65^\circ$ with respect to the Ni easy-axis) to optimize the fidelity. Computational states are defined on the right part of the figure, and the dashed arrow indicates the excitation involved in the Cφ. (b) Lowest levels of compound TRANS-**5** as a function of the field applied along the Ni easy-axis. The eigenstates correspond to the two-qubit states $|00\rangle$ and $|11\rangle$ and to the symmetric and antisymmetic superpositions $|+\rangle \equiv \frac{1}{\sqrt{2}}(|01\rangle + |10\rangle)$ and $|-\rangle \equiv \frac{1}{\sqrt{2}}(|01\rangle - |10\rangle)$. The continuous arrows indicate the transitions involved in the simultaneous rotation of the two qubits.

the implementation of one-qubit gates. However, for the present compounds δE is so small that this potential problem is overcome by exploiting the dispersion of the gaussian pulses.

Fig. 3.4-(b) reports the calculated field-dependence of the energy levels in the TRANS-**5** compound. In this case the two rings are parallel and it is not possible to individually rotate each qubit with uniform pulses. This implies that these systems can be exploited to simulate only Hamiltonian terms invariant by permutation of the two sites.

The entangling two-qubit gate controlled-φ (Cφ) is obtained (for both CIS and TRANS variants) by exciting and de-exciting the $|11\rangle$ component of the wavefunction to the state $|e\rangle$ outside the computational basis (see dashed arrows in Fig. 3.4), corresponding to a rotation of the central Ni^{2+} ion state. This allows us to implement a conditional (two-qubit) dynamics because the energy cost of this rotation depends on the states of the two molecular qubits by an amount of the order of J_{iso}. Hence, Cφ can be implemented by a pulse resonant with the gap indicated by the dashed arrows in Fig. 3.4, followed by a repetition of the same pulse that brings the state back to $|11\rangle$ (see Fig.3.5-(b) for the CIS-**2** variant) with an additional phase φ. The value of φ is controlled by the phase difference between the first and the second pulse. It is worth noting that the sign of J_{iso} is not important for the feasibility of the scheme.

The fidelities $\mathcal{F}$ (Eq. 0.17) obtained in the simulation of one- and two-qubit gates are reported in Table 3.3 for the different compounds. For each compound, the direction and magnitude of the applied field are chosen in order to optimize $\mathcal{F}$. These calculations have been performed by initializing the system in a generic superpositions of the two-qubit basis states, and by performing rotations of $\pi/3$ around the x axis or controlled-φ gate with $\varphi = \pi$.

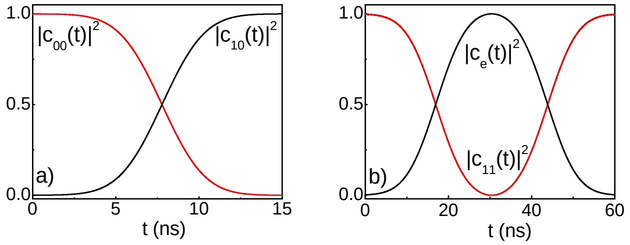

Figure 3.5: Simulation of universal quantum gates. Squared absolute value of the components of the system wave-function $|c_j(t)|^2$ as a function of time, for a single-qubit rotation (a) and Cφ (b). The simulation is performed on the (CIS-**2**) compound, employing a gaussian magnetic pulse $B_\perp(t) = B_{\perp 0}\, e^{-\frac{(t-t_0)^2}{2\tau^2}} \cos \omega t$, with $B_{\perp 0}$=50 G (a) and $B_{\perp 0}$=12.5 G (b). In the variants with larger J_{iso}, the time required for the implementation of Cφ can be substantially reduced by increasing $B_{\perp 0}$.

In view of designing two-qubit proof-of-principle experiments, we note that the presence of a small rhombic anisotropy allows us to implement high-fidelity quantum gates in TRANS variants also in small applied fields. Indeed, the resulting anticrossing in the low-lying energy levels can be exploited to match the two low-energy gaps indicated by continuous arrows in Fig. 3.5-(b), thus effectively decoupling the two qubits in the computational basis (see Table 3.3). For all variants we find $\mathcal{F} \geq 99\%$.

The ring-Ni coupling J_{iso} plays a twofold role in determining $\mathcal{F}$: on the one hand large values of J_{iso} ensure larger fidelities in the implementation of Cφ gates, on the other

Table 3.3: Fidelity of quantum gates. Fidelities of one- ($\mathcal{F}_R$) and two-qubit ($\mathcal{F}_{CZ}$) gates for each variant of Cr$_7$Ni-Ni-Cr$_7$Ni. The first two columns show the intensity (B) of the static magnetic field and the angle (θ) it forms with the central Ni easy axis. The amplitude of the oscillating field employed for CZ ($B_{\perp 0}$) is shown in the last column, while it is always set to 50 G for rotations.

	B	θ	$\mathcal{F}_R$	$\mathcal{F}_{CZ}$	$B_{\perp 0}$
CIS-**1**	9.00 T	13°	99.0	99.9	25 G
CIS-**2**	4.00 T	65°	99.9	99.2	12.5 G
TRANS-**3**	1.00 T	0°	99.9	99.1	10 G
TRANS-**4**	1.17 T	0°	99.9	99.9	25 G
TRANS-**5**	0.57 T	0°	99.9	99.9	25 G

hand they give rise to a not-perfect decoupling of the two qubits during rotations (because of the residual second-order coupling, see Eq. 3.3). Even if J_{iso} is very small in CIS-**2** and TRANS-**3** variants, Cφ can be implemented using oscillating fields of 10-12.5 G. Other variants with larger J_{iso} allow us to employ larger oscillating fields, resulting in shorter gating times, but less spectral resolution. In particular, a value of $|J_{iso}| \gtrsim 2 - 3\ \mu eV$ is sufficient to spectrally resolve this transition even with an oscillating field as large as 25 G.

3.2.4 Quantum Simulation

In the previous section, we have shown that single-qubit rotations and two-qubit gates can be implemented with high fidelities by uniform electromagnetic pulses. Hence, these systems can be exploited to implement quantum simulation algorithms, by decomposing the target time evolution into a sequence of elementary operations as in Ref. [17]. See also Sec. 0.1.5 for an overview on digital quantum simulation. In practice, we adopt a two-step procedure: i) the time-evolution operator of the Hamiltonian which we want to simulate is decomposed in a product of elementary gates by the well-known Trotter-Suzuki formula; ii) these gates are implemented by a sequence of magnetic pulses as

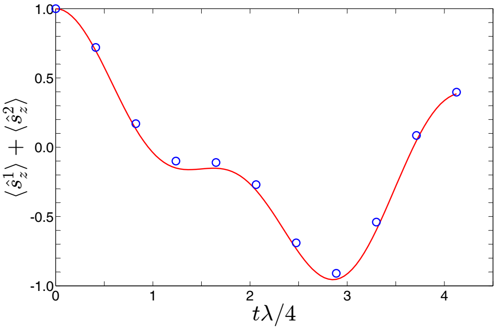

Figure 3.6: Simulation of the transverse-field Ising model. Time oscillations of the longitudinal average magnetization $\langle \sum_i \hat{s}_z^i \rangle$ in a transverse-field Ising model for the case with $\lambda = 2b$ and $N = 2$ qubits. The spins are parallel at time $t = 0$. The exact result (continuous line) corresponding to 10 trotterization steps is well reproduced by the simulation (dots).

described before. For instance, Fig. 3.6 shows the theoretical results (dots) for the quantum simulation with the TRANS-**5** variant of the oscillations of the magnetization in the prototypical Transverse-field Ising model (TIM), compared with the exact result corresponding to 10 trotterization steps [16]. The TIM Hamiltonian for N sites is:

$$\hat{\mathcal{H}}_{\text{TIM}} = \lambda \sum_{k=1}^{N-1} \hat{s}_{kz}\hat{s}_{(k+1)z} + b \sum_{k=1}^{N} \hat{s}_{kx}. \tag{3.4}$$

The duration of the pulse sequence implementing the simulation is about 350 ns, significantly shorter than the expected decoherence time. This provides an example of an already feasible proof-of-principle experiment, which would require measuring the magnetization of one of the existing single crystals after the pulse sequence. Other models can be simulated as described in Ref. [17].

3.2.5 Decoherence

The previously reported simulations considered an "ideal" Hamiltonian evolution, occurring on a time-scale much shorter than the expected qubit decoherence time. A first, quantitative estimate of the performance of the proposed setup in a more realistic scenario can be obtained by including the effect of decoherence in a master equation formalism (see Appendix E). To this aim, we numerically solve the Liouville-von Neumann equation of motion for the system density matrix, subject to the pulse sequence implementing the gates:

$$\dot{\hat{\rho}} = -i\left[\hat{H},\hat{\rho}\right] + \frac{1}{T_2^{ring}} \sum_{i=1,2} \mathcal{D}_{\hat{T}^i_{0+}\hat{T}^i_{0-}}[\hat{\rho}] + \frac{1}{T_2^{swich}} \sum_{k=0,1} \mathcal{D}_{\hat{S}_{k+}\hat{S}_{k-}}[\hat{\rho}]. \tag{3.5}$$

Here T_2^{ring} and T_2^{switch} are the pure dephasing rates of the qubits and of the Ni switch, respectively. The dissipator acting on the $k-$th transition of spin S is given by $\mathcal{D}_{\hat{S}_{k+}\hat{S}_{k-}} = \hat{S}_{k+}\hat{S}_{k-}\hat{\rho}\ \hat{S}_{k+}\hat{S}_{k-} - \frac{1}{2}\left(\hat{S}_{k+}\hat{S}_{k-}\hat{\rho} + \hat{\rho}\hat{S}_{k+}\hat{S}_{k-}\right)$. Here, to describe pure dephasing in an ion with spin S, we need to include all the spin raising and lowering operators $\hat{S}_{k+} = |k+1\rangle\langle k|$ and $\hat{S}_{k-} = \hat{S}^{\dagger}_{k+}$ for $k = 0, ..., 2S-1$. Consequently, only $k = 0$ terms must be included for the qubits and $k = 0, 1$ for the Ni switch. For simplicity, we have assumed the same dephasing time for the two transitions of the Ni switch. Fig. 3.7 (left panel) shows a colormap of the fidelity in the implementation of a controlled-φ gate (with $\varphi = \pi/3$), as a function of the pure dephasing times of the rings and of the switch. It is worth noting that for reasonable values of $T_2 \sim \mu s$ the fidelity remains very high (above 99 %). This is confirmed also by the results reported in Fig. 3.7 (right panel), where the oscillation of the magnetization in the TIM model is well reproduced for $T_2 \sim 10\ \mu s$ and is still captured also for smaller $T_2 \sim \mu s$.

3.3 Co switch

In this section we analyze an alternative supra-molecular complex consisting of two perpendicularly arranged qubits, linked by means of a Co^{2+} ion, synthesized by our chemists co-workers in Manchester. They also characterized the compound by continuous-wave (CW) Electron Paramagnetic Resonance (EPR) spectroscopy. Here we demonstrate

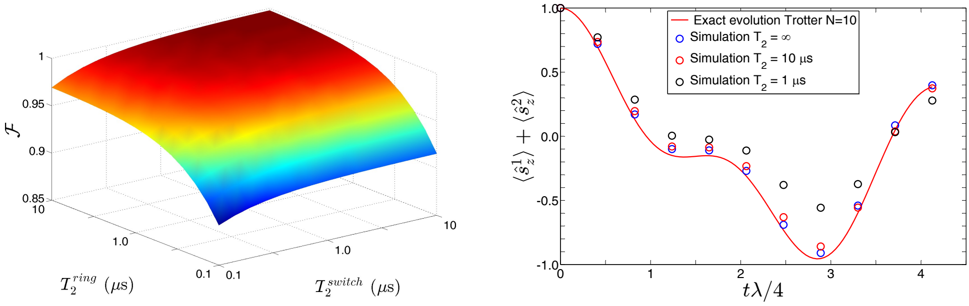

Figure 3.7: Effect of decoherence on the Quantum gates. Left panel: fidelity of the Cφ gate implemented on compound TRANS-**5**, as a function of the pure dephasing rates of the rings (T_2^{ring}) and of the Ni switch (T_2^{switch}). The simulation is performed by numerically solving the master equation for the system density matrix, for $\varphi = \pi/3$ and initializing the two-qubit state in a random initial state. (b) Oscillations of the magnetization in the digital quantum simulation of the TIM on a pair of qubits (compound TRANS-**5**). Different series of points compare results obtained for different values of the dephasing rates.

the high performance of the proposed quantum computing scheme by detailed numerical simulations.
The central Co^{2+} ion has a six-coordinate CoN$_6$ octahedral environment with a cis-arrangement of the two thiocyanate N atoms. The Co–N bond distances are typical of high spin Co^{2+} ions, with the bonds to the thiocyanate ligands shorter than those to terpy or pyridine N-donors. This produces a distorted octahedral, high-spin d^7 Co^{2+} site ($S_{Co} = 3/2$) with an important spin-orbit coupling ($^4T_{1g}$ term in ideal O_h symmetry) which leads to an effective spin 1/2 ground state at low temperature (as also confirmed by EPR spectroscopy). The cis coordination geometry at the Co^{2+} node leads to an almost orthogonal orientation of the two qubits. This asymmetry is one of the requirements for the implementation of a CNOT gate, as we will show below.

3.3.1 EPR Characterization

To gain information about the qubit-qubit interaction and characterize the supra-molecule CW EPR measurements have been performed and analyzed in Manchester. Results are shown in Fig. 3.8. They are well reproduced by assuming a model Hamiltonian consisting of a chain of three $S = 1/2$, interacting via an anisotropic exchange coupling:

$$\begin{aligned} \hat{H} &= \hat{\mathbf{s}}_1 \cdot \underline{\mathbf{J}}_{1C} \cdot \hat{\mathbf{S}}_C + \hat{\mathbf{S}}_C \cdot \underline{\mathbf{J}}_{2C} \cdot \hat{\mathbf{s}}_2 + \\ &+ \mu_B \left(\hat{\mathbf{s}}_1 \cdot \underline{\mathbf{g}}_1 + \hat{\mathbf{S}}_C \cdot \underline{\mathbf{g}}_C + \hat{\mathbf{s}}_2 \cdot \underline{\mathbf{g}}_2 \right) \cdot \mathbf{B}. \end{aligned} \tag{3.6}$$

Here $\hat{\mathbf{s}}_1$ and $\hat{\mathbf{s}}_2$ are the spins of the two rings, while $\hat{\mathbf{S}}_C$ is the effective spin 1/2 modeling the Co ground doublet. The best-fit parameters are reported in Table 3.4.
Implementing interesting quantum algorithms requires long-lived qubits, which can be manipulated many times without errors. In order to check that this key property is preserved, even in the present supra-molecular assembly, pulsed-EPR measurements have been performed in Manchester on the investigated compound. The decoherence time is

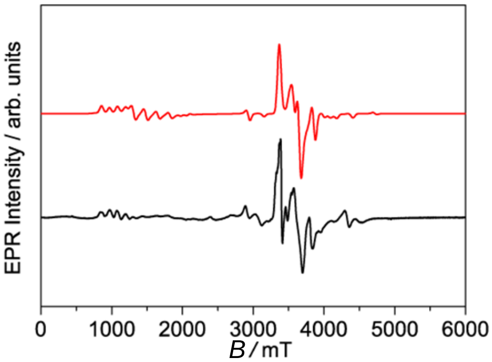

Figure 3.8: EPR spectroscopy of the Co-switch compound. Measured powder W-band (≈ 90 GHz) EPR spectra at 5 K of the Co-switch compound (black) and corresponding simulation (red) using the Hamiltonian 3.6, with the parameters given in Table 3.4.

assessed using a $\pi/2 - \tau - \pi - \tau$ echo sequence, finding remarkably long $T_2 \sim 800$ ns [1]. This demonstrates that the phase memory time is not influenced by fine structural details in the linking of the rings. It is worth noting that these results are extremely promising, as no attempt of optimization of the system for phase memory have been done, and clearly show that Cr_7Ni rings are excellent candidates for the physical implementation of QIP, independently if they are integrated in a supramolecular assembly.

Table 3.4: Parameters of the Co-switch Hamiltonian. Best-fit parameters obtained from EPR spectroscopy for the supra-molecular assembly linked by the Co-switch. Exchange coupling constants are given in μeV.

	g_x	g_y	g_z
Q_1	1.78	1.78	1.74
Co	1.78	4.25	6.50
Q_2	1.78	1.78	1.74
	J_x	J_y	J_z
J_{1C}	35	-84	-42
J_{2C}	17	-42	-84

3.3.2 Simulation of the CNOT gate

In the following, we show that the here reported compound is suitable to implement the CNOT gate, using uniform magnetic pulses as the only manipulation tool. Analogously to the Ni-switch complexes, we define the computational basis within the low-energy subspace where Co^{2+} is frozen into its $M = -1/2$ state, which corresponds to the four lowest levels, shown in red in Fig. 3.9-(a). The four levels correspond to arrangements of the spins on two qubits, $\hat{\mathbf{s}}_1$ and $\hat{\mathbf{s}}_2$, having the relative orientations $|\downarrow\downarrow\rangle$, $|\downarrow\uparrow\rangle$, $|\uparrow\downarrow\rangle$ and $|\uparrow\uparrow\rangle$ respectively, which we label as $|00\rangle$, $|01\rangle$, $|10\rangle$ and $|11\rangle$ in Figure 3.9-(a). In a field of few Teslas the eigenstates are factorised, with negligible entanglement between

---

[1] The decay of the echo intensity has been fitted with a single exponential $I = I_0 e^{-2t/T_2}$

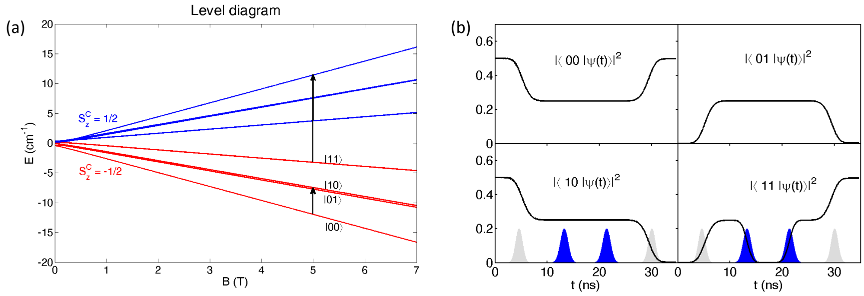

Figure 3.9: A CNOT Gate based on the structure of the Co-switch complex. (a) Field-dependence of the energy levels resulting from the Hamiltonian 3.6. The low-energy group of levels (red), where Co is frozen into its M = –1/2 state, defines the computational basis. The high-energy group of levels, where the Co spin is inverted, is exploited to perform two-qubit gates. (b) Simulation of the pulse sequence implementing CNOT as $\hat{R}_y(\pi/2)\hat{U}_{CZ}\hat{R}_y(-\pi/2)$, where $\hat{R}_y(\theta)$ is a rotation of the target qubit by an angle θ around the y-axis and $\hat{U}_{CZ}$ is the unitary operator implementing a controlled-Z gate. We illustrate the gate by starting at time $t = 0$ with a superposition state $\frac{|0\rangle+|1\rangle}{\sqrt{2}} \otimes |0\rangle$, which transforms under a CNOT gate (with the left qubit acting as control) into the Bell state $\frac{|00\rangle+|11\rangle}{\sqrt{2}}$. The latter state is actually obtained by the pulse sequence implementing $\hat{R}_y(\pi/2)\hat{U}_{CZ}\hat{R}_y(-\pi/2)$, with a fidelity of 99.7%. The envelope of the pulses implementing the two $\hat{R}_y$ rotations and the CZ are outlined at the bottom. Note that performing the CZ gate (two central pulses) requires temporarily leaving the computational subspace. The intensity of the oscillating field at the pulse maximum is 50 G, and we assume a static field is 5 T directed along z.

the rings and the Co^{2+}. Hence it is possible to implement high-fidelity single-qubit rotations by EPR pulses resonant with low-energy gaps [see, e.g., the shorter arrow in Figure 3.9-(a)]. The residual very weak qubit-qubit interaction results in an unwanted evolution of the qubits state, however only on a timescale (ca. 500 ns) much longer than that of the proposed CNOT gate (see discussion below). The combination of the inequivalent and anisotropic ring-Co exchange interaction and of the perpendicular arrangement of the two rings makes the two qubits significantly inequivalent. This makes the $|10\rangle$ and $|10\rangle$ states non-degenerate and therefore in principle we can control whether we perform the $|00\rangle \rightarrow |01\rangle$ or $|00\rangle \rightarrow |10\rangle$ single-qubit rotation.

Conversely, two-qubit gates can be implemented by exciting the switch, i.e., by temporarily bringing the complex to states where the Cobalt ion is in its $M = +1/2$ state (as in the case of the Ni switch). In particular, a controlled phase-shift (Cφ) gate is obtained by a pulse resonant with the transition corresponding to the longer arrow in Figure 3.9-(a), followed by a repetition of the same pulse that would bring the state back with an additional phase φ. The value of φ is controlled by the phase difference between the first and the second pulse. For a pulse with field along the y-direction the implementation of this gate is relatively fast thanks to the large value of g_y for Co^{2+} ion. Moreover, the relatively large exchange interaction in Eq. 3.6 allows us to employ large oscillating fields (50 G), since the desired transition is spectroscopically well resolved from all the others. Consequently, the Cφ gate can be performed in only about 12 ns, with fidelities close to 99.99 %.

The CNOT gate is then obtained by the sequence of gates $\hat{R}_y(\pi/2)\hat{U}_{CZ}\hat{R}_y(-\pi/2)$, where $\hat{R}_y(\theta)$ is a single-qubit rotation of the target qubit by an angle θ around the y-axis (see Sec. 0.1.1) and $\hat{U}_{CZ}$ is the unitary operator implementing the controlled-Z gate. We have numerically resolved the time-dependent Schrödinger equation for the Hamiltonian 3.6 in presence of the pulse sequence implementing the CNOT. Results are reported in Figure 3.9-(b) and show that this two-qubit gate can be obtained with very high fidelity in only 30 ns. As noted above, the two qubits are significantly inequivalent, even if the $\underline{\mathbf{g}}$ tensor of the rings is nearly isotropic. This makes this complex well suited for the quantum simulation of antisymmetric Hamiltonians.

3.3.3 Quantum Simulation of an anti-symmetric Hamiltonian

As an illustrative example, we apply a sequence of single and two-qubit quantum gates to simulate the evolution induced on two S = 1/2 spins by the Dzyaloshinskii-Moriya anti-symmetric exchange interaction $\hat{\mathcal{H}}_a = G_y\left(\hat{s}_{1z}\hat{s}_{2x} - \hat{s}_{1x}\hat{s}_{2z}\right)$. The sequence of quantum gates required to implement the evolution induced by a Hamiltonian term of type $G_y\hat{s}_{1z}\hat{s}_{2x}$ is $\hat{R}_y(\pi/2)e^{-iG_y t\hat{s}_{1z}\hat{s}_{2z}}\hat{R}_y(-\pi/2)$, where $\hat{R}_y(\theta)$ is a rotation of the second qubit about the y-axis and the Ising $G_y t\hat{s}_{1z}\hat{s}_{2z}$ evolution is obtained similarly to the Cφ gate, by simultaneously exciting and de-exciting both components $|00\rangle$ and $|11\rangle$ outside the computational basis to the corresponding states where the Co spin has been tilted. Figure 3.10 shows that the calculated fidelity for the simulation of this model is high, and indeed the agreement with the exact evolution is evident. Here in order to monitor the time evolution induced by $\hat{\mathcal{H}}_a$ on the two-qubit state we have reported the associated evolution of the average total spin of the two qubits $\langle\hat{S}_z\rangle = \langle\hat{s}_{1z} + \hat{s}_{2z}\rangle$. In fact, this observable can be extracted in an actual experiment on an ensemble of molecules by a measurement of the sample magnetization. We have also simulated the evolution due to the other terms of Dzyaloshinskii-Moriya interaction. In particular, for a term $G_z\hat{s}_{1y}\hat{s}_{2x}$ the sequence of gates to be implemented is $\hat{R}^1_x(-\pi/2)\hat{R}^2_y(\pi/2)e^{-iG_y t\hat{s}_{1z}\hat{s}_{2z}}\hat{R}^2_y(-\pi/2)\hat{R}^1_x(\pi/2)$.

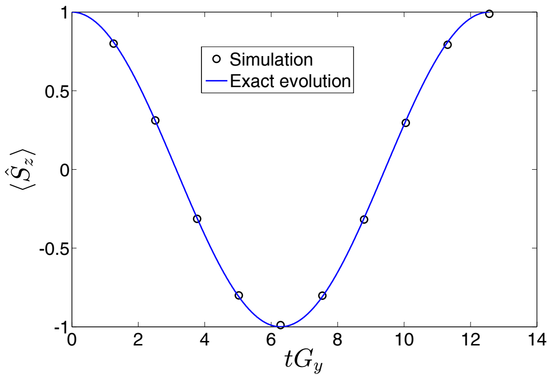

Figure 3.10: Quantum simulation of an antisymmetric Hamiltonian. Oscillation of the expectation value of the magnetization in the quantum simulation of the antisymmetric Hamiltonian $\hat{\mathcal{H}}_a = G_y\left(\hat{s}_{1z}\hat{s}_{2x} - \hat{s}_{1x}\hat{s}_{2z}\right)$. The simulation (points) is performed with the parameters obtained from EPR (Table 3.4) and is in excellent agreement with the exact evolution (continuous line). The time required for the whole simulation is about 70 ns (much shorter than the qubit dephasing time) and the average fidelity is 98.5 %. The intensity of the oscillating field at the pulse maximum is 50 G, and we assume a static field is 5 T directed along z.

For each of this terms, we have obtained fidelity of the order of 99.5 % on a random superposition initial state.

3.3.4 Residual qubit-qubit coupling in the Co-switch compound

We determine the form of the unwanted residual effective ring-ring interaction in the low-energy subspace in which Co is in its $M = -1/2$ state (switch in the off state). By using second-order perturbation theory the Co-qubit coupling leads to a residual qubit-qubit interaction given by

$$\hat{H}_{res} = \Gamma_{xx}\hat{S}_{1,x}\hat{S}_{2,x} + \Gamma_{yy}\hat{S}_{1,y}\hat{S}_{2,y} + \lambda_1\hat{S}_{1,z} + \lambda_2\hat{S}_{2,z} + C, \tag{3.7}$$

with

$$\Gamma_{xx} = -\frac{g_{1,z}J_{1,y}J_{2,x}\big(g^2_{Co,z} - g^2_{2,z}\big) + J_{1,x}\big[J_{2,x}g_{Co,z}\left(2g^2_{Co,z} - g^2_{2,z} - g^2_{1,z}\right) + J_{2,y}g_{2,z}\big(g^2_{Co,z} - g^2_{1,z}\big)\big]}{4\mu_B B_z\left(g^2_{Co,z} - g^2_{1,z}\right)\left(g^2_{Co,z} - g^2_{2,z}\right)}$$

$$\Gamma_{yy} = -\frac{g_{2,z}J_{1,y}J_{2,x}\big(g^2_{Co,z} - g^2_{1,z}\big) + J_{2,y}\big[J_{1,y}g_{Co,z}\left(2g^2_{Co,z} - g^2_{2,z} - g^2_{1,z}\right) + J_{1,x}g_{1,z}\big(g^2_{Co,z} - g^2_{2,z}\big)\big]}{4\mu_B B_z\left(g^2_{Co,z} - g^2_{1,z}\right)\left(g^2_{Co,z} - g^2_{2,z}\right)}$$

$$\lambda_1 = -\frac{J_{1,z}}{2} - \frac{2g_{Co,z}J_{1,x}J_{1,y} + g_{1,z}\left(J^2_{1,x} + J^2_{1,y}\right)}{8\mu_B B_z\left(g^2_{Co,z} - g^2_{1,z}\right)}$$

$$\lambda_2 = -\frac{J_{2,z}}{2} - \frac{2g_{Co,z}J_{2,x}J_{2,y} + g_{2,z}\left(J^2_{2,x} + J^2_{2,y}\right)}{8\mu_B B_z\left(g^2_{Co,z} - g^2_{2,z}\right)}$$

Apart from a constant term and a renormalization of the external field felt by the qubits, we find XX and YY interactions, which induce an unwanted evolution when the switch is turned off, by mixing states $|01\rangle$ and $|10\rangle$. To obtain high-fidelity single qubit gates, these interactions should be small. The expression above shows that these can be controlled by the strength of the applied field or by the size of the Co-ring exchange. With a static field of 5 T the oscillation induced by $\hat{H}_{eff}$ occurs on a timescale of 0.5 μs, which is much longer than the time required for elementary gates. This is clearly shown in Figure 3.11 (left panel), where we report the fidelity of such an idle evolution for a pair of qubits initialized in $\frac{|01\rangle+|10\rangle}{\sqrt{2}}$. We have checked that this state is one of the most error-prone. We see that the timescale of the unwanted evolution (T_{UE}, defined as the time required to reduce the fidelity to 0.9) is 170 ns, much more than the CNOT gating time (34 ns). It is worth noting that by halving the Co-ring exchange interaction we gain an order of magnitude in the timescale of the unwanted interaction (red line), without significantly affecting the gate fidelities. This enhancement is due to the significant splitting (induced by the asymmetric coupling to the switch) between the $|01\rangle$ and $|10\rangle$, which therefore are affected by the residual interaction only at perturbative orders higher than two.

3.4 Scalability

The proposed schemes for quantum information processing can be extended to chains of Cr_7Ni rings, connected through Ni/Co ions. Indeed, we can envisage connecting some of the proposed two-qubit units to form finite chains of qubits with nearest-neighbors

switchable interactions [93].
Given the ability to overcome these issues on the experimental side, it is crucial to gain a deeper insight into the theoretical scalability of the proposed schemes. Indeed, the extension of the two-qubit setup to a multi-qubit register raises some fundamental issues concerning the propagation of errors. In the proposed implementation, we can identify two main sources of errors: pure dephasing of the qubits and imperfect operation of the switch, which leads to a residual inter-qubit interaction still present also in the off state.

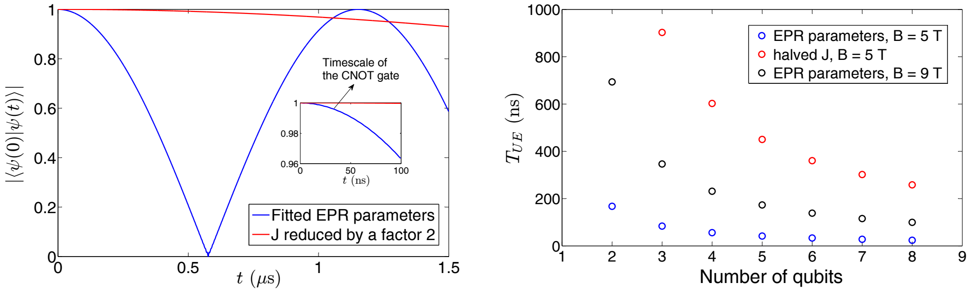

Figure 3.11: Effect of the residual qubit-qubit interaction. Left: fidelity of the idle evolution for a two-qubit state prepared in $\frac{|01\rangle+|10\rangle}{\sqrt{2}}$ as a function of time. Inset: zoom on the timescale of the CNOT gate. Right: unwanted evolution time (T_{UE}) against number of qubits in a one-dimensional chain. T_{UE} is defined as the time required to reduce the fidelity to 0.9. Different sets of points compare the effect of a reduction of the exchange constants or of an increase of the magnetic field. The $N-$qubit state was initialized in $\frac{|0101...\rangle+|1010...\rangle}{\sqrt{2}}$, which was checked to be one of the most error-prone.

First of all, we notice that errors induced by decoherence increase with the overall computational time. We stress that the proposed platform allows us to manipulate simultaneously non-overlapping parts of the register, thus drastically reducing the computation time and decoherence-induced errors with respect to a serial implementation. As already noticed above (Sec. 3.1), this limits the class of target Hamiltonians which can be simulated, but greatly increases the performance of the setup, by reducing the computational time. Suppose, for instance, that we need to induce a two-qubit evolution on each pair of neighboring qubits. This can be performed first by turning on simultaneously the interaction between all the N/2 ″even″ bonds, and then simultaneously on the remaining N/2 ″odd″ bonds. Excitations of the ″even″ switches can be made spectroscopically distinguishable from the excitation of the ″odd″ switches by proper chemical engineering.
In the following, we examine the scaling of the errors with the number of qubits in the register. Both the effect of decoherence and of the residual inter-qubit interaction are enhanced by increasing the number of qubits, since they influence idle and manipulated qubits on an equal footing. First, we focus on the effect of pure dephasing on a set of non-interacting qubits, subject to a Lindblad (Markovian) dynamics. For each qubit, initialized in a pure state $|\psi(0)\rangle = \alpha|0\rangle + \beta|1\rangle$, corresponding to $\hat{\rho}(0) = |\psi(0)\rangle\langle\psi(0)|$, the

time dependence of the fidelity is given by:

$$\mathcal{F}_1 = \sqrt{|\alpha|^4 + |\beta|^4 + 2|\alpha|^2|\beta|^2 e^{-\frac{t}{2T_2}}} = \sqrt{1 - 2|\alpha|^2|\beta|^2 \left(1 - e^{-\frac{t}{2T_2}}\right)}, \tag{3.8}$$

where we have exploited $|\alpha|^2 + |\beta|^2 = 1$ and assumed T_2 as the single-qubit dephasing time. It can be easily verified that the state maximizing the error $\varepsilon = 1 - \mathcal{F}^2$ on a single qubit is that characterized by $|\alpha|^2 = |\beta|^2 = 1/2$. It was also recently shown [94] that the choice $|\psi(0)\rangle^{\otimes N}$ as the initial state for N qubits is the one maximizing the $N-$qubit error ε_N. Its fidelity is simply the product of single qubit fidelities or, equivalently (to lowest order in ε), $\varepsilon_N = N\varepsilon_1 = \frac{N}{2}\left(1 - e^{-\frac{t}{2T_2}}\right)$. Finally, in the limit $t \ll 2T_2$, we find $\varepsilon_N = N\frac{t}{4T_2}$. It is worth noting that, in a parallel implementation, t is limited by the value it assumes for a chain of 3 qubits, whereas in a serial scheme it increases linearly with N. By proper chemical engineering of the qubits, T_2 as large as ~ 15 μs can be obtained. This enables the implementation of several two-qubit gates ($\sim$ 20) even on a chain consisting of 10 qubits (in this case the error is still 0.1).

We now analyze the effect on scalability of an imperfect operation of the switch, for both Ni and Co variants. As a consequence of the always on residual interaction an unwanted evolution of the qubits is induced even in the idle configuration. The effect of this imperfect decoupling between the qubits increases with N, thus limiting the maximum number of qubits which can be independently rotated. For instance, with the present Ni systems quantum gates can be performed only in short chains with $N \simeq 5 - 6$. This number can be significantly increased by improving the performance of the switch. This in turn could be obtained by modifying the ligand cage of the Ni ion in order to increase the zero-field splitting and reduce the harmful residual second-order couplings.

As far as the Co-switch compound is concerned, by halving the Co-ring exchange interaction we gain an order of magnitude in the timescale of the unwanted interaction. This can be easily obtained by coordination chemistry (as demonstrated for the family of Ni complexes) and would become crucial in order to scale the present architecture to a sizeable number of qubits. A plot of the unwanted evolution time against the number of qubits (arranged in a one-dimensional chain) is reported in Figure 3.11 (right panel). The parameters measured by EPR in the proposed compound (blues circles) allow us only to manipulate a few qubits on a chain. Conversely, if the exchange interaction is reduced by a factor 2 (red points), many gates can be implemented even in a linear array of 8 qubits. A similar result can also be obtained by increasing the magnetic field from 5 to 9 T (black circles). We stress, however, that the present compound is already very promising for immediate proof-of-principle experiments.

3.5 Conclusions

Summarizing, we have proposed a scheme for implementing a universal set of one and two-qubit gates in permanently coupled molecular qubits. We have shown that two newly synthesized families of molecular nanomagnets, consisting of pairs of Cr_7Ni bridged via a single divalent metal ion (Ni or Co), are very promising two-qubit assemblies for applying the proposed scheme in proof-of-principle experiments and can constitute the elementary units of future scalable setups, capable of simulating interesting physical models.

The compounds have been extensively studied by means of ab-initio calculations or EPR spectroscopy, thus extracting on all variants the exchange constants, the zero-field-

splitting parameters and the $\underline{\mathbf{g}}$ tensors. Using these results, we have shown that single-qubit rotations and two-qubit gates can be implemented with high fidelities by uniform electromagnetic pulses. Even if the parameters change significantly in the various compounds, quantum gates can always be implemented. Indeed, within our scheme, the feasibility of these gates only relies on the smallness of the qubit-switch exchange coupling with respect to the other energy scales (zero-field splitting of the Ni and difference in Zeeman energy between switch and qubits) and not on their precise values.
These systems can thus be exploited to implement quantum simulation algorithms of prototypical model Hamiltonians. In this respect, the performance of the proposed setup as a quantum simulator has been tested by numerical experiments, finding it to be robust also with respect to errors due to decoherence.

Part of the content of this chapter was published in NPG Sci. Rep. **4**, 7423 (2014) (Ref. [84]).

QIP with local control of the qubit-qubit interaction

CHAPTER 4

Here we propose a protocol to implement the $\sqrt{\text{iSWAP}}$ (SQiSW) 2-qubit gate on a Cr_7Ni-M-Cr_7Ni complex. Contrary to the method introduced in the previous chapter, which employs global fields as a manipulation tool, this scheme is based on a local control of the qubit-qubit interaction. Indeed, it exploits the electric control of a redox-active linker, which can be locally addressed by a tip to reversibly switch on and off the qubit-qubit interaction, thus implementing the SQiSW gate.

Two different classes of compounds have been synthesized by our chemist co-workers in Manchester, with different redox-active linkers acting as a switch: a $Co^{2+,3+}$ ion (**1**) or a triangular $Ru_2^{3+}Co^{2+,3+}$ unit (**2**). The complexes have been characterized by continuous-wave and pulsed EPR spectroscopy and the obtained parameters are used to demonstrate that they are suitable for the implementation of the proposed scheme with remarkably high fidelity.

4.1 Characterization of the compounds

Compounds (**1**) and (**2**) have been structurally and magnetically characterized by X-ray diffraction and EPR spectroscopy, respectively. All measurements and analysis reported in this Section have been carried out by our co-workers in Manchester. Compound (**1**) consists of two equivalent Cr_7Ni rings (arranged in parallel) and linked by a redox-active $Co^{2+,3+}$ switch, as shown in Fig. 4.1-(a).

The EPR continuous-wave spectra of (**1**) are shown in Fig. 4.1-(b), for both the reduced and oxidized forms. Complex (**1**) was initially studied as prepared, while ($\mathbf{1}^{ox}$) was made by oxidation with $AgBF_4$; to complete the cycle (**1**) was regenerated using cobaltocene as a reducing agent. The EPR spectrum of (**1**) depends on the oxidation state of the central cobalt site. Here Q-band EPR is particularly informative, showing three resonances between 1100 and 1500 mT (Fig. 4.1). The spectra of (**1**) can be simulated by considering a simple Hamiltonian:

$$\hat{H} = J\left(\hat{\mathbf{S}}_1 \cdot \hat{\mathbf{S}}_2 + \hat{\mathbf{S}}_2 \cdot \hat{\mathbf{S}}_3\right) + \mu_B\left(\hat{\mathbf{S}}_1 \cdot \underline{g}_1 + \hat{\mathbf{S}}_2 \cdot \underline{g}_2 + \hat{\mathbf{S}}_3 \cdot \underline{g}_3\right) \cdot \mathbf{B}, \tag{4.1}$$

where J is the isotropic interaction between the effective $S_2 = 1/2$ centre on the Co^{2+} site and the two effective $S_{1,3} = 1/2$ Cr_7Ni rings. The spectra can be simulated using $\underline{\mathbf{g}}$-tensor measured for the isolated Co^{2+} complex ($g_x = 2.022$, $g_y = 2.111$, $g_x = 2.215$) and the known $\underline{\mathbf{g}}$-values of Cr_7Ni rings ($g_x = 1.78$, $g_y = 1.78$, $g_x = 1.74$); the only variable here is the ring-Co isotropic exchange interaction, J, which is essential to reproduce the experimental features. A good agreement between the simulated and the experimental spectra was found for $J = 6.0\ \mu eV$. The EPR spectrum of ($\mathbf{1}^{ox}$) is very simple, and resembles that of Cr_7Ni rings; this demonstrates that here Co is in its low spin diamagnetic state. The process is completely reversible: indeed, reduction of ($\mathbf{1}^{ox}$) back to (**1**) regenerates the original spectrum [compare black and blue curves in Fig. 4.1-(b)].
Pulsed-EPR measurements have also been performed in Manchester in order to check if the long decoherence time T_2 of the Cr_7Ni rings is preserved, even in the present redox-active assembly. By fitting the echo-intensity [Fig. 4.1-(c)] with a single exponential, it is found $T_2 = 818$ ns (and $\sim \mu s$ in the oxidized form), at least two orders of magnitude larger than the time required for the elementary gates (see below). This result is really promising, since no attempt to optimize the structure of the compound in order to increase its coherence has been done.

Complex (**2**) crystallises in the hexagonal $P6_122$ space group. Its molecular structure [Fig. 4.2-(a)] consists of two Cr_7Ni rings linked through the *iso*-nicotinate groups to the $[Ru_2^{3+}Co^{2+}O(^tBuCO_2)_6(py)]$ cluster. Fig. 4.2-(b) reports the product of the molar susceptibility and the temperature ($\chi_M T$) for this triangular unit, which should act as a switch in complex (**2**). The temperature dependence of $\chi_M T$ reveals a typical behavior of an octahedral, high-spin d^7 Co^{2+} site ($S_{Co} = 3/2$) with an important spin orbit coupling, interacting with a pair of Ru^{3+} ions strongly coupled by AFM exchange. The unquenched orbital angular momentum raises the room temperature $\chi_M T$ value to 3.11 emu K/mol, well above the spin-only value for a spin-quartet, while the decrease of $\chi_M T$ in the high-temperature region can be attributed to spin orbit effects. The final behaviour is that of an effective spin doublet.This is also confirmed by EPR data, which can be fitted by assuming an anisotropic effective spin 1/2, with $g_x = 5.61$, $g_y = 4.05$ and $g_z = 2.77$.
The EPR spectrum of the supra-molecular complex (**2**) is shown in Fig. 4.2-(c). Different curves correspond to different oxidation state of the triangular unit. Cyclic voltammogram measurements demonstrate that the oxidation locus is the $Co^{2+,3+}$ ion. Data collected at 5 K in K-band can be interpreted again by Hamiltonian 4.1, with an isotropic symmetric coupling between the central switch and the rings ($J = 6.4\ \mu eV$). Pulsed-EPR spin-echo measurements have also been realized, yielding pretty high values of $T_2 = 760$ ns.

4.2 State of the art: electrically gated molecules

Previously, Lehmann and co-workers have theoretically shown [7] that two spins $S = 1/2$ connected by a redox-active unit can be exploited for the implementation of the $\sqrt{\text{SWAP}}$ gate by switching the redox unit with a scanning tunnelling microscope (STM) tip at an appropriate potential. In this way one electron can be added or removed from the redox unit very quickly. The system described in [7] is a polyoxometalate, consisting of two $(VO)^{2+}$ qubits connected to a central mixed-valence core based on the $[PMo_{12}O_{40}]$ Keggin unit. The qubits are weakly magnetically coupled via the delocalized electrons of the central core. This coupling can be switched on and off in an all-electric way.

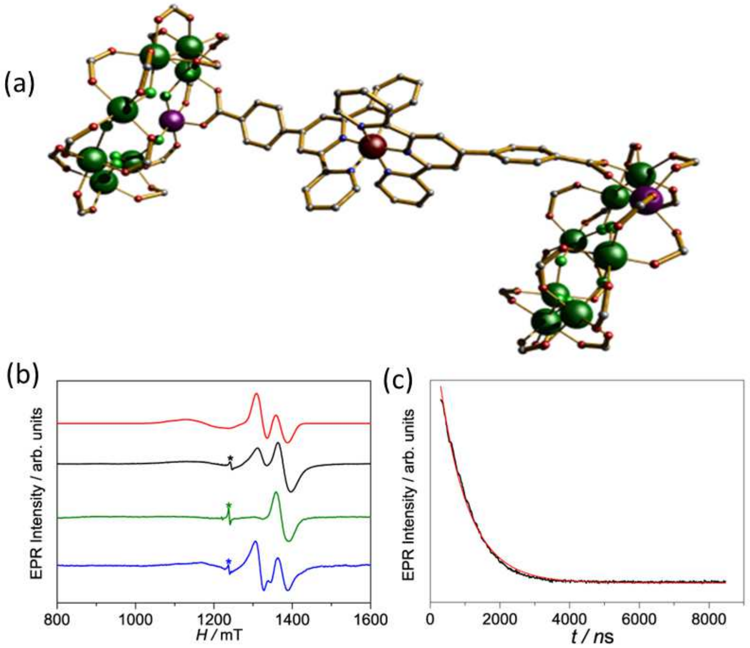

Figure 4.1: Characterization of compound (1). (a) Molecular structure of (**1**) determined by X-ray diffraction. Colour code: Co, brown; Cr, green; Ni, purple; N, cyan; O, red; S, yellow; C, grey; F, pale green. $^{n}Pr_2NH_2^+$ and ClO_4^- ions are not shown (H atoms and *tert*-butyl groups are omitted for clarity). (b) Experimental (black trace) frozen solution Q-band EPR spectra (frequency ~ 34 GHz) of (**1**) and corresponding simulation (red trace) using the Hamiltonian 4.1 and parameters given in the text. Measured frozen solution Q-band EPR spectra after oxidation of (**1**) with $AgBF_4$ (green trace) and subsequent reduction using (**1**) with cobaltocene (blue trace). The sharp peak marked * is a radical impurity. (c) Spin echo decay using a $\pi/2 - \tau - \pi - \tau$ pulse sequence with pulse lengths of 32 and 64 ns for (**1**). The red solid line corresponds to the best fit using an exponential decay function e^{-2t/T_2}, with $T_2 = 818$ ns.

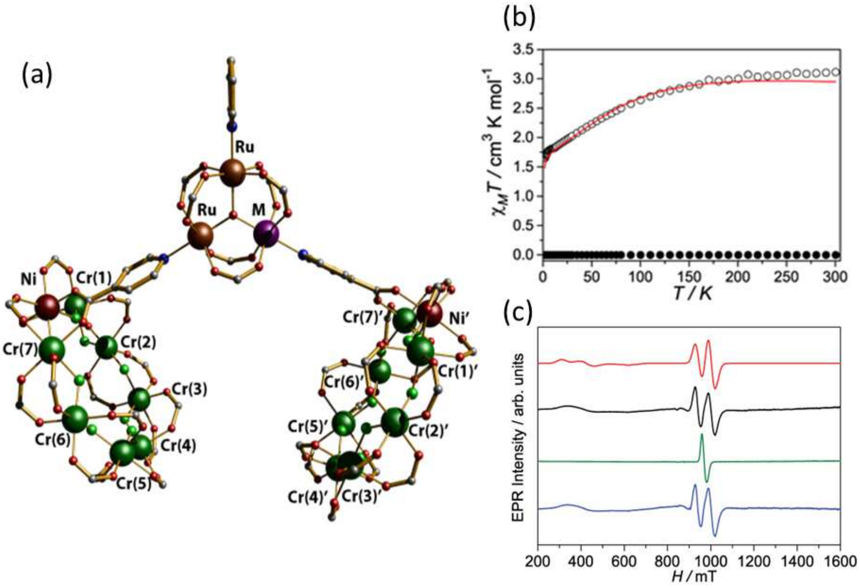

Figure 4.2: Characterization of compound (2). (a) Molecular structure of the neutral dimeric supramolecular assembly of (**2**) with M=Co. Colour code: M, purple; Cr, green; Ni, dark red; Ru, brown; N, cyan; O, red; C, grey; F, pale green. $^{n}\mathrm{Pr_2NH_2^+}$ cations, as well as H atoms and *tert*-butyl groups are not shown for clarity. Please note that the position of the statistically disordered M atom has been arbitrarily assigned. (b) Temperature dependence of the product of the direct current (dc) molar magnetic susceptibility by the temperature ($\chi_M T$) of the triangular switch unit $\mathrm{Ru_2Co}$. The solid red line corresponds to the best-fit curve. (c) Experimental frozen solution K-band EPR spectra of (**2**) (black trace). Simulation of (**2**) (red trace) using the Hamiltonian 4.1 and parameters given in the text. Measured frozen solution K-band EPR spectra (frequency $\sim$ 24 GHz) after oxidation of (**2**) with $\mathrm{[FeCp_2](PF_6)}$ (green trace) and after reducing using (**2**) with cobaltocene (blue trace).

The effective spin Hamiltonian, in the *on* state, is given by:

$$\hat{H} = J_{qq}\hat{\mathbf{S}}_1 \cdot \hat{\mathbf{S}}_3 + J_{qr}\hat{\mathbf{S}}_2 \cdot \left(\hat{\mathbf{S}}_1 + \hat{\mathbf{S}}_3\right) = \\ = \left(J_{qq} - J_{qr}\right)\hat{\mathbf{S}}_1 \cdot \hat{\mathbf{S}}_3 + \frac{J_{qr}}{2}\hat{\mathbf{S}}^2, \tag{4.2}$$

where the last equality is valid apart from a constant. The perfectly entangling $\sqrt{\text{SWAP}}$ gate results from the unitary evolution of two qubits (here $\mathbf{S}_1$ and $\mathbf{S}_3$), coupled by a Heisenberg interaction (see Sec. 0.1.2). In order to achieve this task, starting from Hamiltonian 4.2, one needs to eliminate the evolution induced by the term proportional to the square of the total spin $\hat{\mathbf{S}} = \hat{\mathbf{S}}_1 + \hat{\mathbf{S}}_2 + \hat{\mathbf{S}}_3$. It was demonstrated that particular sets of parameters of the trimer Hamiltonian lead to a pure $\sqrt{\text{SWAP}}$ evolution of the two qubits after specific time intervals. However, high fidelity for the gate is guaranteed only for fixed ratios between the qubit-qubit exchange (J_{qq}) and the qubit-redox unit exchange (J_{qr}). In the here-reported compounds, $J_{qr} = J$ and $J_{qq} = 0$ (see Eq. 4.1), resulting in a very low fidelity of the $\sqrt{\text{SWAP}}$ gate. In fact, for these parameters the scheme of Lehmann and co-workers implements a different two-qubit gate, which is not a perfect entangler, thus affecting the overall depth of circuits based on this gate.

4.3 $\sqrt{\text{iSWAP}}$ gate with local electric control

Here we propose a different and more flexible scheme for the SQiSW gate (defined in Eq. 0.11), which works if the two qubits have the same Zeeman energy but one different to that of the switch in the *on* state. This is the case here for both the examined compounds, where the g-values of the qubits and switches are very different, $g_z = 1.79$ for Cr$_7$Ni rings and $g_z = 2.215/2.77$ for the redox active unit. In the subsequent calculations, we focus on compound (**1**), but a similar analysis holds also for (**2**).

This difference in the g-values means that in magnetic fields of a few T, the ring-Co^{2+} exchange J is small compared to the difference between the Zeeman energies of Co^{2+} ion and of the Cr$_7$Ni rings. Hence, the spin state of the central Co^{2+} site is nearly frozen in the $M = -1/2$ state and has only tiny virtual fluctuations that lead to an effective interaction between the two Cr$_7$Ni qubits given by

$$\hat{H}_{qq} = \Gamma\left(\hat{S}_{1x}\hat{S}_{2x} + \hat{S}_{1y}\hat{S}_{2y}\right) + \lambda\left(\hat{S}_{1z} + \hat{S}_{2z}\right) \tag{4.3}$$

where z is the direction of the applied magnetic field, $\hat{S}_{1\alpha}$ ($\hat{S}_{2\alpha}$) is the component of the first (second) Cr$_7$Ni spin along the α-axis ($\alpha = x, y, z$), and

$$\Gamma = \frac{J^2}{2\mu_B B\left(g_{1z} - g_{Coz}\right)} \qquad \lambda = -\frac{J}{2} + \frac{J^2}{4\mu_B B\left(g_{1z} - g_{Coz}\right)}. \tag{4.4}$$

Thus, when the cobalt ion is in the diamagnetic Co^{3+} oxidation state, the two qubits are decoupled and single qubit operations can be performed with very high fidelity. This can be done by means of uniform magnetic pulses applied along a direction perpendicular to the static field. For the reported simulations we employed an oscillating field with Gaussian envelope $\mathbf{B}(t) = \mathbf{B}_0\cos(\omega t + \phi)e^{-\frac{(t-t_0)^2}{2\tau^2}}$. The frequency ω is chosen to match the Zeeman energy gap for the $M = -1/2 \rightarrow M = 1/2$ transition, while the phase ϕ controls the rotation axis in the xy plane of the Bloch sphere and the pulse duration

τ determines the rotation angle. Hence, we can obtain arbitrary single qubit $\hat{R}_x$ and $\hat{R}_y$ rotations.
Conversely, when we have Co^{2+} oxidation state the state of the two qubits evolves according to Hamiltonian 4.3, with negligible entanglement with the Co^{2+} centre. For specific times, this evolution coincides with the SQiSW gate, apart from single-qubit rotations along z due to the second term in 4.3. These can be obtained by exploiting the decomposition: $\hat{R}_z(\varphi) = \hat{R}_x\left(\frac{\pi}{2}\right)\hat{R}_y(\varphi)\hat{R}_x\left(-\frac{\pi}{2}\right)$.

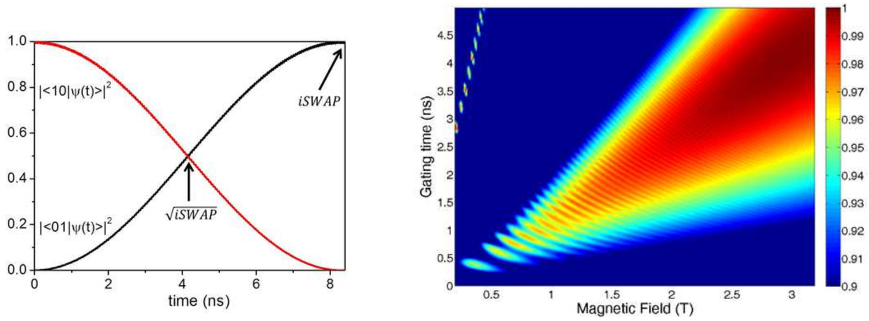

Figure 4.3: Simulation of the SQiSW gate Left: By choosing $|10\rangle \equiv |1/2, -1/2\rangle \otimes |-1/2\rangle_{Co}$ as initial state, we calculate for (**1**) the time-dependence of the trimer wavefunction components on $|10\rangle$ and $|01\rangle \equiv |-1/2, 1/2\rangle \otimes |-1/2\rangle_{Co}$ with B = 3 T. Other components are negligible. Right: Calculated average fidelity $\bar{\mathcal{F}}$ for (**1**) as a function of the magnetic field B and of the gating time, i.e., the time the Co switch is in the on state. The average has been made over four random starting states. For each value of the field, the optimal gating time t_f is the one maximizing $\bar{\mathcal{F}}$. The oscillations corresponding to the fringes in the picture are associated with fluctuations of the Co spin state. As long as their frequency is much larger than $1/t_f$ these fluctuations are negligible, i.e., the perturbative description of Eq. 4.3 is valid.

This perturbative picture is confirmed by the results of detailed calculations for compound (**1**) using the full Hamiltonian 4.1 (Fig. 4.3). Starting from the $|10\rangle$ logical state (i.e. the spin on one Cr$_7$Ni ring +1/2, representing the logical state $|1\rangle$, and on the second ring –1/2, representing $|0\rangle$), we report in Fig. 4.3 (left panel) the time evolution of the trimer wavefunction. In a magnetic field of 3 T, after 4 ns the wavefunction has contributions equals in modulo from $|10\rangle$ and $|01\rangle$, which corresponds to the SQiSW gate, while after 8 ns the two spins are fully exchanged, i.e. we have the $|01\rangle$ state. An extremely good fidelity $\mathcal{F}$ for compound (**1**) is obtained for fields of the order of about 2.5 T or larger, after a suitable gating time t_f of the order of a few ns (right part of Fig. 4.3). For such fields the perturbative picture of Eq. 4.3 holds very well, and $t_f \propto B$ consistently with the form of the effective qubit-qubit coupling $\Gamma \propto 1/B$ (Fig. 4.3, right panel).

4.4 Quantum Simulation

The robustness of the scheme against decoherence has been checked by studying the time-evolution of the system in a master equation formalism. This allows us to include in the simulations the errors due to pure dephasing of the qubits and of the switch unit, as outlined in Appendix E, assuming a markovian dynamics. The dynamics of the supramolecular system is determined by the numerical solution of the Lindblad equation:

$$\dot{\hat{\rho}} = -i\left[\hat{H},\hat{\rho}\right] + \frac{1}{T_2^{swich}}\mathcal{D}_{\hat{S}_{2,+}\hat{S}_{2,-}}[\hat{\rho}] + \frac{1}{T_2^{ring}}\sum_{i=1,3}\mathcal{D}_{\hat{S}_{i,+}\hat{S}_{i,-}}[\hat{\rho}], \tag{4.5}$$

where $\hat{\rho}$ is the system density matrix, $\hat{H}$ the full Hamiltonian 4.1 and

$$\mathcal{D}_{\hat{S}_+\hat{S}_-}[\hat{\rho}] = \hat{S}_+\hat{S}_-\hat{\rho}\hat{S}_+\hat{S}_- - \frac{1}{2}\left(\hat{S}_+\hat{S}_-\hat{\rho} + \hat{\rho}\hat{S}_+\hat{S}_-\right)$$

is the dissipator (introduced in Sec. 3.2.5), depending on the $S = 1/2$ spin operators $\hat{\mathbf{S}}_i$ acting on the two rings and on the Co switch. It accounts for the pure dephasing dynamics induced by the finite value of T_2. Figure 4.4-(a) shows a colormap of the simulated fidelity $\mathcal{F}$ of a SQiSW gate, as a function of the phase memory time of the rings and of the central Co switch. The two qubits are initialized in a random state, with a static field of 3 T. It is worth noting that the dependence on T_2^{ring} is much more pronounced. Conversely, $\mathcal{F}$ is nearly independent of T_2^{Co}, even for values of T_2^{Co} lower than the gate duration (approximately 4 ns). This is due to the fact that only virtual excitations of the switch are exploited to obtain an effective qubit-qubit interaction, and represents a remarkable advantage of the present scheme. We also note that for the measured values of T_2^{ring} the fidelity of the single gate is very high (above 99.7 %).
These encouraging results allow us to propose the use of the present supramolecular system as the basic unit of a digital quantum simulator. This can be done by applying a sequence of single and two-qubit gates to decompose the evolution induced by the target Hamiltonian (see Section 0.1.5). As a proof-of-principle, we consider the simulation of the time-evolution induced by the Heisenberg Hamiltonian:

$$\hat{\mathcal{H}} = \zeta\hat{\mathbf{s}}_1 \cdot \hat{\mathbf{s}}_2 + \beta\left(\hat{s}_{1x} + \hat{s}_{2x}\right) \tag{4.6}$$

where we have added an external magnetic field β which breaks the rotational symmetry. The sequence of required operations is schematically shown in the quantum circuit of Figure 4.4-(b). The Heisenberg Hamiltonian can be decomposed as $\hat{\mathcal{H}} = \zeta(\hat{s}_{1x}\hat{s}_{2x} + \hat{s}_{1y}\hat{s}_{2y} + \hat{s}_{1z}\hat{s}_{2z}) = \frac{\zeta}{2}\left(\hat{\mathcal{H}}_{XY} + \hat{\mathcal{H}}_{XZ} + \hat{\mathcal{H}}_{YZ}\right)$, where $\hat{\mathcal{H}}_{\alpha\beta} = \hat{s}_{1\alpha}\hat{s}_{2\alpha} + \hat{s}_{1\beta}\hat{s}_{2\beta}$ $(\alpha, \beta = x, y, z)$. Then the three blocks [dashed boxes in Fig. 4.4-(b)] are obtained by combining free evolution intervals induced by $\hat{H}_{qq}$ (Eq. 4.3) with proper rotations, in the line of Ref. [95]. Results are shown in panel (c), where we report the calculated time evolution of the total magnetization $\langle\hat{S}_z\rangle = \langle\hat{s}_{1z} + \hat{s}_{2z}\rangle$ of the system, initialized in a state with the two qubits parallel. We note that the expected oscillation (curve) is excellently reproduced, even with the inclusion of the values of T_2 measured by pulsed-EPR.

4.5 Discussion

We have introduced a scheme for implementing quantum gates with molecular qubits linked by a redox active unit, which controls the inter-qubit interaction. We have numerically tested the performance of our scheme on recently synthesized supra-molecular Cr_7Ni dimers, obtaining remarkably high fidelities. Even if not reported, analogous results have been achieved for compound (**2**). In the latter the perturbative picture of Eq. 4.3 holds even better, leading to slightly larger fidelities. Indeed, the qubit-Co coupling is very similar and the Zeeman energy difference is larger, if compared to (**1**), thanks to

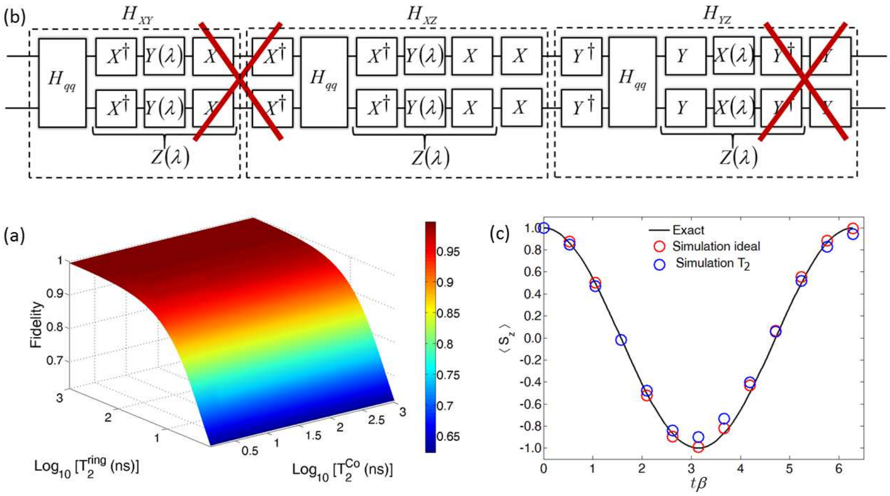

Figure 4.4: Quantum simulation in presence of decoherence. (a) Fidelity of the SQiSW gate as a function of the phase memory time of the rings and of the Co switch. The calculation has been performed with a random initial state and by applying a static field of 3 T on compound (**1**). The optimal gating time for SQiSW has been determined analytically, from Eq. 4.3, as $\pi/2\Gamma$. (b) Quantum circuit for the digital quantum simulation of the Heisenberg model. H_{qq} is the free evolution with the Co in the *on* (reduced) state. The three blocks implementing H_{XY}, H_{XZ} and H_{YZ} are enclosed within dashed boxes; for simplicity, we have introduced the notation $X = \hat{R}_x(\pi/2)$, $Y = \hat{R}_y(\pi/2)$, $Z(\lambda) = \hat{R}_z(\lambda)$. Consecutive direct and inverse unitary gates cancel each other (red crosses), thus simplifying the sequence of operations. (c) Oscillations of the magnetization in the quantum simulation of Hamiltonian 4.6, with the system initialized in a ferromagnetic configuration. The calculated evolution with (blue points) and without (red points) dephasing sources shows an excellent agreement with the expected oscillation (continuous line).

the larger difference between the g values of the ring and of the switch.
The here proposed scheme requires the capability to inject or remove an electron on a timescale much shorter than one ns; typical timescales for such experiments are in the low femtosecond region [7]. In order to be individually addressed by a tip, molecules should be grafted on surfaces, as already shown for Cr_7Ni [35]. In addition, a small static magnetic field is needed, whose direction must be such that the two Cr_7Ni rings have the same Zeeman energy. A potential slight asymmetry in the qubit-switch coupling could be compensated by an asymmetric placement of the STM tip, thus inducing a proper difference in the local magnetic field acting on each qubit.
The performance of the proposed architecture is confirmed by numerical simulations, which include the qubit pure dephasing in a master equation treatment. This suggests that the reported supramolecular assemblies are promising candidates for proof-of-principle experiments involving the implementation of complex sequences of gates. Moreover, this kind of systems could constitute the basic building block of a scalable architecture which could be used to simulate interesting physical models.

The content of this chapter was submitted for peer-review.

First-principle study of anti-ferromagnetic Cr_7M rings

CHAPTER 5

Here we study a class of heterometallic rings in which one divalent metal (M = Ni^{2+}, Mn^{2+}, Zn^{2+}) is embedded in an array of trivalent ions (Cr^{3+}). Some of the examined complexes are also potential qubits.

The examined compounds can be organised in two families: the first one consists of rings which are *purple* in solution and the solid state [96], as opposed to another family of *green* $\{Cr_7M\}$ molecules [97]. At the experimental level, a recent, accurate study of $\{Cr_7M\}$ purple rings was devoted to find a minimal set of parameters to univocally interpret inelastic neutron scattering, electron paramagnetic resonance, magnetometry and specific heat data [98]. Green compounds have also been extensively studied and characterized with several experimental techniques [83].

Our aim, at the theoretical level, is to deduce the full spin Hamiltonian of the examined families of *purple* and *green* rings by means of the recently developed *ab-initio* approach which was introduced in Sec. 1.1. This method has already been used to study the magnetic interactions of the green Cr_8 and Cr_7Ni compounds, finding a remarkable agreement with experiments [47, 84]. The method is based on the construction of many-body models using localized Foster-Boys orbitals as a one-electron basis. All the interactions are deduced systematically, including subtle anisotropic terms, without any assumption on the form of the final spin Hamiltonian. We investigate the topology of exchange and zero-field splitting interactions. The hierarchy of the calculated exchange interactions along each ring reflects the chemical structure of the molecules. This kind of information is not easily accessible by fitting experimental data, when the study is usually devoted to find a minimal set of parameters to describe the relevant interactions [83, 98], but can be obtained by our fully ab-initio approach. The calculated parameters are then used to determine physical observables and mean values which are in very good agreement with those inferred from experiments.

5.1 Many-Body models for Molecular Nanomagnets

Here we introduce a general approach to derive the spin Hamiltonian of MNMs in a systematic way, once the parameters or the generalized Hubbard model (Eq. 1.2) have been calculated self-consistently. We begin our derivation by considering the single ion term of Eq. 1.2:

$$\hat{H}^i_0 = \hat{H}^i_U + \hat{H}^i_{SO} + \hat{H}^i_{CF}, \tag{5.1}$$

where $\hat{H}^i_U$ represents the on-site Coulomb interaction, $\hat{H}^i_{SO} = \lambda_i \sum_m \hat{\boldsymbol{\ell}}_{im} \cdot \hat{\mathbf{s}}_{im}$ the spin-orbit coupling and $\hat{H}^i_{CF} = \sum_{m,\sigma} \varepsilon_m \hat{c}^\dagger_{im\sigma} \hat{c}_{im\sigma}$ the single-electron crystal-field splitting. We work here in the basis of crystal-field orbitals. The eigenvalues and eigenvectors of 5.1 are then computed: $\hat{H}^i_0 |\psi^i_k(n)\rangle = E^i_k(n)|\psi^i_k(n)\rangle$. Here i labels the site, k the eigenstate and n the number of d electrons on site i. This is a good quantum number, since $[\hat{H}^i_0, \hat{N}^i] = 0$, with $\hat{N}^i = \sum_{m,\sigma} \hat{c}^\dagger_{im\sigma} \hat{c}_{im\sigma}$.

Having extracted from first-principles calculations the valence of the examined ion (hence the number $\bar{n}$ of d electrons of the ground state), we focus on the lowest-energy multiplet with $\bar{n}$ electrons. This multiplet can be described through an effective spin S and, in the absence of spin-orbit interaction, it is $(2S+1)$-fold degenerate. Spin-orbit coupling partially removes this degeneracy, leading to a zero-field splitting.

The zero-field splitting tensor is obtained (for $S > 1/2$) by rotating the diagonal matrix of the eigenvalues $E^i_k(\bar{n})$ (limited to the ground multiplet, with $k = 1, ..., 2S+1$) into the basis of the eigenvectors of $\hat{S}_z$: $\hat{S}_z|S,M\rangle = M|S,M\rangle$, thus finding $\hat{H}^i_{ZFS}$. $|S,M\rangle$ states can be obtained, for instance, by applying a small magnetic field along z, which splits the levels of the multiplet according their M value. As a subsequent step, $\hat{H}^i_{ZFS}$ is recast in terms of Stevens operators by means of Frobenius inner product:

$$\hat{H}^i_{ZFS} = \sum_{k,q} b^q_k \hat{O}^q_k(\hat{\mathbf{S}}), \tag{5.2}$$

where

$$b^q_k = \frac{\mathrm{Tr}\left[\hat{O}^{q\dagger}_k \hat{H}^i_{ZFS}\right]}{\sqrt{\mathrm{Tr}\left[\hat{O}^{q\dagger}_k \hat{O}^q_k\right]}}. \tag{5.3}$$

A similar result for $\hat{H}^i_{ZFS}$ (valid for $3d$ compounds, in which the spin-orbit coupling is small with respect to on-site energy splittings) can be obtained by diagonalizing the on site Hamiltonian $\hat{H}^i_U + \hat{H}^i_{CF}$ without spin-orbit interaction, and then considering spin-orbit as a second-order perturbative effect. If $|\phi^i_k(\bar{n})\rangle$ are the eigenstates of $\hat{H}^i_U + \hat{H}^i_{CF}$ with $\bar{n}$ electrons and $\mathcal{E}^i_k(\bar{n})$ the corresponding eigenvalues, we get

$$\begin{aligned} &\langle \phi^i_k(\bar{n})|\hat{H}^i_{ZFS}|\phi^i_j(\bar{n})\rangle \\ &= \sum_{l \neq k,j} \frac{\langle \phi^i_k(\bar{n})|\hat{H}^i_{SO}|\phi^i_l(\bar{n})\rangle\langle \phi^i_l(\bar{n})|\hat{H}^i_{SO}|\phi^i_j(\bar{n})\rangle}{\mathcal{E}^i_k(\bar{n}) - \mathcal{E}^i_l(\bar{n})} \end{aligned} \tag{5.4}$$

Here the sum runs over the single-ion excited states with $\bar{n}$ electrons and $\phi^i_k(\bar{n})$, $\phi^i_j(\bar{n})$ are degenerate and restricted to the ground multiplet. Then we rewrite H^i_{ZFS} on the $|S,M\rangle$ basis and decompose it in Stevens operators, as above.

The general form of the exchange tensor between spins corresponding to different ions is deduced by considering the hopping term of the Hubbard model 1.2:

$$\hat{H}_1^{i,i'} = \sum_{\sigma} \sum_{\mu,\nu} \left(t^{ii'}_{\mu\nu} \hat{c}^{\dagger}_{i\mu\sigma} \hat{c}_{i'\nu\sigma} + t^{i'i}_{\mu\nu} \hat{c}^{\dagger}_{i'\mu\sigma} \hat{c}_{i\nu\sigma} \right) \tag{5.5}$$

acting as a second-order perturbation on the two-sites eigenstates $|\psi^i_k(\bar{n})\psi^{i'}_j(\tilde{n})\rangle$, which are obtained as tensor product of single-site eigenstates with fixed number of electrons, $\bar{n}$ and $\tilde{n}$. This is a good approximation, as far as the hopping integrals are much smaller than the energy required to move an electron among two sites. In practice, this is ensured if electrons are well localized on the metal ions and the spin Hamiltonian description is valid, as verified for all the examined compounds. Hence, the exchange matrix ($\hat{H}^{i,i'}_{ex}$) for the couple of interacting ions i, i', in $\left(2S^i + 1\right)\left(2S^{i'} + 1\right)$ dimension, can be expressed as follows

$$\begin{aligned}
&\langle\, \psi^i_k(\bar{n})\psi^{i'}_j(\tilde{n})|\hat{H}^{i,i'}_{ex}|\psi^i_{k'}(\bar{n})\psi^{i'}_{j'}(\tilde{n})\rangle = \qquad (5.6)\\
&= \sum_{l,m} \frac{\langle\psi^i_k(\bar{n})\psi^{i'}_j(\tilde{n})|\hat{H}_1^{i,i'}|\psi^i_m(\bar{n}+1)\psi^{i'}_l(\tilde{n}-1)\rangle\langle\psi^i_m(\bar{n}+1)\psi^{i'}_l(\tilde{n}-1)|\hat{H}_1^{i,i'}|\psi^i_{k'}(\bar{n})\psi^{i'}_{j'}(\tilde{n})\rangle}{2[E^i_k(\bar{n}) + E^{i'}_j(\tilde{n}) - E^i_m(\bar{n}+1) - E^{i'}_l(\tilde{n}-1)]}\\
&+ \sum_{l,m} \frac{\langle\psi^i_k(\bar{n})\psi^{i'}_j(\tilde{n})|\hat{H}_1^{i,i'}|\psi^i_m(\bar{n}-1)\psi^{i'}_l(\tilde{n}+1)\rangle\langle\psi^i_m(\bar{n}-1)\psi^{i'}_l(\tilde{n}+1)|\hat{H}_1^{i,i'}|\psi^i_{k'}(\bar{n})\psi^{i'}_{j'}(\tilde{n})\rangle}{2[E^i_k(\bar{n}) + E^{i'}_j(\tilde{n}) - E^i_m(\bar{n}-1) - E^{i'}_l(\tilde{n}+1)]}\\
&+ \sum_{l,m} \frac{\langle\psi^i_k(\bar{n})\psi^{i'}_j(\tilde{n})|\hat{H}_1^{i,i'}|\psi^i_m(\bar{n}+1)\psi^{i'}_l(\tilde{n}-1)\rangle\langle\psi^i_m(\bar{n}+1)\psi^{i'}_l(\tilde{n}-1)|\hat{H}_1^{i,i'}|\psi^i_{k'}(\bar{n})\psi^{i'}_{j'}(\tilde{n})\rangle}{2[E^i_{k'}(\bar{n}) + E^{i'}_{j'}(\tilde{n}) - E^i_m(\bar{n}+1) - E^{i'}_l(\tilde{n}-1)]}\\
&+ \sum_{l,m} \frac{\langle\psi^i_k(\bar{n})\psi^{i'}_j(\tilde{n})|\hat{H}_1^{i,i'}|\psi^i_m(\bar{n}-1)\psi^{i'}_l(\tilde{n}+1)\rangle\langle\psi^i_m(\bar{n}-1)\psi^{i'}_l(\tilde{n}+1)|\hat{H}_1^{i,i'}|\psi^i_{k'}(\bar{n})\psi^{i'}_{j'}(\tilde{n})\rangle}{2[E^i_{k'}(\bar{n}) + E^{i'}_{j'}(\tilde{n}) - E^i_m(\bar{n}-1) - E^{i'}_l(\tilde{n}+1)]}
\end{aligned}$$

Then we rotate it from the $|\psi^i_k(\bar{n})\psi^{i'}_j(\tilde{n})\rangle$ to the $|M_1 M_2\rangle$ basis for clarity. In this way, we can decompose it in terms of bilinear spin operators $\hat{S}^i_\alpha \hat{S}^{i'}_\beta$ by exploiting again the Frobenius inner product:

$$\hat{H}^{i,i'}_{ex} = \sum_{\alpha,\beta=x,y,z} \Gamma^{i,i'}_{\alpha\beta} \hat{S}^i_\alpha \hat{S}^{i'}_\beta , \tag{5.7}$$

where

$$\Gamma^{i,i'}_{\alpha\beta} = \frac{\mathrm{Tr}\left[\left(\hat{S}^i_\alpha \hat{S}^{i'}_\beta\right)^{\dagger} \hat{H}_{ex}\right]}{\sqrt{\mathrm{Tr}\left[\left(\hat{S}^i_\alpha \hat{S}^{i'}_\beta\right)^{\dagger}\left(\hat{S}^i_\alpha \hat{S}^{i'}_\beta\right)\right]}} . \tag{5.8}$$

5.2 Ab-initio study of $\{$Cr$_7$M$\}$ rings

Fig. 5.1 shows the single-electron crystal-field states for Mn^{2+} ion, which exhibit the typical structure of d-orbitals in a quasi-octahedral environment: a lower energy t_{2g}-like quasitriplet (a)-(c) and a 1-2 eV higher energy e_g-like quasidoublet (d)-(e).

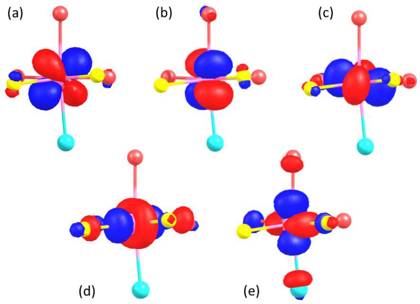

Figure 5.1: Crystal Field single-electron d-orbitals for Mn^{2+} in a purple Cr$_7$Mn ring, obtained by diagonalization of the crystal-field matrix $t^{i,i}_{m,m'}$, for $i =$ Mn, in order (a) to (e) of increasing energy. The quasi-octahedral environment is reflected by the crystal-field splitting: a lower energy t_{2g}-like quasitriplet (a)-(c) and a 1-2 eV higher energy e_g-like quasidoublet (d)-(e). In the contour plot only the Mn quasi-octahedral cage is shown (Mn is purple, O is red, F is yellow and N is light-blue).

For all systems analyzed, we find that the essential spin interactions are described by the spin Hamiltonian

$$H = \sum_{i=1}^{8} \Gamma^{i,i+1} \hat{\mathbf{S}}_i \cdot \hat{\mathbf{S}}_{i+1} + \sum_{i=1}^{8} \hat{\mathbf{S}}_i \cdot \underline{\mathbf{D}}_i \cdot \hat{\mathbf{S}}_i \tag{5.9}$$

where $\Gamma^{i,i+1}$ are the isotropic exchange couplings, $\underline{\mathbf{D}}_i$ is the local zero-field splitting (ZFS) tensor and $i = 8$ corresponds to the divalent M ion. Other terms in the spin Hamiltonian, such as anisotropic or antisymmetric exchange interactions, as well as higher order zero-field splitting parameters, can be systematically deduced as outlined in the previous section. For the examined compounds, we found them to be negligible.

	PURPLE			GREEN		
	Cr	Mn	Ni	Cr	Mn	Ni
$\lvert n\rangle$	ϵ_n					
$\lvert 1\rangle$	0.000	0.000	0.000	0.000	0.000	0.000
$\lvert 2\rangle$	0.201	0.081	0.088	0.010	0.051	0.077
$\lvert 3\rangle$	0.127	0.219	0.250	0.111	0.249	0.206
$\lvert 4\rangle$	2.031	1.387	1.244	2.092	2.275	1.376
$\lvert 5\rangle$	2.205	1.476	1.304	2.141	2.347	1.519
Coulomb Integrals						
$U^{i,i}$	6.00	6.49	6.30	5.98	6.32	6.28
$\mathcal{J}^{i,i}$	0.30	0.35	0.21	0.26	0.34	0.23
λ_i	16.5	20.7	33.5	16.5	20.7	33.5

Table 5.1: Crystal-field energy levels and screened Coulomb integrals for Cr, Ni, Mn ions. Top: Crystal-field energy levels (in eV) for one representative Cr ion and for Mn and Ni ions. Bottom: Screened Coulomb integrals $U^{i,i}$, $\mathcal{J}^{i,i}$ obtained via cLDA (in eV) and spin-orbit coupling λ_i (in meV) [64].

As discussed in Sec. 1.1, the coupling $\Gamma^{i,i+1} = \Gamma^{i,i+1}_{CE} + \Gamma^{i,i+1}_{SE}$ is the sum of a fer-

	$\Gamma^{i,i+1}_{SE}$ (meV)	$\Gamma^{i,i+1}_{CE}$ (meV)	$\Gamma^{i,i'}$ (meV)
Cr_1-Cr_2	1.89	-0.41	1.48
Cr_2-Cr_2	2.93	-0.51	2.42
Cr_3-Cr_2	2.86	-0.43	2.43
Cr_4-Cr_2	2.94	-0.49	2.45
Cr_5-Cr_2	3.04	-0.60	2.44
Cr_6-Cr_2	3.14	-0.49	2.65
Cr_7-Mn	1.80	-0.35	1.45
Mn-Cr_1	2.34	-0.52	1.82
Cr_7-Ni	2.47	-0.36	2.11
Ni-Cr_1	3.02	-0.50	2.52

Table 5.2: Calculated super-exchange ($\Gamma^{i,i+1}_{SE}$) and Coulomb-exchange ($\Gamma^{i,i+1}_{CE}$) couplings, for each pair of nearest neighbors in the examined purple family of rings. The last column reports also the overall exchange coupling $\Gamma^{i,i+1} = \Gamma^{i,i+1}_{SE} + \Gamma^{i,i+1}_{CE}$.

romagnetic (FM) screened Coulomb exchange term, $\Gamma^{i,i+1}_{CE}$, which we obtain via cLDA calculations, and a super-exchange term $\Gamma^{i,i+1}_{SE}$, which can be FM or antiferromagnetic (AFM). Even if all the reported calculations have been done with the full model 1.2, we report here the simple analytical expression that $\Gamma^{i,i+1}_{SE}$ ($i = 1, ..., 7$) assumes if only density-density Coulomb terms are retained; we obtain

$$\begin{aligned}\Gamma^{i,i+1}_{SE} \approx & \frac{2}{9}\sum_{n'=1}^{3}\sum_{n=4}^{5}\frac{|t^{i,i'}_{n',n}|^2+|t^{i,i'}_{n,n'}|^2}{U^{i,i}+\varepsilon_n-\varepsilon'_n} \\ & +\frac{2}{9}\sum_{n'=1}^{3}\sum_{n=1}^{3}\frac{|t^{i,i'}_{n',n}|^2}{U^{i,i}+2\mathcal{J}^{i,i}+\varepsilon_n-\varepsilon_{n'}} \\ & -\frac{2}{9}\sum_{n'=1}^{3}\sum_{n=4}^{5}\frac{|t^{i,i'}_{n',n}|^2+|t^{i,i'}_{n,n'}|^2}{U^{i,i}-3\mathcal{J}^{i,i}+\varepsilon_n-\varepsilon_{n'}}.\end{aligned} \tag{5.10}$$

Eq. 5.10 shows the competition between the first two terms, which yield a positive, i.e., AFM contribution and the FM third term, arising from excitations to empty states. For realistic parameters (and including also spin-flip and pair hopping terms), $\Gamma^{i,i+1}_{SE}$ is AFM. The full ZFS local tensor $\underline{\mathbf{D}}_i$, originating from the combined action of crystal-field and spin-orbit interactions, is determined. We find a triplet ground state for Ni^{2+}, a sextet for Mn^{2+} and a quartet for all Cr^{3+} ions, with effective spins $S = 1$, $S = 5/2$ and $S = 3/2$, respectively. Then, as outlined above, we project the spin-orbit term onto Stevens spin operators, which in the present case reduce to $S_{\alpha,i}S_{\beta,i}$ ($\alpha, \beta = x, y, z$). The spin-orbit constant λ_i for Ni d electrons in Cr_7Ni could not be determined *ab-initio* because NWChem does not provide relativistic calculations for odd-electron systems. Moreover, since relativistic self-consistent calculations are very time-consuming and λ_i is a property of the single ion (and of its local environment, which is always approximately octahedral), we used the typical values reported in [64] for a Ni^{2+} ion in a octahedral cage. As for the Cr^{3+}, we employ the value we obtained self-consistently for green Cr_8 rings [47] and for Mn^{2+} we consider the free-ion value [64], properly screened with the same screening factor calculated for Cr^{3+} ($\sim 1/2$). All these parameters are reported in Table 5.1.

In the reference frame which diagonalizes $\underline{\mathbf{D}}_i$ the zero-field splitting interaction can be expressed as a sum of an axial term d^i and a rhombic term e^i:

$$\hat{\mathbf{S}}_i \cdot \underline{\mathbf{D}}_i \cdot \hat{\mathbf{S}}_i = d^i \left[S_{z,i}^2 - \frac{1}{3} S_i(S_i+1) \right] + e^i \left[S_{x,i}^2 - S_{y,i}^2 \right].$$

Our approach allows us to derive also the $\underline{\mathbf{g}}_i$ tensor on each magnetic ion. To obtain it we need to evaluate the matrix elements of the orbital angular momentum $\hat{\mathbf{L}}_i$ onto the ground spin multiplet states $|S, M\rangle$, corrected to first order in the spin-orbit interaction. Then we compare them with the spin matrices of rank S and we extract the correction $\Delta\underline{\mathbf{g}}$ to the isotropic $\underline{\mathbf{g}} = 2I$ (here I is the identity matrix). For instance, in the case of Cr^{3+} (ground state $S = 3/2$), we find

$$\begin{aligned}
\Delta g_{\alpha z} &= -2 \sum_k \frac{\langle 3/2, 1/2 | \hat{L}_{\alpha,i} | \phi_k^i(\bar{n}) \rangle \langle \phi_k^i(\bar{n}) | \hat{H}_{SO}^i | 3/2, 1/2 \rangle}{\mathcal{E}_k^i(\bar{n})} \\
\Delta g_{\alpha x} &= -\mathrm{Re} \sum_k \frac{\langle 3/2, 1/2 | \hat{L}_{\alpha,i} | \phi_k^i(\bar{n}) \rangle \langle \phi_k^i(\bar{n}) | \hat{H}_{SO}^i | 3/2, -1/2 \rangle}{\mathcal{E}_k^i(\bar{n})} \qquad (5.11) \\
\Delta g_{\alpha y} &= \mathrm{Im} \sum_k \frac{\langle 3/2, 1/2 | \hat{L}_{\alpha,i} | \phi_k^i(\bar{n}) \rangle \langle \phi_k^i(\bar{n}) | \hat{H}_{SO}^i | 3/2, -1/2 \rangle}{\mathcal{E}_k^i(\bar{n})}
\end{aligned}$$

where $|S, M\rangle$ are the eigenstates of S_z on the ground multiplet, $|\phi_k^i(\bar{n})\rangle$ are excited states with unperturbed energy $\mathcal{E}_k^i(\bar{n})$, $\alpha = x, y, z$ and we have set to zero the energy of the ground multiplet. Here only terms to first order in λ_i are retained. Notice that $\underline{\mathbf{g}}_i$ is diagonal in the reference frame which diagonalizes $\underline{\mathbf{D}}_i$.

5.2.1 Results for *purple* rings

Self-consistent calculations for these molecules containing hundreds of atoms are very time consuming and reaching convergence is often a hard task. This is particularly difficult for molecules containing an odd number of electrons (such as Cr$_7$Ni and Cr$_7$Zn), due to the impossibility of using damping or other convergence accelerators with NWChem quantum chemistry code. Consequently, we could not perform self-consistent runs on a single Cr$_7$Zn, but we considered the even-electrons structure (Cr$_7$Zn)$_2$ [1]. The values of $\Gamma^{i,i+1}$ calculated in all the (Cr$_7$M)$_2$ for Cr-Cr bonds are the same (within a $3-4\%$ error), independently from M. This ensures a complete transferability of the local Cr parameters calculated for the even-electrons Cr$_7$Mn on the other molecules. We did not perform any geometry optimization: calculations were carried on using the structure of the single molecule provided by X-ray diffraction.

The super-exchange and Coulomb-exchange parameters obtained for each bond are listed in Table 5.2. It is interesting to compare the results with the molecular structure, reported in Fig. 5.2. If we consider the Cr-M bond (both in the case of Cr$_7$Mn and of Cr$_7$Ni) we find $\Gamma^{7,M} < \Gamma^{M,1}$. This can be understood by examining Figure 5.2-(b): an additional carboxylate exchange path is present in the M-Cr$_1$ bond, which is absent in the Cr$_7$-M bond. Moreover, as demonstrated by DFT calculations on Cr$_9$ molecular ring reported in

---

[1] Here the two molecules are taken sufficiently far apart to make their interaction negligible. In order to reduce the computational effort, we replaced CH$_3$ groups by Hydrogens (according to the hydrogen-termination technique [53]). As previously tested on similar compounds, this structural modification leads only to a slight enhancement of all the exchange constants $\Gamma^{i,i+1}$, while preserving the hierarchy of the interactions.

Ref. [99], the carboxylate bridge provides the most relevant contribution to the exchange interaction, while the fluorine path (yellow) gives a smaller contribution. Indeed, both the overlap between localized neighbouring orbitals and the hopping integrals are larger along the carboxylate (see Table 5.3). The same analysis also holds for the Cr-Cr bonds.

$t^{1,2}_{n,n'}$	$\|1\rangle$	$\|2\rangle$	$\|3\rangle$	$\|4\rangle$	$\|5\rangle$
$\|1\rangle$	1.406	2.561	2.080	-2.606	0.131
$\|2\rangle$	-2.287	-0.630	-7.417	1.421	2.553
$\|3\rangle$	-2.436	-1.157	-1.786	-5.518	4.871
$\|4\rangle$	-5.296	3.368	0.596	-5.240	4.364
$\|5\rangle$	2.757	-1.856	0.095	4.518	1.999
$t^{4,5}_{n,n'}$	$\|1\rangle$	$\|2\rangle$	$\|3\rangle$	$\|4\rangle$	$\|5\rangle$
$\|1\rangle$	-4.523	5.484	-2.895	-5.342	-5.692
$\|2\rangle$	4.223	3.192	0.447	2.170	4.942
$\|3\rangle$	1.572	2.288	-6.098	-2.499	0.240
$\|4\rangle$	-3.967	1.979	3.255	2.408	-4.617
$\|5\rangle$	-5.311	5.663	3.297	-3.735	-3.102

Table 5.3: Hopping integrals (in meV) of purple Cr_7Mn obtained via LDA for sites $\{i, i'\} = \{1, 2\}$ (top) and $\{i, i'\} = \{4, 5\}$ (bottom). Notice that the presence of an additional carboxylate super-exchange bridge in bond 4-5 leads to significantly larger hopping integrals and consequently $\Gamma^{4,5}_{SE} > \Gamma^{1,2}_{SE}$ (see Figure 5.2 and discussion in the text).

We find essentially two values of the exchange couplings: the first one ($\Gamma^{1,2}$) involves two carboxylate groups and a fluorine bridge. The resulting coupling is, in this case, similar to that found for the green variants [47], which show the same structure along the Cr-Cr bond (see subsection below). The second one is substantially the same for all the other homometallic bonds and is remarkably larger, due to substitution of Fluorine with Oxygen in the Cr-Cr path. An additional path is provided by the Cr-O-C-C-O-Cr bridge, as shown in Fig. 5.2-(c), but it is longer than the others and gives only a small contribution to the exchange couplings.

Finally, Fig. 5.3 reports the local ZFS parameters d^i and e^i obtained by diagonalizing the $\underline{\mathbf{D}}_i$ tensors, along with the rhombicity factor $\left|e^i/d^i\right|$. The local z axes are found to be almost perpendicular to the plane of the ring for all the ions, while the x and y axes are rotated from ion to ion. Fig. 5.4 shows these local z axes for *purple* Cr_7Mn, which almost follow the direction of the lobes of the highest-energy crystal-field orbitals.

5.2.2 Comparison with *green* rings

A similar analysis can be done also for the *green* variants of Cr_7M anti-ferromagnetic rings. Fig. 5.5 reports the exchange constants for the green rings: they are found to be more uniform if compared to the purple family of compounds. This can be directly related to the structure: indeed, the super-exchange paths in the green variants always involve a single Fluorine bridge and two carboxylates, as opposed to the more complex structure of bridges found in the purple complexes.

The correction to the isotropic $\underline{\mathbf{g}}_i$ tensor induced by spin-orbit interaction is found to be very small for Cr and Mn ions in all the examined compounds. For instance, in the case of Cr^{3+} ions, we get $1.98 < g_{\alpha\alpha} < 2$ (referred to the local principal axes). It is more interesting to study the anisotropy of the $\underline{\mathbf{g}}_i$ tensors for the Ni^{2+} ions. The results for

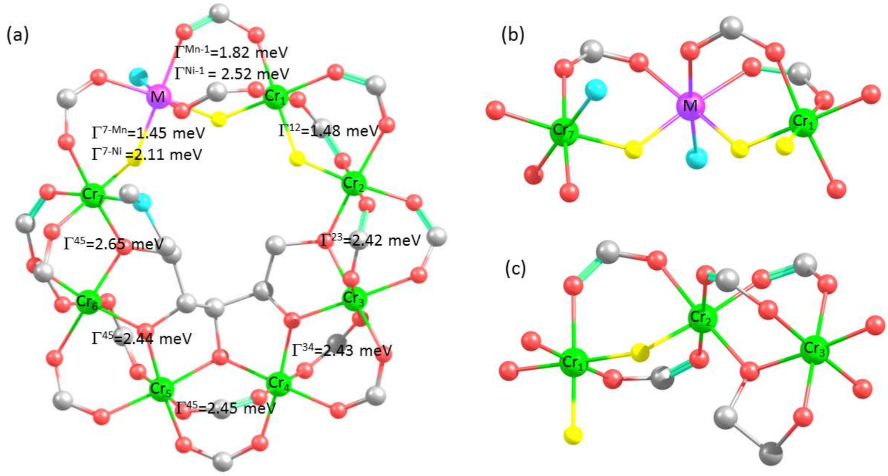

Figure 5.2: (a) Structure of the Cr_7M purple family of compounds, with calculated isotropic exchange couplings indicated (in meV) for each pair of nearest neighbouring magnetic ions. Hydrogens are not shown for clarity, while Carbons are grey, Nitrogens are light-blue, Fluorines are yellow, Oxygens are red, Chromiums are green, M (=Ni, Mn) is purple. The different couplings found for the Cr_7-M and M-Cr_1 bonds reflect the structure of the molecule, as can be seen in the fragment reported in (b). As for the Cr-Cr couplings, we essentially find two different values, depending on the presence of a Fluorine or a carboxylate bridge, as shown in (c).

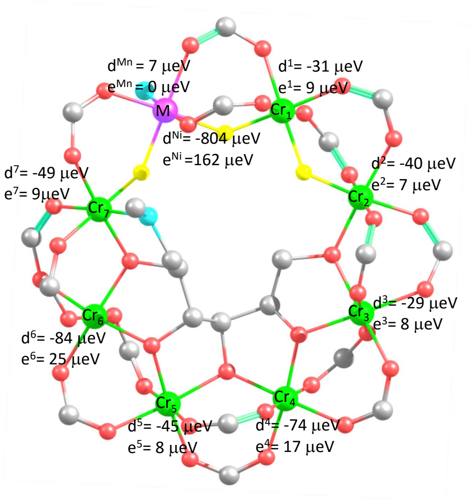

	d^i (μeV)	$\|e^i\|$ (μeV)	$\|e^i/d^i\|$
Cr_1	-31	9	0.28
Cr_2	-40	7	0.16
Cr_3	-29	8	0.27
Cr_4	-74	17	0.23
Cr_5	-45	8	0.18
Cr_6	-84	25	0.30
Cr_7	-49	9	0.18
Mn	7	0	0.00
Ni	-804	162	0.20

Figure 5.3: Structure of the Cr_7M molecule, with calculated zero-field splitting parameters d^i and e^i (in μeV) indicated for each magnetic ion and M=Ni, Mn, in the reference frame of the principal axes of $\underline{\mathbf{D}}_i$ tensor. We find easy-axis anisotropy for all ions, except for Mn^{2+} and Zn^{2+}, which is diamagnetic. The last column of the table reports the rhombicity factor $|e^i/d^i|$.

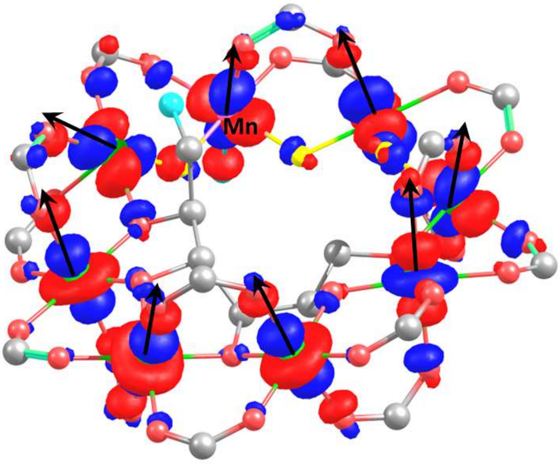

Figure 5.4: Highest-energy crystal-field orbital for each magnetic ion and direction of the local z-axis for purple Cr$_7$Mn. CH$_3$ groups are not shown for clarity.

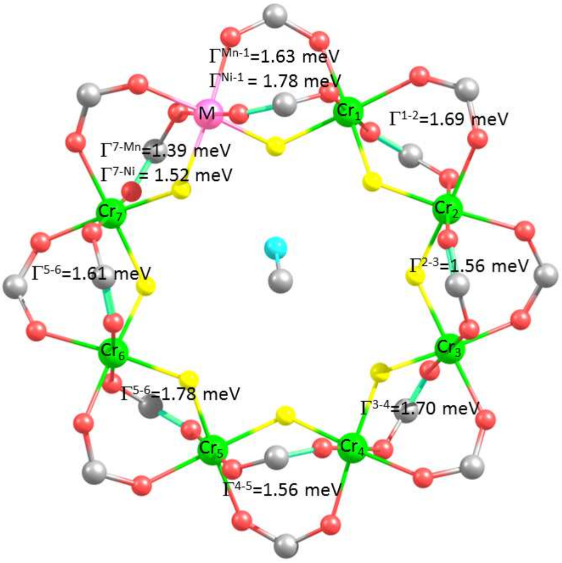

Figure 5.5: Structure and calculated exchange integrals in the *green* rings.

both *green* and *purple* Cr$_7$Ni rings are shown in Table 5.4. The diagonal components are referred to the local principal axes, which are the same also for the zero-field splitting $\underline{\mathbf{D}}_i$ tensor. We find larger $\Delta\underline{\mathbf{g}}_i$ for the purple variant with respect to its green analog. This difference is induced by the smaller excitation crystal-field energies $\mathcal{E}_k^i(\bar{n})$ appearing in the denominator of Eq. 5.11. For the lowest gap we find 15500 (17900) cm^{-1} in the green ring and 14700 (16200) cm^{-1} in the purple one. Values in brackets are determined from electronic absorption spectra [98]. The larger the crystal field gaps, the smaller the magnetic anisotropy, due to less mixing of the ground spin multiplet with the excited multiplets. This is also reflected by the zero-field splitting tensor: the local $\left|d^{Ni}_{green}\right| = 0.48$ meV< $\left|d^{Ni}_{purple}\right| = 0.80$ meV. Fig. 5.6 shows the direction of the anisotropy axes on the Ni ion in the green Cr_7Ni compound. A similar situation is found also for the corresponding purple variant, with the z axis almost perpendicular to the plane of the ring and the x and y axis which follow the direction of the ligands in the crystal cage and of the lobes of the highest energy crystal-field orbitals. It is worth noting that the rhombicity $\left|e^{Ni}/d^{Ni}\right|$ is much larger in the purple variant (0.23) than in the green one (0.06), in agreement with a larger deviation of the structure from an octahedral cage. This effect leads to a sizeable difference of the in plane components of the $\underline{\mathbf{g}}_{Ni}$ tensor.

	g_{xx}	g_{yy}	g_{zz}
green	2.07 (–)	2.08 (–)	2.15 (–)
purple	2.08 (2.18)	2.16 (2.18)	2.28 (2.25)

Table 5.4: Diagonal components of the $\underline{\mathbf{g}}$-tensor for the Ni^{2+} ions in green and purple Cr_7Ni rings. Experimental findings (fitted from EPR data) are shown in brackets [98].

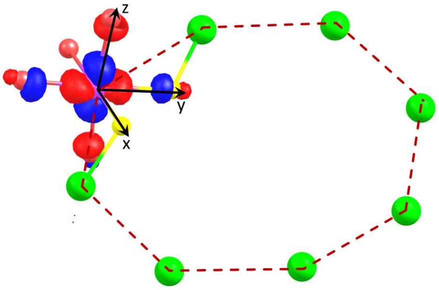

Figure 5.6: Direction of the main anisotropy axes for the Ni^{2+} ion in the green variant of Cr_7Ni. The highest-energy crystal field orbital on the Ni and the ligands surrounding it are also shown, while the rest of the molecule is only schematically depicted.

5.3 Comparison with experimental results

The models used to fit experimental data [83, 98] assume only two values for the exchange couplings ($\Gamma^{Cr,Cr}$ and $\Gamma^{Cr,M}$) and two values of the ZFS parameters (d^{Cr}, e^{Cr}, d^{M}, e^{M}), uniform along the ring. A first, immediate comparison of the exchange constants can be done by considering average values:

$$\Gamma^{Cr,Cr} = \frac{1}{6}\sum_{i=1}^{6}\Gamma^{i,i+1}\ , \quad \Gamma^{Cr,M} = \frac{1}{2}\left[\Gamma^{M,1} + \Gamma^{7,M}\right]\ .$$

These are reported in the first lines of Table 5.6 for both green and purple compounds. Alternatively, we can directly calculate the exchange splittings obtained by diagonalizing the isotropic part of the spin Hamiltonian deduced from first principles and compare them with experimental inelastic neutron scattering peaks [83, 98]. Results are shown in Table 5.5 and are in good agreement (within a 30 % error) with experiments. Finally, we calculate the effective D and E values (of the whole molecule) for the lowest $S > 1/2$ multiplet and compare them with experimental findings (when available). Results are shown in Table 5.6. The agreement is good for D (errors bounded by 33 %), while E is generally underestimated (but these are very small numbers).

		Theory	Exp	$S \to S'$
Purple	Cr_7Ni	1.81	1.52	$1/2 \to 3/2$
	Cr_7Mn	2.18	1.49	$1 \to 2$
	Cr_7Zn	1.20	1.09	$3/2 \to 1/2$
Green	Cr_7Ni	1.362	1.224	$1/2 \to 3/2$
	Cr_7Mn	1.678	1.515	$1 \to 2$
	Cr_7Zn	0.9484	0.842	$3/2 \to 1/2$

Table 5.5: Splitting (in meV) between total spin ground and first excited multiplet S, obtained by assuming the full pattern of exchange constants calculated from first principles (second column) and measured by inelastic neutron scattering [83, 98] (third column). The last column indicates the total spin multiplets involved in the transition.

	Green		
	Cr_7Ni	Cr_7Mn	Cr_7Zn
$\Gamma^{Cr,Cr}$	1.65 (1.46)	1.65 (1.46)	1.65 (1.43)
$\Gamma^{Cr,M}$	1.75 (1.70)	1.49 (1.37)	0 (0)
D	0.125 (0.083)	-0.143 (-0.095)	-0.077 (-0.053)
E	0.007 (–)	-0.003 (–)	0.003 (–)
E/D	0.056 (–)	0.023 (–)	0.040 (–)
	Purple		
	Cr_7Ni	Cr_7Mn	Cr_7Zn
$\Gamma^{Cr,Cr}$	2.31 (1.72)	2.31 (1.72)	2.31 (1.72)
$\Gamma^{Cr,M}$	2.32 (2.59)	1.63 (1.03)	0 (0)
D	0.123 (0.079)	-0.083 (-0.061)	-0.061 (-0.040)
E	0.017 (0.007)	-0.006 (-0.0146)	0.003 (0.010)
E/D	0.142 (0.086)	0.073 (0.239)	0.041 (0.264)

Table 5.6: Comparison between the calculated average parameters for the *green* and *purple* heterometallic Cr_7M rings. In brackets results fitted from experimental data (see Ref. [98, 83]) are shown. All values are in meV.

5.4 Spin density

We finally report (Figure 5.7) a plot of the electron spin-density, for Cr_7Ni purple ring. This is defined, for each ion, as the expectation value $\langle \hat{S}_z^i(\mathbf{r}) \rangle = \frac{1}{2} \langle \sum_m \hat{c}^\dagger_{im\uparrow} \hat{c}_{im\uparrow} - \hat{c}^\dagger_{im\downarrow} \hat{c}_{im\downarrow} \rangle$ on the ground state. We calculate it by diagonalizing the spin Hamiltonian, with parameters deduced ab-initio, in an applied magnetic field. Then we express the ground spin state, which in the present case is substantially characterized by $S = 1/2, M = -1/2$, in second quantization form to compute the desired expectation value and its dependence

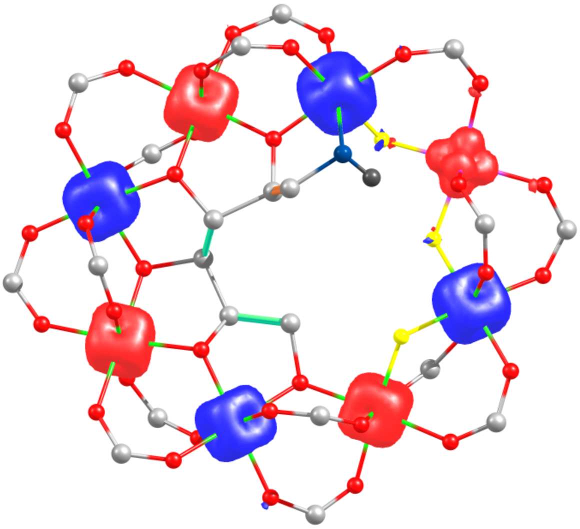

Figure 5.7: Spin density on the ground state of $\mathbf{Cr_7Ni}$ purple ring, $\langle \hat{S}_z(\mathbf{r}) \rangle$, in an applied field perpendicular to the ring of 5 T. The ground state is characterized by $S = 1/2, M = 1/2$. Isovalues of 0.005 electrons/a.u. have been used. Different colors correspond to the positive (red) and negative (blue) values of the spin density. CH_3 groups are not shown for clarity.

on spatial coordinates. The picture is similar to that reported in Ref. [100] and obtained by broken-symmetry calculations on a green Cr_7Ni ring.

5.5 Conclusions

Summarizing, we have presented a detailed *ab-initio* study of two families of AFM Cr_7M molecular rings. The study is performed by means of a recently developed first-principle approach, which is based on the construction of system-specific many-body models, written on a basis of localized Foster-Boys orbitals. The method allows us to deduce the spin Hamiltonian without any a priori assumption on its form and with no free parameters. By explicitly including strong correlation effects (not simply at a static mean-field level) we can calculate the full pattern of exchange and zero-field splitting couplings, finding a very good agreement with experimental results. Moreover, an analysis of the super-exchange paths leads to a more detailed understanding of the origin of the exchange interactions between neighbouring metal ions, which cannot be inferred from experiments.

Coherent spin dynamics in molecular Cr_8Zn wheel

CHAPTER 6

Controlling and understanding transitions between molecular spin states allows the selection of the most suitable ones for performing quantum gates. Here we present a detailed investigation of single crystals of a polynuclear Cr_8Zn molecular wheel [101, 102], carried on by analysis of thermodynamic measurements (magnetization, torque and specific-heat), nuclear spin-lattice relaxation and 241 GHz Electron Paramagnetic Resonance (EPR) spectroscopy in high magnetic field. Magnetometry data, NMR and continuous wave EPR spectra are well reproduced by spin Hamiltonian calculations.

Having established a sound spin Hamiltonian model, we study the dephasing time (T_2) of some interesting transitions, in correspondence to a well-defined anti-crossing between states of different total spin. To this aim, we analyze results of pulsed spin echo experiments. The temperature dependence of T_2 down to 1.3 K was modeled by considering both hyperfine and intermolecular dipolar interactions [102]. In particular, we evidence that the dipolar contribution is completely suppressed at the lowest temperature. Overall, these results shed light on the effects of the decoherence mechanisms, whose understanding is crucial to exploit chemically engineered molecular states as a resource for quantum information processing.

6.1 Decoherence in Molecular Nanomagnets

In order to use MNMs as building blocks of future quantum devices, it is crucial to understand and control their decoherence [4]. Spin dephasing, which is induced by dipolar interactions with neighboring electronic and nuclear spins, is the dominant decoherence mechanism at low temperature, where the spin-lattice relaxation rate becomes very small [103, 104, 105]. This originates from inter-molecular dipolar and hyperfine interactions with the magnetic nuclei. If MNMs are diluted in a non-magnetic matrix or frozen in solution, the effect of dipolar interactions is strongly suppressed and decoherence is mainly due to the hyperfine coupling of each molecule with surrounding nuclear spins [106]. This leads to a dynamics of the nuclear spin-bath which depends on the spin state of the molecule. Indeed, if we prepare the system in a pure, factorized state of the electron ($|\psi\rangle$) and nuclear spin component ($|\mathcal{N}\rangle$) state, represented by the density operator $\hat{\rho}_0 = |\psi\rangle\langle\psi| \otimes |\mathcal{N}\rangle\langle\mathcal{N}|$, the off-diagonal elements of the reduced electron spin density matrix (coherences) decrease in time because the nuclear configuration $|\mathcal{N}\rangle$ evolves differently in the different components of $|\psi\rangle$. The decay of the coherences occurs on the timescale of the nuclear spin dynamics (usually tens to hundreds of μs).

In an ensemble of magnetic molecules, another source of dephasing is represented by the Overhauser field. This random magnetic field yields a renormalization of the molecular energy gaps, resulting from the hyperfine coupling to static but highly disordered nuclear-spin configurations, differing in the various molecules. Even if faster, these effects can be removed with spin-echo techniques.

Dephasing effects may also result from internal rotations about bond axes, leading to nuclear spin flips (spectral diffusion) [30]. The characteristic spin dephasing time (T_2) can be improved by suppressing the unwanted interactions of electronic spins with the environment. Careful optimization of the molecular species allowed the improvement of T_2 in mononuclear [107, 108, 109, 110] and polynuclear complexes [30, 32], by choosing suitable organic ligands, minimizing nuclear magnetic moments and motional degrees of freedom. The effects of the hyperfine interactions on the dephasing in Cr-based isolated rings have been theoretically considered by taking into account both inhomogeneous broadening and electron-nuclear entanglement in Ref. [106].

A characteristic of molecular spin clusters is the presence of anisotropic terms in the Hamiltonian that may mix different total spin states, thus making accessible otherwise forbidden EPR transitions. The contribution of such terms to decoherence is not yet studied, because this information is not accessible for randomly oriented clusters in frozen solutions. In some cases the orientation of the spin clusters can be preserved after the dilution in isostructural diamagnetic matrices [32, 111]. Another approach is provided by high frequency–high field pulsed Electron Paramagnetic Resonance (EPR) spectroscopy, which allows the direct investigation of non-diluted single crystals. At low temperature, the magnetic field can polarize the molecular spins and suppress the dephasing induced by the spin-bath fluctuations.

In the following, we report a study of the coherent spin dynamics in a single crystal of $[^i(C_3H_7)_2NH_2][Cr_8ZnF_9(O_2CC^tBu)_{18}]$, hereafter Cr_8Zn. Cr_8Zn belongs to a family of heterometallic wheels [112] and is characterized by a cyclic structure with eight Cr^{3+} ions ($s_{Cr} = 3/2$) and one non-magnetic Zn^{2+} (Figure 6.1). An analogous Cr_8Cd variant was investigated by magnetometry [113, 114] on powder samples. Its spin structure shows finite-size effects, that give rise to a non-collinear spin arrangement and to the accumulation of spin density at the edges of the open wheel [115].

6.2 Model spin Hamiltonian

The pattern of the energy levels of Cr_8Zn was previously studied by powder Inelastic Neutron Scattering (INS) [116]. In zero field, the ground state is a singlet (total spin $S = 0$), with first ($S = 1$) and second ($S = 2$) excited multiplets respectively separated by energy gaps of 3.5 K and 12 K.

The thermodynamic properties on a single crystal of Cr_8Zn have been investigated by our coworkers in Modena (prof. Affronte's group), who performed magnetization, specific heat and torque measurements (see Section 2.1 for a description of these techniques). The magnetic energy level structure in the vicinity of the level crossings has also been probed by NMR nuclear spin-lattice relaxation measurements performed by F. Adelnia and prof. A. Lascialfari in Pavia. We have interpreted these data on the basis of the spin

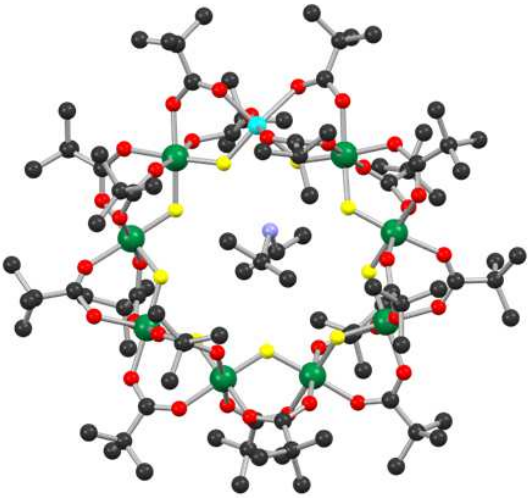

Figure 6.1: Structure of the Cr_8Zn molecular wheel. Color scheme: Cr, green; Zn, cyan; F, yellow; O, red; C, black; N, blue. H atoms omitted for clarity.

Hamiltonian:

$$\hat{H}_0 = J\sum_{i=1}^{7}\hat{\mathbf{s}}_i\cdot\hat{\mathbf{s}}_{i+1} + d\sum_{i=1}^{8}\hat{s}_{zi}^2 + e\sum_{i=1}^{8}\left(\hat{s}_{xi}^2 - \hat{s}_{yi}^2\right) + \sum_{i>j=1}^{8}\hat{\mathbf{s}}_i\cdot\underline{\mathbf{D}}_{ij}\cdot\hat{\mathbf{s}}_j + g\mu_B\mathbf{B}\cdot\sum_{i=1}^{8}\hat{\mathbf{s}}_i \quad (6.1)$$

where $\hat{\mathbf{s}}_i$ is the spin operator of the i^{th} Cr ion in the ring. In the following we assume that the site $i = 9$ is occupied by the Zn^{2+} ion. The first term describes the isotropic exchange interactions between nearest neighboring Cr^{3+} ions, the second and third terms account for single-ion zero-field splitting. The minimal model assumed here for the non-axial single-ion anisotropy is a simple effective way to account for the presence of non-axial terms arising from the non-regular ring structure and/or from the non-collinearity of local easy axes[1]. The last term is a Zeeman interaction with the external magnetic field. Also included are intramolecular magnetic dipole-dipole interactions (fourth term in Eq. 6.1), with couplings $\underline{\mathbf{D}}_{ij}$ calculated in the point dipole approximation (no additional free parameters).

This model is sufficient to provide a good description of low-temperature magnetization and specific heat data, which are shown in the next section. They are well reproduced by choosing $J = 1.32$ meV, $d = -28$ μeV and $e = 3$ μeV, as assumed in Ref. [116] to fit inelastic neutron scattering (INS). Due to the Zeeman effect, the ground state changes from $|S, M\rangle = |0, 0\rangle$ to $|1, -1\rangle$, and from $|1, -1\rangle$ to $|2, -2\rangle$, in applied magnetic fields (lying in the plane of the ring) of $B_{C1} \sim 2.15$ and $B_{C2} \sim 6.95$ T, respectively (see level diagram in Fig. 6.2). As shown below, torque measurements at different angles suggest the presence of a sizeable level-repulsion at B_{C2}, which is not predicted by Hamiltonian 6.1. This is also in agreement with NMR nuclear spin-lattice relaxation rate experimental results, and can be modeled by adding a Dzyaloshinskii-Moriya (DM) interaction term

---

[1] We have checked that a more complex form of the local zero-field splitting tensors (with easy axes tilted with respect to the normal to the plane of the ring axis and rotated from site to site) yields very similar results on thermodynamic, as well as EPR measurements.

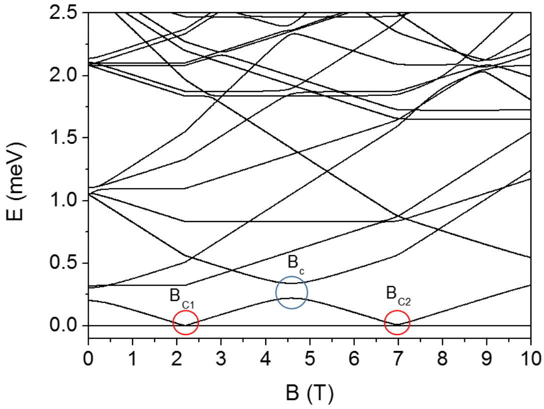

Figure 6.2: Energy levels of Cr$_8$Zn single crystal for $\theta = 90°$. Magnetic field dependence of the low-lying energy levels of Cr$_8$Zn calculated according to Eq. 6.2, with $J = 1.32$ meV, $d = -28$ μeV, $e = 3$ μeV and $G_z = 16$ μeV. The field lies in the plane of the ring ($\theta = 90°$). The two ground state level (anti-)crossings B_{C1} and B_{C2} are indicated in red, while the excited states level anti-crossing B_C is indicated in blue. The energy of the ground state is set to zero for each value of the magnetic field.

perpendicular to the plane of the ring, i.e. by assuming

$$\hat{H} = \hat{H}_0 + \hat{H}_{DM}, \tag{6.2}$$

with

$$\hat{H}_{DM} = G_z \sum_{i=1}^{7} \left(\hat{S}_{x,i}\hat{S}_{y,i+1} - \hat{S}_{y,i}\hat{S}_{x,i+1} \right). \tag{6.3}$$

It is worth noting that, although other ways can be found to obtain an anti-crossing between $S = 2$ and $S = 1$ multiplets, this mechanism is able to reproduce the correct angular dependence (see discussion below). In addition, we stress that the introduction of $\hat{H}_{DM}$ with G_z determined from torque measurements, does not alter the interpretation of other experimental results. Indeed, EPR, magnetization and specific heat data can be fitted also with the simplified model of Hamiltonian 6.1 and are only marginally affected by the introduction of $\hat{H}_{DM}$.

The field-dependence of the energy levels, calculated by using Hamiltonian 6.2, is shown in Fig. 6.2. This model yields a very small ground state anti-crossing at B_{C1} and a sizeable one at B_{C2}. The excited states level anti-crossing B_C shown in the blue circle of Fig. 6.2 is also predicted and experimentally verified by specific heat and NMR measurements.

6.3 Thermodynamic measurements

Magnetization $M(B)$ and specific heat $C(B)$ measurements have been performed in house (by A. Ghirri and co-workers in Modena) by means of a cryomagnetic system with ^{3}He insert, that allows to reach temperatures as low as 0.3 K and a superconducting coil operating up to $B = 7$ T. All measurements have been done on Cr$_8$Zn single crystals. Magnetization was measured by Hall probes made of 2DEG semiconducting heterojunctions. Heat capacity was measured by the relaxation method using two-τ constants in a commercial set-up. High Field torque and heat capacity measurements have been performed at LNCMI laboratory in Grenoble (F). For torque measurements, a CuBe cantilever was used, as described in Ref. [72] and in Sec. 2.1. The experimental apparatus was sensitive to the y component of the torque vector (t_y) acting on the sample in a magnetic field B, which was applied in the xz plane at an angle θ from z, that is the axis perpendicular to the Cr_8Zn ring's plane. Rotations of the sample were performed around the y axis [see inset Fig. 6.5-(a)].

6.3.1 Magnetization

We first present the experimental results for the magnetization versus field at low temperatures, with the magnetic field lying in the plane of the ring ($\theta = 90°$). A clear steplike increase in magnetization is observed for temperatures up to 1 K, while at T = 2 K the magnetization is approximately proportional to the field [Fig. 6.3-(a)]. At low magnetic fields ($B < B_{C1}$), M is observed to be zero as a direct evidence of a singlet ground state, while the magnetization rapidly increases at 2.15 and 6.95 T, corresponding to the first and second ground state level crossings.

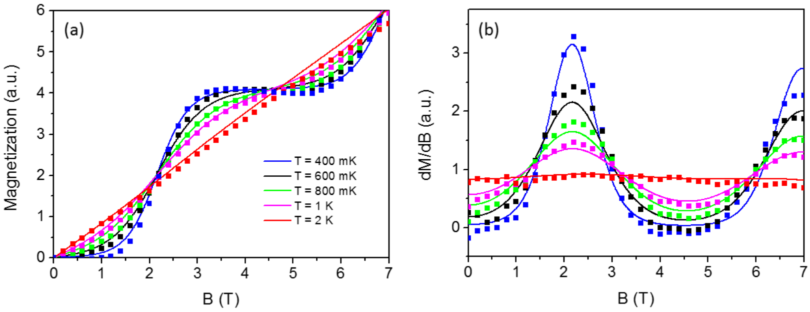

Figure 6.3: Magnetization vs magnetic field. Magnetic field dependence of the magnetization (a) and of dM/dB (b) measured at T = 0.4, 0.6, 0.8, 1, 2 K, with the magnetic field applied in the plane of the ring ($\theta = 90°$). Solid lines show the theoretical calculations resulting from Hamiltonian 6.2, with a Gaussian distribution of the exchange constants (J-strain) with standard deviation $\sigma_J = 0.04\ J$.

The calculations of M vs B and of dM/dB are reported in Figs. 6.3-(a) and 6.3-(b), respectively (solid lines). As stated above, even if the effect of the additional DM term (see Eq. 6.3) on the magnetization is found to be negligible, the theoretical (continuous) curves reported in Fig. 6.3 are calculated by numerically diagonalizing the full spin Hamiltonian 6.2. We note that the measured peak in dM/dB centered at B_{C2} appears to be broader than the one centered at B_{C1}. This could be due to a distribution of parameters in the spin Hamiltonian resulting from some local disorder (J-*strain*). In particular, different molecules in the crystal could have slightly different values of J. This, in turn, implies a distribution of values of the crossing fields centered at the nominal B_{C1} or B_{C2}. Notice that the effect of J-strain is much more pronounced in the proximity of B_{C2} than B_{C1}, since the exchange energy gap between the $S = 2$ and $S = 1$ multiplets (which cross at B_{C2}) is about three times the exchange energy gap between the $S = 1$ and $S = 0$ multiplets, involved in the crossing at B_{C1}. Hence, we observe a change induced by a given variation of J three times as large on B_{C2} with respect to B_{C1}, i.e. $\frac{\partial B_{C2}}{\partial J} \approx 3\frac{\partial B_{C1}}{\partial J}$. This behavior explains the much more pronounced broadening of the peak at B_{C2} when compared to the one at B_{C1}. We have reproduced this broadening by introducing a Gaussian distribution of the exchange constant J, with standard deviation $\sigma_J = 0.04\ J$, in line with what assumed for Cr$_7$Ni in Ref. [87]. The reported value of σ_J was also used to fit the broadening effects in the torque and in the NMR nuclear-spin-relaxation measurements, as will be shown in the following sections.

6.3.2 Specific Heat

Measurements of specific heat at low temperature as a function of the external magnetic field has been proved to be very useful to investigate level crossing effects also in the presence of a gap at the crossing field leading to a level anti-crossing (see Section 2.1). The experimental results on a single crystal of Cr$_8$Zn with the magnetic field applied in the plane of the ring ($\theta = 90°$) are shown in Fig. 6.4-(a) at three different temperatures (points), and compared to the simulated behavior (lines), obtained from the eigenvalues of the spin Hamiltonian 6.2. As can be seen, the theoretical curves are in good agreement with the experimental results. The small disagreement found for the peak at T = 0.4 K at high magnetic field is within the experimental accuracy, considering that a small temperature drift is possible at such low T. The uncertainty in the subtraction of the non-magnetic background contributing to the specific-heat (which is a particularly hard task) limits the precision in determining the size of a possible anti-crossing in the ground state. The minimum at $B_{C1} = 2.15$ T is in good agreement with the curves calculated from the spin Hamiltonian 6.2. Moreover, the experimental evidence of level-repulsion between the excited multiplets S = 2 and S = 0 at $B_C = 4.5$ T (see minimum in Fig. 6.4-(a) at T = 0.4 K) is well reproduced by our model, as it can be observed in the level scheme reported in Fig. 6.2 (blue circle).

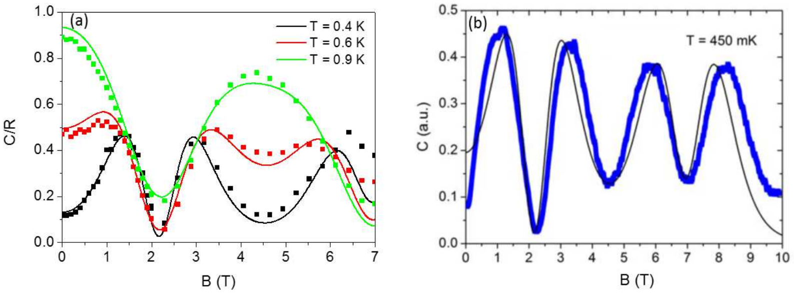

Figure 6.4: Specific Heat vs magnetic field. (a) Magnetic field dependence of the specific heat measured at T = 0.4, 0.6, 0.9 K, with $\theta = 90°$. (b) Specific heat as a function of magnetic field at T = 0.45 K. The solid lines represent the specific heat calculated with the energy levels determined from the diagonalization of Hamiltonian 6.2, by including both the DM interaction (which induces a level repulsion at B_{C2}) and J-*strain* effects.

In order to gain deeper insight on the energy gap evolution for the second level crossing field, we have also analyzed heat capacity measurement up to 10 T at low temperature, performed at the High Magnetic Fields Laboratory in Grenoble. We find again a good agreement between experimental data and the theoretical curves [Fig. 6.4-(b)], obtained from the spin Hamiltonian 6.2. The anti-symmetric exchange interaction (Eq. 6.3), which induces a sizeable anti-crossing, as well as the Gaussian broadening of the exchange constants are responsible for the non-zero value of the specific heat at B_{C2}. The additional broadening of the fourth experimental peak can be ascribed to heating of the sample while increasing the magnetic field.

6.3.3 Torque

In order to get independent information on the ground state level crossings, we have investigated torque measurements at different angles. As shown in Fig. 6.5-(a), the experimental magnetic torque signal at T = 50 mK presents the typical step-like behavior due to the transitions of the ground state to multiplets with progressively higher S values [73]. Torque measurements at high field show the presence of a small peak for an angle $\theta = 49.9°$, which is absent at the other reported angles ($-2°$, $9°$). A peak in the torque suggests the presence of an avoided crossing [74]. An anti-crossing between $S = 2$ and $S = 1$ multiplets (with the correct angular dependence) can occur due to the presence of a small (but finite) Dzyaloshinskii-Moriya interaction [117]. Other mechanisms can induce a level repulsion at B_{C2}, such as the introduction of local anisotropy axes slightly tilted from the z-axis of the magnetic field or the assumption of non-uniform d_i values. However, we have checked that the angular dependence of the anti-crossing, together with the size of the induced gap, are not easily reproduced by Hamiltonians taking into account the tilting of local anisotropy axes and/or non-uniform values of d_i. Conversely, the inclusion of a Dzyaloshinskii-Moriya (DM) term (Eq. 6.3) in the spin Hamiltonian leads to the appearance of a peak in the simulated torque at $49.9°$ which is very small or absent at the other measured angles, as shown in Fig. 6.5-(b).

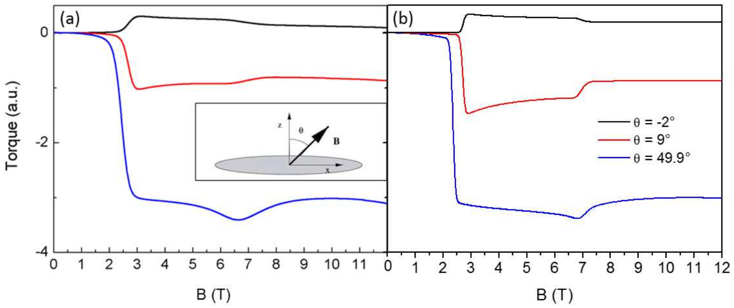

Figure 6.5: Torque vs magnetic field at different angles. Magnetic torque signal taken at the High Magnetic Fields Laboratory in Grenoble on Cr_8Zn single crystal at T = 50 mK: (a) experimental data (inset: experimental set up); (b) theoretical simulations.

For simplicity we have not included G_x and G_y component of the DM interaction, since their contribution to the anti-crossing is very small. A good fit (Fig. 6.5) is obtained by fixing $G_z = 0.016$ meV $= 0.012\ J$. This is in agreement with the theoretical model [118], which predicts $G \approx \frac{2-g}{2} J$. Since for Cr^{3+} $g = 1.98$ we should expect $G \approx J/100$, which is close to the fitted parameter. The situation is different from the odd-numbered open-ring Cr_7Zn, in which a sizeable S-mixing and level repulsion is induced by uniform single-ion and axial anisotropies [73]. In Fig. 6.6 we also plot the experimental data (a) of the torque at various temperatures and the results of the theoretical calculations (b). We note that the experimental peaks are well reproduced by assuming the Gaussian distribution of the exchange constants discussed above, with $\sigma_J = 0.04\ J$. The introduc-

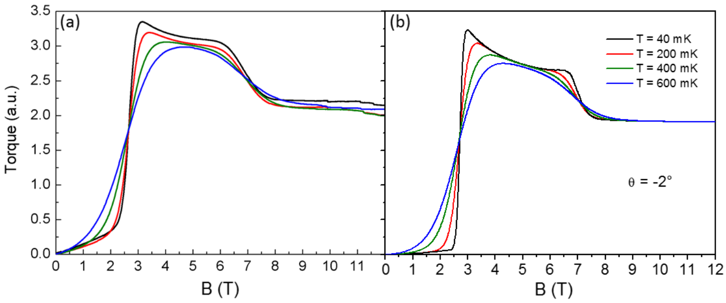

Figure 6.6: Torque vs magnetic field at different temperatures. Field dependence of the torque signal taken at $\theta = -2°$ on Cr_8Zn single crystal for several temperatures, reported in the legend: (a) experimental data; (b) theoretical simulations.

tion of *J-strain* allows us to obtain theoretical peaks with broadening in agreement with the experimental one (in contrast to the narrower peaks given by calculations when this effect is neglected).

6.4 Nuclear Spin-Lattice Relaxation rate

Results obtained from thermodynamic measurements are also confirmed by proton nuclear spin-lattice relaxation rate (NSLR) near the level crossings B_{C1} and B_{C2}. A discussion of NSLR in molecular nanomagnets and of its link to electronic relaxation can be found in Ref. [119, 120]. Following Ref. [121], here we will adopt the following expres-

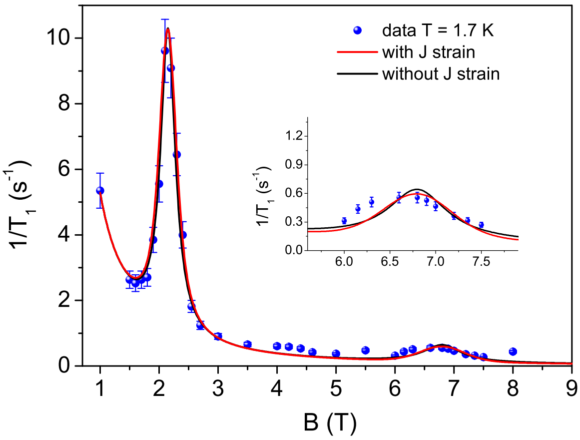

Figure 6.7: NSLR. ^{1}H spin-lattice relaxation as a function of magnetic field in Cr_8Zn at T = 1.7 K. The solid line is the fit according to Equation 6.4, including (red) or neglecting (black) J-strain effects. The red fit is able to better reproduce the line-shape, by assuming smaller gaps, in agreement with the model Hamiltonian 6.2 and with thermodynamic measurements. The inset is a zoom close to the second level crossing.

sion for the NSLR:

$$\frac{1}{T_1} = \chi T A^2 \left[\frac{\Gamma_1(T)}{\Gamma_1(T)^2 + \omega_L^2} + \frac{\Gamma_2(T)}{\Gamma_2(T)^2 + (\omega_L - \Delta_i)^2} \right]. \tag{6.4}$$

The first contribution is the quasi-elastic term which arises from the fluctuations of the magnetization of the molecule. These fluctuations are due to spin-phonon interaction and are modeled with a Lorenzian spectral density function at the Larmor frequency ω_L, with broadening Γ_i. The second term is the inelastic contribution which arises from direct transitions between nuclear Zeeman states accompanied by a transition in the magnetic state of the molecule, with broadening Γ_2. This term is important only very close to a level crossing and becomes dominant when the gap Δ_i is of the order of the broadening Γ_2. The constant A^2 in Eq. 6.4 is the average square of the dipolar interaction between protons and magnetic ions and is temperature and field independent. In the case of Cr$_8$Zn the term χT in Eq. 6.4 is also a constant since we are considering NMR measurements at fixed temperature (1.7 K) and the susceptibility $\chi = dM/dB$ is almost field independent at this temperature [see red curve in Fig. 6.3-(b)]. This situation is clearly distinguished from the one found in Cr$_8$ where the field dependence of χT leads to a peak at level crossing with both elastic and inelastic contributions, which are thus difficult to separate [121].
The NSLR experimental results as a function of the external magnetic field are shown in Fig. 6.7. The peaks at the level crossings can be fitted by Eq. 6.4 with the gap between the ground and the first excited state expressed as

$$\Delta_i = \sqrt{\delta_{i-1,i}^2 + \left[g\mu_B \left(B_{Ci} - B\right)\right]^2}, \tag{6.5}$$

where $i = 1, 2$ for the first (B_{C1}) and second (B_{C2}) level crossing, respectively. $\delta_{i-1,i}$ represents the level repulsion gap leading to a level anti-crossing. If *J-strain* effects are completely neglected, the experimental data can be fitted but large values of the anti-crossing gaps (black line in Figure 6.7) must be assumed: $\delta_{01} = 0.09$ K and $\delta_{12} = 0.56$ K, which are not in agreement with the thermodynamic results and the theoretical predictions. Thus we decided to include in the fitting the effect of J-strain due to a distribution of J values, as described in Sec. 6.3. We performed a fit (red line in Fig. 6.7) based on Eq. 6.4, by assuming a distribution of the crossing fields, B_{C1} and B_{C2}, induced by the Gaussian distribution of the exchange constants discussed above, with standard deviation $\sigma_J = 0.04\ J$. The values of the anti-crossing gap obtained from the fit are now in agreement with those predicted by the model (Eq. 6.2) used to explain torque measurements: $\delta_{01} = 0.01$ K at B_{C1} and $\delta_{12} = 0.19$ K at B_{C2}. Furthermore, the inclusion of J-strain explains the significantly more pronounced broadening of the peak at B_{C2} when compared to the one at B_{C1} (see full points in Fig. 6.7). The value of B_{C1} which fits the first peak in Fig. 6.7 is 2.15 T, in good agreement with that derived from magnetization and specific heat, while the second peak is centered at 6.8 T. This value is slightly lower than the one inferred from thermodynamic measurements (6.95 T), but still compatible since magnetic field steps are spaced 0.1 T apart.
It is interesting to note that the order of magnitude of $\Gamma_1 = 1.4 \times 10^6$ rad/s, as determined above for the quasielastic contribution, is close to the one obtained from extrapolating at low temperature the temperature dependence of the correlation frequency derived from the analysis of the NSLR results in Cr$_8$ and Cr$_8$Zn [122] at higher temperature. This comparison indicates that far from level crossing the NSLR is determined at all temperatures by the phonon-induced relaxation dynamics. Also the value of $A^2 = 0.14 \times 10^{12}$ rad^2/s^2

is in reasonable agreement with the one obtained in Cr_8 [121]. The values of the interaction parameter A^2 and of the broadening parameter Γ_1 are the same at both the first and the second level crossing. $\chi T = 0.46$ emu K/mol is obtained from the magnetization measurements. Finally the value of Γ_2 depends on the examined peak. We obtain $\Gamma_2 = 2.4 \times 10^{10}$ rad/s for the first level crossing and $\Gamma_2 = 0.2 \times 10^{10}$ rad/s for the second.

6.5 High-frequency EPR

The energy level structure of Cr_8Zn probed by thermodynamic, INS and NMR measurements was also explored by means of 241 GHz continuous wave EPR spectroscopy. Moreover, pulsed spin echo experiments are used to probe the coherent spin dynamics of mixed total-spin states. Measurements were performed on single crystals by A. Ghirri, H. van Tol and S. Hill at the National High Magnetic Field Laboratory (NHMFL), in Tallahassee, Florida (USA). Differently from thermodynamic measurements, continuous wave (cw) and pulsed EPR experiments were performed on hexagonal crystals which contain two molecules per unit cell. For the measurements presented in Figure 6.8, the magnetic field (B) was applied at an angle of $\theta = 15°$ and $75°$ with respect to the normal to the wheels. Cw-EPR spectra measured at 2.5 K on a single-crystal of Cr_8Zn show three EPR transitions between 8 and 10 T, whose resonance fields and intensities differ for $\theta = 15°$ and $75°$ (Figure 6.8). A further (weak) excitation is visible at 4.3 T. The cw-EPR study at different temperatures (Figure 6.9) suggests that the resonances at 8.4 T and 9.1 T ($\theta = 15°$) originate from the $S = 2$ state, which is the ground multiplet at these fields. The experimental spectra are reproduced by the same spin Hamiltonian

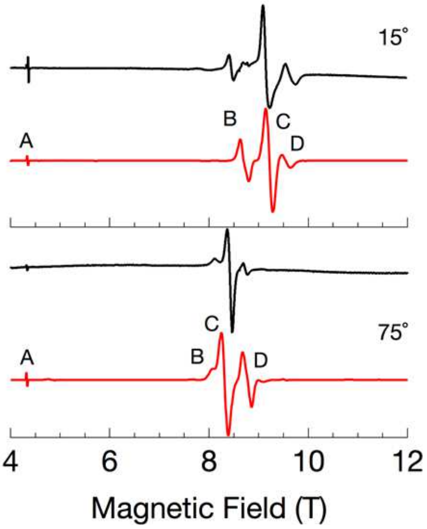

Figure 6.8: cw-EPR spectra measured at 241 GHz and different angles. Black and red lines respectively display experimental and simulated spectra. (Figure used with permission from Ref. [102].)

6.1 used to interpret thermodynamic measurements (see previous section) and INS data on a deuterated Cr_8Zn variant [116]. Here we prefer to keep the model as simple as possible, neglecting the DM term 6.3. In fact, we have checked that its inclusion in the

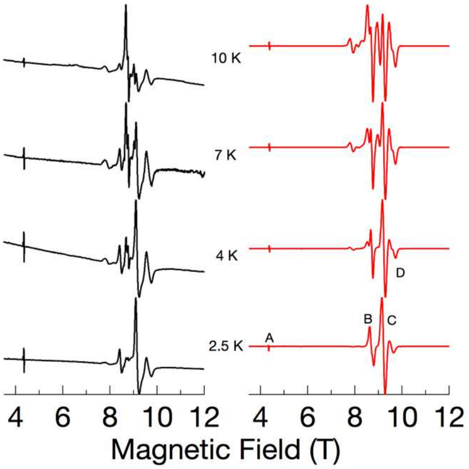

Figure 6.9: cw-EPR spectra at several temperatures measured at 241 GHz on a Cr_8Zn single crystal ($\theta = 15°$). Black and red lines respectively correspond to experimental and simulated spectra.

spin Hamiltonian only marginally affects the simulated spectra. A good fit to the experimental data is found with $J = 1.23$ meV, $d = -28$ μeV, $e = 3$ μeV and $g = 1.98$ (Figure 6.8)[2]. These parameters are close to those reported for other Cr_8Zn [116] and Cr_8Cd [113, 115] derivatives[3]. Figure 6.10-(a) shows the pattern of the lowest-lying energy levels calculated for $\theta = 15°$. As in Cr_8Cd crystals [115], there is a level anti-crossing at about 8.5 T, which is due to the mixing of the total spin eigenstates $|S, M'\rangle = |0, 0\rangle$ and $|2, -1\rangle$, being M' the component of the total spin along **B**. This feature emerges as a combined effect of zero-field splitting (see Eq. 6.1) and a finite transverse field component ($\theta \neq 0°$). The comparison between experimental and calculated spectra allows the labeling of observed EPR transitions [Figures 6.8 and 6.10-(a)]. Resonance A is a transition with $\Delta M = 2$ between $|1, -1\rangle$ and $|1, 1\rangle$, which is possible for $\theta \neq 0°$. At higher field, two resonances, labeled B and C, are observed near the anti-crossing at 8.5 T. The transitions calculated from the SH 6.1 are (apart from small corrections) from the ground state $|2, -2\rangle$ to the mixed state $\alpha|0, 0\rangle + \beta|2, -1\rangle$. At different magnetic field, the relative composition of the mixed state varies and the simulations indicate $0.77|0, 0\rangle + 0.64|2, -1\rangle$ for B, and $0.37|0, 0\rangle + 0.93|2, -1\rangle$ for C. The compositions in terms of different total-spin states directly reflect the significantly different observed intensities. Indeed, the larger intensity of the C transition results from the larger component of the magnetic $|2, -1\rangle$ state in the excited level. Lastly, the fourth resonance (D) belongs to excited multiplets, and therefore is weak at low temperature.

6.6 Decoherence mechanisms probed by pulsed-EPR

Efficient suppression of electron spin bath fluctuations without dilution requires the polarization of the Cr_8Zn crystal [103]. In Figure 6.10-(b) we report the Boltzmann pop-

---

[2] To account for the relative intensity of the measured peaks we have assumed a crystal misalignment of 3° with respect to the directions perpendicular (15°) and parallel (75°) to the hexagonal face.

[3] The zero field splitting parameters are the same reported in Ref. [116] for the deuterated Cr_8Zn variant, while a slight reduction of J (less than 7%) has been applied to fit EPR spectra.

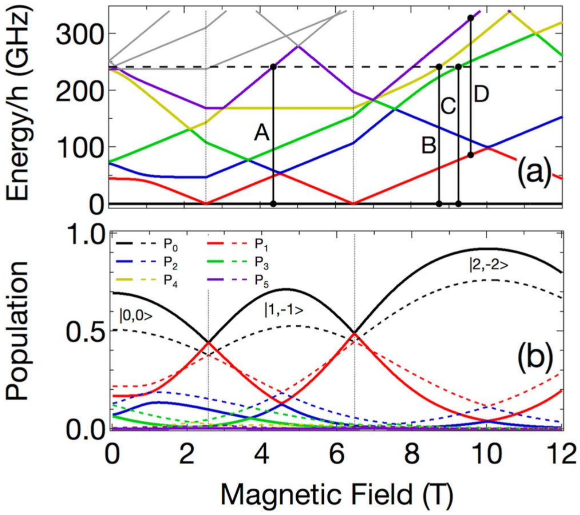

Figure 6.10: (a) Calculated energy levels as a function of B ($\theta = 15°$). The vertical black lines are the observed EPR transitions. The horizontal dashed line indicates the frequency of the microwave excitation (241 GHz). (b) Population of the lowest lying energy levels as a function of B, calculated for T = 1.5 K (solid lines) and 2.5 K (dashed lines). (Figure used with permission from Ref. [102].)

ulation $P_i = e^{-E_i(B)/k_B T}/Z$ of the lowest-lying energy levels as a function of B. Here E_j are the eigenvalues of Hamiltonian 6.1. In the range 8 - 12 T the population of the ground state $|2,-2\rangle$ is maximized. In correspondence to the resonance field of B and C, it reaches respectively 0.84 and 0.94 at 1.5 K. At 2.5 K, these values decrease to 0.69 and 0.73 respectively, showing a steep reduction within a temperature range of 1 K. The nuclear spin bath, conversely, is not polarized and can be assumed to be in an infinite-temperature state.

Spin-echo experiments have thus been performed with the two-pulse Hahn echo sequence ($\pi/2 - \tau - \pi - \tau -$echo), to investigate the coherent dynamics of transitions B and C. The echo-detected EPR spectrum was measured initially as a function of B [Figure 6.11-(a)]. The duration of the pulses was adjusted to maximize the echo signals, and the $\pi/2$ pulse typically ranged between 140 ns and 200 ns. Because the corresponding excitation bandwidth of the applied pulses ($\sim$ 0.15 mT) was much smaller than the EPR line-width, a very small fraction of the Cr_8Zn spins were actually manipulated in the T_2 measurements. The transitions in the echo-detected EPR spectrum match the low temperature cw-EPR spectra in Figure 6.8, and are labeled accordingly. At 1.35 K we observed a significant enhancement of the echo signal with respect to the 2.17 K data. The transition C is still the strongest, while the intensity of B is about one third [Figure 6.11-(a)]. The transition D is barely visible as it arises from excited states.

The decay of the echo intensity, measured by varying the delay 2τ, can be fit with a mono-exponential function $I = I_0 e^{-2\tau/T_2}$ [Figure 6.11-(b)], from which we derived $T_2(B) = 657$ ns and $T_2(C) = 475$ ns from least-square fitting. The two transitions thus have similar decay rates with a ratio $T_2(B)/T_2(C) \approx 1.4$ at the lowest temperature, which is reasonable for the not too different composition of the involved states. Spin echo measurements were repeated for $1.35 < T < 2.17$ K, and the rate $1/T_2$ extracted from the mono-exponential fits was plotted as a function of T [Figure 6.11-(c)]. We note that $1/T_2$ has a somewhat stronger temperature dependence for C than for B. In the following we discuss this behavior on the basis of a model for decoherence in molecular spin clusters. In the case of non-diluted single-crystals of Fe_8 in high magnetic field, the dominant relaxation mechanism has been ascribed to collective excitations mediated by intermolecular dipolar interactions and by phonons, while the contribution from nuclei was estimated to be low [103, 104]. In the examined magnetic field range, Cr_8Zn has a $S = 2$ ground state. Thus the intermolecular dipolar interaction is significantly reduced in comparison to Fe_8 ($S = 10$). However, its effects are still present in a non-diluted crystal, as suggested by the strong temperature dependence of the echo decay in the range 1.35 - 2.17 K [Figure 6.11-(c)].

To model the spin echo decay in a single-crystal of Cr_8Zn we have considered the effect of dipolar intermolecular and hyperfine interactions, and the phonon contribution. However, using the magneto-elastic coupling constant determined for Cr_8 and Cr_7Ni parent compounds [123], we find that the latter gives a negligible contribution. The phonon contribution to the spin-echo decay was investigated within the theoretical framework of Ref. [119] and based on the irreversible evolution of the density matrix produced by spin-phonon interactions. Since we deal with times much longer than those characterizing the coherent dynamics, we can apply the secular approximation and decouple the evolution of the diagonal terms of the density matrix from the off-diagonal ones. Within this picture, we consider as the main source of relaxation the modulation of local crystal fields by phonons, which can be modeled in terms of the rate matrix W, whose matrix elements W_{st} represent the probability per unit time of a transition between the eigenstates $|t\rangle$ and $|s\rangle$ of the molecular Hamiltonian. By assuming a spherically symmetric magnetoelastic coupling of each ion, we obtain:

$$W_{st} = \gamma^2 \pi^2 \Delta_{st}^3 n\left(\Delta_{st}\right) \sum_{i,j=1}^{8} \sum_{q_1,q_2=x,y,z} \langle s|\hat{O}_{q_1,q_2}(\hat{\mathbf{s}}_i)|t\rangle\langle t|\hat{O}_{q_1,q_2}(\hat{\mathbf{s}}_j)|s\rangle, \tag{6.6}$$

where $n(x) = \left[e^{\hbar x/k_B T} - 1\right]^{-1}$, $\Delta_{st} = \left(E_s - E_t\right)/\hbar$ and $\hat{O}_{q_1,q_2}(\hat{\mathbf{s}}_i) = \left(\hat{s}_{q_1,i}\hat{s}_{q_2,i} + \hat{s}_{q_2,i}\hat{s}_{q_1,i}\right)/2$ are quadrupolar operators. γ is proportional to the spin-phonon coupling strength (assumed to have spherical symmetry), and in AF rings is usually determined by fitting NMR data. By using the same value of γ obtained in [123] for Cr_7Ni, we find that phonons give only a marginal contribution to level lifetimes at low temperature (2.2 K or lower)[4].

We thus focus on the other mechanisms of decoherence. Each Cr_8Zn molecule experiences the combined effects of the external magnetic field and a random time-dependent field resulting from the surrounding electron and nuclear spins. The decay of the echo intensity is due primarily to this time-dependent field which, in contrast to static effects, cannot be refocused by spin-echo techniques. As the measurements were carried out in high magnetic fields, single spin-flip processes are suppressed by the large Zeeman energy gaps, and spin bath fluctuations are dominated by energy-conserving flip-flops transitions between single-molecule eigenstates $|j\rangle$ and $|k\rangle$. These occur with a probability proportional to the product of their populations $P_j = e^{-E_j/k_B T}/Z$ at temperature T [103]:

$$\frac{1}{T_2} = C \sum_{j>k} M_{j,k} P_j P_k + \Gamma. \tag{6.7}$$

---

[4] We define the s-level lifetime as $\tau_{life}^{(s)} = -W_{ss}^{-1} = \left[\sum_t W_{ts}\right]^{-1}$. Then the phonon contribution to the dephasing rate $1/T_2$ is $(1/\tau_{life}^{(s)} + 1/\tau_{life}^{(t)})/2$

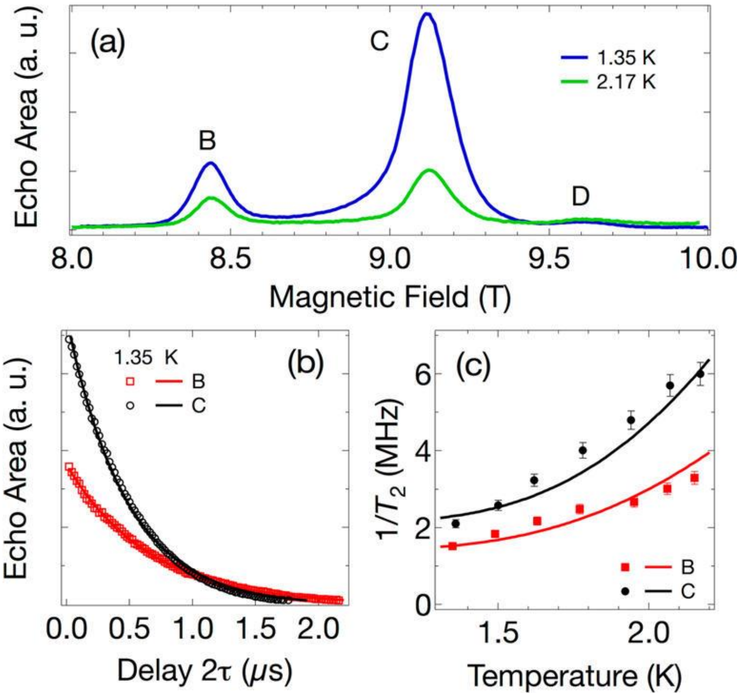

Figure 6.11: (a) Echo-detected EPR spectrum measured at 1.35 K and 2.17 K ($\theta = 15^{\circ}$). (b) Decay of the integrated echo area measured at 8.436 T (transition B, red squares) and 9.116 T (transition C, black circles). Solid lines show the fit to a single-exponential function. (c) Temperature dependence of the decay rate $1/T_2$ extracted for transitions B and C. (Figure used with permission from Ref. [102].)

To account for inter-molecular interactions while keeping the model as simple as possible, we follow Ref. [103] and represent each molecule as a magnetic dipole of spin S. Within this approximation, the matrix elements $M_{j,k}$ are given by:

$$M_{j,k} = \left| \langle jk | \hat{S}_{x'1} \hat{S}_{x'2} + \hat{S}_{y'1} \hat{S}_{y'2} | kj \rangle \right|^2 \tag{6.8}$$

where x' and y' are orthogonal to $\mathbf{B}$ and $|jk\rangle \equiv |j\rangle \otimes |k\rangle$ is the tensor product of single-molecule eigenstates $|j\rangle$ and $|k\rangle$, belonging to a pair of dipolar-interacting molecules, namely 1 and 2. Other terms bilinear in the spin operators are not included, because they do not induce energy-conserving flip-flop transitions. Γ is a temperature-independent term, which originates from the interaction with the magnetic nuclei.

The temperature dependence of $1/T_2$ predicted by this model is shown in Figure 6.11-(c). Here C and Γ are transition dependent fitting parameters. To reduce the number of free parameters we assumed the same C/Γ ratio for both transitions. Given the simplicity of the model, the agreement is remarkably good and reproduces the correct temperature dependence. At low temperature, decoherence is mainly due to the hyperfine interaction (Γ term in Eq. 6.7) and we obtain $\Gamma_B = 1.30$ MHz, $\Gamma_C = 1.97$ MHz, while the dipolar contribution almost vanishes at 1.35 K. From the fitting we also find $C = 220$ MHz for transition B, properly scaled to 333 MHz for transition C (keeping the C/Γ ratio fixed on the two transitions). These numbers are in reasonable agreement with previous findings ($C = 34$ MHz) for the dephasing rates of $S = 1/2$ free radicals [124]. We note that C crucially depends on the molecular concentration and on the spin of the magnetic units ($S = 2$ in the examined case), which determines the strength of the fluctuations of the bath field. The measured T_2 is comparable to the one measured for diluted and non-perdeuterated Cr_7Ni and Cr_7Mn rings [105], confirming that, at 1.35 K, the spin bath fluctuation is effectively suppressed. Conversely, the decay of T_2 upon increasing the temperature is caused by inter-molecular electron dipole-dipole interactions.

6.7 Conclusions

In conclusion, we have investigated the level structure of Cr_8Zn by means of low temperature magnetization, specific heat, torque, NMR $1/T_1$ and continuous wave EPR measurements. Results are interpreted on the basis of a spin model Hamiltonian, which confirms previous INS studies on the same compound. High-frequency pulsed electron paramagnetic resonance has been used to probe two different 241 GHz EPR transitions in a single-crystal of Cr_8Zn. The $1/T_2$ dephasing rate, measured by spin echo experiments, shows similar values for two examined EPR transitions involving superposition of different total-spin states. On the basis of a theoretical model that includes intermolecular dipolar and hyperfine interactions, we correctly reproduce its temperature dependence. By applying a high magnetic field we show that the effect of dipolar interactions is completely suppressed at the lowest temperature, even in a non-diluted crystal. These results clarify the origin of decoherence mechanisms in molecular clusters and show how these can be coherently manipulated by high frequency-high field EPR.

The content of this chapter was published in J. Chem. Phys. **143**, 244321 (2015) (Ref. [101]) *and* J. Phys. Chem. Lett. **6**, 5062 (2015) (Ref. [102]).

Odd-numbered AF rings as prototypical frustrated systems

CHAPTER 7

Odd-numbered anti-ferromagnetic (AF) molecular wheels are prototype systems to study the effects of spin frustration. Here we investigate the spin dynamics of two odd-number odd-electron rings (Cr_8Mn and Cr_9, both synthesized by prof. Winpenny's group in Manchester) exhibiting competing exchange interactions that lead to a $S = 1/2$ ground state. The study is carried on by analyzing the results of Inelastic Neutron Scattering measurements.

Geometrical magnetic frustration is a well-known issue in bulk compounds and it occurs when the classical magnetic energy cannot be simultaneously minimized for all individual two-spin interaction terms [125]. As pointed out by Schnack [126], there exist two different approaches to frustration. The first one considers the graph of interactions between the participating spins, thus classifying all systems with competing interactions as frustrated. The second approach shifts the attention on the properties arising from frustration. In this respect, the degeneracy of the ground state is an essential requirement. This can be considered as the most strict definition of frustration in the field of molecular magnetism and is due to O. Kahn. The two viewpoints can be partially reconciled by Schnack's definition, which considers frustration as the opposite of bipartiteness.

As a first approximation, all the here examined systems can be described by the Heisenberg Hamiltonian: $\hat{H} = \sum_{i,j} J_{i,j} \hat{\mathbf{s}}_i \cdot \hat{\mathbf{s}}_j$. Hence, following Lieb, Schultz, and Mattis [127], a spin system is called bipartite if it can be decomposed into subsystems A and B such that all the exchange parameters fulfil $J_{i_A,j_B} \geq \gamma^2$, $J_{i_A,j_A} \leq \gamma^2$, $J_{i_B,j_B} \leq \gamma^2$. Here i_A (i_B) indicate metal ions belonging to sublattice A (B), γ is a real number which determines the partition and AF interactions are represented by positive exchange parameters.

Usually only nearest neighbors exchange interactions are relevant. Hence, Kahn's definition only applies to odd rings with half integer spins, exhibiting a perfectly regular pattern of interactions ($J_{i,j} \equiv J$ for each pair of nearest neighbors on the wheel). Indeed, in the case of homometallic rings consisting of ions with half-integer spins, this condition leads to a degenerate ground state. A physical consequence of a degenerate ground state is that these spin systems are very likely to be perturbed by small interactions, beyond isotropic exchange. Conversely, Schnack's definition extends the classification of

frustrated systems to AF odd rings with integer spins or with a not degenerate $S = 1/2$ ground state, thus including some heterometallic complexes (with the proper pattern of exchange interactions).
Due to the presence of a degenerate ground state, the synthesis of large, regular odd-membered rings is particularly hard. In fact, the system tends to rearrange its structure in order to remove that degeneracy, ending up with a lower-energy ground state. Consequently, only a few examples of odd-membered rings are known. Moreover, most of them are heterometallic, thus breaking the ideal C_n geometrical symmetry. This is the case for the here reported Cr_8Mn (Section 7.1), which is frustrated according to Schnack's definition, and for the previously studied Cr_8Ni, which was visualized as a magnetic Möbius strip [128, 129, 130].
The study of odd homometallic rings is restricted to metal triangles [131, 132], a small number of pentagons, a single heptagon [133] and some Fe_9 [134] and Cr_9 [99, 135, 136, 137] enneagons. However, all of them show a significant gap between the lowest spin multiplets, thus being excluded from Kahn's categorization. Here we report (Section 7.2) the study of a regular Cr_9 variant. Our analysis of INS data, collected by T. Guidi at ISIS facility, show that the molecule has a pair of $S = 1/2$ spin states at low energy, separated by only 1.25 K. Hence, the dynamics of the system above 2 K can be practically described as that of a *Kahn frustrated* enneagon.

7.1 Cr_8Mn spin dynamics probed by INS

In this section we report the study of a heterometallic nine metal ring, $[H_2Ni(C_3H_7)_2]$ $[Cr_8MnF_9(O_2C^tBu)_{18}]$ (in the following Cr_8Mn), which has both an odd number of metal ions and an odd number of electrons. The structure is shown in Fig. 7.1. We derive the microscopic spin Hamiltonian and the energy spectrum of this molecule by analyzing magnetisation and INS measurements collected by M. Baker in Grenoble (ILL facility). Finally, we exploit the experimentally parameterized Hamiltonian model to investigate the ground state of Cr_8Mn and find that the internal spin structure fluctuates between opposite chiralities [138].

7.1.1 Magnetic measurements

At both 2 and 4 K the magnetization increases with applied magnetic field without reaching saturation within the measured range up to 7 T [Figure 7.2-(b)]. At 300 K $\chi T = 16$ cm^3 K mol^{-1}, slightly less than the calculated value of 18.78 cm^3 K mol^{-1} for eight uncoupled s = 3/2 and one s = 5/2 spin with $g_{Cr} = 1.96$ and $g_{Mn} = 2.0$. On decreasing temperature the molecular susceptibility (χ) steadily increases before flattening off at around 25 K at a value of around 0.17 cm^3 K mol^{-1}, indicating the presence of a significant antiferromagnetic exchange interaction. At lower temperatures χ increases rapidly confirming the expected non-zero spin ground state. Magnetic data are well reproduced by the spin Hamiltonian:

$$\hat{H} = J_{CrCr} \sum_{i=1}^{7} \hat{\mathbf{s}}_i \cdot \hat{\mathbf{s}}_{i+1} + J_{CrMn} \left(\hat{\mathbf{s}}_1 \cdot \hat{\mathbf{s}}_0 + \hat{\mathbf{s}}_8 \cdot \hat{\mathbf{s}}_0 \right) + g_{Cr} \mu_B \mathbf{B} \cdot \sum_{i=1}^{8} \hat{\mathbf{s}}_i + g_{Mn} \mu_B \mathbf{B} \cdot \hat{\mathbf{s}}_0, \quad (7.1)$$

where $\hat{\mathbf{s}}_1$ to $\hat{\mathbf{s}}_8$ represent Cr sites with spin 3/2 and $\hat{\mathbf{s}}_0$ represents Mn with spin 5/2; J_{CrCr} is the isotropic exchange interaction between nearest neighbor Cr-sites and J_{CrMn} is the isotropic exchange interaction between the Mn site and its neighboring Cr-sites. The structural similarity of Cr_8Mn with other Cr based rings provides a well-defined starting

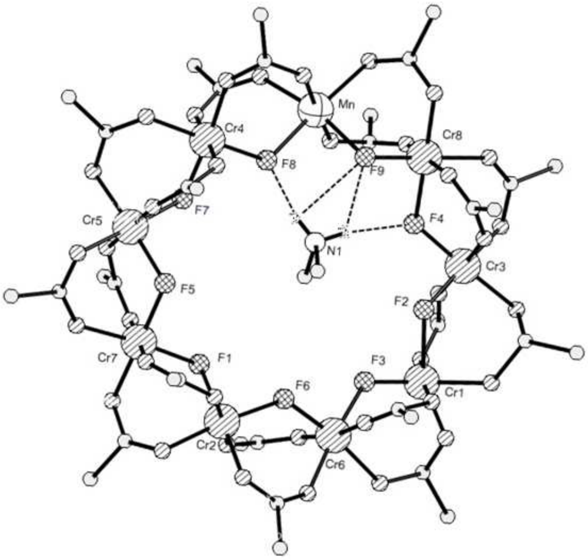

Figure 7.1: The structure of Cr_8Mn in the crystal. Methyl-groups excluded for clarity. H-atoms excluded for clarity except those on the ammonium cation. O-atoms shaded, C-atoms open circles. (Figure used with permission from Ref. [138].)

point. The nearest neighbor Heisenberg exchange couplings, J_{CrCr} and J_{CrMn}, are the dominant terms in the Hamiltonian; there is no justification for including longer range couplings. The magnetic data can be fitted with the parameters: J_{CrCr} = 1.32 meV, J_{CrMn} = 1.28 meV, $g_{Cr} = 1.96$ and $g_{Mn} = 2.0$.

7.1.2 Inelastic Neutron Scattering

INS energy spectra were measured with an incident neutron wavelength of 5.0 Å on the FOCUS spectrometer at 1.5 and 6.0 K and then on IN5, to probe a wider dynamical range and enhance the energy resolution. Several magnetic excitations are clearly resolved. Comparison of the spectra at different temperatures indicates a weak excitation in the shoulder of the elastic scattering line, labeled **I** (Figure 7.3a). Subtraction of 1.5 – 6.0 K data (inset of Figure 7.3b) indicates that this excitation comes from the ground state (cold) and is centered at approximately 0.42 meV. An excitation centered at 1.22 meV, labeled **II**, also shows greatest intensity at the base temperature. Two excitations emerge on increasing the sample temperature to 6.0 K, labeled **i** and **ii** at 1.7 and 2.0 meV, respectively (Figure 7.3c). These two excitations originate from a low-lying excited state and involve transitions to further excited states at higher energies. A high resolution (8.0 Å) instrument setting enables the clear separation of transition **I** from the elastic line and at 6.0 K the equivalent excitation is also observed at negative neutron energy transfers (Figure 7.3b). The temperature dependence of **I** and **II** clearly identifies the transitions as cold excitations. With a shorter neutron wavelength of 3.2 Å additional cold excitations labelled **III** and **IV** are accessed (Figure 7.3c), with peak centers at 2.5 and 3.6 meV respectively. From Figure 7.3a it becomes evident that transition **II** exhibits a slight asymmetry, which is not evident for transition **I**. The neutron momentum transfer of **II** has a maximum at 1.2 $Å^{-1}$ (Figure 7.3d), consistent with the intermetallic distance be-

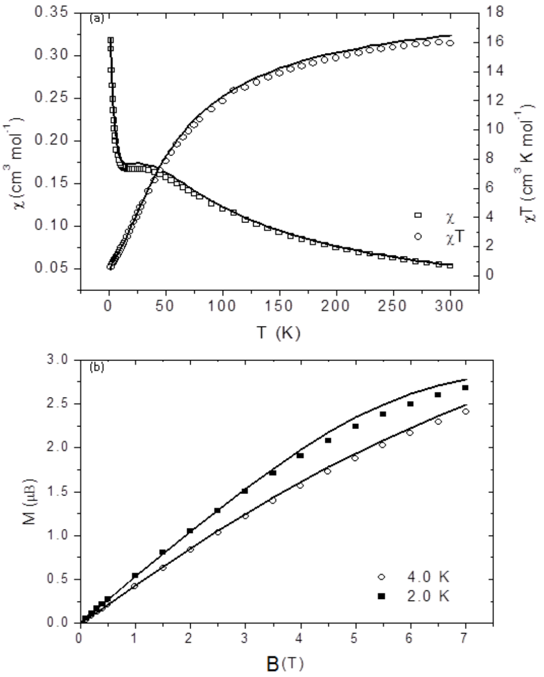

Figure 7.2: Magnetic measurements on polycrystalline samples of Cr_8Mn. (a) χ and χT against T recorded in a 0.1 T applied field. (b) M versus B measured at 2 and 4 K. (Figure used with permission from Ref. [138].)

tween nearest neighbor metal ions within the Cr_8Mn ring, relating to strong correlations between neighboring spins within the cluster.

The exchange parameters used to reproduce magnetization data also allow us to simulate the main INS features. However to obtain the precise position for INS transition **I** and to correctly describe the splitting of transition **II**, an additional exchange parameter needs to be introduced. The simplest choice, which also keeps the overall C_2 symmetry of the Hamiltonian, is to introduce the additional free parameter between Cr ions $\hat{\mathbf{s}}_4$ and $\hat{\mathbf{s}}_5$. Increasing slightly the exchange between these two ions by $J_{4-5}/J_{CrCr} = 1.05$ brings the simulated INS peak **I** into position with the measured results and well reproduces the asymmetry of transition **II**. Since the measured transitions are much broader than expected from the instrument resolution, the width of the peaks (assumed to be Gaussian) has been determined by fitting the experimental data.

The calculated exchange energies of the lowest total spin multiplets of Cr_8Mn and the observed INS transitions are shown in Figure 7.4. As J_{CrCr} is similar to J_{CrMn}, Cr_8Mn is characterized by a low-spin $S = 1/2$ ground doublet due to the competition between exchange interactions in an odd-membered antiferromagnetic ring. We note that the additional J_{4-5} parameter splits the transitions labeled as **IIa** and **IIb**, reproducing the asymmetry in the measured peak.

The broadening of the measured INS peaks (probably due to strain effects originating from disorder in the position of the ions) hinders the determination of the small anisotropy terms of the Hamiltonian. The single ion d_{Cr} and d_{Mn} values for the ax-

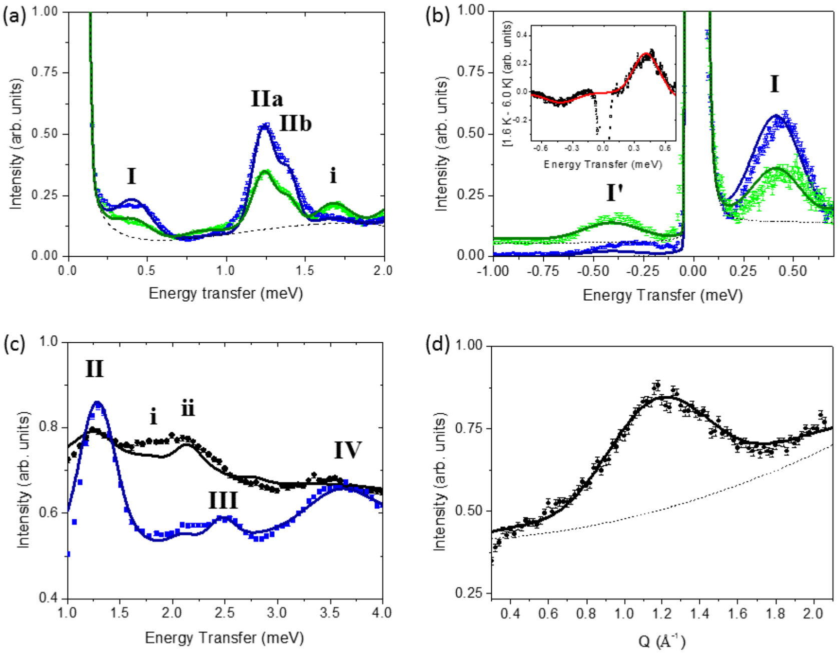

Figure 7.3: INS spectra of Cr$_8$Mn. (a) 5 Å spectra measured at T = 1.5 K (blue squares) and 6.0 K (green circles). (b) 8.0 Å spectra measured at 1.6 (blue squares) and 6.0 K (green circles). The inset shows 6.0 K spectrum subtracted from the 1.6 K spectrum (black squares) with equivalent simulation (solid red line). (c) 3.2 Å spectra at 1.8 K (blue squares) and 15.0 K (black circles). (d) Intensity as a function of the neutron momentum transfer for excitation **II**. Solid lines are simulations based on the Hamiltonian and parameters given in the text; a non-liner background function is represented as a broken line.

ial anisotropy obtained by measurements on similar compounds (e.g., Cr$_8$Zn [116, 102], $d_{Cr} = -28$ μeV and Cr$_7$Mn [83], $d_{Mn} = -3$ μeV) were included within the Hamiltonian and are compatible with the simulation of INS results. The effective ZFS $D_S = \sum_{i=0}^{8} \Gamma_i d_i$ for the lowest spin multiplets in Cr$_8$Mn and Cr$_8$Ni rings compared to their bipartite counterparts [83] (Cr$_7$Mn and Cr$_7$Ni) reflects the non-collinear internal spin structure. In the nine-metal rings the projection coefficients [69], Γ_i, linking single ion terms with the ZFS of low energy spin manifolds, change sign around the ring in contrast to the bipartite case, where sub-lattices align parallel with each other, thus adding constructively. We have calculated D_S for the lowest $S > 1/2$ spin multiplet of some odd- and even-numbered anti-ferromagnetic rings using D_{Cr} and D_{Mn} derived from Cr$_7$Mn [83]. The axial anisotropy calculated for the first excited state of Cr$_8$Mn (characterized by $S = 3/2$) is $D_{S=3/2} = -0.00978$ meV, much smaller than for the related bipartite counterparts Cr$_7$Ni and Cr$_7$Mn, where $D_{S=3/2} = 0.073855$ meV and $D_{S=1} = -0.05962$ meV, respectively. The projection of single ion anisotropies onto the low lying spin states was also found [129] to be very small for Cr$_8$Ni despite the large Ni single ion anisotropy term.

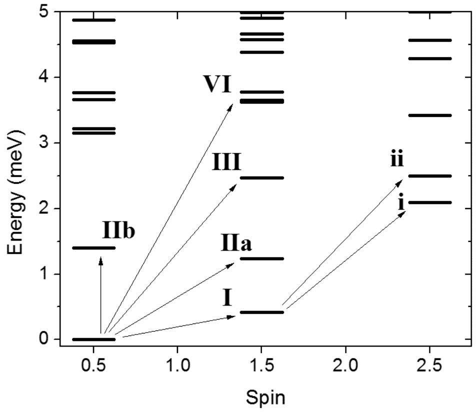

Figure 7.4: Energy levels of Cr_8Mn. Calculated low-lying isotropic exchange energy levels for Cr_8Mn against spin number; arrows label the transitions identified by INS. (Figure used with permission from Ref. [138].)

7.1.3 Spin structure of the ground state

The energy level scheme classifies Cr_8Mn as a frustrated system, according to Schnack's definition. For Cr_8Mn the bridging ligands are chemically equivalent around the ring but the presence of the Mn^{2+} $s = 5/2$ spin breaks the C_9 symmetry, thus leading to an isolated spin multiplet ground state. Since J_{CrCr} and J_{CrMn} are similar in magnitude the isolated spin ground state is characterized by $S = 1/2$. Other regimes of parameters, such as J_{CrMn} significantly less AF than J_{CrCr}, would yield an $S = 5/2$ ground state and consequently to a non-frustrated system.

The microscopic Hamiltonian model describing the spin dynamics of Cr_8Mn was used to investigate the nature of the ground state internal spin structure. Figure 7.5-(a) shows the calculated nearest neighbor spin pair correlations $\langle \hat{\mathbf{s}}_i \cdot \hat{\mathbf{s}}_{i+1} \rangle$. These are stronger amongst the Cr(1)-Mn-Cr(8) unit due to the larger spin moment of Mn^{2+} ($s = 5/2$) with respect to Cr^{3+} ($s = 3/2$). This creates a rigid Cr-Mn-Cr spin unit where the spins are antiparallel that couples to the remaining chain of Cr ions. Consequentially, non-collinearity between the AF coupled spins is distributed around the remaining chain of Cr ions. Spin pair correlations between Mn and the eight Cr ions [Figure 7.5-(b)] further demonstrate this notion: the Mn-Cr(1) and Mn-Cr(8) correlations are large in magnitude, while $\langle \hat{\mathbf{s}}_{Mn} \cdot \hat{\mathbf{s}}_{Cr(4)} \rangle$ and $\langle \hat{\mathbf{s}}_{Mn} \cdot \hat{\mathbf{s}}_{Cr(5)} \rangle$ show expectation values close to zero, indicating a nearly perpendicular arrangement of the spins. Treating the spins as classical vectors (with length $\sqrt{s_i(s_i+1)}$) results in a similar behavior of the correlations with respect to the quantum spin model (red symbols in Figure 7.5). It is interesting to calculate the effect of an applied magnetic field on the ground state (i.e. where B is significant but sufficiently less than the $S = 1/2$ to $S = 3/2$ crossing field). Figure 7.5-(c) shows how an external field breaks the spherical symmetry of the isotropic Hamiltonian: due the larger magnetic moment of Mn^{2+} with respect to the Cr^{3+} ions, the Mn ion tends to align parallel to the field thus producing a node on the opposite side of the ring.

Two views of one of the classical configurations of minimum energy are shown in Figure 7.6-(a,b), for the isotropic Heisenberg Hamiltonian. Due to the rotational invariance, this is only one of the infinite configurations minimizing the classical energy. It is important

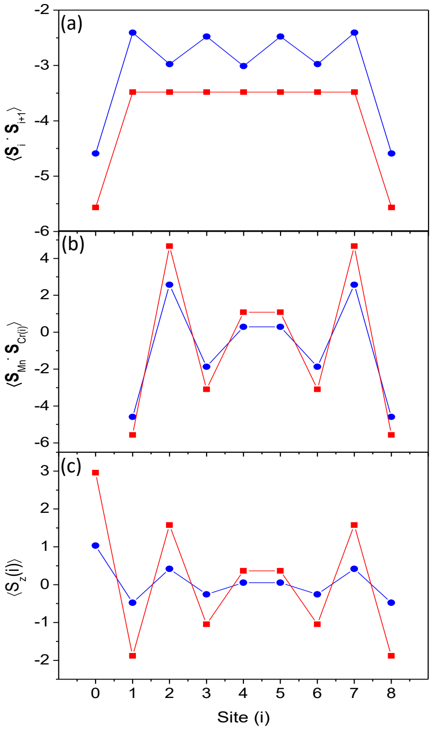

Figure 7.5: Spin pair correlations within the $S = 1/2$ spin ground state based on the exchange term in Hamiltonian 7.1, where Mn is at site $i = 0$ and equivalent to site $i = 9$. (a) Nearest neighbour spin pair correlations around the Cr$_8$Mn ring. (b) Mn-Cr spin pair correlations. The calculations for the quantum (blue circles) and classical (red squares) spin case are similar. (c) The local expectation values of $\hat{s}_{i,z}$ with an applied magnetic field of 0.1 T for each site (i). The Mn ion tends to align parallel with the applied field causing the localisation of a node at the opposite side of the ring at sites i = 4 and 5.

to note that all the classical spin vectors lie on the same plane, i.e. $\chi_{ijk} = \mathbf{s}_i \cdot \mathbf{s}_j \times \mathbf{s}_k = 0 \quad \forall\, i, j, k$. This quantity, known as scalar chirality for the spins ijk, can be interpreted as a measure of the solid angle between the three spins. In order to investigate the planarity of the quantum spin state, we have decomposed the ground state spin wave-function onto the eigenstates of the scalar chirality operator $\hat{\chi} = \sum_i \hat{\mathbf{s}}_i \cdot \hat{\mathbf{s}}_{i+1} \times \hat{\mathbf{s}}_{i+2}$ (usual cyclic boundary conditions are applied). Results are shown in Figure 7.6-(c): similarly to the classical situation, the expectation value $\langle\psi_0|\hat{\chi}|\psi_0\rangle$ vanishes in the ground state doublet. However, the quantum ground state results in an equal superposition of chirality eigenstates with opposite eigenvalues. Hence, the spin configuration in the quantum ground state fluctuates between non-planar states corresponding to opposite eigenvalues of $\hat{\chi}$. Finally, the calculated field dependence of the isotropic exchange energy levels for Cr$_8$Mn is shown in Figure 7.7. The change in the total spin of the ground state (level crossing) occurring at about 3.7 T, predicted by diagonalization of spin Hamiltonian 7.1, was observed by muon spectroscopy [138].

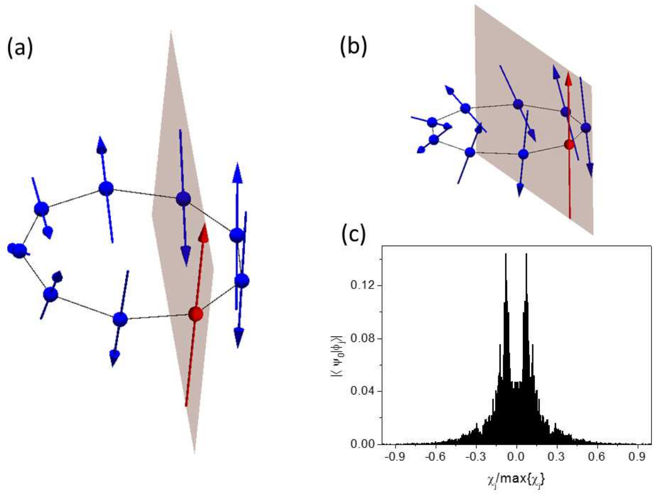

Figure 7.6: Spin structure (a)-(b) Two views of one of the configurations minimizing the energy of the exchange part of the classical version of the Hamiltonian, equation 7.1. The blue and red arrows represent Cr and Mn spins, respectively, with length $\sqrt{s_i(s_i+1)}$. Due to the larger magnetic moment of the Mn ion (red arrow) if compared to the Cr ions, the neighbouring Cr ions are locked in an almost collinear, antiparallel configuration. Moreover, a node is induced on the opposite side of the ring. All the spins belong to the same plane, as can be checked by computing the scalar chirality χ_{ijk} on each set of three spins i, j, k. (c) Decomposition of the spin Hamiltonian ground state $|\psi_0\rangle$ onto the eigenstates $|\phi_j\rangle$ of the chirality operator, $\hat{\chi}|\phi_j\rangle = \chi_j|\phi_j\rangle$. The ground state results in an equal superposition of states with opposite chirality eigenvalues. Hence, in contrast with the classical situation (where the chirality is zero, indicating a planar spin configuration), the ground state fluctuates between states with opposite chirality.

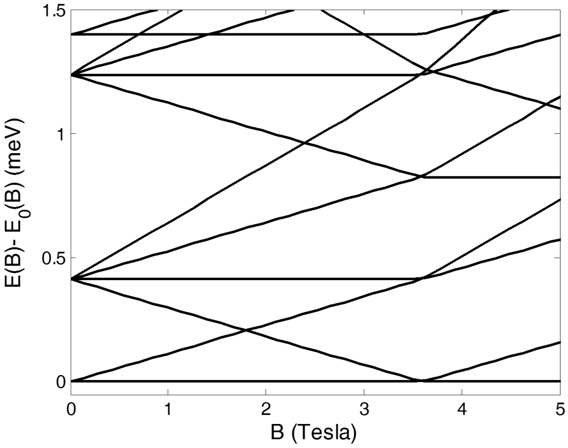

Figure 7.7: Isotropic exchange energy levels vs field for Cr_8Mn. The predicted level crossing at about 3.7 T was observed by muon spectroscopy [138]. (Figure used with permission from Ref. [138].)

7.2 Spin dynamics of homometallic Cr_9 ring

In this section we investigate the spin dynamics of the newly synthesized Cr_9 ring. In particular, we point out that this system exhibits a quasi-frustrated behaviour (according to the strict Kahn classification), displaying a very small gap between the two lowest-lying energy doublets. This is the consequence of its regular structure, close to C_9 symmetry (Figure 7.8). Given this regular structure, we have studied the compound in order to assess to what degrees it shows spin frustration.

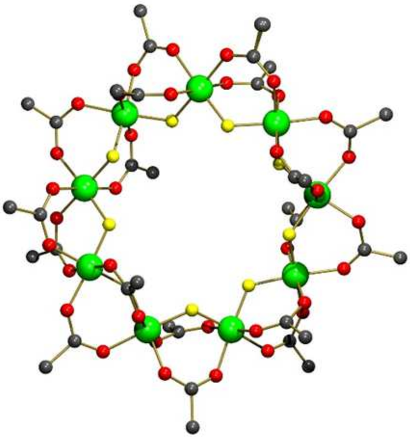

Figure 7.8: Crystal structure of Cr_9 in $P2_1/C$. Cr (green), F (yellow), O (red), C (grey). Pivalate carbons, hydrogen atoms and solvent omitted for clarity.

Magnetic measurements, both variable temperature susceptibility, $\chi(T)$ and variable field magnetisation, $M(B)$, show the expected behaviour for an anti-ferromagnetic exchange between the Cr^{3+} centres, and can be fitted to a Hamiltonian containing a single exchange interaction of 1.35 meV (Figure 7.9). The size of the exchange interaction is slightly smaller than those found in similar Cr based AF rings [28, 83, 116]. These thermodynamic measurements confirm the presence of an $S = 1/2$ ground state and support

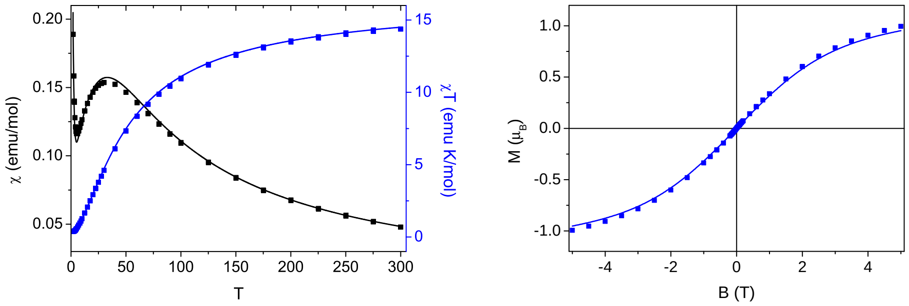

Figure 7.9: Magnetometry of Cr_9. Left: Susceptibility and product of susceptibility by temperature versus temperature. Right: Magnetization against applied magnetic field.

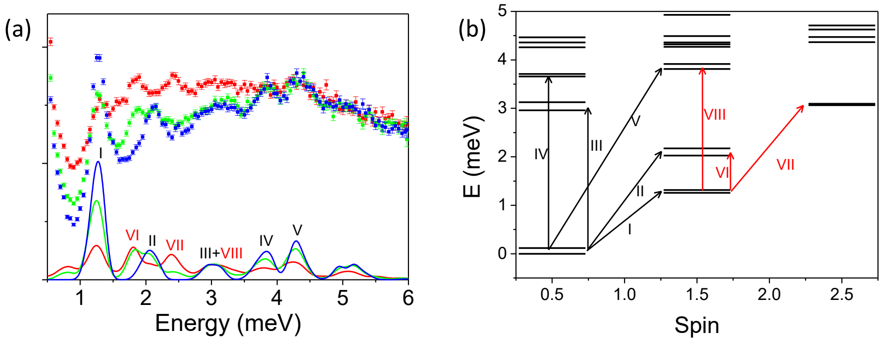

Figure 7.10: Powder INS spectra for Cr_9. (a) Data recorded at 7.4 meV incident neutron energy. Experimental (squares) and simulated (solid lines) spectra shown for 1.5 K (blue), 7 K (green) and 15 K (red) with peaks labelled corresponding to transitions in the diagram below. Background not modeled. (b) Isotropic exchange diagram derived using calculated $J = 1.32$ meV and $J'/J = 1.2$.

the presence of spin frustration, but they are comparatively insensitive with respect to spectroscopic techniques. The presence of an $S = 1/2$ ground state is also demonstrated by EPR measurements performed in Manchester (not reported here).

7.2.1 Inelastic Neutron Scattering

Inelastic neutron scattering is the technique of choice to assess the degree of frustration in this system, because it probes the spin dynamics and it can directly detect the possible splitting of the two ideally degenerate ground doublets. INS data have been collected on Cr_9 with the high-resolution time-of-flight LET spectrometer at ISIS. Figure 7.10 reports the results obtained with 7.4 meV incident neutron energy at 1.5, 7 and 15 K. The dominant peak at low temperature [blue data on Figure 7.10-(a)] corresponds to the transition between the lowest energy $S = 1/2$ and $S = 3/2$ multiplets, labelled transition **I** [Figure 7.10-(b)]. At higher resolution ($\lambda = 2.4$ meV), a splitting of this peak is observed (Figure 7.11), *vide infra*. Higher-energy peaks are observed at all temperatures, corresponding to transitions from the $S = 1/2$ ground state to higher energy excited levels of the $S = 3/2$ and higher $S = 1/2$ states (transitions **II**, **V** and **III**, **IV** respectively). At 15 K (red data in Figure 7.10), hot transitions can be observed due to additional excitations from the lowest energy $S = 3/2$ eigenstate (transitions **VI**, **VII**, **VIII**). The seemingly temperature independent broad peak at 3 meV is due to overlap of two peaks corresponding to one cold and one hot transition (transitions **III**, **VIII**). All these results are well reproduced by a model Hamiltonian displaying perfect C_9 symmetry, thus demonstrating that the spin dynamics of Cr_9 is very close to that of a perfectly frustrated antiferromagnetic ring. To assess quantitatively the real degree of frustration, we have analyzed high resolution ($\lambda = 1$ meV) measurements (Figure 7.11). These measurements revealed a small splitting of 0.1 meV between the two ground $S = 1/2$ doublets (see the inset of Figure 7.11), witnessing a small removal of frustration. Hence, these results demonstrate that the spin dynamics of 7.11 is essentially equal to that of a perfectly frustrated ring, apart from low frequency.

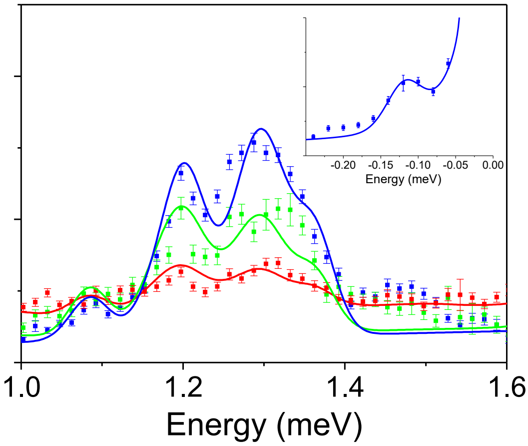

Figure 7.11: High-resolution powder INS spectra for Cr$_9$. INS spectrum of transition **I** at $\lambda = 2.4$ meV. Experimental (squares) and simulated (lines) data at 1.5 (blue), 7 (green) and 15 (red) K are shown. Background correction applied. Inset: Experimental and simulated data for $\lambda = 1$ meV corresponding to the intra-multiplet $S = 1/2$ transition between the two lowest-energy doublets.

The INS data can be well reproduced by using the spin Hamiltonian

$$\hat{H} = J \sum_{i=1}^{8} \hat{\mathbf{s}}_i \cdot \hat{\mathbf{s}}_{i+1} + J' \hat{\mathbf{s}}_9 \cdot \hat{\mathbf{s}}_1 + d \sum_{i=1}^{9} \hat{s}_{zi}^2 + \sum_{i,j>i=1}^{9} \hat{\mathbf{s}}_i \cdot \underline{\mathbf{D}}_{ij} \cdot \hat{\mathbf{s}}_j \tag{7.2}$$

where for simplicity we model the splitting of the lowest-energy doublets by breaking the C$_9$ symmetry of the enneagon on one bond with the introduction of two exchange constants J and J'. Here $\hat{\mathbf{s}}_i$ are spin operators at site i and d is the axial single-ion zero-field-splitting parameter. The last term describes intra-molecular magnetic dipole-dipole interactions, with couplings $\underline{\mathbf{D}}_{ij}$ calculated in the point-dipole approximation (no additional free parameters). We have found $J = 1.32$ meV, $J' = 1.2J = 1.58$ meV and $d = -0.022$ meV. It is worth noting that the average value of the exchange constants is the same found from magnetometry. In addition, this model reproduces the observed splitting of the peak corresponding to transition **I** ($S = 1/2 \rightarrow S = 3/2$, see Figure 7.11), resulting from the combined action of the zero-field splittings and of the slight removal of the ideal C$_9$ symmetry. We evidence a very good agreement between the calculated and measured spectra (Figures 7.10 and 7.11). Figure 7.10-(b) reports the energy-level diagram calculated with the isotropic part of Eq. 7.2. The calculated transitions match the energy and pattern of the observed peaks, further confirming the present model. Finally the dependence of transition **I** on the neutron momentum transfer is reported in Figure 7.12. The good agreement between experimental data and the simulated curve confirms the structure of the involved eigenstates.

7.2.2 Spin Chirality

The internal spin structure of the ground state can be investigated via analysis of the spin chirality. Here we recall two different definitions of spin chirality [139]: the first one

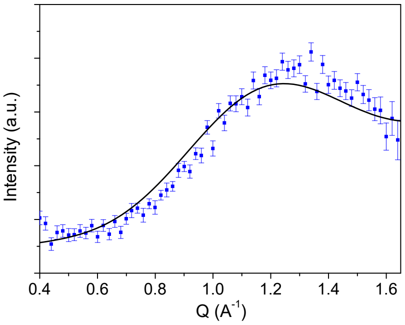

Figure 7.12: Q-dependence powder INS spectra for Cr_9. Intensity as a function of the neutron momentum transfer for excitation **I**, at 7.4 meV incident neutron energy, T = 1.5 K and integrating from 1 to 1.6 meV of transferred energy.

is scalar chirality, already introduced to study Cr_8Mn:

$$\hat{\chi} \equiv \frac{1}{N} \sum_{i=1}^{N} \hat{\mathbf{s}}_i \cdot \hat{\mathbf{s}}_{i+1} \times \hat{\mathbf{s}}_{i+2}, \tag{7.3}$$

where $N + 1 = 1$ and $N + 2 = 2$. As pointed out in Sec. 7.1, this is a measure of the planarity of the spin configuration. Here the operator has been normalized to the number of examined bonds.

The second is vector chirality. This is certainly the most intuitive definition of chirality, since it directly refers to the geometric image of the spin configuration. On a spin wheel, we define it as

$$\hat{\mathbf{K}} \equiv \frac{1}{N} \sum_{i=1}^{N} \hat{\mathbf{s}}_i \times \hat{\mathbf{s}}_{i+1}, \tag{7.4}$$

where we assume $N + 1 = 1$. This quantity indicates the sense of spin rotation when moving on an oriented loop (such as a ring). In a system described by isotropic nearest neighbors exchange interactions, each element of the sum can also be interpreted as a spin current operator flowing from site i to site $i + 1$ [139].

Figure 7.13 shows the decomposition of the ground doublet of Cr_9 ($|\psi_0\rangle$) in terms of the eigenstates of the scalar chirality $|\phi_j\rangle$ and of the z component of the vector chirality, $|\zeta_j\rangle$. On the horizontal axis the corresponding eigenvalues are reported, defined according to $\hat{\chi}|\phi_j\rangle = \chi_j|\phi_j\rangle$ and $\hat{K}_z|\zeta_j\rangle = \kappa_j|\zeta_j\rangle$.

We find that the quantum ground state of Cr_9 reproduces the behaviour of the classical model, showing that the spins are non-collinear but lie in the same plane (indeed $\langle\psi_0|\hat{\chi}|\psi_0\rangle = 0$). However, the quantum ground state results in an equal superposition of chirality eigenstates with opposite eigenvalues. Hence, Cr_9 fluctuates between non-planar states with opposite chirality. This behavior is similar to that of Cr_8Mn, even if here the most regular topology of the exchange interactions leads to narrower peaks in the decomposition of the ground state. In other words, the ground state results in a superposition of fewer values of the chirality, with probability of finding $\chi = 0$ close to zero. This behaviour, however, is not peculiar of odd-membered rings. Indeed, also even AF heterometallic rings (with $S \neq 0$ ground state) can show a fluctuating scalar

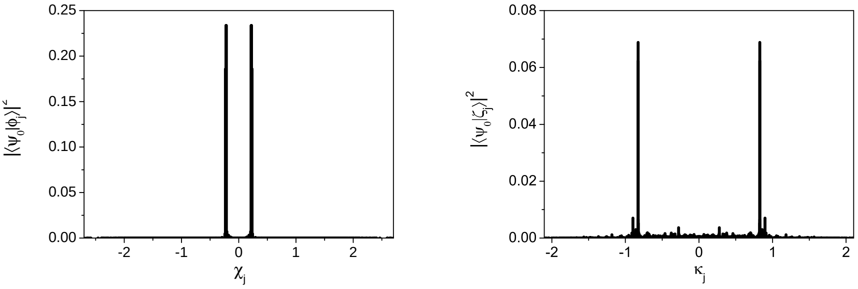

Figure 7.13: Chirality of Cr$_9$. Decomposition of the spin Hamiltonian ground state $|\psi_0\rangle$ onto the eigenstates $|\phi_j\rangle$ of the scalar chirality (left) and $|\zeta_j\rangle$ of the vector chirality (right), defined in the text.

chirality.

What discriminates between even and odd-membered rings is the vector chirality. The calculation of the vector chirality of the ground state is cumbersome, since it requires the diagonalization of huge matrices (for Cr$_9$ the size is above 30000). We calculate here the z component, exploiting the symmetry of the Heisenberg Hamiltonian with respect to $\sum_i \hat{s}_{zi}$ to block-factorize it. By analyzing $\hat{K}_z$ for several even and odd-membered rings (with $N = 3, 4, ..., 9$) consisting of half integer spin ions (S=1/2, 3/2), we have found that the vector chirality has a dominant component with $\kappa = 0$ for even rings (even for those characterized by a ground state with $S \neq 0$, such as Cu$_7$Mn), while it shows 0 expectation value, but components of opposite sign for odd rings. This is the case for both homo- (such as Cu$_9$ or Cr$_9$) and hetero-metallic rings (such as Cu$_8$Cr or Cu$_8$Mn).

7.2.3 Single Crystal maps

We report in Figure 7.14 preliminary results of 4-dimensional INS measurements that we have performed on single-crystals of Cr$_9$ on IN5 spectrometer at ILL, along the lines of Section 2.3.3. Measurements are performed by rotating the sample with respect to the incident neutron beam. An array of position-sensitive detectors is used to assess the number of neutrons scattered at each value of energy and momentum transferred, thus obtaining the full $(\omega, \mathbf{Q})$ dependence of the scattered intensity. Since the sample does not display cylindrical symmetry, the neutron absorption varies as a function of the rotation angle. To account for this self-shielding effect, we have applied a proper correction to the data [140].

The plot represents the intensity map as a function of the components of the transferred momentum lying in the plane of the ring, for the most intense peak at 1.3 meV (reported in Figure 7.11). The data (left panel) are compared to the map calculated (right) with the model inferred from powder measurements. The agreement is good: indeed, the expected modulation of the intensity is found also in the experimental map.

7.3 Conclusions

To sum up, we have used inelastic neutron scattering to probe the spin dynamics of two odd-membered anti-ferromagnetic rings, namely Cr$_9$ and Cr$_8$Mn. These are prototype

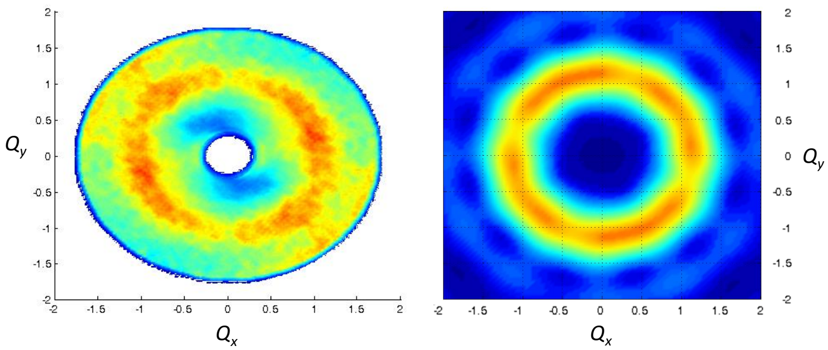

Figure 7.14: Vectorial Q-dependence of INS intensity for a single-crystal of Cr$_9$. The figure compares the measured intensity (left) with that calculated on the basis of spin Hamiltonian 7.2, as a function of the components of **Q** lying in the plane of the ring (right). The maps refer to the peak at 1.3 meV (energy integration range from 1.2 to 1.4 meV).

systems to investigate the effects of frustration. As a result of competing exchange interactions, both of them show a non collinear spin structure for the $S = 1/2$ ground state. In particular, the regular structure of Cr$_9$ leads to a pattern of exchange interactions close to C$_9$ symmetry. This is witnessed by the tiny splitting (1.25 K) of the two lowest energy doublets and results in a dynamics which is essentially the same of an ideally frustrated system for energies above 1 meV.
The ground state of Cr$_9$ is shown to fluctuate between states of opposite scalar and vector chirality. However, the expectation values $\langle\hat{\chi}\rangle$ and $\langle\hat{K}_z\rangle$ are both found to be zero. A state with given vector chirality could emerge as a result of a sizeable Dzyaloshinskii-Moriya interaction, whose study in this kind of AF rings could be of fundamental interest to understand their quantum behavior.

Part of the content of this chapter was published in Chem. Eur. J. **22**, 1779 (2016) (Ref. [138]).

Part II

Hybrid spin-photon qubits

Circuit QED

CHAPTER 8

In this second part we introduce a scheme for quantum information processing and quantum simulation based on a hybrid architecture of spin ensembles (SEs) strongly coupled to single photons within superconducting coplanar waveguide resonators (CWRs). The basic units of this setup are introduced in this chapter, focusing on both the theoretical framework and state-of-the-art technological achievements. Together with SEs and CWRs, we also provide (for completeness) a brief outlook on superconducting qubits. Their role is somehow limited in the present scheme, if compared to more standard cQED implementations. Indeed, they are used only to implement two-qubit gates and not to encode the qubits. In this way, their possibly short coherence time only marginally affects the computation.

8.1 Theoretical background

The formalism developed in this section can be easily understood by exploiting the analogy between superconducting resonators and optical cavities [141]. Indeed, a waveguide resonator containing an artificial atom (such as a superconducting qubit) can be described by using the same formalism employed in quantum optics to model the interaction of an atom with the quantized field in a Fabry-Perot cavity. The cavity mirrors are replaced by capacitors in the waveguide (gaps in the central conductor), while the artificial atom is represented as a parallel capacitor and nonlinear SQUID inductor, forming an anharmonic oscillator. In cavity QED the confinement of the radiation field is exploited to enhance the interaction between atoms and light, which otherwise would be very weak. Analogously, in circuit QED the microwave radiation is very strongly confined in a waveguide, thus making possible to reach the strong coupling between the microwave field and the artificial atom.

8.1.1 Circuit quantization

Circuit QED systems are conveniently designed and described as electric circuits. The Hamiltonian of such circuits can be derived systematically via circuit quantization. This section briefly reviews the general scheme for circuit quantization, discussed in a more systematic and detailed way in Refs. [142, 143, 144].

There are two key types of on-chip electronic components that we can use: *lumped elements* and *distributed elements* [141]. The two types are distinguished by their size, compared to the wavelength of microwave radiation at the relevant frequency. For lumped elements, the size of the component is much smaller than the wavelength, whereas for distributed elements, the size of the component is roughly the same size as the wavelength, or bigger. In lumped elements the field has such a short distance to propagate that it is not necessary to consider how it travels from one place to another. The behaviour of the component is completely defined by currents and voltages. It is the motion of the electrons that carries the signals (the information) and the circuit operates in a way similar to standard electronics. Conversely, in the case of a distributed element, the propagation of the fields from one part of the circuit to another becomes a critical effect. It is now the radiation that carries the signals (the information). Within a quantum circuit, lumped elements are capacitors, inductors, LC resonators, resistors, Josephson junctions, as opposed to distributed elements, such as coplanar waveguides. These can, however, be treated as a continuum limit of lumped elements (see below).

The standard approach to circuit QED is to start from a lumped-element circuit diagram for a non-dissipative circuit and systematically proceed first to the classical Hamiltonian and then to its canonical quantization. Within the lumped element approximation the circuit is described as a network, where nodes are connected by two-terminal circuit components such as capacitors and inductors. Each two-terminal component b is characterized by a voltage $v_b(t)$ across it and a current $i_b(t)$ through it. With the aim of deriving a Hamiltonian description of the circuit, it is more convenient to introduce charges $Q_b(t)$ and fluxes $\Phi_b(t)$ variables, defined as:

$$\begin{aligned} Q_b(t) &= \int_{-\infty}^{t} i_b(t')dt' \\ \Phi_b(t) &= \int_{-\infty}^{t} v_b(t')dt', \end{aligned} \tag{8.1}$$

with $v_b(-\infty) = i_b(-\infty) = 0$. In the following, we will introduce two categories of components, capacitive or inductive type. Any component of a physical circuit can be represented as a combination of these inductors and capacitors. For instance, we can model a physical tunnel junction as a nonlinear inductor (Josephson element) in parallel with a linear capacitor. External voltage and current sources can be represented by very large capacitors or inductors. We are now in a position of proceeding with the introduction of the classical Hamiltonian, according to the following steps:

1. Model the circuit as a network of two-terminal capacitors and inductors and, if possible, simplify the circuit by applying the usual rules for combining linear components in series or parallel.

2. Choose a node of the circuit as ground and describe the other nodes as active.

3. Define a spanning tree T of the network (i.e., a graph without loops including all nodes).

4. For each active node n, introduce a node flux, defined as as the time-integral of the

voltage on the (unique) path on T from that node to ground:

$$\phi_n(t) = \sum_b S_{nb} \int_{-\infty}^{t} v_b(t')dt'. \tag{8.2}$$

$S_{nb} = 0$ if the path on T from ground to n does not pass through b and otherwise $S_{nb} = \pm 1$, depending on the orientation of the path.

5. Express the capacitive contribution T to the energy as a function of the branch voltages, and the inductive contribution V in terms of the branch fluxes.
6. Recast T and V in terms of the node fluxes and their time derivatives.
7. Write the Lagrangian

$$\mathscr{L}(\phi_1, \dot{\phi}_1, ..., \phi_N, \dot{\phi}_N,) = T - V. \tag{8.3}$$

8. Introduce node charges as the conjugate variables of the node fluxes:

$$q_n = \frac{\partial \mathscr{L}}{\partial \dot{\phi}_n}. \tag{8.4}$$

9. Apply a Legendre transform to obtain the Hamiltonian

$$H(\phi_1, q_1, ..., \phi_N, q_N) = \sum_{i=1}^{N} \dot{\phi}_i q_i - \mathscr{L}. \tag{8.5}$$

The quantum Hamiltonian is then obtained by replacinig classical variables with quantum operators obeying the canonical commutation relations:

$$[\hat{\phi}_n, \hat{q}_m] = i\hbar\delta_{mn}. \tag{8.6}$$

8.2 Resonators

8.2.1 Quantum LC oscillator

As a simple, illustrative example of circuit quantization we consider the LC oscillator of Fig. 8.1. Choosing the inductive branch as the spanning tree (in bold in Fig. 8.1), the Lagrangian is:

$$\mathscr{L} = \frac{C\dot{\phi}^2}{2} - \frac{\phi^2}{2L} \tag{8.7}$$

and the corresponding Hamiltonian is that of the harmonic oscillator

$$H = \frac{q^2}{2C} + \frac{\phi^2}{2L}. \tag{8.8}$$

Here we have omitted the index n since the circuit has only one active node. The Hamiltonian may be quantized as follows

$$\hat{H} = \hbar\omega\left(\hat{a}^\dagger\hat{a} + \frac{1}{2}\right) \tag{8.9}$$

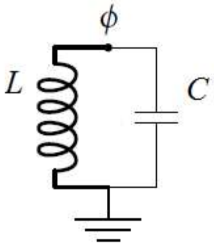

Figure 8.1: Quantum LC oscillator. The spanning tree is chosen to be the inductive branch (bold), while the ground node is set as the bottom node. A single active node (with node flux ϕ) remains [142].

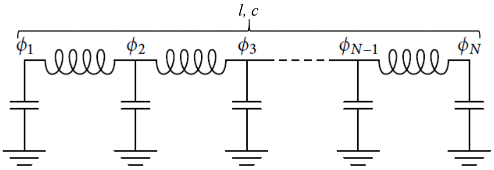

Figure 8.2: Circuit representing a transmission line resonator. The transmission line is modeled as a continuum limit of a chain of LC oscillators [142], with inductance per unit length l and capacitance per unit length c. Here open boundary conditions are applied.

by introducing the creation and annihilation operators:

$$\hat{\phi} = \sqrt{\frac{\hbar Z}{2}}\left(\hat{a}+\hat{a}^\dagger\right) \tag{8.10}$$

$$\hat{q} = -i\sqrt{\frac{\hbar}{2Z}}\left(\hat{a}-\hat{a}^\dagger\right). \tag{8.11}$$

Here $Z=\sqrt{\frac{L}{C}}$, $\omega=\frac{1}{\sqrt{LC}}$ and $\left[\hat{a},\hat{a}^\dagger\right]=1$.

8.2.2 Transmission line

A transmission line can be considered as the continuum limit of a chain of LC oscillators. Let's consider here a transmission line of length d, with capacitance per unit length c and inductance per unit length l. The corresponding circuit is shown in Fig. 8.2. We choose the capacitive branches as the spanning tree and we mark the ground node. If we assume there are no externally-applied magnetic fluxes, the Lagrangian reads

$$\mathscr{L}(\phi_1,\dot{\phi}_1,...,\phi_N,\dot{\phi}_N) = \sum_{i=1}^{N}\frac{\Delta c\dot{\phi}_i^2}{2} - \sum_{i=1}^{N-1}\frac{(\phi_{i+1}-\phi_i)^2}{2\Delta l}, \tag{8.12}$$

where $\Delta = d/N$. In the continuum limit $N\to\infty$ the sum turns into an integral:

$$\mathscr{L}[\phi(x,t),\dot{\phi}(x,t)] = \int_0^d \frac{c\dot{\phi}(x,t)^2}{2} - \frac{1}{2l}\left(\frac{\partial\phi(x,t)}{\partial x}\right)^2 dx. \tag{8.13}$$

We can now derive the corresponding Euler-Lagrange equation of motion for $\phi(x,t)$, given by:

$$\frac{\partial^2 \phi}{\partial x^2} - \frac{1}{v^2}\frac{\partial^2 \phi}{\partial t^2} = 0, \tag{8.14}$$

with $v = 1/\sqrt{lc}$ the wave velocity. Solutions to equation 8.14 are of the form:

$$\phi(x,t) = \sum_{n=1}^{\infty} A_n \cos\,(k_n x + \alpha_n)\,\cos\,(k_n v t + \beta_n), \tag{8.15}$$

where A_n, k_n, α_n and β_n are fixed by the boundary conditions. For the case of open-circuit boundary conditions at $x = 0$ and $x = d$, as shown in the figure, we have

$$\left(\frac{\partial \phi}{\partial x}\right)_{x=0} = \left(\frac{\partial \phi}{\partial x}\right)_{x=d} = 0. \tag{8.16}$$

which gives $\alpha_n = 0$, $k_n = n\pi/d$. (A_n and β_n are determined by the initial conditions). By substituting (8.15) into (8.13) and integrating out the x dependence we get

$$\mathscr{L}(\Phi_1, \dot{\Phi}_1, ..., \Phi_N, \dot{\Phi}_N) = \sum_{i=1}^{N} \frac{C_n \dot{\Phi}_n^2}{2} - \frac{\Phi_n^2}{2L_n}, \tag{8.17}$$

where $\Phi_n(t) = A_n \cos\,(k_n v t + \beta_n)$. Therefore, we end up with an effective Lagrangian for a circuit consisting of uncoupled LC oscillators with effective capacitances $C_n = cd/2$, effective inductances $L_n = 2dl/n^2\pi^2$ and resonant frequencies $\omega_n = nv\pi/d$. Thus, the quantum Hamiltonian for a transmission line cavity is

$$\hat{H} = \hbar \sum_n \omega_n \left(\hat{a}_n^\dagger \hat{a}_n + \frac{1}{2}\right). \tag{8.18}$$

Often we are interested in the behavior of a circuit only in the vicinity of a particular frequency; hence we consider only one mode (usually the fundamental, $n = 1$) and ignore the dynamics of the other modes.

8.2.3 Tunable resonators

Coplanar waveguide resonators can be modeled as transmission lines, according to the formalism developed above. We are particularly interested in resonators whose frequency can be externally tuned.

The resonant frequency of a one-dimensional resonator depends on the boundary conditions [145]. Let's consider a cavity with length d. Then, a quarter-wavelength resonator ($d = \lambda/4$) is obtained by opening one end of the cavity, while connecting the opposite end to the ground. In this way, the spatial distribution of the superconducting phase along the resonator shows a maximum at the open end and a node at the grounded end. The corresponding frequencies of the eigenmodes are $\omega_n = (\pi v/d)(n + 1/2)$, where v is the velocity of the electromagnetic waves in the cavity. Conversely, if the second end is also open, the eigenmode frequencies become $\omega_n = (\pi v/d)n$. Boundary conditions can be varied by properly connecting a dc-SQUID to the resonator, for instance at the right hand ($x = d$). Ideally, by changing the biasing magnetic flux through the SQUID by half a flux quantum, we could sweep the eigenmode frequencies within the interval $(\pi v/d)n \leq \omega_n \leq (\pi v/d)(n + 1/2)$. These two situations correspond to a very large

(formally infinite) Josephson energy of the SQUID (node) and to a Josephson energy approaching zero (antinode). In practice these interval is narrower due to a finite maximum and non-zero minimum energy of the SQUID, as explained below.
The SQUID is formed by two large Josephson junctions and is modeled by the Lagrangian:

$$\mathscr{L}_{SQUID} = \sum_{i=1,2} \left[\frac{\hbar^2 C_s/2}{2(2e)^2} \dot{\phi}_{s,i}^2 + E_{Js,i} \cos \phi_{s,i} \right], \tag{8.19}$$

where $\phi_{s,i}$ are the phases across the junctions and $E_{Js,i}$ are the corresponding Josephson energies. These variables are related by the flux quantization relation, $\phi_{s,1} - \phi_{s,2} = f$, to an external magnetic flux, $\tilde{\Phi} = \Phi_0 / 2\pi f$ threading the loop. Here $\Phi_0 \equiv h/2e$ is the flux quantum. Neglecting the self-inductance of the ring, the SQUID can be described as a single Josephson junction with effective capacitance C_s and flux-dependent Josephson energy [145]

$$E_{Js}(f) = \sqrt{E_{Js,1}^2 + E_{Js,2}^2 + 2E_{Js,1}E_{Js,2} \cos f}.$$

In the phase regime, we can adopt the harmonic approximation and express the SQUID Lagrangian as

$$\mathscr{L}_{SQUID} = \frac{\hbar^2 C_s}{2(2e)^2} \dot{\phi}_s^2 - \frac{E_{Js}(f)}{2} \phi_s^2, \tag{8.20}$$

where $\phi_s = (\phi_{s,1} + \phi_{s,2})/2$ a part from a constant phase shift which can be neglected in case of adiabatic flux variations. The SQUID Josephson energy may be varied between $E_{Js}^{max} = E_{Js,1} + E_{Js,2}$, when $f = 0$ and $E_{Js}^{min} = |E_{Js,1} - E_{Js,2}|$ at $f = \pi$. In case of perfect SQUID symmetry we could obtain $E_{Js}^{min} = 0$.
In the bulk of the cavity, the phase of the resonator obeys Eq. 8.14. The boundary conditions at the cavity open end are expressed by Eq. 8.16, while at the cavity right end we require $\phi(d, t) = \phi_s(t)$. Using the bulk solution for Eq. 8.14, we get the dispersion equation for the cavity eigenmodes [145]:

$$(kd) \tan(kd) = \frac{(2e)^2}{\hbar^2} L_r E_{Js}(f) - \frac{C_s}{C_r} (kd)^2, \tag{8.21}$$

where L_r and C_r are the inductance and the capacitance of the resonator. The solutions to this transcendental equation can be obtained graphically; they form an infinite set of eigenmodes, with frequencies $\omega_k = kv$. The zeros of the function $(kd)\tan(kd)$ correspond to an open right end of the cavity (disconnected SQUID, $kd = n\pi$), while singular points correspond to a closed end (short circuited SQUID, $kd = \pi/2 + n\pi$). These limits can be only achieved by assuming a variation of E_{Js} between ∞ and 0, thus tuning the resonator frequencies between $n\pi/\sqrt{L_r C_r}$ and $(\pi/2 + n\pi)/\sqrt{L_r C_r}$. In practice, this range is limited by the value of the parameter $(2e^2/\hbar^2) L_r E_{Js}(0)$ (which should be chosen large) and the minimum value of $E_{Js}(\pi)$, allowed by the SQUID asymmetry.
In the limit of small detuning, Eq. 8.21 yields, for a given mode, the solution [146]:

$$\omega_r(f) = \frac{\omega_0}{1 + L_s(f)/L_r}. \tag{8.22}$$

Here the SQUID is represented as a lumped element inductor with the tunable inductance $L_s(f) = \Phi_0 / 4\pi I_c |\cos(f/2)|$, and I_c is the critical current of each SQUID junction. Large values of $E_{Js}(0)$ may be accomplished by connecting N SQUIDs into an array, as reported in Refs. [146, 147]. These enter Eq. 8.22 as a series of non-linear inductance

$NL_s(f)$. Here we have described the SQUID in the harmonic approximation. However, the integrated resonator-SQUID system is nonlinear, due to the insertion of Josephson junctions within the SQUID loop. In some cases (at peak currents approaching I_c), nonlinear corrections to the spectrum of the harmonic oscillator induced by the SQUID may be taken into account [145].

8.3 Spin Ensembles

We consider a superconducting resonator containing an ensemble of N non-interacting spins $s = 1/2$, each described by the Pauli spin lowering and raising operators $\hat{\sigma}_j^{\pm}$. We now examine the coupling of the spin ensemble (SE) with a single photonic mode. The interaction of the jth spin, located at $\mathbf{r}_j$, with the cavity mode $\hat{a}$, can be expressed as:

$$\hat{H}_{int,j} = g_j \left(\hat{\sigma}_j^+ + \hat{\sigma}_j^-\right) \left(\hat{a}^\dagger + \hat{a}\right). \tag{8.23}$$

Here $g_j = g_S \mu_B B_0(\mathbf{r}_j)/2$ is the single-spin coupling to the photon, depending on the zero-point magnetic field of the cavity mode $B_0(\mathbf{r}_j)$. Assuming the spin-cavity detuning to be small if compared to the resonator frequency ω_c and to the spin gap, we can apply the rotating-wave approximation, thus reducing the interaction Hamiltonian to

$$\hat{H}_{int} = \sum_{j=1}^{N} g_j \left(\hat{a}\, \hat{\sigma}_j^+ + \hat{a}^\dagger \hat{\sigma}_j^-\right), \tag{8.24}$$

where we have neglected the counter-rotating terms $\hat{a}\, \hat{\sigma}_j^-$ and $\hat{a}^\dagger \hat{\sigma}_j^+$.
Then we introduce the collective spin lowering operator $\hat{b} = \frac{1}{\bar{g}\sqrt{N}} \sum_{j=1}^{N} g_j \hat{\sigma}_j^-$ and its adjoint $\hat{b}_j^\dagger$. We use $\bar{g} \equiv \sqrt{\sum_j |g_j|^2/N}$ to indicate the average single spin-photon coupling strength. In the limit of small number of excitations (i.e. if the sample is strongly polarized), the Holstein-Primakoff approximation holds. Hence, $\hat{b}$ and $\hat{b}^\dagger$ are bosonic operators, obeying the commutation relation $[\hat{b}, \hat{b}^\dagger] = 1$ [148]. Therefore, the collective spin-wave excitation behaves like a harmonic oscillator and H_{int} takes the form:

$$\hat{H}_{int} = \sqrt{N}\bar{g} \left(\hat{a}\, \hat{b}^\dagger + \hat{a}^\dagger \hat{b}\right), \tag{8.25}$$

i.e. the collective interaction between the spin and photon excitations leads to a $\sqrt{N}$ enhancement, relative to the single spin coupling strength. This makes feasible to experimentally reach the *strong coupling regime* between a SE and a micro-wave resonator, i.e. the condition under which the coupling strength exceeds the decay rates of both the resonator and the SE. The lowest two spin oscillator states are $|\psi_0\rangle \equiv |\downarrow_1 \ldots \downarrow_N\rangle$ and $|\psi_1\rangle = \hat{b}^\dagger |\psi_0\rangle = \frac{1}{\bar{g}\sqrt{N}} \sum_{j=1}^{N} g_j\, |\downarrow_1 \ldots \uparrow_j \ldots \downarrow_N\rangle$. These will be employed, together with photons, to encode qubits in our quantum computation scheme.
We note that there are N degenerate levels corresponding to one spin flip, but $|\psi_1\rangle$ is the only one which is coupled to the resonator. The other modes (which, in a regular lattice, would correspond to wave-numbers $k \neq 0$) can be exploited for storing quantum information, for instance by means of the holographic encoding introduced in Ref. [148]. It is important to note that the coupling of $|\psi_1\rangle$ with the other $N-1$ dark modes induces (for large N) an irreversible leakage of the spin excitation, a phenomenon known as inhomogeneous broadening. This unsolved issue will be addressed in detail in Chapter

11. In particular, we will show that by operating the hybrid spin-photon qubits in the so-called *cavity-protected* regime (i.e. with small spin-resonator detunings), quantum information can be processed with coherence times no longer limited by inhomogeneous broadening.

8.4 Superconducting qubits

Harmonic oscillators, whether resulting from spin ensembles or as resonators modes, are the fundamental building blocks of our quantum computation architecture. However, harmonic oscillators are not sufficient for implementing two-qubit gates. Indeed, even if the quantized harmonic oscillator has discrete energy levels, these are uniformly spaced apart. Therefore, we cannot selectively address a specific pair of levels and induce a transition only between them. An artificial atom, such as a superconducting qubit, can provide the necessary anharmonicity. This is obtained by the introduction of a Josephson element into the circuit, which is the only known dissipation-free nonlinear circuit element [143]. There exist various setups which incorporate a junction, leading to different kinds of superconducting qubits, ranging from phase qubits [149], to flux [150, 151] and charge qubits [152]. An overview of these different topologies can be found in Ref. [153]. If the introduced anharmonicity is large enough, each of these units can be described as a two- or three-level system.

Here we provide a detailed description of the charge qubits and then a brief outlook of other superconducting circuits. The charge qubit consists of an LC oscillator (similar to the one of Figure 8.1), in which the linear inductor is replaced by a nonlinear Josephson junction. Depending on the parameters characterizing the systems, different regimes can be identified: one limit is known as the Cooper Pair Box (CPB) regime and shows a large anharmonicity, dominating over all other energy scales. In the other limit, the transmon regime, the anharmonicity is a small perturbation on the harmonic behavior.

8.4.1 Flux quantization and Josephson junctions

The pure quantum behaviour that superconductors show at macroscopic scales is probably what makes them always so fascinating and attractive for the scientific community. The reason of such a macroscopic display of atomic-scale phenomena, as explained elegantly by the theory of Bardeen, Cooper and Schrieffer, is that in a superconductor electron pairs are condensed into a macroscopic wave-function. This leads to two phenomena which are essential for qubits [153].The first is flux quantization. If a closed ring is cooled down below its superconducting transition temperature in presence of a magnetic field which is then switched off, the magnetic flux through the ring - maintained by a circulating supercurrent - is quantized in integer values of $\Phi_0 \equiv h/2e$, the flux quantum. This follows from the requirement that the wave-function be single valued.

The second phenomenon is Josephson tunnelling. A Josephson junction consists of two superconductors separated by an insulating barrier (typically 2-3 nm thick), through which Cooper pairs can tunnel coherently. The supercurrent I through the barrier is related to the gauge-invariant phase difference $\varphi(t)$ between the phases of the two superconductors by

$$I = I_0 \sin\varphi, \tag{8.26}$$

where I_0 is the critical current. The time evolution of this phase difference is described by the equation of motion

$$\dot{\varphi} = \frac{2e}{\hbar}V = \frac{2\pi}{\Phi_0}V, \tag{8.27}$$

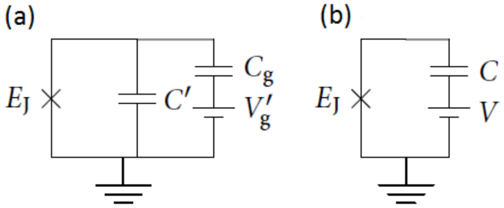

Figure 8.3: Circuit representing a charge qubit. (a) Circuit representing a charge qubit capacitively coupled to a gate voltage [142]. If compared with Fig. 8.1, the linear inductor has been replaced with a Josephson junction with energy E_J. (b) Equivalent circuit, with $C = C_g + C'$ and $V = \frac{C_g}{C_g+C'} V_g$.

where V is the potential difference between the superconductors. If we now take the time derivative of 8.26, we obtain $\dot{I} = I_0 \cos\varphi\,\dot{\varphi} = \frac{2eVI_0}{\hbar}\cos\varphi = \frac{2\pi V I_0}{\Phi_0}\cos\varphi$. A comparison with Faraday's law, $V = -L\dot{I}$, yields

$$|L_j| = \frac{\Phi_0}{2\pi I_0 \cos\varphi} = \frac{\Phi_0}{2\pi\sqrt{I_0^2 - I^2}} \quad \text{(where } I < I_0\text{)}. \tag{8.28}$$

Hence, the Josephson junction is a dissipationless device with a nonlinear inductance. It also has an intrinsic capacitance C. We note that the junction behaves as a nonlinear oscillator with a resonant angular frequency $\omega_P(I) = 1/\sqrt{LC} = \sqrt{2\pi\sqrt{I_0^2 - I^2}/C\Phi_0}$. For $I < I_0$ the system can be described as a particle in a potential well [153]. Classically, it oscillates at the plasma oscillation frequency $\omega_P(I)$. In the quantum picture, the energy in the well is quantized and the particle can tunnel across the barrier. Both the level quantization and the occurrence of quantum tunnelling of the junction were detected as a clear signature of the quantum behaviour of the system. It is worth noting that the nonlinearity of the Josephson inductance leads to an anharmonic spacing of the energy levels within the well. If the well were harmonic, the energy spacings would be identical, and we would not be able to distinguish the quantum case from the classical one.
This means, in turn, that the variables, that have been so far regarded as classical, should be replaced by operators. The two relevant operators are that corresponding to φ, associated with the Josephson coupling energy, and that for the Cooper-pair number difference across the capacitance, related to the charging energy. Below we will show how these canonically conjugate operators may be quantized.

8.4.2 Charge qubits

Charge qubits are *islands*, i.e. pieces of superconductor with only capacitors and Josephson junctions connecting them to the rest of the circuit, without any d.c. connection. Hence, it is meaningful to speak about the number of Cooper-pairs which have tunneled to the island.
As explained above, the Josephson junction is described as a nonlinear inductor. The corresponding (inductive) contribution to the energy is $-E_J \cos\hat{\varphi}$. This potential term of the Hamiltonian is periodic in the flux due to the discreteness of Cooper pair charges. E_J is an intrinsic property of the junction, depending on the superconducting gap and on the barrier transparency. The dimensionless gauge invariant phase is defined as $\hat{\varphi} = 2\pi\hat{\phi}/\Phi_0$

and sets the energy scale of the nonlinearity. $\hat{\varphi}$ is the quantum operator directly corresponding to the phase difference across the junction (see previous paragraph). If we also introduce the number operator $\hat{n} = -\hat{q}/2e$, which counts how many Cooper-pairs have crossed the junction, and the charging energy $E_C = q^2/2C$, the Hamiltonian can be written in the form:

$$\hat{H} = 4E_C(\hat{n} - n_g)^2 - E_J \cos\hat{\varphi}. \tag{8.29}$$

We have also included an effective offset charge n_g, which is necessary to take explicitly into account a gate electrode with a d.c. bias voltage, connected to the charge qubit as shown in Fig. 8.3. The discrete eigenvalues of the number operator $\hat{n}$ correspond to the number of Cooper-pairs that have crossed the junction and the corresponding wave-function is periodic in the flux operator $\hat{\varphi}$. Consequently, the commutation relation between the conjugate variables $\hat{n}$ and $\hat{\varphi}$ can be written as $\left[e^{i\hat{\varphi}}, \hat{n}\right] = -e^{i\hat{\varphi}}$. Hamiltonian 8.29 can be diagonalized analytically and the eigenvalues may be written as:

$$\epsilon_m(n_g) = E_C a_{2[n_g + K(m,n_g)]}\left(-E_J/2E_C\right), \tag{8.30}$$

where $a_\mu(p)$ denotes Mathieu's characteristic value and $K(m, n_g)$ is an integer-valued function which orders the eigenvalues [44]. However, in view of doing numerical calculations, it is more convenient to rewrite the Hamiltonian 8.29 on the charge basis $\{|n\rangle\}$:

$$H = 4E_C \sum_{n=-N}^{N} (n - n_g)^2 |n\rangle\langle n| - E_J \sum_{n=-N}^{N-1} \left(|n+1\rangle\langle n| + |n\rangle\langle n+1|\right). \tag{8.31}$$

This expression makes evident that the Josephson (off-diagonal) term describes the tunneling of the Cooper-pairs. The number of states to be retained depends on the specific problem and on the ratio E_J/E_C.

The first proposed superconducting qubits were Cooper-pair-boxes, corresponding to a regime in which $E_J/E_C \sim 1$ [43]. In that case, the eigenvalues are approximately quadratic with n_g, except in the vicinity of the level crossing, were a gap of the order of E_J opens. This leads to very high anharmonicity, but also to remarkable charge fluctuations, which induce decoherence. This harmful effect can be reduced by operating in proximity of the so-called *sweet-spots* or charge-degeneracy points (corresponding to $n_g = 1/2$), where $\partial\epsilon_m/\partial n_g = 0$. The transmon qubit was introduced to completely avoid the problem [44], by working in a regime in which $E_J/E_C \gg 1$, i.e. using a much larger capacitor. In that case charge fluctuations are suppressed (see charge dispersion in Figure 8.4). The asymptotic behaviour of the Mathieu's functions for $E_J/E_C \gg 1$ leads to

$$\epsilon_m(1/2) - \epsilon_m(0) \approx (-1)^m E_C \frac{2^{4m+5}}{m!}\sqrt{\frac{2}{\pi}}\left(\frac{E_J}{2E_C}\right)^{\frac{m}{2}+\frac{3}{4}} e^{-\sqrt{8E_J/E_C}}. \tag{8.32}$$

It is important to note that charge dispersion $\epsilon_m(1/2) - \epsilon_m(0)$ decreases exponentially with $\sqrt{E_J/E_C}$. This impressive gain in the insensitivity to charge noise yields a loss of anharmonicity. We stress that sufficient anharmonicity is required by any quantum computation architecture to selectively address the desired transitions. The absolute and relative anharmonicity may be computed by means of perturbation theory, in the limit of large E_J/E_C [44]. In that case we can expand the cosine in series of small angles $\hat{\varphi}$ and neglect the periodic boundary conditions. Then the Hamiltonian reduces to a perturbed harmonic oscillator:

$$\hat{H}_{tr} = \sqrt{8E_C E_J}\left(\hat{\alpha}^\dagger\hat{\alpha} + \frac{1}{2}\right) - E_J - \frac{E_C}{12}\left(\hat{\alpha} + \hat{\alpha}^\dagger\right)^4, \tag{8.33}$$

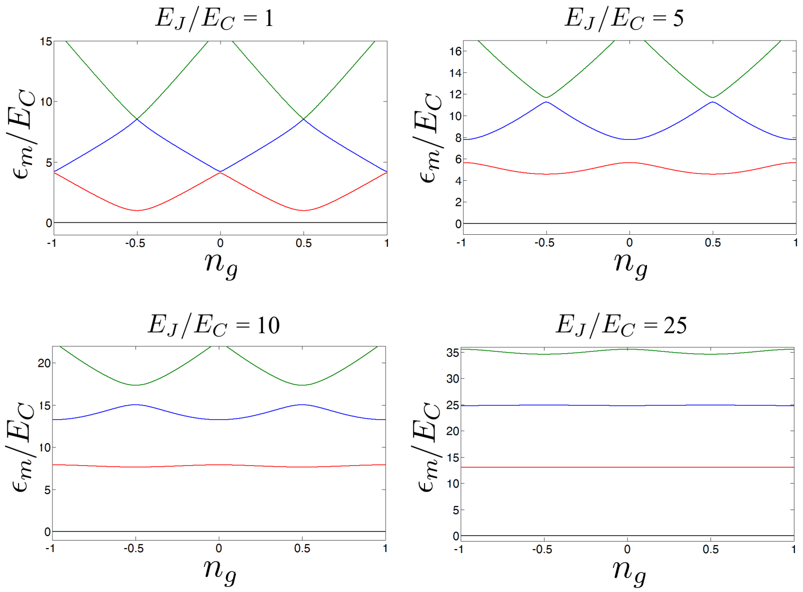

Figure 8.4: Charge dispersion. Dependence of the charge-qubit eigenvalues on the gate voltage n_g (charge dispersion). For each value of n_g, the ground state energy has been set to zero. Different panels refer to different values of the E_J/E_C ratio. The Cooper-pair box regime corresponds to $E_J/E_C \sim 1$ and leads to high anharmonicity, but also large charge fluctuation. In the opposite situation $E_J \gg E_C$ (transmon regime) charge fluctuations are drastically reduced.

where $\hat{\alpha}$ and $\hat{\alpha}^\dagger$ denote the regular annihilation and creation operators for the harmonic oscillator approximating the transmon; the quartic perturbation describes the leading order anharmonicity and we have fixed $n_g = 1/2$ (charge degeneracy point). This leads to a first order correction to the harmonic levels of the form

$$E_l^{(1)} = -\frac{E_C}{12} \langle l| \left(\hat{\alpha} + \hat{\alpha}^\dagger\right)^4 |l\rangle = -\frac{E_C}{4} \left(2l^2 + 2l + 1\right), \tag{8.34}$$

where $|l\rangle$ are the harmonic oscillator eigenstates and the perturbation introduces a mixing of $|l\rangle$ with $|l \pm 2\rangle$ and $|l \pm 4\rangle$. The resulting asymptotic relative anharmonicity is $\frac{E_1 - E_0}{E_0} \simeq -\sqrt{\frac{E_C}{8E_J}}$, from which we see that the exponential gain in charge noise was paid with the small price of a power-law decrease of anharmonicity. This allows us to find an optimal working point for the superconducting device, in a regime of E_J/E_C which ensures both reasonably long coherence times and sufficient anharmonicity. The Cooper pair number operator can be expressed (for large E_J/E_C) as $\hat{n} = \frac{-i}{\sqrt{2}} \left(\frac{E_J}{8E_C}\right)^{\frac{1}{4}} \left(\hat{\alpha} - \hat{\alpha}^\dagger\right)$.

8.4.3 Coupling to the resonator

The charge qubit can be embedded within a superconducting transmission line resonator. The derivation of the interaction Hamiltonian may be obtained following the full network analysis reported in Ref. [44]. A simplified scheme to model the coupling of the transmon with a CWR (as well as to a gate voltage and to an external magnetic

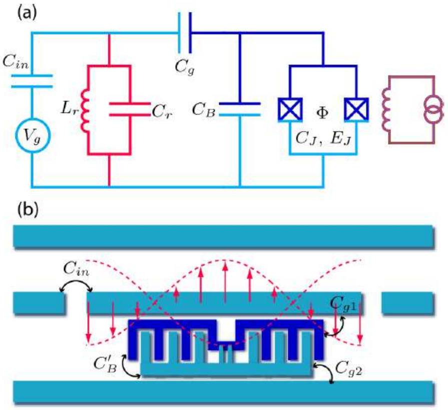

Figure 8.5: (a) Effective circuit diagram of the transmon qubit, consisting of two Josephson junctions (with capacitance C_J and energy E_J). The qubit is coupled to a coplanar waveguide resonator (red), connected to a gate voltage V_g, and to an external inductance (violet). It is also shunted by an additional capacitance C_B. (b) Simplified scheme of the transmon embedded in a coplanar resonator, whose second harmonic is represented by a dashed line. (Figure used with permission from Ref. [44].)

flux) is sketched in Fig. 8.5. In order to maximize the coupling, the transmon should be placed in correspondence to a voltage antinode, as shown in the picture for the coupling to the second harmonic of the resonator. As explained in Sec. 8.2, the resonator is described as a quantum LC oscillator. In the realistic limit of large resonator capacitance $C_r \gg C_\Sigma$ (here C_Σ is the total capacitance of the circuit), the interaction is modeled by the quantum Hamiltonian:

$$\hat{H}_{int} = 2\beta e V^0_{rms} \hat{n} \left(\hat{a} + \hat{a}^\dagger\right) = \hbar \sum_{i,j} g_{i,j} |i\rangle\langle j| \left(\hat{a} + \hat{a}^\dagger\right), \tag{8.35}$$

where $\beta = C_g/C_\Sigma$, $V^0_{rms} = \sqrt{\hbar\omega_r/2C_r}$ is the root mean square voltage of the local oscillator and $\omega_r = 1/\sqrt{L_r C_r}$ denotes the resonator frequency. The last equality is obtained by rewriting the Hamiltonian on the basis of the uncoupled transmon states $|i\rangle$, with $\hbar g_{i,j} = 2\beta e V^0_{rms} \langle i|\hat{n}|j\rangle$. Recalling the expression deduced for the number operator in the asymptotic limit $E_J \gg E_C$, we find that the only non-zero matrix elements are between states $|j\rangle$ and $|j \pm 1\rangle$:

$$|\langle j+1|\hat{n}|j\rangle| \approx \sqrt{\frac{j+1}{2}} \left(\frac{E_J}{8E_C}\right)^{1/4}. \tag{8.36}$$

The couplings $g_{i,i+k}$ with $k > 1$ decay upon increasing E_J/E_C. Interestingly, due to the quartic form of the leading anharmonic perturbation 8.33, matrix elements between states with an even difference k fall off exponentially, while those with an odd k exhibit a power-law decay. Finally, by exploiting the rotating-wave approximation to eliminate counter-rotating terms, we get the effective generalized Jaynes-Cummings Hamiltonian:

$$\hat{H}_{JC} = \sum_j \hbar\Omega_j |j\rangle\langle j| + \hbar\omega_r \hat{a}^\dagger\hat{a} + \hbar \sum_i g_{i,i+1} \left(|i\rangle\langle i+1|\hat{a}^\dagger + |i+1\rangle\langle i|\hat{a}\right). \tag{8.37}$$

It is worth noting that the parameters β and E_J/E_C can be separately tuned, thus allowing the experimenter to control both the coupling strength and the transition frequencies.

8.4.4 Dispersive limit

Coherent control and readout of superconducting charge qubits can be achieved in the dispersive limit, as shown in milestone works [37, 38]. Even if our novel scheme operates in the resonant rather than in the dispersive regime, it is worth mentioning this established approach. In the limit of large qubit-resonator detuning $|\delta| = |\omega_r - \Omega_1| \gg g_{01}$, the Hamiltonian can be recast in the form [37]:

$$\hat{H}_{disp} \approx \hbar \left[\omega_r + \frac{g_{01}^2}{\delta}\hat{\sigma}_z\right] \hat{a}^\dagger \hat{a} + \frac{\hbar}{2}\left[\Omega_1 + \frac{g_{01}^2}{\delta}\right]\hat{\sigma}_z, \tag{8.38}$$

where we have eliminated the interaction term from the generalized Jaynes-Cummings model 8.37, expanding to lowest order in g_{01}/δ. Here $\hat{\sigma}_z = |0\rangle\langle 0| - |1\rangle\langle 1|$ is the usual Pauli matrix and Ω_1 is the gap between the two lowest levels of the superconducting qubits. On the one hand, this expression points out an ac Stark shift of the qubit frequency operated by the cavity, by an amount $(n + 1/2)g_{01}^2/\delta$ (n being the number of photons). On the other hand, we can interpret it as dispersive shift of the cavity transition by $\hat{\sigma}_z g_{01}^2/\delta$.

Operating in the dispersive regime can be very useful for non-demolition readout of both the qubit and resonator state. Specifically, the readout proceeds by irradiating the cavity by means of a microwave field close to its resonance frequency. Depending on its state, the qubit dispersively shifts the resonator frequency. Consequently, a measurement of the phase or amplitude of the transmitted field is sufficient to infer the state of the qubit [37]. Similarly, if the resonator is initialized with at most a single photon, we can induce the resonant absorption of the photon by an auxiliary charge qubit. Then one reads the state of the qubit as outlined above and infers whether there was a photon in the resonator or not.

8.4.5 Flux and phase qubits

A flux qubit is a superconducting loop interrupted by one [150] or three Josephson junctions [154]. The loop is threaded by an externally applied magnetic flux, close to $\Phi_0/2$. Varying the flux bias controls the energy level separation of this effectively two-level system. At half a flux quantum, the two lowest states are symmetric and antisymmetric superpositions of two classical states with clockwise and anticlockwise circulating currents. The qubit can be engineered such that the two lowest eigenstates are energetically well separated from the higher ones [151]. For a detailed theoretical description of the circuit modeling a flux qubit, see Ref. [155]. Flux qubits operate at E_J/E_C ratios similar to those of the transmon, i.e., $E_J/E_C \sim 10^2$. Accordingly, flux qubits reach an insensitivity to charge noise comparable to that of the transmon. However, they will typically show a significantly larger susceptibility to flux noise. Remarkably, flux qubits can be directly coupled to magnetic moments through the field induced by the supercurrents in the loop [156].

Even larger E_J/E_C ratios characterize phase qubits, which usually operate in a regime $E_J/E_C \sim 10^4$. They consist of a single current-biased Josephson junction [149]. Phase qubits trade in a slight increase in critical-current noise sensitivity for a drastic suppression of charge noise.

8.5 State of the art technology

8.5.1 Superconducting resonators

Microwave superconducting resonators can be broadly classified into *coplanar* and *microstrips*. They are both planar devices characterized by a layered structure, differing for the geometry of the pattern. A substrate of one or more dielectric materials (Silicon, Silicon Oxide, Alumina, Sapphire, Magnesium Oxide), typically 0.1-1 mm thick, is grown on a ground plane. Over the substrate a superconducting layer is patterned, usually by lithographic techniques. Its typical thickness goes from hundred of nanometers to few microns.

In microstrip lines a conducting strip is placed on the top of the dielectric substrate. Conversely, coplanar geometry consists of a central conducting strip with two ground planes on the sides, separated from the strip by a small gap (see Figure 9.1 below). To confine the electromagnetic fields the line needs then to be cut along the propagation direction, thus inducing the partial reflection of the signal and giving rise to standing waves. Additional transmission lines (launchers) are used for input-output, separated from the resonator by a small gap. Different realizable dimensions, approximately going from microns to millimeters, allow us to work with different frequencies, ranging from hundred of Megahertz to tens of Gigahertz.

The propagation of electromagnetic waves within resonators can be studied in detail by solving the Maxwell equations with the proper boundary conditions. This allows us to design resonators operating at the desired frequency and with tailored configuration of the fields. In particular, in order to maximize the magnetic coupling with spin ensembles, the magnetic field generated near the line edges should be enhanced. This can be done by fabricating narrow constrictions [157]. Superconducting circuits with dimensions well below 100 nm can be fabricated, and even repaired, by either etching with a focused ion beam or by using the same ion beam to induce the growth of a superconducting material from a gas precursor.

The resonator quality factor is defined as:

$$Q \equiv \frac{\omega_r}{\Delta\omega}, \tag{8.39}$$

where $\Delta\omega$ is the half-power bandwidth, i.e. the bandwidth over which the power of vibration is greater than half the power at the resonant frequency. The Q factor determines the cavity performance, being inversely proportional to the damping rate of the photons stored within the resonator. Hence, achieving high Q values is crucial to reduce photon loss, an essential requisite of the here proposed quantum computation scheme. The intrinsic resonator quality factor is mainly limited by insertion losses, which occur at the capacitive coupling gaps of the resonators (coming from fringing fields of the electromagnetic radiation inside the gap region) and radiative losses, which interest the top face of the resonator, exposed to the surrounding medium and crossed by currents. Generally microstrip devices are more affected by radiation losses because of the lacking of lateral ground planes that force the field lines close to them. Conductors losses are suppressed by using superconducting devices, while any coupling to external lines has the effect of reducing the intrinsic (unloaded) quality factor. Great improvements in increasing Q has led to the realization of superconducting Nb-based resonators with quality factors as high as 10^7 [158]. Experimentally, the resonator frequencies have already been shown to be variable on a nanosecond time scale [159, 160], and up to tenths of the fundamental-mode frequency [147, 161]. In addition, resonators can be assembled in a series of lumped elements, realizing large arrays of different geometries: more than 200 superconducting resonators were recently fabricated on a single chip [40].

Finally, a particularly promising class of microwave resonators has been recently put forward, consisting of coplanar devices made of layered $YBa_2Cu_3O_7$ [162]. Thanks to its high critical temperature and nearly insensitivity to external magnetic fields up to 7 T, this setup could be coupled with many different spin systems, whose transition frequencies can be tuned by applying high magnetic fields at will.

8.5.2 Superconducting qubits

We briefly discuss some specific physical implementations of the superconducting qubits described above. For a more detailed overview, we refer to [153, 163] and references therein. The Hamiltonian of these systems can be properly designed. By varying the E_J/E_C ratio we can obtain devices operating in different regimes, from Cooper-pair boxes to transmon, flux and phase qubits. Strong coupling (with coupling constants in the 100-300 MHz range) of charge qubits with single photons within superconducting resonators has been demonstrated for the first time in [38]. Single-qubit rotations are usually obtained by irradiating the qubit with classical microwave fields [37], while the dispersive coupling of a pair of qubits, mediated by the cavity bus, was achieved, e.g., in [41]. Another scheme, based on the proposal of Ref. [164], uses the avoided crossing between $|11\rangle$ and $|02\rangle$ states to implement a controlled-Z gate, as demonstrated, for instance, in [165]. A different, semiresonant approach for implementing high-fidelity controlled-Z gates was introduced in [42], and then improved with novel devices, consisting of linear arrays of cross-shaped transmons [166]. The idea is to exploit the third level of the transmon to obtain a conditional excitation of the $|11\rangle$ component of the two-qubit wave-function, by absorbing-emitting a photon.

Almost all Josephson junctions for superconducting qubits are fabricated using an insulating tunnel barrier between superconducting electrodes. Recently, a ”gatemon” device was proposed, based on a semiconductor tunnel barrier, which enables an electrostatic control of the Josephson energy via a gate voltage [167].

To date, the best transmon qubits are three-dimensional systems showing coherence times of the order of tens of μs [168, 169]. These are properly designed to minimize dissipation coming from the dielectrics surrounding the metal of the qubit, and to minimize radiation of energy into other electromagnetic modes or the circuit environment. Important progresses have also been realized in the readout of the qubit state. In this respect, a particularly useful and powerful technique is the so called “quantum non-demolition” measurement. This has been applied, e.g., in Ref. [170], to perform transmission measurements on a cavity, dispersively coupled to a 3D transmon. The shift of the cavity frequency allows the non-demolition read out of the qubit-state. The fidelity of the measurement also benefits from the improved coherence times of the qubits. However, even though important advances have been made to increase the coherence times of superconducting qubits, other physical systems, such as spin ensembles (SEs), would provide much more stability. Indeed, the implementation of complex quantum algorithms, as well as quantum error correction schemes, requires long-lived qubits, which can undertake long sequences of gates. This motivates our current research, aiming to find more robust architectures for quantum information processing, as illustrated in the following chapters.

Quantum Information Processing with Hybrid Spin Photon Qubit encoding

Chapter 9

We introduce here a scheme to perform quantum-information processing that is based on a hybrid dual-rail spin-photon qubit encoding [171]. The proposed qubits consist of spin-ensembles coherently coupled to microwave photons in coplanar waveguide resonators. Single- and two-qubit quantum gates are performed solely by shifting the resonance frequencies of the resonators on a ns timescale. An additional cavity containing a transmon is exploited as an auxiliary degree of freedom to implement two-qubit gates. The generality of the scheme allows its potential implementation with a wide class of spin systems.
We estimate the quantum-gate fidelity by simulating the driven dynamics through a master-equation approach [172]. High values of the fidelity can be achieved even in the presence of the main decoherence sources, namely, cavity-photon loss, and pure dephasing of the superconductive elements that are involved in the two-qubit gates. This result allows one to envision the scalability of such elements to a quantum-computing architecture made of an array of hybrid spin-photon qubits. Analogous results are obtained for a simpler, nonscalable setup, which we propose here in order to simplify the realization of the first proof-of-principle experiments.

9.1 Introduction

A classical computer is made of a variety of physical components specialized for different tasks. In the same way, a quantum computer will probably be a hybrid device exploiting the best characteristics of distinct physical systems. In this spirit, much work has recently been done to achieve strong coupling of high-quality factor coplanar-waveguide resonators with superconducting artificial atoms, such as Cooper-pair boxes (CPBs) [38, 41, 43] and transmons [44] and/or spin ensembles (SEs) [45, 46]. While a single CPB can be strongly coupled to the quantized cavity field by electric-dipole interaction, the coupling of a single spin with the microwave photons stored inside the

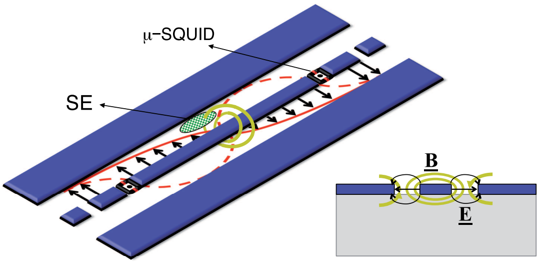

Figure 9.1: Sketch of a tunable coplanar superconducting resonator. The effective resonator length can be tuned by inductively coupled micro-SQUIDs. The fundamental (third) harmonic of the resonator is schematically shown with a solid (dashed) line. The cavity-SE coupling is maximized at the magnetic field antinodes (rotational lines). Inset: cross-section of the resonator on an insulating substrate. (Figure used with permission from Ref. [171].)

resonator is due to magnetic-dipole interaction and is much weaker. However, strong coupling is possible by means of SEs: in such case the spin-cavity coupling is enhanced by a $\sqrt{N}$ factor, where N is the total number of spins (see Sec. 8.3). Megahertz interaction strengths have been achieved either with N substitution (NV-) centers in diamond [45] or Cr^{3+} spins in Al_2O_3 [46].

Superconducting qubits coupled to a microwave cavity field were proposed for quantum information processing (QIP) [152, 164, 165], using classical fields [152] or external voltages [173] as a manipulation tool. The strong anharmonicity provided by these artificial atoms allows one to control the number of photonic excitations introduced in the resonator. However, the coherence time of such superconducting qubits is still a limiting factor. To this aim, during the last years several theoretical works have considered the possibility of joining the fast processing of superconducting qubits to the long coherence times of SEs [174, 175, 176, 148, 177], which can be naturally exploited as quantum memories. Cavity photons can be used as a bus to transfer the quantum state from superconducting qubits to spin ensembles, and to couple distant superconducting qubits, leading to an effective interaction necessary to perform two-qubit gates [145]. Recently, it has been theoretically shown that a minimal architecture solely based on SEs can be exploited for full QIP [178], by employing a measurement-based scheme in which photons are still used as a quantum bus.

Here we introduce a qualitatively different approach based on a hybrid spin-photon encoding of the qubits. Our scheme differs from previous ones because the spin and photon degrees of freedom enter on an equal footing in the definition of the qubit. A charge qubit is exploited as a nonlinear element which effectively couples each pair of neighboring qubits. This allows us to to perform all the manipulations simply by tuning the resonance frequencies of coplanar superconducting resonators (Fig. 9.1), coupled to SEs and to the charge qubit. As illustrated in Sec. 8.5, $Q \sim 10^6 - 10^7$ have been experimentally demonstrated [158], while the resonator frequencies have already been shown to be variable on a ns timescale [160], and up to tenths of the fundamental-mode frequency ω_c^0 [147, 161]. Besides, they can be assembled in large arrays [40]. Such capabilities, along with the possibility of individually addressing the resonators, represents a prerequisite for scalability. As to the spins, the few requisites of the scheme can be fulfilled by a large variety of systems, ranging from diluted transition-metal or rare-earth ions to molecular nanomagnets [20]. In our hybrid encoding, each physical qubit is represented by a resonator mode and a SE. We describe the quantum gates in the elementary unit of a

scalable setup, namely two resonators containing different SEs, where each qubit is encoded in the state of a distinct SE-resonator pair.
In order to assess the feasibility of the proposed approach in relation to the state-of-the art technology, it is important to gain a quantitative understanding of the main decoherence processes and of their effect on the quantum gates. Hence, we report a detailed study on the effects of relaxation and dephasing on the system dynamics, by simulating the quantum gates within a master equation formalism. Such decoherence channels are considered for each element involved in the quantum computation, namely photons, SEs and charge qubit. We find that the most important source of errors is given by photon loss. However, for reasonably high (but technologically achievable) values of the quality factor ($Q \approx 10^5 - 10^6$), one can reach high values of the quantum-gate fidelity ($> 95\%$).

9.2 Hybrid spin-photon qubit encoding

We consider a resonant cavity containing a single photon in a mode of frequency ω_c, and an ensemble of N identical and non-interacting spins $1/2$, initially prepared in the ground state $|\psi_0\rangle \equiv |\downarrow_1 \ldots \downarrow_N\rangle$. The spins can be initialized in the state $|\psi_0\rangle$, e.g., by cooling them down in a static magnetic field. If the resonator mode is tuned to match the gap of the two-level system, ω_1, after some time the SE will collectively absorb the photon and evolve into the state $|\psi_1\rangle = \frac{1}{\sqrt{N}} \sum_{q=1}^{N} |\downarrow_1 \ldots \uparrow_q \ldots \downarrow_N\rangle$. We note that $|\psi_1\rangle$ is the only mode strongly coupled to the cavity among the N degenerate levels corresponding to one spin-flip. The explicit form assumed here for $|\psi_1\rangle$ implies that all the spins have the same coupling to the corresponding photonic mode. However, the precise form of $|\psi_1\rangle$ is not important for the feasibility of the scheme, provided that the corresponding transition is strongly coupled to the resonant cavity mode. The generalized expression for $|\psi_1\rangle$ can be found for instance in Ref. [179]. Transitions between $|\psi_0\rangle$ and $|\psi_1\rangle$ are described by $\hat{b}_1 = \frac{1}{\sqrt{N}} \sum_{q=1,N} |\downarrow\rangle\langle\uparrow|_q$ and $\hat{b}_1^\dagger$ [45, 148]. In the low-excitation regime, the collective excitations of the SE can be described as a harmonic oscillator and $[\hat{b}_1, \hat{b}_1^\dagger] = 1$ (see Sec. 8.3).
Within the single-excitation subspace of the system formed by a resonator mode and a SE, we introduce the hybrid encoding of the qubit μ:

$$\begin{aligned} |0\rangle_\mu &\equiv \hat{b}_\mu^\dagger |\emptyset\rangle = |\psi_1^\mu, n_\mu = 0\rangle, \\ |1\rangle_\mu &\equiv \hat{a}_\mu^\dagger |\emptyset\rangle = |\psi_0^\mu, n_\mu = 1\rangle, \end{aligned} \tag{9.1}$$

where $\hat{a}_\mu^\dagger$ is the photon creation operator, n_μ is the photon occupation number of the cavity mode coupled with the SE and $|\emptyset\rangle = |\psi_0, n_\mu = 0\rangle$ is the vacuum state. Thus, the logical state of the qubit depends on whether the excitation is stored within the spin ensemble or in the quantized electromagnetic field of the resonator.

9.3 Description of the scalable setup

To achieve universal QIP it is sufficient to perform a two-qubit quantum gate such as the controlled$-Z$ (CZ), and arbitrary single-qubit rotations around two non-parallel axes (see Sec. 0.1). Hereafter, we describe our scheme for the quantum-gate implementation in the basic unit of a scalable setup, i.e., a system of two qubits ($\mu = \mathcal{A}, \mathcal{A}'$), encoded in the hybrid states of two distinguishable SEs coupled to the modes of two different coplanar resonators, as in Fig. 9.2-(a). In its general form, the scheme can be implemented within any bipartite lattice of cavities [180]. Both SEs consist of effective $s = 1/2$

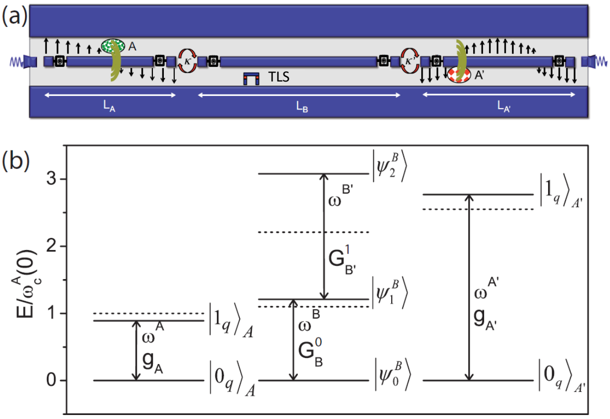

Figure 9.2: (a) Representation of an elementary unit of the scalable setup. (b) Level diagram (solid line) of the two spin systems used to define the qubits and of the interposed charge qubit (TLS), which is used to implement CZ gates. The individual spin-photon coupling strengths are indicated as g_γ, corresponding to transition frequency ω^γ between single-spin states $|0_q\rangle_\gamma$ and $|1_q\rangle_\gamma$ ($\gamma = A, A'$). The TLS-cavity couplings are indicated with capital letters. Dashed lines represent the idle frequencies of the cavity modes.

spins, but with different energy gaps: ω^A is coupled to the harmonic of frequency ω_c^A in the cavity of $\mathcal{A}$, while $\omega^{A'}$ to the harmonic of frequency $\omega_c^{A'}$ in the cavity of $\mathcal{A}'$, as in the level scheme of Fig. 9.2-(b). A third unit $\mathcal{B}$, which is not used to encode qubits, is located in between the qubits $\mathcal{A}$ and $\mathcal{A}'$. It includes a resonator coupled to a nonlinear element, such as a charge qubit, which we exploit to implement CZ [181]. For reasonable values of the Josephson and charge energies [38] the charge qubit (see Section 8.4) is characterized by the anharmonic spectrum reported in the central part of Fig. 9.2-(b). Hereafter we consider only the three lowest levels of the charge qubit and label it as TLS (three-level system). We stress that the transmon is not used to encode the qubits, and is left in its ground state always but during the implementation of the two-qubit gates. In the cavity of $\mathcal{B}$ we consider two different harmonics, ω_c^B and $\omega_c^{B'}$, respectively close to the gaps Ω^B and $\Omega^{B'}$ of the TLS. In the idle configuration, the cavity modes $A - B$ and $B' - A'$ are detuned and qubits encoded in different cavities evolve independently from one another. Hence, single-qubit rotations can be implemented by varying the resonance frequency of the relevant resonator, while the TLS is left in its ground state and no photons are present in resonator $\mathcal{B}$. The interaction between neighboring qubits is switched on when the two cavities $\mathcal{A}$ and $\mathcal{A}'$ are brought into resonance with $\mathcal{B}$ and photons can jump from cavities $\mathcal{A}$ and $\mathcal{A}'$ to $\mathcal{B}$. As explained below, CZ gates can be obtained by exploiting a two-step Rabi oscillation of the TLS between its ground state $|\psi_0^B\rangle$ and the excited state $|\psi_2^B\rangle$ [Fig. 9.3-(b)]. A three-level superconducting system was exploited for performing CZ gates in a different scheme in [42].

The total Hamiltonian of the system reads:

$$\hat{H} = \hat{H}_{spin} + \hat{H}_{TLS} + \hat{H}_{ph} + \hat{H}_{int} + \hat{H}_{hop} \, . \tag{9.2}$$

The first term describes the SEs of the qubits $\mathcal{A}$ and $\mathcal{A}'$, as independent harmonic oscillators [160] ($\hbar \equiv 1$):

$$\hat{H}_{spin} = \omega^A \hat{b}_A^\dagger \hat{b}_A + \omega^{A'} \hat{b}_{A'}^\dagger \hat{b}_{A'} \, . \tag{9.3}$$

As stated above, the charge qubit is treated as an effective three-level system (TLS). Indeed, we consider the superconducting qubit at the charge degeneracy point, in a regime $E_J \approx 6E_C$. Within this range of parameters, the spectrum is highly anharmonic. Hence, we can safely truncate the Hilbert space to the three lowest levels. Its Hamiltonian is given by:

$$\hat{H}_{TLS} = \Omega^B|\psi_1^B\rangle\langle\psi_1^B| + (\Omega^{B'} + \Omega^B)|\psi_2^B\rangle\langle\psi_2^B|. \tag{9.4}$$

The time-dependent photonic term is entirely responsible for the manipulation of the qubits. It can be expressed as:

$$\hat{H}_{ph} = \sum_{\gamma=A,A',B,B'} \omega_c^\gamma(t)\hat{a}_\gamma^\dagger\hat{a}_\gamma\,, \tag{9.5}$$

where $\omega_c^\gamma(t) = \omega_c^\gamma(0) + \Delta_c^\gamma(t)$. Hereafter, we will use the interaction picture, with $\hat{H}_0 = \hat{H}_{spin} + \hat{H}_{TLS} + \hat{H}_{ph}(t=0)$. Hence, within the rotating-wave approximation the spin-photon and TLS-photon coupling Hamiltonians take the form:

$$\begin{aligned}\hat{H}_{int} &= G_B\left[\hat{a}_B^\dagger|\psi_0^B\rangle\langle\psi_1^B|e^{i(\omega_c^B-\Omega^B)t} + \text{h.c.}\right]\\ &+ G_{B'}\left[\hat{a}_{B'}^\dagger|\psi_1^B\rangle\langle\psi_2^B|e^{i(\omega_c^{B'}-\Omega^{B'})t} + \text{h.c.}\right]\\ &+ \sum_{\gamma=A,A'}\bar{G}_\gamma\left[\hat{a}_\gamma^\dagger\hat{b}_\gamma e^{i(\omega_c^\gamma-\omega^\gamma)t} + \text{h.c.}\right].\end{aligned} \tag{9.6}$$

Here, the coupling constants $\bar{G}_\gamma$ are enhanced by a factor $\sqrt{N}$ with respect to their single-spin counterparts (see Sec. 8.3).

Finally, the last term in Eq. 9.2 describes the photon-hopping processes induced by the capacitive coupling between the modes A and B (A' and B') of the neighboring cavities [182]:

$$\begin{aligned}\hat{H}_{ph-ph} = &-\kappa\hat{a}_A^\dagger\hat{a}_B e^{i(\omega_c^A-\omega_c^B)t}\\ &-\kappa'\hat{a}_{A'}^\dagger\hat{a}_{B'}e^{i(\omega_c^{A'}-\omega_c^{B'})t} + \text{h.c.}.\end{aligned} \tag{9.7}$$

By properly engineering the two different cavities, the coupling between other modes can be easily made negligible.

9.4 Quantum gates

In order to perform one- and two-qubit gates, we exploit the absorption (emission) of the photons entering the hybrid encoding (Eq. 9.1). These processes can be straightforwardly controlled by tuning the frequencies of the cavity modes by a quantity Δ_c^γ for suitable time intervals. We will refer to such variations of the resonator frequencies as *shift pulses*. In order to make the manipulation experimentally easier, we choose [see Fig. 9.2-(b)] $\omega_c^B(0)$ to be intermediate between $\omega_c^A(0)$ and Ω^B, while $\omega_c^{A'}(0)$ is close to $\omega_c^{B'}(0)$, and $\omega_c^{B'}(0)$ is close to $\Omega^{B'}$.

9.4.1 Single-qubit rotations

In the idle configuration $\Delta_c^\gamma(t) = 0$, the resonator frequencies are significantly detuned from the spin energy gaps ($|\omega_c^\gamma(0) - \omega^\gamma| \gg \bar{G}_\gamma$) and $\hat{H}_{int}$ is ineffective. In addition, the

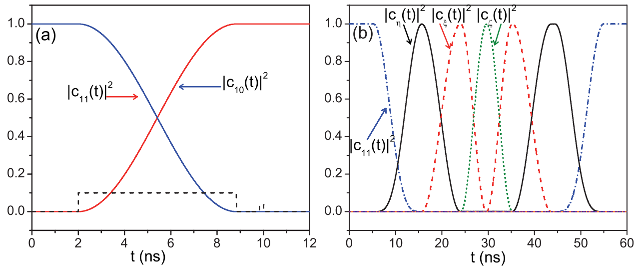

Figure 9.3: Single- and two-qubit gates. (a) Calculated time-dependence of the components of $|\psi(t)\rangle$ in a single-qubit rotation $R_x(\pi)$. Dashed black lines represent $\Delta_c^\gamma(t)/\omega_c^\gamma(0)$. Negligible components are not shown. (b) Time-dependence of the main components of $|\psi(t)\rangle$ in a CZ gate. Auxiliary states $|\eta\rangle_{AA'}$, $|\xi\rangle_{AA'}$ and $|\zeta\rangle_{AA'}$ are described in Eq. 9.13. (Figure used with permission from Ref. [171].)

cavity modes A and A' are far-detuned from B and B' ($|\omega_c^A - \omega_c^B| \gg \kappa, |\omega_c^{A'} - \omega_c^{B'}| \gg \kappa'$) and the effect of inter-cavity coupling is negligible. Hence, single-qubit gates can be performed independently on each qubit.

In particular, off-resonance pulses are employed to obtain a rotation by an arbitrary angle about the z axis of the Bloch sphere. These induce a phase difference between the $|0\rangle_\mu$ and $|1\rangle_\mu$ states of the hybrid qubits (Eq. 9.1). We assume for simplicity step-like pulses, $\Delta_c^\gamma(t) \equiv \delta_c^\gamma\, \theta(\tau/2 - |t - t_0 - \tau/2|)$, so that a generic phase shift $\hat{R}_\varphi$ is performed, with $\varphi = -\delta_c^\gamma \tau$. In the basis $\{|0\rangle_\mu, |1\rangle_\mu\}$, such rotation takes the form:

$$R_{\varphi=\delta_c^\gamma \tau} = \begin{pmatrix} 1 & 0 \\ 0 & e^{-i\delta_c^\gamma \tau} \end{pmatrix}. \tag{9.8}$$

This coincides with a rotation around the z axis up to an overall phase, being $\hat{R}_z(\varphi) = e^{-i\hat{\sigma}_z\varphi/2} = e^{-i\varphi/2}\hat{R}_\varphi$ and $\sigma_{\alpha=x,y,z}$ the Pauli matrices. Conversely, rotations $\hat{R}_x(\varphi)$ about the x axis (see Eq. 0.2), are obtained by resonant processes in which the frequency of the cavity mode is tuned to match the corresponding energy gap of the SE ($\delta_c^\gamma = \omega^\gamma - \omega_c^\gamma(0)$, with $\gamma = A, A'$) for the proper amount of time, $\tau = \varphi/2\bar{G}_\gamma$. The time evolution of qubit μ in the resonant regime can be determined analytically. We start from the following single-qubit Hamiltonian:

$$\begin{aligned} \hat{H}_\mu &= \omega^\mu \hat{b}_\mu^\dagger \hat{b}_\mu + \omega_c^\mu \hat{a}_\mu^\dagger \hat{a}_\mu \\ &+ \bar{G}_\mu[\hat{a}_\mu^\dagger \hat{b}_\mu e^{i(\omega_c^\mu - \omega^\mu)t} + \hat{a}_\mu \hat{b}_\mu^\dagger e^{-i(\omega_c^\mu - \omega^\mu)t}], \end{aligned} \tag{9.9}$$

in which we take into account only the relevant interactions involving qubit μ, neglecting photon hopping terms. Then we set $\delta_c^\mu = \omega^\mu - \omega_c^\mu$ and we determine analytically the time evolution of a state initialized (in interaction picture) in a general superposition $\alpha|0\rangle_\mu + \beta|1\rangle_\mu$ of the single-qubit basis. At $t = 0$ the cavity is largely detuned ($\delta_c^\mu \gg \bar{G}_\mu$) from the spin gap and the resonance condition $\omega^\mu = \omega_c^\mu$ is established at $t = t_0$. As the Hamiltonian conserves the total number N_{ex} of excitations, we can reduce to the subspace $N_{ex} = 1$, where

$$H_\mu = \begin{pmatrix} \omega^\mu & \bar{G}_\mu \\ \bar{G}_\mu & \omega^\mu \end{pmatrix}. \tag{9.10}$$

The single-qubit evolution (in interaction picture) is expressed by the following unitary matrix

$$U_1 = \begin{pmatrix} \cos(\bar{G}_\gamma \tau) & -i\, e^{-i\delta_c^\gamma t} \sin(\bar{G}_\gamma \tau) \\ -ie^{i\delta_c^\gamma t_0} \sin(\bar{G}_\gamma \tau) & e^{-i\delta_c^\gamma (t-t_0)} \cos(\bar{G}_\gamma \tau) \end{pmatrix} \qquad (9.11)$$

where $\tau = t - t_0$. By comparing Eq. (0.2) and (9.11), we note that the additional phase $\varphi = -\delta_c^\gamma \tau$ of the $|1\rangle_\mu$ qubit state is straightforwardly corrected by an $\hat{R}_{-\varphi}$ rotation. Furthermore, in order to obtain a rotation about the x axis of the Bloch sphere, we need to choose t_0 as an integer multiple of $2\pi/\delta_c^\gamma$. This auxiliary degree of freedom can be exploited to obtain a rotation about an arbitrary axis in the xy plane. In fact, by applying $\hat{R}_{-\varphi}$ and then U_1, we obtain the unitary matrix:

$$U_2 = \begin{pmatrix} \cos(\bar{G}_\gamma \tau) & -i\, e^{-i\delta_c^\gamma t_0} \sin(\bar{G}_\gamma \tau) \\ -ie^{i\delta_c^\gamma t_0} \sin(\bar{G}_\gamma \tau) & \cos(\bar{G}_\gamma \tau) \end{pmatrix}, \qquad (9.12)$$

which has the form of a general rotation about an axis $\mathbf{n} = (n_x, n_y, 0)$, see Eq. 0.6.
A simulation of the $\hat{R}_x(\pi)$ gate is reported in Fig. 9.3-(a) in terms of the overlaps $c_{ij}(t) = \langle i_A j_{A'} | \psi(t) \rangle$ between the system state $|\psi(t)\rangle$ and the logical two-qubits states $|i_A j_{A'}\rangle = |i_A\rangle \otimes |j_{A'}\rangle$ $(i, j = 0, 1)$.

9.4.2 Controlled-Z gate

The implementation of two-qubit gates requires the coupling between the degrees of freedom that are used to encode the two qubits. The CZ gate is performed with a two-step Rabi oscillation of the TLS between $|\psi_0^B\rangle$ and $|\psi_2^B\rangle$ accompanied by the absorption and emission of the two photons entering the definition of the two qubits. A multi-step pulse sequence is adopted, involving the auxiliary states

$$\begin{aligned} |\eta\rangle &= |\emptyset\rangle \otimes |\psi_0^B, n_B = 1, n_{B'} = 1\rangle, \\ |\xi\rangle &= |\emptyset\rangle \otimes |\psi_1^B, n_B = 0, n_{B'} = 1\rangle, \\ |\zeta\rangle &= |\emptyset\rangle \otimes |\psi_2^B, n_B = 0, n_{B'} = 0\rangle, \end{aligned} \qquad (9.13)$$

where $|\emptyset\rangle = \otimes_{\mu = A, A'} |\psi_0^\mu, n_\mu = 0\rangle$ is the vacuum state of the two-qubit register. We schematically explain the effect of such sequence on two qubits initialized in state $|1_\mathcal{A} 1_{\mathcal{A}'}\rangle$:

1. The first step corresponds to the hopping of the photons from the modes A and A' into the cavity modes B and B' of the unit $\mathcal{B}$, by means of two simultaneous π-pulses that bring the two pairs of modes into resonance. This induces the transition $|1_\mathcal{A} 1_{\mathcal{A}'}\rangle \longrightarrow |\eta\rangle$.

2. As a second step, the photon of frequency ω_c^B is tuned to Ω^B by means of a π-pulse, which transfers the excitation from the mode B to the intermediate level $|\psi_1^B\rangle$ of the TLS, carrying the system into the state $|\xi\rangle$.

3. Then, a 2π-pulse brings the mode of frequency $\omega_c^{B'}$ into resonance with $\Omega^{B'}$, thus inducing a complete Rabi flopping between the states $|\xi\rangle$ and $|\zeta\rangle$. In this process, a phase π is added to $|\xi\rangle$.

4. Finally, the repetition of the first two steps brings the state back to $|1_\mathcal{A} 1_{\mathcal{A}'}\rangle$, with an overall phase π. By properly setting the delay of the two π pulses corresponding to the previous steps (or by performing single-qubit phase shifts), the associated absorption and emission processes yield a zero additional phase.

Conversely, the other basis states don't acquire any phase, as required for the CZ gate. In fact, the basis state $|0_{\mathcal{A}}1_{\mathcal{A}'}\rangle$ has only the high-energy photon which is driven to mode B', but is off-resonance with the Ω^B gap, and hence is not absorbed. Instead, $|1_{\mathcal{A}}0_{\mathcal{A}'}\rangle$ contains only the low-energy photon, which is absorbed by the TLS, bringing it to the first excited state $|\psi_1^B\rangle$. However, the following Rabi flop doesn't occur, due to the absence of the higher-energy photon. Finally, the state $|0_{\mathcal{A}}0_{\mathcal{A}'}\rangle$ is completely unaffected by the pulse sequence, because of the absence of both photons.

The same analysis carried on for single-qubit rotations in the previous subsection holds also for two-qubit gates. Indeed, each pair of states involved in the resonant processes exploited to obtain CZ evolves according to Eq. 9.11, with the only difference that in 2π processes the choice of t_0 is not relevant. In this way additional trivial phases acquired during 2π photon-hopping processes or during the second step of the evolution described here can be straightforwardly eliminated by short $\hat{R}_z$ operations as in the implementation of $\hat{R}_x$.

The time evolution of the two-qubit state $|\psi(t)\rangle$ (initialized in $|11\rangle$) induced by this pulse sequence is reported in Fig. 9.3-(b). These simulations have been performed by assuming fundamental frequencies $\omega_c^A(0)/2\pi = 22$, $\omega_c^{A'}(0)/2\pi = 21$ and $\omega_c^B(0)/2\pi = 12.5$ GHz [46], and using the first and second harmonic (second and third harmonics) for the $\mathcal{A}$ and $\mathcal{A}'$ ($\mathcal{B}$) cavities. With this choice, photon hopping between modes other than those included in Eq. 9.7 is negligible. We find remarkably high fidelities ($\mathcal{F}$) for both single qubit rotations and controlled-Z, above 99.9%, for initial states belonging to the computational basis and also corresponding to linear superpositions of the basis states. Even larger values of $\mathcal{F}$ can be obtained by using larger frequencies or larger detunings.

The frequency is varied up to $\pm 0.1\ \omega_c^0$ for the fundamental harmonic, and proportionally for the others. Similar detunings have been experimentally shown in Ref. [147]. We have assumed realistic values of the TLS-cavity $G_\gamma^j/2\pi = 30 - 45$ MHz and SE-cavity coupling rates $\bar{G}_\gamma/2\pi = 30$ MHz, corresponding to $N \sim 10^{12}$ spins [45], and tunneling rate $\kappa/2\pi = 25$ MHz, which has already been shown experimentally [182]. Larger values of G_γ and κ would reduce the gating times, but would also increase the fidelity-loss, unless compensated by larger detunings.

9.5 Effect of decoherence

The interaction of the system with the environment tends to introduce errors in the implemented quantum gates. Hereafter, we introduce the formalism that will be employed to simulate the dynamics in an open-system scenario, in order to assess the robustness of the present scheme with respect to the relevant decoherence sources [172].

9.5.1 Master equation approach

The time evolution of the system density matrix $\hat{\rho}$ is described within a Markovian approximation and a Lindblad-type dynamics (see Appendix E), with the Liouville-von Neumann equation of motion:

$$\frac{d}{dt}\hat{\rho} = -i\left[\hat{H},\hat{\rho}\right] + \sum_j \Gamma_j \mathcal{D}_{\hat{x}_j}[\hat{\rho}] + \sum_j \gamma_j \mathcal{D}_{\hat{x}_j^\dagger \hat{x}_j}[\hat{\rho}], \tag{9.14}$$

being Γ_j and γ_j respectively the damping and pure-dephasing rates of the field $\hat{x}_j$. The dissipator term for an arbitrary operator, $\hat{x}$, is given by

$$\mathcal{D}_{\hat{x}}[\hat{\rho}] = -\frac{1}{2}\left(\hat{x}^\dagger \hat{x}\hat{\rho} + \hat{\rho}\hat{x}^\dagger \hat{x}\right) + \hat{x}\hat{\rho}\hat{x}^\dagger. \tag{9.15}$$

The density matrix approach followed in the present work allows us to include the effects of relaxation and pure dephasing on each element involved in the scheme. If the operator $\hat{x}_i$ destroys an excitation in the system, terms like $\mathcal{D}_{\hat{x}_i}[\hat{\rho}]$ account for energy losses, while pure dephasing processes are described by $\mathcal{D}_{\hat{x}_i^\dagger \hat{x}_i}[\hat{\rho}]$. We note that the former ones provide the most important contribution for photons [183] (with $\hat{x}_j = \hat{a}_j$, $j = A, A'$), while the latter ones are dominant for the TLS operating in between the CPB and transmon regime ($\hat{x}_j = |\psi_j^B\rangle\langle\psi_{j+1}^B|$, $j = 0, 1$) [1]. Hence, we initially study the fidelity of the quantum gates as a function of the photon loss rate and the TLS pure dephasing rate. We then include two further sources of errors. The first one is represented by energy losses from the superconducting nonlinear element, which however is not expected to appreciably alter the gate fidelity, being the loss rate usually smaller than the pure dephasing rate. The second one is given by the pure dephasing of the spin-ensemble, whose effect on the system dynamics is similarly small.

For the simulations, we represent each field as a matrix in the Fock-states basis, and truncate it at a number of total excitations previously checked for convergence. The total Hamiltonian, Eq. 9.2, and the density matrix master equation of the whole system, Eq. 9.14, are built by tensor products of these operators. Then, the equation of motion for $\hat{\rho}$ is numerically integrated, in the interaction picture, by using a standard Runge-Kutta approximation.

9.5.2 Numerical results

In order to investigate the effects of decoherence on quantum-information processing, the numerical simulation of single- and two-qubit gates reported above has been reproduced by using the master equation formalism outlined above. Since the time required to implement the two-qubit CZ gate is much longer than that corresponding to the single-qubit rotations, this gate is the most error-prone. Therefore, we consider CZ as a test bed for the robustness of our quantum-information processing scheme. As a figure of merit for the CZ (0.1.4), we compute its fidelity $\mathcal{F} = \sqrt{\langle\psi|\hat{\rho}|\psi\rangle}$, where $\hat{\rho}$ is the final density matrix and $|\psi\rangle$ the target state.

First, we investigate the effects of photon leakage and pure dephasing of the TLS. For each cavity mode, we have assumed a photon-leakage rate that is proportional to the relative mode-frequency, $\Gamma_i = \omega_c^i/Q$, while the quality factor is the same for all the relevant cavity modes [184]. Furthermore, we notice that the same dephasing rate has also been assumed for the two Lindblad operators, $\hat{x}_j^\dagger \hat{x}_j = |\psi_{j+1}^B\rangle\langle\psi_{j+1}^B|$ ($j = 0, 1$), acting on the two relevant TLS transitions, without loss of generality. Figure 9.4-(a) reports the fidelity as a function of the resonators quality factor Q. Different curves refer to different values of the TLS dephasing time $T_2^{TLS} = 1/\gamma_{TLS}$, chosen in a realistic range. In particular, the lower bound of $T_2^{TLS} = 0.1$ μs is typical of charge qubits, in the regime $E_C \geq E_J$ [185]. Dephasing times of the order of $T_2^{TLS} = 10$ μs have already been demonstrated experimentally [153] for charge qubits in the transmonic regime $E_J \approx 10\ E_C$, which is close to the range of parameters we are exploring ($E_J \approx 6\ E_C$). With such values of T_2^{TLS} and with Q approaching 10^6, we obtain a fidelity above 99%. In Fig. 9.4-(b) the fidelity is

---

[1] All the calculations reported in this chapter consider $E_J/E_C \approx 6$.

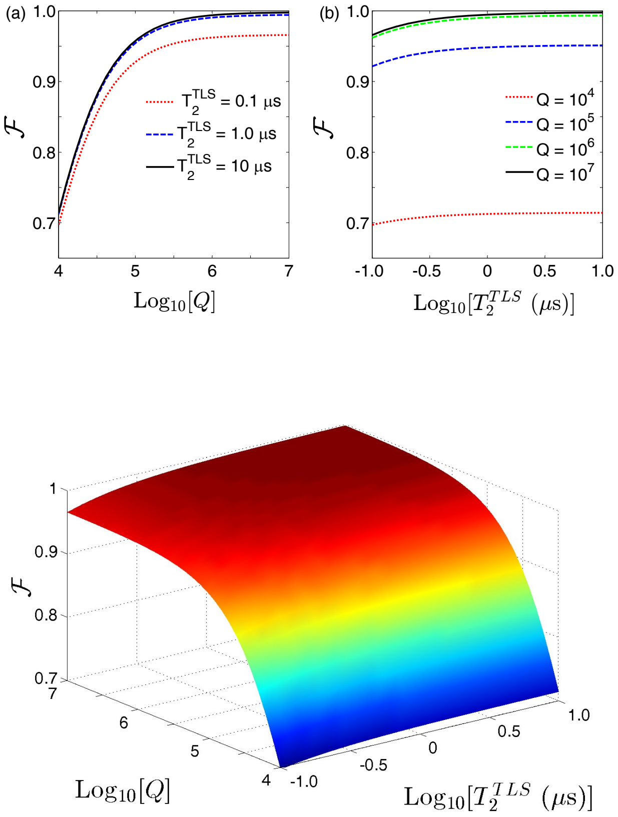

Figure 9.4: Fidelity of the CZ gate as a function of the quality factor Q of the resonators, for different values of the TLS dephasing time, T_2^{TLS} (a), and of the TLS dephasing time, T_2^{TLS}, for different values of the quality factor, Q (b). The system is initialized in the superposition of the computational basis states $(|0_{\mathcal{A}}0_{\mathcal{A}'}\rangle + |1_{\mathcal{A}}1_{\mathcal{A}'}\rangle)/\sqrt{2}$. (c) Two-dimensional surface of $\mathcal{F}(Q, T_2^{TLS})$. Both Q and T_2^{TLS} are varied in a realistic range, which can be reached with available technology. The gate fidelity is represented both by the colors and by the height of the surface.

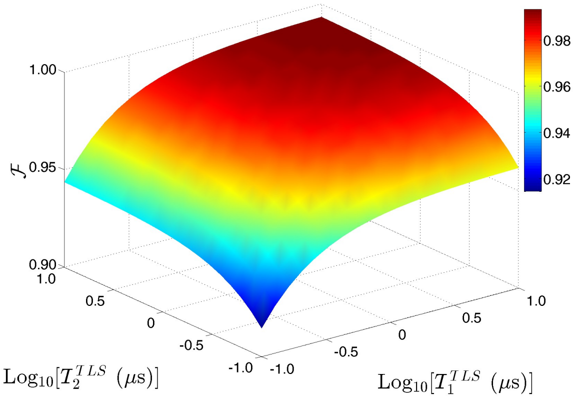

Figure 9.5: CZ-gate fidelity as a function of T_1^{TLS} and T_2^{TLS}, assuming $Q = 10^6$. The calculated fidelity is represented both by the colors and by the height of the surface.

plotted as a function of T_2^{TLS}, for different values of Q. The dependence of the fidelity on T_2^{TLS} is much weaker than that on Q. This results from the fact that the excited states of the TLS are populated only for a fraction of the total gating time. Figure 9.4-(c) reports the overall dependence of the CZ-gate fidelity on the cavity quality factor and on the TLS dephasing time. For the simulation reported in Fig. 9.4, the system is initialized in a superposition state, $(|0_\mathcal{A}0_{\mathcal{A}'}\rangle + |1_\mathcal{A}1_{\mathcal{A}'}\rangle)/\sqrt{2}$. This state is one of the most error prone, as it introduces in the calculation the relative phase between $|1_\mathcal{A}1_{\mathcal{A}'}\rangle$ (in which both photons are subject to damping and dephasing) and $|0_\mathcal{A}0_{\mathcal{A}'}\rangle$, which is completely unaffected by the pulse sequence. Consequently, other superposition states lead to similar or slightly larger fidelities.

Typically, T_1^{TLS} is larger than T_2^{TLS} in charge qubits close to the transmon regime. In any case, we have checked that the inclusion of a relaxation term for the TLS does not reduce appreciably the gate fidelity. A colormap of the CZ-gate fidelity as a function of T_1^{TLS} and T_2^{TLS} is reported in Figure 9.5. We note a slightly more pronounced dependence of $\mathcal{F}$ on the relaxation time T_1^{TLS} than on the dephasing time T_2^{TLS}. However, in the regime examined here we can assume $T_2^{TLS} \approx 10\,\mu s$ and $T_1^{TLS} > T_2^{TLS}$, leading (in a cavity with $Q = 10^6$) to values of $\mathcal{F}$ above 99%.

As far as photons are concerned, it has been experimentally shown that pure dephasing of the cavity modes is practically negligible (see, e.g., Ref. [183], where the measured value of the dephasing time T_2^{ph} approximately corresponds to twice the value of the photon decay time T_1^{ph}).

Finally, we have included in the equation of motion a pure dephasing term, acting on the spin ensembles. The calculated fidelity at the end of a CZ gate is plotted in Fig. 9.6 as a function of the spin-ensemble dephasing time T_2^{SE}, for different values of Q. We note that for $T_2^{SE} > 1\,\mu$s, the fidelity of a single gate (which takes about 50 ns) is nearly independent of T_2^{SE}, whereas the dependence on Q is much more pronounced. In that limit, the spin dephasing rate does not appreciably affect the system dynamics.

9.6 Proof-of-principle experiment

We describe here a simpler, not scalable setup, which could be exploited for the first proof-of-principle demonstrations of the present scheme. This setup includes a single cavity, coupled to a TLS and an ensemble of equally oriented $s = 1$ spins, as schematically shown in Fig. 9.7. The setup reported here is not straightforwardly scalable because increasing the number of qubits within a single cavity implies the use of an increasing number of distinct harmonics.

We refer here not to disordered diluted systems, but to crystals of equally oriented magnetic ions diluted in a non-magnetic matrix (see, e.g., Ref. [186]). In the low-excitation regime, the spin ensemble can be modeled by two independent harmonic oscillators, related to two different magnetic-dipole transitions from the $m = 0$ ground state of the single spin, namely those to the $m = -1$ and $m = 1$ states. This can be achieved by properly choosing a system with easy-plane magnetic anisotropy, which provides a zero-field splitting between the $m = 0$ ground state and the excited $m = \pm 1$ doublet, and in presence of a small static magnetic field. The corresponding creation operators (excitation energies) are given by $\hat{b}_A^\dagger = \frac{1}{\sqrt{N}} \sum_{q=1}^N |-1\rangle\langle 0|_q$ and $\hat{b}_{A'}^\dagger = \frac{1}{\sqrt{N}} \sum_{q=1}^N |1\rangle\langle 0|_q$ (ω^A and $\omega^{A'}$), while the ground state of the SE is $|\psi_0\rangle = |0_1 \dots 0_N\rangle$. These spin modes, together with the modes A and A' of the single cavity, allow us to introduce here a dual-rail encoding equivalent to that defined in Eq. 9.1 for the scalable architecture:

$$
\begin{aligned}
|0_{\mathcal{A}} 0_{\mathcal{A}'}\rangle &= \hat{b}_A^\dagger \hat{b}_{A'}^\dagger |\emptyset\rangle, \ |0_{\mathcal{A}} 1_{\mathcal{A}'}\rangle = \hat{b}_A^\dagger \hat{a}_{A'}^\dagger |\emptyset\rangle, \\
|1_{\mathcal{A}} 0_{\mathcal{A}'}\rangle &= \hat{a}_A^\dagger \hat{b}_{A'}^\dagger |\emptyset\rangle, \ |1_{\mathcal{A}} 1_{\mathcal{A}'}\rangle = \hat{a}_A^\dagger \hat{a}_{A'}^\dagger |\emptyset\rangle, \qquad (9.16)
\end{aligned}
$$

where $|\emptyset\rangle = |\psi_0, n_A = 0, n_{A'} = 0\rangle$. For the qubit manipulation, and specifically for the two-qubit gate, we exploit the lowest three levels ($|\psi_0^B\rangle$, $|\psi_1^B\rangle$ and $|\psi_2^B\rangle$) of a charge qubit, with transition energies Ω^B and $\Omega^{B'}$, as in the scalable scheme. Besides, the two harmonics of the resonator that are taken into account have frequencies ω_c^A and $\omega_c^{A'}$: ω_c^A is intermediate between ω^A and Ω^B, while $\omega_c^{A'}$ is intermediate between $\omega^{A'}$ and $\Omega^{B'}$. In this way, the cavity mode ω_c^A ($\omega_c^{A'}$) can be coupled both to the spin gap ω^A ($\omega^{A'}$) and to the superconducting gap Ω^B ($\Omega^{B'}$). As in the scalable setup, the TLS does not enter the definition of the qubits, for it remains in its ground state in all the computational space.

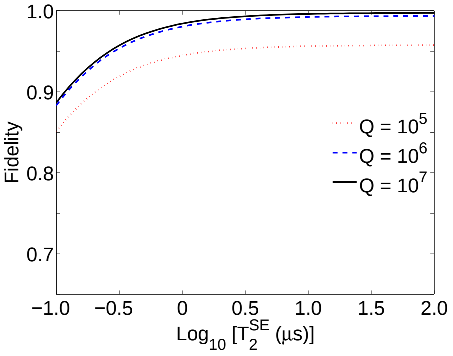

Figure 9.6: Fidelity of the CZ gate as a function of the spin-ensemble dephasing time, $T_2^{SE} = 1/\gamma_{SE}$. The three curves are referred to different Q factors and are calculated assuming $T_2^{TLS} = 10\ \mu s$. (Figure used with permission from Ref. [172].)

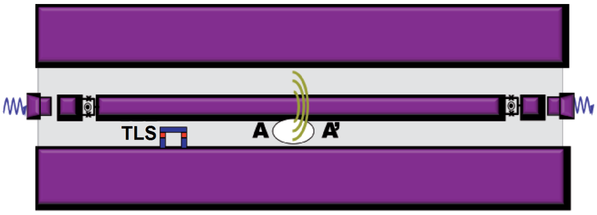

Figure 9.7: Sketch of the elementary unit of the non-scalable setup for proof-of-principle experiments. Qubits $\mathcal{A}$ and $\mathcal{A}'$ are now encoded by using two different states of the same spin ensemble of $s = 1$ spins, coupled to two different harmonics of the same cavity.

Single-qubit rotations are implemented in a way similar to that described for the scalable setup: rotations about the z axis of the Bloch sphere, $\hat{R}_z(\varphi)$, are realized by means of off-resonant pulses, while $\hat{R}_x(\varphi)$ are performed by tuning ω_c^γ to ω^γ for the proper amount of time ($\gamma = A, A'$). However, as the photons that are involved in the encoding of the two qubits correspond to different harmonics of the same cavity, the $\hat{R}_z(\varphi)$ rotations applied to qubit A and A' are not independent. Indeed, by applying a pulse of amplitude $2\delta_c$ to the second harmonic for a time τ, one also varies the phase of the third harmonic by an amount of $3\delta_c\tau$. In the two-qubit basis, we thus obtain the transformation:

$$\hat{R}_{zz}(\tau) = \begin{pmatrix} 1 & 0 & 0 & 0 \\ 0 & e^{-2i\delta_c\tau} & 0 & 0 \\ 0 & 0 & e^{-3i\delta_c\tau} & 0 \\ 0 & 0 & 0 & e^{-5i\delta_c\tau} \end{pmatrix}. \tag{9.17}$$

A rotation of, e.g., the first qubit can however be performed without affecting the second one, by exploiting the equality:

$$\hat{R}_{zz}(\tau)\,[\hat{R}_x(\varphi) \otimes \hat{I}]\,\hat{R}_{zz}(\tau) = \hat{R}_y(\varphi) \otimes \hat{I}, \tag{9.18}$$

which holds for $\tau = 3\pi/2\delta_c$ [2]. In this way, we demonstrate the ability to implement independent $\hat{R}_y$ rotations on each qubit. This, together with rotations about the x axis, allows us to obtain any single-qubit gate.
The CZ gate can be implemented as in the scalable setup. Here, however, a single resonator is involved, and no photon-hopping is needed: this reduces the overall time required to implement the quantum gate. Figure 9.8 is a colormap of the fidelity in a CZ gate, as a function of the two parameters accounting for the two included sources of errors: the resonator quality factor Q, accounting for photon leakage, and the TLS dephasing time T_2^{TLS}. The plot is similar to that of Fig. 9.4: the larger Q and T_2^{TLS}, the larger the fidelity. However, as the implementation of a single CZ gate here is faster, the photon leakage is less relevant: slightly larger values of the fidelity correspond to the same values of Q. In Fig. 9.9-(a) we plot the expectation value of the number operators as a function of time, i.e. $\langle \hat{a}_A^\dagger(t)\hat{a}_A(t)\rangle = \mathrm{Tr}[\hat{\rho}(t)\hat{a}_A^\dagger\hat{a}_A]$, and analogously for the other fields. The rates corresponding to photon loss and pure dephasing of the TLS are given by $Q = 10^6$ and $T_2^{TLS} = 10\ \mu$s. The system is initialized in state $|1_\mathcal{A}1_{\mathcal{A}'}\rangle$. Panel

---

[2] An equation analogous to (9.18) holds also for a rotation of the second qubit, i.e. $\hat{R}_{zz}(\tau)\ [I \otimes \hat{R}_x(\varphi)]\ \hat{R}_{zz}(\tau) = I \otimes \hat{R}_y(\varphi)$. In that case, however, $\tau = \pi/4\delta_c$.

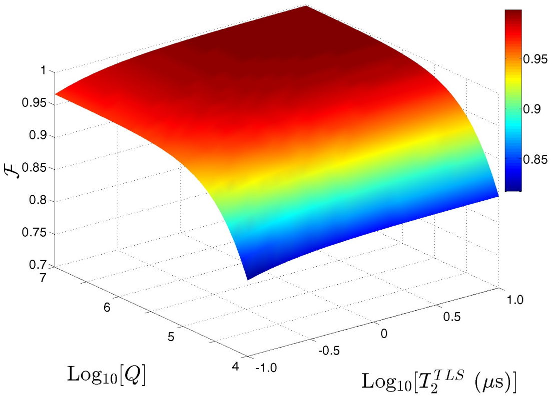

Figure 9.8: Fidelity of the CZ gate in the non-scalable setup as a function of Q and T_2^{TLS}. The calculated fidelity is represented both by the colors and by the height of the surface.

(b) displays the profile of the step-like pulse sequence employed in the simulation: the first π-pulse brings photon of frequency ω_c^A into resonance with the TLS gap Ω^B, leading to the absorption of photon A. The second one is a 2π-pulse which induces a full Rabi flop between states $|\psi_1^B\rangle$ and $|\psi_2^B\rangle$. Then an off-resonant pulse is used to implement a rotation about z axis which corrects the unwanted phase acquired during the Rabi oscillation. Finally, a π-pulse brings the system to state $-|1_{\mathcal{A}}1_{\mathcal{A}'}\rangle$, while the other basis states are unaffected.

9.7 Discussion

Here we briefly discuss the possible consequences of the above decoherence mechanisms on quantum-information processing. We have shown that the main source of error in our scheme is represented by photon loss. Conversely, since the TLS is excited only during part of the implementation of the CZ gate, $T_2^{TLS} > 1$ μs is sufficient to guarantee a high fidelity of the gates. Quality factors somewhat smaller than 10^5 already lead to fidelity values $\mathcal{F} > 0.90 - 0.95$, but it could be realistic to assume $Q \approx 10^6 - 10^7$, as shown in Ref. [158]. In the limit of $Q = 10^8$, the photon lifetime would reach 0.3 ms, very close to the coherence time of the best spins. Within this timescale, several quantum gates could be performed on the proposed setup, leading to the implementation of complex quantum algorithms, as well as the simulation of different quantum systems. Other decoherence sources, such as relaxation of the TLS, are found to be ineffective, in a realistic range of parameters.

In the reported simulations the cavity frequency is modulated by means of step-like pulses. We have checked that the same results can be achieved by linearly varying the resonator frequency on a timescale $\gg 1/\omega_c^\gamma(0)$: this regime is well within the validity of the rotating-wave approximation and no generation of unwanted photons due to dynamical-Casimir effect is observed [187].

Even if tuning of the resonator harmonics by external magnetic fields might introduce extra-dissipation to the photonic degrees of freedom, it has been shown that Q-factors are preserved within a factor of 3 in the whole frequency modulation range [147]. We also point out that these effects are mainly attributed to thermal noise, which might be

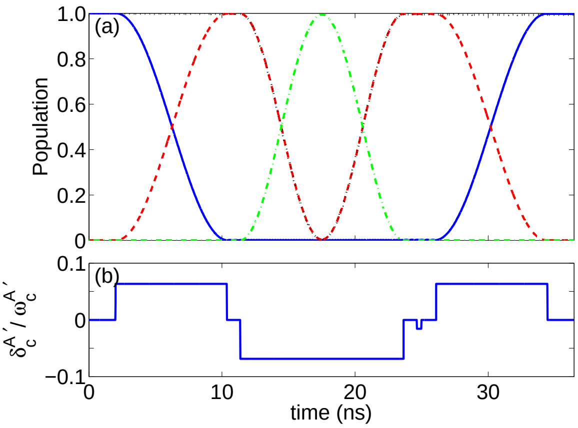

Figure 9.9: (a) Population of the fields as a function of time during a CZ gate, with the system initialized in state $|1_{\mathcal{A}}1_{\mathcal{A}'}\rangle$. The continuous, dashed, dotted-dashed, and dotted lines represent the time dependences of $\langle \hat{a}^{\dagger}_{A}\hat{a}_{A}\rangle$, $\langle|\psi^{B}_{1}\rangle\langle\psi^{B}_{1}|\rangle$, $\langle|\psi^{B}_{2}\rangle\langle\psi^{B}_{2}|\rangle$, and $\langle \hat{a}^{\dagger}_{A'}\hat{a}_{A'}\rangle$, respectively. (b) Pulse sequence which represents the relative frequency variations of the cavity during the implementation of the CZ in the non-scalable setup. (Figure used with permission from Ref. [172].)

further reduced by working at lower temperatures and using high-frequency resonators, as the ones assumed in the present work. In single spins, the dephasing time can reach the value of $0.1 - 1$ ms [186]. An additional source of decoherence in SEs is represented by inhomogeneous broadening [188, 189]. This is essentially due to the presence of disorder, which spreads the emitter's bare frequencies and spin-photon couplings within the ensemble. We will address in detail this issue in Chapter 11, also introducing an efficient scheme to overcome this drawback.

The fact that the dominant source of errors is given by photon loss represents a potential advantage for the implementation of quantum computation. In fact, within the dual-rail encoding we propose, the photon loss corresponds to a locatable error, and can in principle be detected without requiring any redundant multi-qubit encoding [190]. We note that the same effect is produced by inhomogeneous broadening of the spin-ensemble, which can induce the leakage of the subsystem state out of the computational space. In fact, in the presence of inhomogeneities, the state $|\psi^{\mu}_{1}\rangle$ decays into other collective modes of the spin ensemble, which are decoupled from the cavity mode (see below). Therefore, neither photon loss nor inhomogeneous broadening of the SE induce an undesired bit flip or phase shift. These can only result from imperfections in the pulses that are used for the quantum gate implementation. In one-way quantum computing [191], the presence of only locatable errors was shown to result in a significant increase of the error rate that is compatible with fault-tolerant quantum computation [192].

A class of spin systems that provides interesting and yet unexplored possibilities in this respect is represented by molecular nanomagnets [20]. For example, high-spin molecules possess magnetic-dipole transitions (e.g., those between the states $|M = 0\rangle$ and $|M = \pm 1\rangle$) whose amplitude is roughly proportional to the spin length. This, along with the possible localization of the molecules in the nm-sized constrictions of the resonator, enabled by efficient deposition techniques, might allow one to achieve the strong coupling regime even with a single molecule [157]. Such an achievement would eliminate the contribution to decoherence resulting from inhomogeneous broadening. In this way the only relevant source of error of the spins is given by pure dephasing of the single molecule (see Figure 9.6), whose coherence time can reach values of several μs [30]. A further opportunity is represented by the suppression of the intrinsic decoherence time of the spins. This could in principle be achieved by exploiting protected degrees of freedom within the molecular spin cluster, such as spin chirality [193].

In summary, we have developed a scheme for quantum-information processing with spin ensembles in superconducting coplanar resonators, exploiting a hybrid spin-photon encoding of the qubits. Our scheme is qualitatively different from previous ones because the spin and photon degrees of freedom enter the definition of the qubit on an equal footing. In this way, the evolution can be induced simply by tuning the cavity frequency to the spin-energy gaps. Arbitrary single and two-qubit gates are implemented, over much shorter times than typical decoherence times of cavity-photons and spin-ensembles. Promising candidates for the spin degrees of freedom are diluted magnetic ions or molecular nanomagnets. The application of this scheme to an $ABAB...$ array of cavities enables general quantum algorithms as well as quantum simulators [40, 17] to be implemented (see Chapter 10).

The content of this chapter was published in Phys. Rev. Lett. **111**, 110501 (2013) (Ref. [171]) and Phys. Rev. A **89**, 052308 (2104) (Ref. [172]).

Digital quantum simulators in a scalable architecture of hybrid spin-photon qubits

CHAPTER 10

There is a large number of problems that are well known to be hardly tractable with standard computational approaches and resources, mainly due to the many-body nature of strongly correlated many particle systems. To overcome this limitation, the idea of a quantum simulator was originally proposed by Feynman [14]: any arbitrary complex quantum system could in fact be simulated by another quantum system mimicking its dynamical evolution, but under the experimenter control (see Sec. 0.1.5). Over the past twenty years, different approaches have been proposed to realize quantum simulators of the most relevant models in condensed matter physics, quantum field theories, and quantum chemistry [15]. Lately, superconducting circuits and resonators have emerged as an extremely promising platform for quantum information and quantum simulation architectures [39, 40, 95, 194, 195, 196, 197]. Within this framework, the first and unique theoretical proposal for a general-purpose digital simulator has been put forward only very recently [95]. In this proposal qubits encoded in transmons are dispersively coupled through a photon mode of a single resonator, and such coupling is externally tuned by controlling the transmon energies. However, the reported fidelities and the intrinsic serial nature of this setup (i.e., the need of addressing each pair of qubits sequentially), may hinder the scalability to a sizeable number of qubits. In addition, superconducting units are not ideal for encoding qubits owing to their relatively short coherence times. Indeed, spin-ensembles [45, 198, 199] or even photons [42, 173] have been proposed as memories to temporarily store the state of superconducting computational qubits.

Here we consider an array of superconducting resonators as the main technological platform, on which hybrid spin-photon qubits are defined by introducing strongly coupled spin ensembles (SEs) in each resonator [171, 172], as described in Chapter 9. One- and two-qubit quantum gates can be implemented by individually and independently tuning the resonators modes through external magnetic fields, as explained in the previous chapter. This setup can realize a universal digital quantum simulator [200], whose scalability to a large array is naturally fulfilled by the inherent definition of the single qubits, represented by each coupled SE-resonator device. The possibility to perform a large number of two-qubit gates in parallel makes the manipulation of such large arrays much faster than in a serial implementation, thus making the simulation of complex target Hamiltonians possible in practice.

Ensembles of effective $s = 1$ spins are used in the hybrid encoding, which allows to exploit the mobility of photons across different resonators to perform two-qubit gates between physically distant qubits. This is done much more efficiently than by the straightforward approach of moving the states of the two qubits close to each other by sequences of SWAP gates, and makes the class of Hamiltonians which can be realistically addressed much larger. Long-distance operations arise whenever mapping the target system of the simulation onto the register implies two-body terms between distant qubits. Besides the obvious case of Hamiltonians with long-range interactions, this occurs with any two-dimensional model mapped onto a linear register, or with models containing N-body terms, including the many-spin terms which implement the antisymmetric nature of fermion wavefunctions.

The time evolution of a generic Hamiltonian is decomposed into a sequence of local unitary operators, which can be implemented by means of elementary single- and two-qubits gates. Then we combine these elementary gates in order to mimic the dynamics of spin and Hubbard-like Hamiltonians for fermions. We explicitly report our results for the digital quantum simulation of the transverse-field Ising model on 3 qubits, the tunneling dynamics of a spin one in a rhombic crystal field and the Hubbard Hamiltonian. We use a time-dependent Hamiltonian for this hardware including the effects of decoherence in a Lindblad formalism, thus performing extensive numerical experiments on our specific device, directly showing the feasibility of the proposed digital quantum simulation.

10.1 A scalable architecture for quantum simulation

The proposed quantum simulator is schematically shown in Fig. 10.1. It consists of a one- or two-dimensional (1D or 2D) lattice of superconducting resonators where hybrid spin-photon qubits are defined. We notice that large arrays of such resonators have already been shown experimentally [40, 182]. In this schematic implementation, qubits are encoded within square boxes. Each box represents a coplanar resonator containing an ensemble of (effective) $s = 1$ spins, whose collective excitations correspond to the transitions from the $m = 0$ single-spin ground state to the $m = \pm 1$ excited states, and can be modeled by two independent harmonic oscillators. Red lines represent the transition energies (continuous $m = -1$, dashed $m = 1$ transitions, respectively), while the blue line indicates the resonator frequency. This is varied within a nanosecond time-scale by means of SQUID devices properly connected to the resonator [147, 159, 161], in order to match the spin transition frequencies. In the hybrid qubit encoding, a dual-rail representation of the logical units is introduced where the $|0\rangle_\mu$ and $|1\rangle_\mu$ states of qubit μ are defined in the single-excitation subspace of each resonator. The logical state $|0\rangle_\mu$ ($|1\rangle_\mu$) corresponds to zero (one) photons and a single (zero) quantum in the $m = -1$ oscillator in cavity μ. This encoding is detailed in Sec. 9.2. The $m = 1$ oscillator represents an auxiliary degree of freedom that is exploited to store the photonic component of the qubit, if needed (e.g., to perform two-qubit gates between distant qubits, see below).

The basic unit of the scalable array (introduced in Chapter 9) is represented by a pair of qubits connected by an interposed auxiliary resonator containing a superconducting transmon device (circular box), which is employed to perform two-qubit gates and is

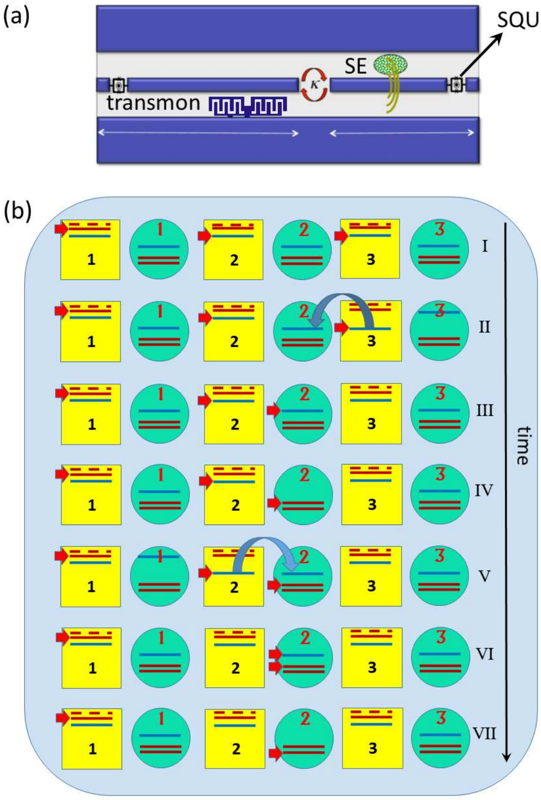

Figure 10.1: (a) Elementary unit of the scalable setup, consisting of an *auxiliary* and a *logical* resonator. The latter includes an ensemble of $s = 1$ spins, placed at the antinodes of the magnetic field (rotational lines) of the cavity mode. The *auxiliary* resonator contains a nonlinear element (transmon) coupled to the electric field of the fundamental mode. (b) Detailed sequence of time steps required to produce controlled-φ two-qubit gate between qubits $\mu = 2$ and $\mu = 3$. *Logical* cavities are represented by square boxes, whereas *auxiliary* resonators are depicted as circular boxes. Blue lines represent photon frequencies (ω_c^μ in the *logical* and $\tilde{\omega}_c^j$ in the *auxiliary* cavities). The transmon (Ω_{01} and Ω_{12}) and spin (ω_{-1}, continuous, and ω_1, dashed) transition energies are indicated by red lines. (I) qubits are initially into state $|1_2 1_3\rangle$, with the excitations (red arrows) stored into the photonic degrees of freedom (blue lines); (II) *logical* cavity 3 is brought into resonance with the *auxiliary* resonator $j = 2$, thus (III) bringing the photon to the auxiliary cavity. In the meantime *auxiliary* resonator 3 is detuned from the others to avoid unwanted photon hoppings. In (IV) the photon is absorbed by the transmon ($|\psi_{0,j=2}\rangle \rightarrow |\psi_{1,j=2}\rangle$ transition). The same hopping process (V) is repeated for the photon originally in cavity 2, which is brought to the *auxiliary* resonator (VI) and then absorbed and emitted by the transmon ($|\psi_{1,2}\rangle \rightarrow |\psi_{2,2}\rangle$ transition) in a semi-resonant Rabi process (VII). The procedure is then repeated to bring photons back to *logical* cavities 2 and 3, leading the state back to $|1_2 1_3\rangle$ with an additional phase φ acquired during the semi-resonant process.

treated as a three level system. The setup is simplified with respect to that of the previous chapter, as each resonator contains a single photonic mode. It should be emphasized that this nonlinear superconducting element is not used to encode information, and *it is left in its ground state always except during the implementation of the two-qubit gates*. Consequently, its possibly short coherence times affect the quantum simulation only marginally. Other types of superconductor based qubits [177], such as flux [154] or Xmon [166] qubits, can be exploited as well. Here we focus on transmon qubits [44], which are commonly used thanks to their low sensitivity to charge noise.
In the following, we shall refer to the square boxes of Fig. 10.1 as the *logical* cavities labelled with Greek letters, while the circular ones are the *auxiliary* cavities labeled by Latin letters. Photon hopping between neighboring resonators is allowed by capacitive coupling. Formally, such a complex system can be described by the total Hamiltonian

$$\hat{H} = \hat{H}_{spin} + \hat{H}_{tr} + \hat{H}_{ph} + \hat{H}_{int} + \hat{H}_{ph-ph} \,. \tag{10.1}$$

The first term describes the SEs as independent harmonic oscillators [160] ($\hbar \equiv 1$):

$$\hat{H}_{spin} = \sum_m \sum_\mu \omega_m \hat{b}^\dagger_{m,\mu} \hat{b}_{m,\mu} \,, \tag{10.2}$$

where $\hat{b}^\dagger_{m,\mu}$ creates a spin excitation in level $m = \pm 1$ of resonator μ. The transmons are treated as effective three-level systems, with transition energies Ω_{01} and Ω_{12}, and described by

$$\hat{H}_{tr} = \sum_j \Omega_{01} |\psi_{1,j}\rangle\langle\psi_{1,j}| + (\Omega_{12} + \Omega_{01}) |\psi_{2,j}\rangle\langle\psi_{2,j}|. \tag{10.3}$$

The time-dependent photonic term is entirely responsible for the manipulation of the qubits. It can be expressed as:

$$\hat{H}_{ph} = \sum_\mu \omega^\mu_c(t) \hat{a}^\dagger_\mu \hat{a}_\mu + \sum_j \tilde{\omega}^j_c(t) \hat{\tilde{a}}^\dagger_j \hat{\tilde{a}}_j \,, \tag{10.4}$$

where $\omega^\mu_c(t) = \omega^\mu_c(0) + \delta^\mu_c(t)$ and a similar expression holds for $\tilde{\omega}^j_c(t)$. $\hat{a}^\dagger_\mu$ ($\hat{a}_\mu$) creates (destroys) a single photon in the *logical* resonator μ, while $\hat{\tilde{a}}^\dagger_j$ ($\hat{\tilde{a}}_j$) creates (destroys) a single photon in the *auxiliary* cavity j. Hereafter, we will use the interaction picture, with $\hat{H}_0 = \hat{H}_{spin} + \hat{H}_{tr} + \hat{H}_{ph}(t = 0)$. Hence, within the rotating-wave approximation the spin-photon and transmon-photon coupling Hamiltonian takes the form:

$$\begin{aligned} \hat{H}_{int} &= G_{01} \sum_j \left[\hat{\tilde{a}}^\dagger_j |\psi_{0,j}\rangle\langle\psi_{1,j}| e^{i(\tilde{\omega}^j_c - \Omega_{01})t} + \text{h.c.} \right] \\ &+ G_{12} \sum_j \left[\hat{\tilde{a}}^\dagger_j |\psi_{1,j}\rangle\langle\psi_{2,j}| e^{i(\tilde{\omega}^j_c - \Omega_{12})t} + \text{h.c.} \right] \\ &+ \sum_{m=1,-1} \sum_\mu \bar{G}_m \left[\hat{a}^\dagger_\mu \hat{b}_{m,\mu} e^{i(\omega^\mu_c - \omega_m)t} + \text{h.c.} \right] . \end{aligned} \tag{10.5}$$

Finally, the last term in Eq. (10.1) describes the photon-hopping processes induced by the capacitive coupling between the modes in neighboring cavities [182]:

$$\hat{H}_{ph-ph} = -\kappa \sum_{\langle \mu,j \rangle} \hat{a}^\dagger_\mu \hat{\tilde{a}}_j e^{i(\omega^\mu_c - \tilde{\omega}^j_c)t} + \text{h.c.} \,. \tag{10.6}$$

Single- and two-qubit gates are efficiently implemented by tuning individual resonator modes, as shown in Refs. [171, 172]. Arbitrary single-qubit rotations within the Bloch sphere as well as controlled-phase (Cφ) gates can be realized, as explained in 9.4.1, and illustrated in Figure 10.1-(b) for the pair of qubits 2-3. In particular, the Cφ gate is obtained by means of a semi-resonant process (during which the resonator is detuned from the transmon gap by a small amount δ_{12}), which is exploited to induce an arbitrary phase on the $|1_2 1_3\rangle$ component of the wavefunction [42]. A pulse of duration $\Delta t = \frac{\pi}{\sqrt{G_{12}^2+\delta_{12}^2/4}}$, where $\delta_{12} = \Omega_{12} - \tilde{\omega}_c^2$ is the detuning between the resonator mode and the $|\psi_{1,2}\rangle \rightarrow |\psi_{2,2}\rangle$ transition of the transmon, adds a phase $\varphi = \pi - \pi \frac{\delta_{12}}{\sqrt{\delta_{12}^2+4G_{12}^2}}$ to the system wavefunction. The CZ gate (see Sec. 9.4.2) is recovered in the limit of $\delta_{12} = 0$.

The present setup offers two remarkable benefits: the first is that using the hybrid encoding with an ensemble of effective $s = 1$ spins ensures the possibility of implementing Controlled-phase gates between distant qubits, with no need of performing highly demanding and error-prone sequences of SWAP gates. Long-distance two-qubit interactions are a key-resource for the digital simulation of many interesting physical Hamiltonians. They appear each time that a multi-dimensional target system is mapped onto a linear chain of qubits or in models with N-body terms. Among these, a particular interest is assumed by problems involving interacting fermions in two or higher spatial dimensions, which are often intractable for classical computers. For instance, solving the two-dimensional Hubbard model is considered by many as the ultimate goal of the theory of strongly correlated systems. This is done by bringing the photon components of the two qubits into neighboring *logical* resonators by a series of hopping processes. The operations outlined in Fig. 10.1-(b) are then performed to implement a Cφ gate between neighboring qubits, and the photon components are finally brought back to the starting position by reverting the series of hoppings. Transferring the photons with no corruption and without perturbing the qubits encoded in the interposed *logical* cavities is made possible by temporarily storing the photon component of these interposed qubits into the $m = 1$ spin oscillator.

In addition, quantum simulations can be performed in parallel to a large degree, with resulting reduction of simulation times. This is made possible by the definitions of the single qubits, represented by each coupled SE-resonator device, and by the local control of each *logical* or *auxiliary* resonator. Non-overlapping parts of the register can then be manipulated in parallel. For instance, in simulating a Heisenberg chain of N spins $s = 1/2$, the N two-qubits evolutions which appear at each time-step in the Trotter decomposition are performed first simultaneously on all $N/2$ ”even” bonds and then simultaneously on the remaining $N/2$ ”odd” bonds. Thus the simulation time of each Trotter step does not increase with N.

10.2 Numerical experiments

While it is obvious that a universal quantum computer can be used in principle to simulate any Hamiltonian, the actual feasibility of such simulations needs to be quantitatively assessed by testing whether the complex sequences of gates needed are robust with respect to errors due to decoherence. Here we numerically solve the density matrix master equation for the model in Eq. 10.1 with the inclusion of the main decoherence processes, i.e., photon loss and dephasing of the transmons [172].

In the following, we will consider the *fidelity* (0.1.4) as a valuable figure of merit for the target Hamiltonians to be simulated. For the simulations shown in the following,

	time	$\mathcal{F}_I$	$\mathcal{F}_D$	$\mathcal{F}_D^L$
$\mathcal{H}_x^{(1)}$	6.4 ns	99.99 %	99.94 %	99.79 %
$\mathcal{H}_z^{(1)}$	0.5 ns	99.99 %	99.98 %	99.90 %
$\mathcal{H}_{yy}^{(2)}$	85.8 ns	99.87 %	99.24 %	98.96 %
$\mathcal{H}_{zz}^{(2)}$	61 ns	99.91 %	99.45 %	99.20 %
$\mathcal{H}_{yz}^{(2)}$	85.8 ns	99.79 %	99.13 %	98.87 %

Table 10.1: Simulation of the elementary terms of the Hamiltonian. Fidelity and time required to simulate the elementary terms of the Spin Hamiltonian. The fidelity has been calculated by assuming a random initial state. The second and third column show a comparison between the ideal fidelity (calculated in the absence of decoherence) and the real one (calculated assuming a Lindblad dynamics, with $Q = 10^6$ and $T_2^{tr} = 10\ \mu s$). The implemented evolution is $\hat{U} = \exp\left[-i\mathcal{H}_{\alpha\beta}^{(1,2)}\tau\right]$, with $\alpha, \beta = x, y, z$ and with $b\tau = \lambda\tau = \pi/2$. The last column reports the fidelities corresponding to a setup operating at lower frequencies, $\omega_1/2\pi = 16.05$ GHz, $\omega_{-1}/2\pi = 15.7$ GHz, $\omega_c(0)/2\pi = 14$ GHz, $\tilde{\omega}_c(0)/2\pi = 11.85$ GHz and $\Omega_{01}/2\pi = 9.2$ GHz, $\Omega_{12}/2\pi = 8.3$ GHz.

we have chosen these operational parameters: $\omega_1/2\pi = 37$ GHz, $\omega_{-1}/2\pi = 35$ GHz, $\omega_c(0)/2\pi = 31$ GHz, $\tilde{\omega}_c(0)/2\pi = 28$ GHz and $\Omega_{01}/2\pi = 21.7$ GHz, $\Omega_{12}/2\pi = 19.6$ GHz (see the level scheme inside each cavity in Fig. 10.1). We also assume realistic values of the SE-resonator $\bar{G}_{\pm 1}/2\pi = 40$ MHz, transmon-resonator $G_{01}/2\pi = 30$ MHz, $G_{12}/2\pi = 40$ MHz and photon-photon $\kappa/2\pi = 30$ MHz couplings, respectively [46, 182]. The transmon parameters correspond to a ratio between Josephson and charge energies $E_J/E_C = 25$ [177]. In this regime the dephasing time T_2^{tr} exceeds several μs while keeping a 10% anharmonicity. The two chosen spin gaps can easily be achieved with several diluted magnetic ions possessing a $S > 1/2$ ground multiplet, just by applying a small magnetic field along a properly chosen direction. We have chosen resonator frequencies ω_c and $\tilde{\omega}_c$ larger than usual experiments (e.g., twice the typical frequencies reported in Ref. [46]), since this helps improving the maximal fidelity of gates. However, we emphasize that the results do not qualitatively depend on these specific numbers. Indeed, high fidelities are also obtained by using resonator frequencies smaller than in [46] (see Table 10.1).

10.2.1 Digital simulation of spin Hamiltonians

The simulation of interesting physical models can be handled by digital techniques, as outlined in Section 0.1.5.

The time required and the fidelity for the simulation of each term of a generic spin Hamiltonian are calculated by using a Lindblad master equation formalism (see Appendix E) and are listed in Table 10.1. We notice that the predicted fidelities are very high, even after the inclusion of realistic values for the main decoherence channels, especially for the photon loss rate Γ_μ, which is related to the resonators quality factor (Q) by $\Gamma_\mu = \omega_c^\mu/Q$. The high fidelity obtained for these elementary steps allows us to combine many of them to simulate multi-spin models.

As a prototypical example we report the digital quantum simulation of the transverse field Ising model (TIM) on a chain of 3 qubits:

$$\hat{\mathcal{H}}_{TIM} = \lambda\left(\hat{s}_{1z}\hat{s}_{2z} + \hat{s}_{2z}\hat{s}_{3z}\right) + b\left(\hat{s}_{1x} + \hat{s}_{2x} + \hat{s}_{3x}\right) , \qquad (10.7)$$

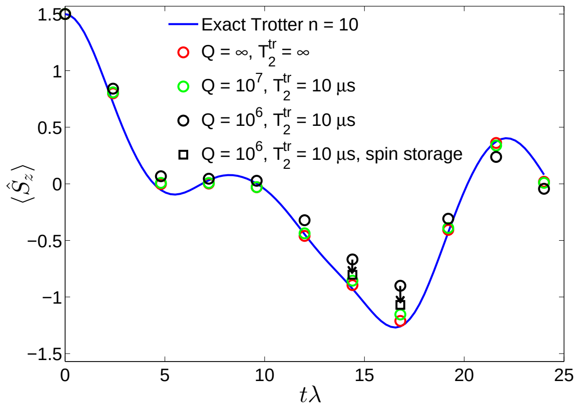

Figure 10.2: Oscillations of the magnetization in the transverse-field Ising model. The simulation is performed on a chain of 3 qubits, in the case $b = \lambda/2$. The plot reports the expectation value of the total magnetization $\langle \hat{S}_z \rangle = \text{tr}[\hat{\rho}(\hat{s}_{1z} + \hat{s}_{2z} + \hat{s}_{3z})]$ on the final state of the system, simulated for different values of the resonator quality factor (points) and compared with the exact evolution (line).

where $\hat{s}_{i\alpha}$ are spin-1/2 operators. Figure 10.2 shows the oscillations of the magnetization, $\text{Tr}[\hat{\rho}(\hat{s}_{1z} + \hat{s}_{2z} + \hat{s}_{3z})]$, for a spin system initialized in a ferromagnetic configuration. Here $\hat{\rho}$ is the three-qubit density matrix obtained at the end of the $n = 10$ Trotter steps of the simulation. The exact Trotter evolution (continuous line) is compared to the simulated one (points). In particular, red circles represent the ideal evolution, without including any source of decoherence. Errors are, in that case, only due to a non-ideal implementation of the quantum gates (see discussion below). Conversely, green and black circles are calculated including the most important decoherence channels, namely photon loss (timescale $1/\Gamma_\mu$) and pure dephasing of the transmon (timescale T_2^{tr}). As in the implementation of single gates discussed in Section 9.5, it turns out that photon loss is the most important environmental source of errors, while $T_2^{tr} \approx 10\ \mu s$ [153] is sufficient to obtain high fidelities at the end of the simulation. Indeed, the transmon is only excited during the implementation of two-qubit gates. The simulation has been performed for different values of the resonators quality factor. By decreasing Q the average fidelity decreases from 96.5% (infinite Q) to 94.6% ($Q = 10^7$) and 84.6% ($Q = 10^6$). For high but realistic [158] values of $Q = 10^7$ the calculated points are close to the ones obtained in the ideal case (with infinite Q): in that case the gating errors still dominate the dynamics. Finally, by exploiting the auxiliary $m = 1$ oscillator to store the photon component of the hybrid qubits when these are idle, the effects of photon loss are reduced and the fidelity significantly increases. The improvement is evident in Fig. 10.2, by comparing black circular and square points; the final fidelity raises from 84.6% to 92% thanks to this storage. We stress again that the simulation time of each Trotter step does not increase for larger systems containing more than 3 spins. Indeed, even if more gates are needed, these can be applied in parallel to the whole array, independently of the system size. Below we shall also discuss the extension to a larger number of qubits.

The simulation of Hamiltonians involving $S > 1/2$ spin ensembles can be performed by encoding the state of each spin-S onto that of $2S$ qubits. As an explicit example, we consider a chain of $S = 1$ spins, labelled $\hat{\mathbf{S}}_i$, with nearest-neighbor exchange interactions

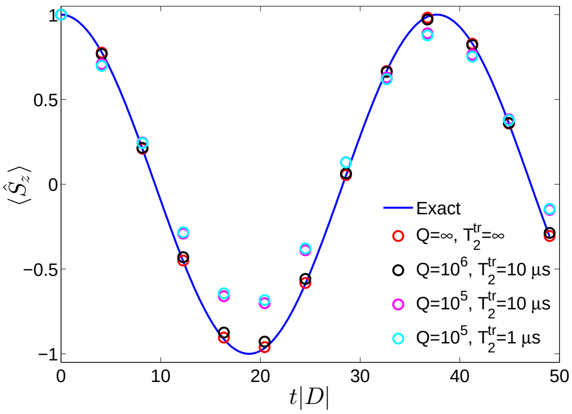

Figure 10.3: Tunneling of the magnetization in a spin-1 system. Line: exact time evolution of $\langle \hat{S}_z \rangle$ for a single $S = 1$ spin with $|D/E| = 12$, after Eq. (10.8). As it is well known, the system oscillates between states with opposite magnetization due to quantum tunneling across the anisotropy barrier. Points: digital quantum simulation obtained by the time evolution of two hybrid qubits for different values of the resonator quality factor, Q, and of the transmon coherence time, T_2^{tr}, respectively.

and single-spin crystal-field anisotropy, described by the Hamiltonian

$$\hat{\mathcal{H}}_{s1} = \sum_i \lambda \hat{\mathbf{S}}_i \cdot \hat{\mathbf{S}}_{i+1} + \sum_i \left[D\hat{S}_{iz}^2 + E\left(\hat{S}_{ix}^2 - \hat{S}_{iy}^2\right)\right] ,$$

which reduces to the paradigmatic Haldane case for $D = E = 0$ and $\lambda > 0$. By rewriting each spin-1 operator as the sum of two spin-1/2 ones ($\hat{S}_{i\alpha} = \hat{s}_{iA\alpha} + \hat{s}_{iB\alpha}$), $\hat{\mathcal{H}}_{s1}$ can be mapped onto a $s = 1/2$ Hamiltonian, $\hat{\tilde{\mathcal{H}}}_{s1}$, with twice the number of spins. Indeed, if each A-B pair of qubits is initialized into a state with total spin equal to one, the dynamics of $\hat{\tilde{\mathcal{H}}}_{s1}$ coincides with that of $\hat{\mathcal{H}}_{s1}$ and can be simulated along the lines traced above. A proof-of-principle experiment, which could be implemented even by the non-scalable single-resonator setup described in Section 9.6, would be the simulation of a single spin $S = 1$ experiencing tunneling of the magnetization. In this simple case we find (apart from a constant term):

$$\hat{\tilde{\mathcal{H}}}_{s1} = 2D\hat{s}_{zA}\hat{s}_{zB} + 2E\left(\hat{s}_{xA}\hat{s}_{xB} - \hat{s}_{yA}\hat{s}_{yB}\right) . \tag{10.8}$$

Figure 10.3 reports the comparison between the exact and the simulated evolution of the magnetization, assuming $D < 0$ and $|D/E| = 12$, for different values of Q and T_2^{tr}. Interestingly, quantum oscillations of $\langle \hat{S}_z \rangle$ are well captured by the simulation even for $Q = 10^5$, and the fidelity is practically unaffected by a reduction of transmon coherence time to $T_2^{tr} = 1\ \mu$s.

The simulation of many-spin models with $S > 1$ typically requires two-qubit gates involving non-nearest-neighbor qubits. These can be handled with no need of SWAP gates as outlined above.

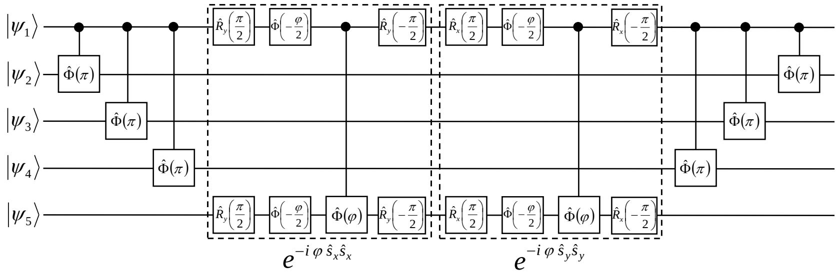

Figure 10.4: Quantum circuit description for the simulation of the hopping part of the Fermi-Hubbard model on a two-dimensional lattice. Here we explicitly show the case of $\hat{\mathcal{H}}_\lambda = -\lambda\left(\hat c_1^\dagger \hat c_5 + \hat c_5^\dagger \hat c_1\right)$, with $\varphi = 2\lambda\tau$. $\hat R_x(\theta)$ and $\hat R_y(\theta)$ indicate single-qubit rotations about x or y axis of the Bloch sphere, while $\hat\Phi(\varphi)$ is the single-qubit phase gate.

10.2.2 Digital simulation of Fermi-Hubbard models

The numerical simulation of many-body fermionic systems is a notoriously difficult problem in theoretical condensed matter. In particular, quantum Monte Carlo algorithms usually fail due to the so-called sign-problem [201]. Our digital quantum simulator setup enables to efficiently compute the quantum dynamics of interacting fermions, even on an arbitrary two-dimensional lattice. Although we focus on the paradigmatic Fermi-Hubbard Hamiltonian, the proposed scheme can be generalized to the quantum simulation of several other fermionic models, such as the Anderson impurity model. The target Hamiltonian describing a two-dimensional $N \times M$ lattice of Wannier orbitals is

$$\hat{\mathcal{H}}_{Hub} = -\lambda \sum_{\langle\mu,\nu\rangle,\sigma} \hat c^\dagger_{\mu,\sigma}\hat c_{\nu,\sigma} + U\sum_\mu \hat c^\dagger_{\mu,\uparrow}\hat c_{\mu,\uparrow}\hat c^\dagger_{\mu,\downarrow}\hat c_{\mu,\downarrow}, \tag{10.9}$$

where $\langle\mu,\nu\rangle$ are nearest neighbors ($\nu = \mu \pm 1$, $\nu = \mu \pm M$) and $\hat c_{\mu,\sigma}$ are fermionic operators. In order to simulate this Hamiltonian with our setup, we exploit the Jordan-Wigner transformation to map fermion operators $\hat c_\mu$ onto spin ones $\hat s_\mu$ [202, 203, 204]. However, if such a transformation is applied to the Hubbard model 10.9 in more than one dimension, the hopping (first) term results into XY spin couplings whose sign depends on the parity of the number of occupied states that are between μ and ν in the chosen ordering of the Wannier orbitals [205]. This aspect makes the simulation of a fermionic system much more demanding than any typical spin system, because the resulting effective spin Hamiltonian contains many-spin terms. To illustrate how we address this key issue, here we consider the simpler case of the hopping of spinless fermions on a lattice (the general case of interacting spin fermions is discussed below). The target Hamiltonian can be mapped into the following spin model:

$$\hat{\mathcal{H}}_\lambda = -\lambda \sum_{\langle\mu<\nu\rangle} (-1)^{\hat\alpha}\hat s^+_\mu \hat s^-_\nu + \text{h.c.}, \tag{10.10}$$

where $\hat\alpha = \sum_{\gamma=\mu+1}^{\nu-1}\hat c^\dagger_\gamma \hat c_\gamma \equiv \sum_{\gamma=\mu+1}^{\nu-1}(\hat s^z_\gamma + \frac{1}{2})$. We simulate this n-body interaction by taking care of the state-dependent phase, similarly to Refs. [206, 207]. The sign factor in Eq. 10.10 is obtained by performing a conditional evolution of the qubits interposed between the specifically addressed sites, μ and ν, depending on the state of μ. This corresponds to a series of controlled-Z (CZ) gates between qubit μ and each of the qubits γ interposed between μ and ν. Hence, the sequence of gates to be implemented at each Trotter step is the following:

$$\prod_{\mu<\gamma<\nu} \hat{U}_{CZ_{\mu,\gamma}} e^{-i\lambda\tau(\hat{s}_\mu^+\hat{s}_\nu^- + \hat{s}_\nu^+\hat{s}_\mu^-)} \prod_{\mu<\gamma<\nu} \hat{U}_{CZ_{\mu,\gamma}}. \tag{10.11}$$

For instance, in Fig. 10.4 we show the quantum circuit for the implementation of $\hat{\mathcal{H}}_\lambda^{1,5} = -\lambda(\hat{c}_1^\dagger\hat{c}_5 + \hat{c}_5^\dagger\hat{c}_1)$: controlled-phase gates (with $\varphi = \pi$) between qubit $|\psi_1\rangle$ and each of the qubits interposed between $|\psi_1\rangle$ and $|\psi_5\rangle$, namely $|\psi_2\rangle$, $|\psi_3\rangle$ and $|\psi_4\rangle$, are sequentially performed before and after the central block (dashed boxes), which implements the XY evolution: $\hat{U}_{XY} = \exp\{-i\varphi(\hat{s}_{1x}\hat{s}_{5x} + \hat{s}_{1y}\hat{s}_{5y})\}$. The latter consists of two controlled-φ gates (with $\varphi = 2\lambda\tau$), preceded and followed by proper single-qubit rotations, implementing respectively $\hat{s}_x\hat{s}_x$ and $\hat{s}_y\hat{s}_y$ terms of the interaction, as schematically explained in Fig. 10.4. By exploiting the high mobility of the photons entering into the hybrid encoding, Hamiltonian terms involving distant qubits can be simulated straightforwardly. In fact, this is a remarkable advantage with respect to alternative solid-state platforms for quantum information processing. We stress that, in spite of the increment in the number of gates required to address the sign issue, a large number of hopping terms can still be implemented in parallel.

10.2.3 Interacting fermions with spin

To extend the quantum simulation of two-dimensional Hubbard models to the case of fermionic systems with spin, we need to encode each fermion operator into a pair of qubits, corresponding to spin up and spin down. To achieve this, we exploit a generalization of the Jordan-Wigner transformation [208]. For this mapping we need to introduce two different spin 1/2 operators $\vec{\hat{S}}$ and $\vec{\hat{T}}$, with $\hat{S}_{2\mu-1}^z = \hat{c}_{\mu\uparrow}^\dagger\hat{c}_{\mu\uparrow} - \frac{1}{2}$ and $\hat{T}_{2\mu}^z = \hat{c}_{\mu\downarrow}^\dagger\hat{c}_{\mu\downarrow} - \frac{1}{2}$, describing respectively odd and even qubits (ordered by rows in the two-dimensional lattice).

$$\begin{aligned} \hat{S}_{2\mu-1}^+ &= \hat{c}_{\mu\uparrow}^\dagger e^{i\pi\sum_{\nu=1}^{NM}\hat{c}_{\nu\downarrow}^\dagger\hat{c}_{\nu\downarrow} + i\pi\sum_{\nu=1}^{\mu-1}\hat{c}_{\nu\uparrow}^\dagger\hat{c}_{\nu\uparrow}} \\ \hat{T}_{2\mu}^+ &= \hat{c}_{\mu\downarrow}^\dagger e^{i\pi\sum_{\nu=1}^{\mu-1}\hat{c}_{\nu\downarrow}^\dagger\hat{c}_{\nu\downarrow}}. \end{aligned} \tag{10.12}$$

It can be shown that these operators satisfy the usual angular momentum commutator algebra, and that $\left[\hat{S}_{2\mu-1}^\alpha, \hat{T}_{2\nu}^\alpha\right] = 0$. We assume that the fermion variables are ordered by rows in the Hamiltonian. The efficiency of the scheme would be increased by using a 2-dimensional setup consisting of N rows and $2M$ columns. We can write the Hubbard Hamiltonian in terms of the spin variables introduced above

$$\begin{aligned} \hat{H}_{Hub}^s &= -\lambda \sum_{\mu,\nu>\mu=1}^{NM} (-1)^{\sum_{\gamma=\mu+1}^{\nu-1}(\hat{S}_{2\gamma-1}^z + \frac{1}{2})} \hat{S}_{2\mu-1}^+\hat{S}_{2\nu-1}^- + \text{h.c.} \\ &- \lambda \sum_{\mu,\nu>\mu=1}^{NM} (-1)^{\sum_{\gamma=\mu+1}^{\nu-1}(\hat{T}_{2\gamma}^z + \frac{1}{2})} \hat{T}_{2\mu}^+\hat{T}_{2\nu}^- + \text{h.c.} \\ &+ U\sum_{\mu=1}^{NM}\hat{S}_{2\mu-1}^z\hat{T}_{2\mu}^z + \frac{U}{2}\sum_{\mu=1}^{NM}\left(\hat{S}_{2\mu-1}^z + \hat{T}_{2\mu}^z\right) + \frac{NMU}{4}, \end{aligned} \tag{10.13}$$

where μ and ν are nearest neighbors on the two-dimensional fermionic lattice, such that $\nu = \mu + 1$ (horizontal neighbors) or $\nu = \mu + M$ (vertical neighbors) with the present labeling. Odd (even) qubits encode spin up (spin down) variables. Since the hopping term does not act if $\langle \hat{c}^{\dagger}_{\mu\sigma}\hat{c}_{\mu\sigma}\rangle = 1$ (i.e. $\hat{c}^{\dagger 2}_{\mu\sigma} = 0$), we can start directly with $\gamma = \mu + 1$, and the exponential in expressions like $\hat{S}^{+}_{\mu} \exp\{i\pi \sum_{\gamma=\mu+1}^{\nu-1}(\hat{S}^{z}_{\gamma} + \frac{1}{2})\}\hat{S}^{-}_{\nu}$ can be factorized. We note that in the case of horizontal neighbors the phase factor cancels out and that in $\hat{H}^{s}_{Hub}$ do not appear terms $\hat{S}^{+}_{2\mu-1}\hat{T}^{-}_{2\nu}$, as we are not considering spin-flip processes.

To simulate such evolution we can proceed in a way analogous to the spinless case. Here, however, two different series of $CZ_{\mu,\gamma}$ should be carried out, depending if we are considering the hopping of spin ↑ or spin ↓ fermions. The former involves only odd values of γ, the second only even. Notice that, in a 2-dimensional register, we need to transfer photons to implement $\hat{S}^{+}_{2\mu-1}\hat{S}^{-}_{2\nu-1}$ or $\hat{T}^{+}_{2\mu}\hat{T}^{-}_{2\nu}$ each time we have to couple a pair of fermions belonging to the same row (due to the alternating ↑-↓ mapping), but in that case $\prod \hat{U}_{CZ_{\mu,\gamma}}$ is not required. The term $\prod \hat{U}_{CZ_{\mu,\gamma}}$, needed to correct the *sign problem*, is necessary only if $\nu = \mu + M$ (no photon transfer in that case is needed).

10.3 Discussion

We have proposed a digital quantum simulator based on hybrid spin-photon qubits, encoded in an array of superconducting resonators strongly coupled to spin ensembles. Within this quantum computing architecture, quantum gates are implemented by a single operational tool, namely by tuning the resonators frequencies. We have shown the feasibility of the scheme with state-of the-art superconducting arrays technology, which allows the high fidelity simulation of a large class of multi-qubits spin and fermionic models. To test our predictions, we have performed numerical simulations of the master equation for the system density matrix, including the most important decoherence channels such as photon loss and pure-dephasing of the transmon involved in two-qubit entangling gates.

Sources of errors. We analyze here the sources of error that affect the quantum simulation, and point out possible solutions. Three main simulation errors can be found: digital errors (arising from the Trotter-Suzuki approximation), gating errors (due to imperfect implementation of the desired unitaries), and decoherence errors (due to the interaction of the quantum simulator with the environment). While digital errors can obviously be reduced by increasing the number of Trotter steps or by using higher-order decompositions, gating errors are accumulated by repeating a large number of quantum operations. Similarly, the interaction of the system with the environment becomes much more pronounced if the simulation time increases.

As far as decoherence mechanisms are concerned, we first notice that the present setup *limits the role of the transmon*, which is not involved in the definition of the qubits. All transmons are kept in their ground states apart from the specific transmons involved in two-qubit gates, which are excited only for a short time. Thus, typical state-of-the-art technology, which ensures transmon dephasing times of the order of tens of microseconds, is sufficient to obtain high fidelity quantum simulations of relatively large systems. Coherence times of single spins are so long that their effect on quantum simulations can be disregarded. However, a potential drawback of spin ensembles is the presence of disorder which spreads the transition frequencies within the ensemble (inhomogeneous broadening). This eventually results in an irreversible population leakage from the superradiant mode (our logical $|0\rangle_{\mu}$, strongly coupled to the resonator) into dark modes out of the computational basis. We will introduce in the next Chapter 11 a scheme to prevent this damping effect, by operating in a *cavity-protection* regime, i.e. with a small spin-resonator detuning.

Photon loss represents the main source of decoherence in our hybrid dual-rail encoding. Its effect monotonically increases with the overall computational time, since both idle and manipulated qubits are influenced by it. We stress that the proposed platform allows us to manipulate simultaneously non-overlapping parts of the register, thus drastically reducing the overall computation time and decoherence-induced errors with respect to a serial implementation. Indeed, a pessimistic estimate of the decoherence error ($\epsilon = 1 - \mathcal{F}^2$) on N qubits subject to photon loss is given by $1 - e^{-NT\frac{\omega_c}{Q}} \approx NT\frac{\omega_c}{Q}$, where T is the total time of the simulation. This is obtained by considering the probability for the system prepared in the state with the maximum number of photons ($|1\rangle_1 \otimes ... \otimes |1\rangle_N$) to be still in the same state after time T. For simple Hamiltonians (e.g. the TIM or the Heisenberg model), in a serial implementation T scales with N, whereas in a parallel scheme T is independent of N. For example, the three-spins transverse Ising model reported above can immediately be extended to simulate longer spin chains, by addressing simultaneously first the "odd-bonded" and then the "even-bonded" qubits. Hence, the parallel implementation proposed here leads to a gain in the fidelity scaling as $\simeq e^{CN(N-2)}$, with respect to an analogous serial scheme. This makes the present architecture very competitive, in view of scaling it to a relatively large array.

In this parallel implementation, for simulation times much smaller than the characteristic photon loss damping time ($\sim \frac{Q}{\omega_c N}$), errors are mainly due to gate imperfections. Using the numbers reported in the third column ($\mathcal{F}_I$) of Table 10.1, we can heuristically estimate the number of gates allowed by the proposed platform. For simplicity, we follow Ref. [95] and assume single-gate errors as independent and add them. As a threshold, we require the overall fidelity after the implementation of the full sequence to be above 90%. This would allow us to perform more than 1000 single-qubit rotations or $\sim$ 120 controlled-Z two-qubit gates. For instance, in the extension of the simulation of the transverse field Ising model to $N = 10$ qubits, the estimated gating error ϵ_g for each Trotter step is still very small, below 0.02 (corresponding to a fidelity of 99%). In the case of the more demanding $N = 10$ Heisenberg model we find $\epsilon_g = 0.07$.

We note that gating errors are mainly due to the relatively small difference ($\tilde{\delta}$) between the photon frequency and transmonic gaps in the auxiliary cavities, which induces a residual interaction that is never completely switched off. This leads to a leakage of a fraction $G/\tilde{\delta}$ of the wave-function, which decreases the fidelity. Here we use the tunability of the resonator frequency as the only tool to process quantum information, but the flux control of the Josephson energy of the transmons [44, 209] can also be exploited to increase the detuning, thus leading to even larger fidelities. This additional degree of freedom would in turn allow us to employ larger values of the transmon-resonator couplings (commonly reported in literature), thus reducing the time required to implement two-qubit gates and hence the effect of decoherence. To keep the experimental demonstration of the proposed scheme as easy as possible, in the above simulations we have employed the tunability of the resonators as the only manipulation tool, using parameters which are a trade-off between the two effects of reducing the gating time and increasing the leakage.

We finally remark that quantum error correction (QEC) would also represent a powerful tool to improve the performance of the digital simulator. QEC schemes can be embedded in the present setup. For instance we could introduce ancillae qubits to implement the three qubit bit-flip and phase-flip codes [11]. These consist of single qubit rotations, two qubit gates between each ancilla and the logical qubit and a three qubit Toffoli gate

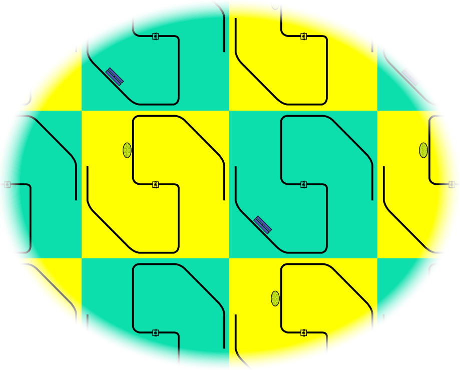

Figure 10.5: Schematic representation of a two-dimensional implementation of the digital quantum simulator. Dark lines show superconducting coplanar resonators routed such that each resonator is coupled to four adjacent resonators. Yellow boxes indicate *logical* resonators containing ensembles of $s = 1$ spins near the magnetic field antinodes, while green boxes indicate *auxiliary* resonators containing transmons near voltage antinodes. Flux biasing of the resonator SQUIDs could be accomplished using microwave lines placed on another layer.

(or equivalently a controlled-controlled-Z gate). In a one-dimensional logical array, the ancillae can be placed just above and below each logical qubit, connected to a common auxiliary resonator. In this way the ancillae can directly interact with the logical qubit, allowing us to implement two-qubit gates between them. The controlled-controlled-Z gate can be obtained without decomposing it into a more demanding sequence of two qubit gates, in a way similar to that proposed for the controlled-Z gate, by exploiting the fourth level of the transmon to induce a 3-step Rabi flop. The detailed description of this scheme is beyond the scope of this work and will be given elsewhere.

Two-dimensional arrays. While any model can be implemented onto a one-dimensional register (e.g., the one schematically illustrated in Fig. 10.1) at the cost of requiring long-range two-qubit gates, it is clear that a register topology directly mimicking the target Hamiltonian would greatly reduce the simulation effort. In particular, there are several important Hamiltonians defined on two-dimensional lattices whose simulation would greatly benefit from a two-dimensional register. Here, we point out that our scheme is straightforwardly usable on such a register, but its experimental realization necessarily requires the implementation of two sub-lattices of cavities, alternatively coupled to spin and transmon qubits, respectively. Fortunately, resonator arrays with complex network topologies are realistically possible, already, as each cavity can easily couple to multiple other resonators. Fig. 10.5 displays the schematic drawing of a potential two-dimensional layout showing how such sub-lattices could feasibly realize a two-dimensional simulator. From a technological point of view, we notice that similar lattices with transmon qubits have been fabricated with more than 200 coupled cavities [40]. While local tuning in such a lattice would require local flux bias on a separate layer, this need for local control lines applies to any adjustable quantum simulator. On the other hand, we notice that a recent technology has shown promising results to bring flux lines to the interior part of a lattice made of a small number of nodes, e.g. by using Aluminum airbridge crossovers to route microwave signals into a target resonator [210].

Summary. In conclusion, the proposed setup exploits the best characteristics of distinct physical systems: the long coherence times of the spins, which can encode quantum information and protect it from decoherence, and the mobility of photons entering this hybrid encoding of qubits. In the end, this allows to realize long-range two-body interactions between distant qubits without the need for much more demanding SWAP gates. Moreover, on-site tunability and scalability make this architecture extremely appealing and competitive with respect to alternative proposals, either based on superconducting arrays or on different technologies.

The content of this chapter was published in NPG Sci. Rep. **5**, 16036 (2015) (Ref. [200]).

Long-lasting quantum information processing in a cavity-protection regime

CHAPTER 11

Implementing complex sequences of gates is crucial for any quantum computing architecture to become practical. This requires long-lived qubits which can be manipulated many times without errors. We focus here on the hybrid setup introduced in Chapter 9, in which hybrid spin-photon qubits replace the superconducting units to encode information [171, 172]. In such a novel setting a single manipulation tool (the tunability of resonators frequencies) is sufficient to implement a universal set of gates. However, inhomogeneous broadening (IB) of SEs remains the major challenge to overcome before any of these proposals can practically be realized. It was recently pointed out that a strong spin-cavity coupling can provide a protection mechanism for spin-based memories as long as the spin flip energy is close to the resonator frequency [189, 188], which has been experimentally demonstrated very recently [211].

While great attention has been recently focused on the storage of excitations in the SE, a proposal to implement single or sequences of gates with high-fidelity by long-lived SEs is still lacking. In this Chapter, we address this unsolved issue by operating the hybrid spin-photon qubits in a cavity-protected regime, thus exploiting the spins not only for storing but also for processing quantum information for long times. We show that by combining a suitable spin-1 system with a proper time-dependent tuning of the resonators frequency, a universal set of gates can be implemented with coherence times no longer limited by IB. This paves the way to the actual scalability of this hybrid architecture. On the one hand, as discussed in Chapter 10, scalability is made possible by the inherent definition of the long-lived qubits, represented by coupled SE-resonator devices that can be repeated in an array. On the other hand, the mobility of photons and the use of spin-1 ensembles are crucial to perform two-qubit gates between physically distant qubits, without much more demanding SWAP gates. These resources make the class of problems that can be realistically addressed much larger. As test examples, we report full numerical experiments for the digital quantum simulation of the XY model on a pair of qubits and for the quantum Fourier transform on a chain of three qubits, which

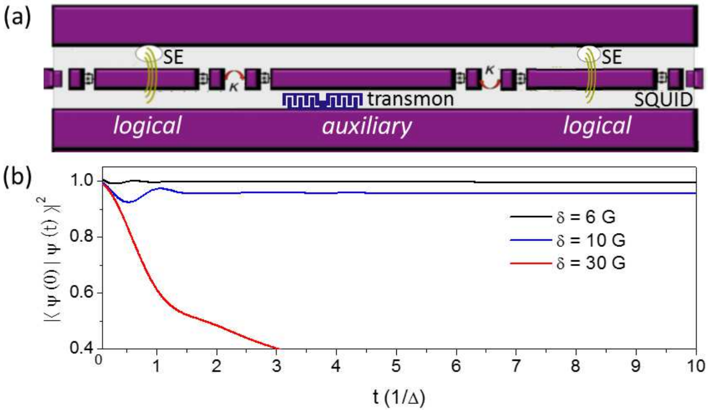

Figure 11.1: (a) Elementary unit of the scalable setup. *Logical* resonators include an ensemble of $s = 1$ spins placed at the antinode of the magnetic field (rotational lines) of the cavity mode. The *auxiliary* resonator contains a transmon coupled to the electric field. The frequency of each resonator is tuned by means of a SQUID [147]. (b) Evolution of the super-radiant mode coupled to a bath of dark modes, calculated for different values of the spin-resonator detuning δ, while keeping the collective spin-resonator coupling G_{-1} to 30 MHz. We have assumed a gaussian distribution for the spin gaps, with FWHM $\Delta = 1$ MHz. The system is initialized into an eigenstate of the single qubit Hamiltonian, $|\psi(0)\rangle_\mu = \cos\frac{\theta}{2}|0\rangle_\mu + \sin\frac{\theta}{2}|1\rangle_\mu$, in order to point out the effect of the coupling with the dark modes. By decreasing δ, the system is more protected. $\delta = 6\,G_{-1}$ ensures that only 1% of the wave-function is lost for long times.

constitutes the fundamental building block of the Shor's factoring algorithm [11]. The robustness of the scheme is demonstrated by realistically including the main sources of decoherence in a master equation formalism, and working with state-of-the-art parameters. Remarkably, the experimental realization of the present proposal only requires assembling elements that have already been separately demonstrated.

11.1 Setup

We recall here the definition of the terms entering the system Hamiltonian. As in the previous chapter, each qubit is encoded in a coplanar superconducting waveguide resonator, strongly coupled to an ensemble of effective $s = 1$ spins. The photon and the two collective excitations of the SE from $m = 0$ to $m = \pm 1$ are described as boson fields ($\hat{a}_\mu$ and $\hat{b}_{\mu,m}$), with Hamiltonians $\hat{H}_{ph} = \omega_c^\mu(t)\hat{a}_\mu^\dagger \hat{a}_\mu$ and $\hat{H}_{spin} = \sum_m \omega_m \hat{b}_{\mu,m}^\dagger \hat{b}_{\mu,m}$, where μ labels the resonators. In the rotating-wave approximation, photons are coupled to the collective m excitation of the SE through $\hat{H}_{spin-ph} = \sum_m G_m(\hat{a}_\mu^\dagger \hat{b}_{\mu,m} + \hat{b}_{\mu,m}^\dagger \hat{a}_\mu)$. The logical state $|0\rangle_\mu$ ($|1\rangle_\mu$) corresponds to zero (one) photons and a single (zero) quantum in the $m = -1$ spin-oscillator in cavity μ.
The elementary unit of the scalable array is shown in Fig. 11.1-(a): it consists of two *logical* resonators encoding two qubits, and an interposed *auxiliary* cavity containing a non-linear three-level system such as a transmon, which is used for two-qubit gates. This is described by $\hat{H}_{tr} = \Omega_{01}|\psi_{1,\mu}\rangle\langle\psi_{1,\mu}| + (\Omega_{12} + \Omega_{01})|\psi_{2,\mu}\rangle\langle\psi_{2,\mu}| + (g_{01}\hat{a}_\mu|\psi_{1,\mu}\rangle\langle\psi_{0,\mu}| + g_{12}\hat{a}_\mu|\psi_{2,\mu}\rangle\langle\psi_{1,\mu}| + \text{h.c.})$. Photon hopping is induced by capacitive coupling between neighboring resonators, $\hat{H}_{ph-ph} = -\kappa\sum_\mu(\hat{a}_\mu^\dagger \hat{a}_{\mu+1} + \text{h.c.})$. In the following, *logical* cavities will be labeled with odd μ, while *auxiliary* ones with even μ.

11.2 Inhomogeneous Broadening of the spin ensemble

A certain degree of spin inhomogeneity is unavoidable in real SEs, and may result from slightly disordered spin environments or by random magnetic fields produced by surrounding nuclear magnetic moments. In the spin-wave representation, the effect of such disorder is the dynamical coupling of the collective (*super-radiant*) ($k = 0$) mode with the subradiant ($k \neq 0$) ones. Here k is a quantum number labeling the one-boson states (and it coincides with the wave-vector of the magnons in a translationally-invariant arrangement of the spins). A transition to these subradiant modes can be regarded as an irreversible population leakage out of the subspace $\{|\psi_0\rangle, |\psi_1\rangle\}$, and thus of the computational space. Due to IB, the (*super-radiant*) spin-excitation (the only one that couples to the photon field) spontaneously decays into the quasi-continuum of decoupled, *dark*, spin modes. In the absence of cavity-spin coupling, this happens within a timescale of order $\hbar/\Delta$, Δ being the width of the distribution of gaps in the SE.

A possible way to deal with IB is to revert the associated Hamiltonian evolution by echo techniques [212, 213, 199], but implementing them within our encoding would be very demanding. Pulses should act with very high fidelity, and should be controlled independently for each *logical* resonator with the proper timing to restore qubits before they undergo gates. To date, the practical implementation of such schemes, which also require to tune the resonator quality factor in order to avoid emitting a microwave echo from the inverted spin ensemble, is still difficult.

Here we exploit only the tunability of individual resonator modes [160, 147] to solve the problem and efficiently implement quantum gates. These are performed by keeping the SE in a *cavity-protection* regime [188, 189]: strong SE-resonator coupling induces an energy gap between the computational (super-radiant) and the non-computational (dark) modes [189], thus effectively decoupling them. The mechanism has already been experimentally demonstrated in the resonant regime [211]. Out of resonance ($\delta = \omega_{-1} - \omega_c(0) \gg G_{-1}$) and in presence of strong coupling ($G_{-1} \gg \Delta$), the resonator has a dispersive effect which shifts the energy of the superradiant mode by $\epsilon = -G_{-1}^2/\delta$. Provided that $\epsilon \gg \Delta$ and that the tail of the emitter's bare frequencies distribution $\rho(\omega)$ falls off sufficiently fast (as in the case of a Gaussian profile) [188], the superradiant mode is energetically separated from the subradiant modes and the resonator protects the information stored into the spin ensemble.

However, reducing δ leads to unwanted oscillations of a significant fraction ($\sim G_{-1}/\delta$) of the wave-function between logical states $|0\rangle_\mu$ and $|1\rangle_\mu$. The one-qubit Hamiltonian $\hat{H}_{1q}$, within the single excitation subspace, can be written as $\hat{H}_{1q} = G(|0\rangle\langle 1| + |1\rangle\langle 0|) + \delta|1\rangle\langle 1|$, i.e., in matrix form:

$$H_{1q} = \begin{pmatrix} 0 & G \\ G & \delta \end{pmatrix}, \tag{11.1}$$

The eigenvectors of $\hat{H}_{1q}$ can be recast in the form $|\psi_-\rangle = \cos\frac{\theta}{2}|0\rangle - \sin\frac{\theta}{2}|1\rangle$ and $|\psi_+\rangle = \sin\frac{\theta}{2}|0\rangle + \cos\frac{\theta}{2}|1\rangle$, with $\theta = \mathrm{acot}\frac{\delta}{2G}$ and corresponding eigenvalues $E_\pm = \frac{\delta}{2} \pm \sqrt{G^2 + \delta^2/4}$. The unitary matrix which describes the semi-resonant evolution associated to $\hat{H}_{1q}$, in interaction picture is

$$U = e^{-i\frac{\delta\tau}{2}} \begin{pmatrix} \cos\nu\tau + \frac{i\delta}{\sqrt{\delta^2+4G^2}}\sin\nu\tau & -\frac{2iGe^{-i\delta t_0}}{\sqrt{\delta^2+4G^2}}\sin\nu\tau \\ -\frac{2iGe^{i\delta t_0}}{\sqrt{\delta^2+4G^2}}\sin\nu\tau & \cos\nu\tau - \frac{i\delta}{\sqrt{\delta^2+4G^2}}\sin\nu\tau \end{pmatrix}$$

where $\tau = t - t_0$, t_0 is the time at which U starts to act and we assumed Schrödinger and interaction picture coincident at $t = 0$. The oscillation frequency is $\nu = \sqrt{G^2 + \delta^2/4}$. [1] These semi-resonant oscillations can be compensated within our scheme, because they merely represent single-qubit rotations (see below).

As a first step, we numerically determine the time evolution of the single-qubit wavefunction, $|\psi(t)\rangle_\mu$, coupled to a bath of dark modes, using the formalism of Ref. [188]. The system is described by a non-hermitian Hamiltonian $\hat{H}_{eff}$ obeying a Schrödinger-like equation $\frac{d}{dt}|\psi(t)\rangle_\mu = -i\hat{H}_{eff}|\psi(t)\rangle_\mu$, and involving the spin frequencies spread according to a gaussian distribution and the complex photon frequency $\tilde{\omega}_c^\mu = \omega_c^\mu - i\Gamma/2$, where $\Gamma = \omega_c^\mu/Q$ is the photon loss rate and Q the quality factor of the resonator. The time evolution of the qubit wavefunction is obtained by the Laplace transform method. We compute $|\psi(t)\rangle_\mu = L^{-1}[(s + iH_{eff})^{-1}|\psi(0)\rangle_\mu]$, where $L[f(t)] \equiv F(s) = \int_0^\infty e^{st} f(t) dt$. Results are shown in Fig. 11.1-(b) for a state initially prepared in $|\psi(0)\rangle_\mu = \cos\frac{\theta}{2}|0\rangle_\mu + \sin\frac{\theta}{2}|1\rangle_\mu$, which is an eigenstate of the single qubit Hamiltonian with $\cot\theta = \frac{\delta}{2G_{-1}}$. Thus, the observed evolution of $|\psi(t)\rangle_\mu$ is entirely due to the coupling of the qubit with the dark modes. We have assumed a realistic coupling $G_{-1} = 30$ MHz and a SE with gaussian broadening and FWHM $\Delta = 1$ MHz [160, 188]. The cavity-protection mechanism is enhanced on decreasing the detuning δ: for $\delta = 6\,G_{-1}$ only $\approx 1\%$ of the wave-function is lost in the dark modes at long times. As expected, this is lower than the upper bound ($4\sigma^2\delta^2/G_{-1}^4 \approx 2.8\%$) obtained in Ref. [189]. Hence, in this regime the SE coherence times increases by orders of magnitudes and approaches the intrinsic single-spin time. The damping induced by IB can then be safely neglected. The next task is to embed this cavity-protection mechanism within an efficient quantum computation scheme, which is by no means trivial.

11.3 Choice of the spin system

The robustness of the scheme relies on the choice of a suitable spin system. The ideal spin system has a narrow distribution of the energy gaps, which decays faster than a Lorentzian. Good candidates are ordered systems, or spin systems with gaussian broadening, possibly isotropic and diluted in a non-magnetic matrix, so as to avoid dipolar interactions, which typically lead to lorentzian line-shapes. Another important mechanism of decoherence is represented by hyperfine interactions between electronic and nuclear spins. These tend to reduce the intrinsic decoherence time of the individual spins, and introduce a gaussian broadening of the transition energies. At least the largest contribution to the hyperfine couplings, represented by the contact term, can be avoided by considering spin systems where the magnetic ions have non-magnetic nuclei. Moreover, the spin gaps should be close to the frequency of current circuit QED resonators.

Hence, the best systems are the so-called S-ions (like Fe^{3+} or Gd^{3+}) whose orbital angular momentum vanishes because of Hund's rules. This makes them practically insensitive to disorder in the environment. In addition, the number of nuclear spins should be minimized, as these produce random quasi-static magnetic fields causing IB. Linewidths as small as a fraction of Gauss are indeed observed in diluted magnetic semiconductors,

---

[1] Notice that this expression is valid only if the semi-resonant evolution is followed by a phase gate $\hat{R}_z[-(\omega_c - \omega_{-1})\tau]$. In resonance $\delta = 0$ and we obtain a rotation in XY plane, where the rotation axis is determined by the choice of t_0. In semi-resonant conditions δ and G are comparable and it is not possible to trivially obtain a R_z rotation. However, R_z rotations are essential for any algorithm. U reduces to $R_z(\delta\tau)$ only in the limit of very large detuning ($\delta \gg G$). In that case the semi-resonant oscillations become very fast and involve a negligible part of the wave-function.

such as Fe^{3+} in ZnS [214, 215, 216], whose nuclei are mostly spinless. Even narrower lines are observed for P-doped Si [217]. We note that the use of $s > 1$ spins increases G_{-1}, and thus the protection mechanism. The proper choice of the spin system leads to a degree of cavity protection much higher than that reported in the milestone experiment of Ref. [211], where the SE consisted of standard NV centers. This is not an ideal choice, since the spin-photon coupling is small (~ 8 MHz), and the gap distribution is broad (~ 9 MHz) and relatively fat-tailed.

To keep the experimental demonstration as easy as possible, we assume $\omega_c^\mu = 14$ GHz for the *logical*, and 10.2 GHz for the *auxiliary* resonators, lower than the frequencies employed in Ref. [46]. SEs fitting our scheme with a 14 GHz resonator can be easily found: Fe^{3+} impurities in the same Al_2O_3 matrix employed in [46] display suitable gaps with an applied magnetic field of ~ 70 mT forming an angle of $\sim 70^\circ$ with the anisotropy axis (given an easy-plane anisotropy with $D = 5.15$ GHz [218]).

11.4 QIP with inhomogeneously broadened SE

In the hybrid encoding, single-qubit rotations, $\hat{R}_x$ and $\hat{R}_y$, are obtained by temporarily bringing the frequency of the μ-th cavity, ω_c^μ, into resonance with the spin gap ω_{-1}, whereas $\hat{R}_z$ is obtained by a non-resonant variation of ω_c^μ. The main consequence of working in a protected regime is the occurrence of unwanted one-qubit oscillations with frequency $\nu = \sqrt{G_{-1}^2 + \delta^2/4}$. These can be incorporated in the implementation of gates by choosing a starting time $\tilde{t}_s = 2n\pi/\nu$. However, gate starting times t_s cannot be chosen at will. For instance, the axis of one-qubit rotations in the x, y plane is selected by t_s [172]. The problem of matching the two constraints is solved by adding a *rephasing gate*, consisting in significantly increasing δ (thus freezing unwanted oscillations) for a time $\Delta t_s = t_s - \tilde{t}_s$, with $\delta\, \Delta t_s = 4\pi n$. We stress that Δt_s is orders of magnitude shorter than that characterizing the damping due to IB. Hence, this temporary loss of cavity protection has no effects on the overall computation.

Two-qubit controlled-phase gates are implemented by sequentially moving the photonic component of *logical* resonators into the same *auxiliary* cavity, and inducing a two-step Rabi-flop involving the transmon. The only part that is affected by the unwanted oscillations is the photon hopping between *logical* and *auxiliary* cavities, whose starting time needs to be chosen again as $t_s = 2n\pi/\nu$. Notice that a rephasing gate is also needed during the photon hopping processes, in order to avoid the oscillation of a significant fraction of the wave-function. In fact, this would result in an incomplete transfer of the photonic component of the wave-function. Again, hopping processes occur on times much shorter than the SE damping time, and could be further reduced by increasing κ.

Finally, in the not protected regime the photonic component of the wave-function acquires a phase. This results in an $\hat{R}_z$ rotation which can be compensated by slightly changing the detuning (in order to produce the desired identity evolution).

To test the performance of this scheme we first numerically determine the fidelity of a universal set of gates. In all the calculations reported below we also include decoherence effects. These are mainly due to photon loss and pure dephasing of the transmon [172], parameterized by the resonators quality factor (Q) and by the transmon dephasing time (T_2^{tr}) in the equation of motion:

$$\dot{\hat{\rho}} = -i\left[\hat{H}, \hat{\rho}\right] + \sum_\mu \frac{\omega_c^\mu}{Q} \mathcal{D}_{\hat{a}_\mu}[\hat{\rho}] + \frac{1}{T_2^{tr}} \sum_{\mu,i} \mathcal{D}_{|\psi_{i,\mu}\rangle\langle\psi_{i,\mu}|}[\hat{\rho}]. \tag{11.2}$$

	$\hat{R}_x(\pi/2)$	$\hat{R}_z(\pi/2)$	$\hat{U}_{CNOT}$	$\hat{\mathcal{H}}^{(2)}_{yy}$	$\hat{\mathcal{H}}^{(2)}_{zz}$	$\hat{\mathcal{H}}^{(2)}_{yz}$
t	6.3 ns	0.5 ns	86.2 ns	86.2 ns	64.5 ns	86.2 ns
$\mathcal{F}$	99.77 %	99.85 %	98.75 %	98.66 %	99.02 %	98.50 %

Table 11.1: Fidelity ($\mathcal{F}$) and duration of single- ($\hat{R}_x(\phi)$ and $\hat{R}_z(\phi)$) and two-qubit gates (controlled-NOT), and to simulate the elementary terms of a generic two-body spin Hamiltonian (for $\lambda\tau = \pi/2$). Single-qubit rotations corresponds to simulating single-spin terms in the spin Hamiltonian (with $\phi = b\tau$). The fidelity has been computed on a random initial state, by assuming a Lindblad dynamics, with $Q = 10^6$ and $T_2^{tr} = 10\ \mu s$, and operating in a cavity-protected regime with $\delta = 6\,G_{-1}$.

Here $\mathcal{D}_{\hat{x}}[\hat{\rho}] = -\frac{1}{2}\left(\hat{x}^\dagger\hat{x}\hat{\rho} + \hat{\rho}\hat{x}^\dagger\hat{x}\right) + \hat{x}\hat{\rho}\hat{x}^\dagger$ and $\hat{H}$ is the full system Hamiltonian. We assume the resonator frequency $\omega_c(0)/2\pi = 14$ GHz and the photon hopping $\kappa = 30$ MHz. For the SE we use excitation frequencies $\omega_{-1}/2\pi = 14.18$ GHz, $\omega_1/2\pi = 12$ GHz and SE-photon couplings $G_{-1} = 30$ MHz, $G_{+1} = 33$ MHz. For the auxiliary resonator we assume a frequency $\tilde{\omega}_c(0)/2\pi = 10.2$ GHz, transmon gaps $\Omega_{01}/2\pi = 9.2$ GHz, $\Omega_{12}/2\pi = 8.3$ GHz and transmon-photon couplings $g_{01} = 30$ MHz, $g_{12} = 40$ MHz. At last, we use a detuning $\delta = 6\,G_{-1}$ for cavity protection. These parameters correspond to state-of the art-technology [177, 39]. Results for elementary gates are listed in Table 11.1. It is worth noting that fidelities are very high, even with the inclusion of the most important decoherence channels and by operating in the cavity-protection regime.

11.5 Numerical experiments

Here we report numerical experiments demonstrating the performance of our scheme in solving some paradigmatic problems. As a first implementation we consider a digital quantum simulator. Digital techniques have been recently proposed in a superconducting circuitry architecture [95] and proof-of-principle demonstrations on a limited number of qubits have just been realized [196]. As explained in Section 0.1.5 and in Chapter 10, they are based on the decomposition [16] of the evolution operator of the target Hamiltonian $\hat{\mathcal{H}}$ into the product of terms acting on short time intervals. Since many problems can be mapped into a spin Hamiltonian, we focus on elementary terms consisting of one- ($\hat{\mathcal{H}}^{(1)}_\alpha$) and two-qubit ($\hat{\mathcal{H}}^{(2)}_{\alpha\beta}$) Hamiltonians, of the form: $\hat{\mathcal{H}}^{(1)}_\alpha = b\hat{s}_\alpha$ and $\hat{\mathcal{H}}^{(2)}_{\alpha\beta} = \lambda\hat{s}_{1\alpha}\hat{s}_{2\beta}$. The corresponding time evolution operator can be implemented by means of single- and two-qubit gates [17]. The fidelities calculated for the simulation of these elementary steps (Table 11.1) are very high, thus demonstrating the effectiveness of our scheme. A proof-of-principle experiment that could be readily performed is the simulation of the dynamics resulting from an XY interaction ($\hat{\mathcal{H}}_{XY} = \lambda[\hat{s}_{1x}\hat{s}_{2x} + \hat{s}_{1y}\hat{s}_{2y}]$) between two spins $s = 1/2$, which is also the central step in the simulation of hopping processes in fermion Hamiltonians. Figure 11.2-(a) shows that the time evolution is very well reproduced (solid circles). These results can be compared with those obtained in a non-protected regime (large spin-resonator detuning). The effect of IB is assessed by including in the master equation a damping term acting on the SE collective excitations $\gamma\sum_{\mu,m}\mathcal{D}_{\hat{b}_{\mu,m}}[\hat{\rho}]$, with $\gamma = \Delta/2\pi = 1$ MHz (empty circles), representing the irreversible leakage of the spin excitation in the dark modes [189]. It is evident that in the non-protected regime IB would lead to completely unreliable results.

The expectation values of relevant operators in the computation of $\mathcal{H}_{xx}$ are reported as a colormap in panel (b). Notice the oscillations of the bosonic occupations induced by the

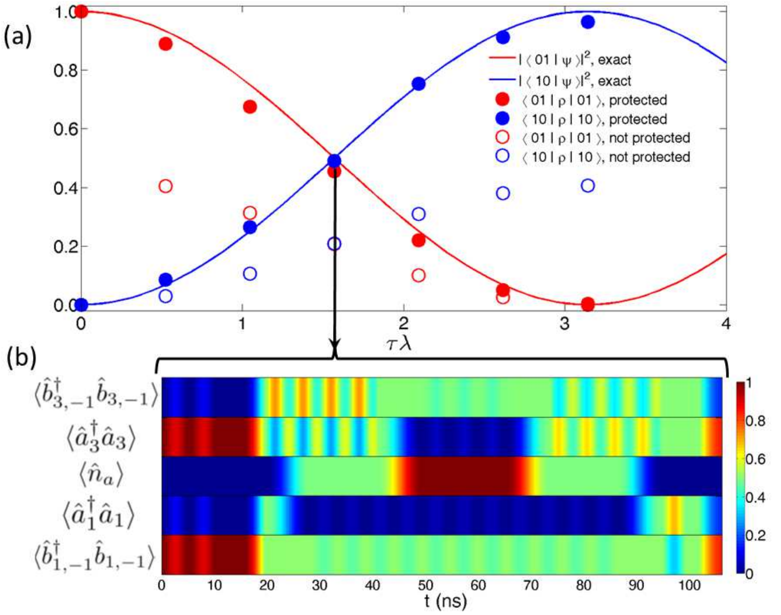

Figure 11.2: (a) Simulation of the XY model with two hybrid qubits. Lines represent the exact evolution, whereas points are calculated with the Lindblad formalism ($Q = 10^6$, $T_2^{tr} = 10\ \mu s$) within the cavity protection regime (solid circles) or not (empty). (b) Time-dependence of the expectation values of number operators during the first half of the simulation of $\mathcal{H}_{XY}$ for the point $\tau\lambda = \pi/2$. The operator $\hat{n}_a = \hat{a}^\dagger_2\hat{a}_2 + |\psi_{1,2}\rangle\langle\psi_{1,2}| + 2|\psi_{2,2}\rangle\langle\psi_{2,2}|$ represents the total number of excitations in the *auxiliary* resonator.

cavity-protection regime. We finally stress that the scheme, besides defeating IB, enables the implementation of a large number of two-qubit gates in parallel.

We now consider a chain of three qubits. An interesting example (see Sec. 0.1.3) is the implementation of the quantum Fourier transform (QFT), which constitutes the basic building block of powerful algorithms, such as Shor's and the quantum phase estimation algorithms [11]. The quantum circuit implementing QFT is shown in Fig. 11.3-(a): it consists of three Hadamard and three controlled-phase gates. Fig. 11.3-(b) is a schematic view of the hardware: *logical* resonators are represented by squared, odd-numbered boxes, while *auxiliary* resonators are circular and even-numbered. The implementation of the QFT involves two-qubit gates between physically distant qubits: here a controlled-$\hat{R}_z(\frac{\pi}{4})$ between qubits 1 and 5 is required [highlighted box in panel (a)]. To achieve this we do not need to fully transfer the state of qubit 1 into cavity 3 by means of a sequence of error-prone two-qubit gates, because the 1-3 SWAP is replaced by a much less demanding photon hopping process. Once the photon components of the two qubits involved in the controlled operation have been brought into neighboring *logical* resonators, the controlled-phase gate is implemented, and the photon components are finally brought back. We now illustrate this photon-transfer process, by reporting in Fig. 11.3-(c) the time-dependence of bosonic excitations, for a simple initial state $\frac{1}{\sqrt{3}}|0_1 0_3 0_5\rangle + \sqrt{\frac{2}{3}}|1_1 1_3 1_5\rangle$. In the idle phase (step I), each qubit is subject to oscillations between its photon and spin components, induced by the cavity-protected regime. After an integer number of oscillations, the photonic component of qubit 3 is absorbed

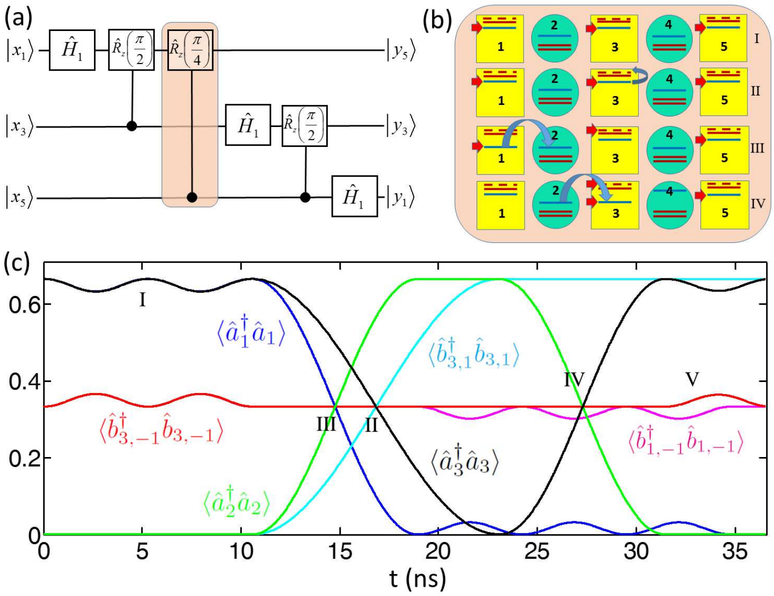

Figure 11.3: (a) Quantum circuit implementing the QFT on three qubits. Each Hadamard gate can be decomposed into the product of two rotations: $\hat{H}_1 = i\hat{R}_y(\pi/2)\hat{R}_z(\pi)$. (b) Sketch of the three-qubit setup and of the elementary operations required to transfer a photon from *logical* resonator 1 to *logical* resonator 3. Here we show the $|1_1 1_3 1_5\rangle$ component of the wave-function, with the excitations (red arrows) stored into the photonic degrees of freedom (blue lines). Red (continuous and dashed) lines represent the excitation energies of the spin oscillators ($m = -1$ and $m = 1$). (c) Expectation values of the photon ($\hat{a}_\mu$) and spin boson ($\hat{b}_{\mu,m}$) occupations in the photon-transfer process shown in (b), with the state initialized into $\frac{1}{\sqrt{3}}|0_1 0_3 0_5\rangle + \sqrt{\frac{2}{3}}|1_1 1_3 1_5\rangle$. Oscillations of $\hat{a}_5$ and $\hat{b}_{5,m}$ are not shown for clarity.

into the $m = 1$ spin oscillator (II). Simultaneously, cavity 1 is brought into resonance with the neighboring *auxiliary* resonator 2, thus inducing a photon hopping (III). Then the same process is repeated with cavities 2 and 3, while detuning the *auxiliary* resonator 4 in order to avoid unwanted hoppings (IV). Finally qubits 1 and 5 are kept far from resonance for $\sim$ ns to rephase their oscillations with those of the qubit 3 (V). We note that the photon component of qubit 3 is stored into the $m = 1$ spin oscillator only for the time required to the photonic component of qubit 1 to cross the resonator ($\sim 15\ ns$). Indeed, the photon coming from resonator 1 is immediately subject to hopping towards *auxiliary* cavity 4, in order to implement a Cφ. We have performed a numerical experiment by solving Eq. 11.2 for the whole QFT implementation for several random initial states. We find an average fidelity of about 93.6%, which is remarkably good since all the most important decoherence mechanisms have been taken into account. The total time required for the QFT on three qubits is about 300 ns.

These non-trivial examples illustrate the potential scalability of the proposed setup to a sizeable number of qubits. In particular, the use of effective $s = 1$ spin ensembles is crucial to exploit the mobility of photons and implement two-qubit gates between physically distant qubits, without needing high-demanding and error-prone sequences of SWAP gates.

11.6 Conclusions

In conclusion, we have shown that a quantum computation scheme based on a hybrid spin-photon qubit encoding can solve the major issue of inhomogeneous broadening, by operating in a cavity-protected regime. We have corroborated this result by performing extensive numerical experiments on test examples, using parameters corresponding to state-of-the-art technology and concretely proposing spin systems suitable for an experimental implementation. The very high fidelity obtained in the simulation of paradigmatic algorithms, together with the enhanced coherence times of SEs opens the path to the scalability of the proposed architecture to a large array of resonators.

The content of this chapter was submitted for peer-review.

Conclusions and perspectives

CHAPTER 12

To sum up, in this thesis we have presented two different approaches to the physical implementation of a quantum computing architecture, both based on spin technologies. These are particularly promising, since spin degrees of freedom are substantially protected from the interaction with the environment and can be manipulated with electromagnetic fields.

In the first one qubits are encoded in the ground doublet of anti-ferromagnetic molecular rings of Cr_7Ni, which display pretty long coherence times at low temperature. Thanks to recent advances in coordination chemistry, pairs of Cr_7Ni can be properly linked by an interposed magnetic ion, such as Ni^{2+} or Co^{2+}. We have shown that a universal set of one and two-qubit gates can be implemented either by uniform magnetic pulses, either by a local electric control of the Co^{2+} redox-active unit. In both cases, the divalent ion connecting the two Cr_7Ni rings acts as a switch of the effective inter-qubit interaction. Two-qubit complexes fitting the requisites of the present proposal have already been synthesized and characterized. These compounds have been studied by means of first-principle calculations, as well as by advanced experimental techniques such as electron paramagnetic resonance, magnetometry and inelastic neutron scattering. The recently developed ab-initio approach is based on the construction of system-specific many-body models, describing strong-correlation effects between the localized d electrons, and on the subsequent derivation of the low-energy spin Hamiltonian. This is then reduced by exploiting the symmetry properties of the examined system and diagonalized, in order to compute the observables and compare with experiments. Understanding the effects and the origin of the decoherence mechanisms is crucial to exploit chemically engineered molecular states as a resource for quantum information processing. These are modeled by considering intermolecular-dipolar, spin-phonon and hyperfine interactions, thus reproducing the observed experimental behaviour of the dephasing rate in a single crystal of Cr_8Zn anti-ferromagnetic wheel.

The second architecture consists of macroscopic hybrid spin-photon qubits, represented by spin ensembles strongly coupled to single photons, stored within coplanar superconducting waveguide resonators. This technology exploits the best characteristic of distinct physical systems, namely the long coherence times of the spins and the mobility of photons, which allows to realize long-range two-body interactions between distant qubits. The tunability of the resonator frequency is exploited as the only manipulation tool to implement single and two-qubit entangling gates, by bringing the photons into resonance with the spin gaps. On-site tunability and scalability make this architecture extremely promising. We stress that the proposed scheme is based on state-of-the-art technology and its experimental realization only requires assembling elements that have already been separately demonstrated.

In both the proposed setups, a detailed investigation of the effects of decoherence on the system dynamics has been carried out. All the most important damping and pure dephasing channels have been included by numerically solving the Lindblad equation of motion for the system density matrix. The very high fidelity obtained in the simulation of quantum gates makes both these platforms extremely appealing for proof-of-principle experiments involving the implementation of complex sequences of gates. Moreover, they could constitute the basic building block of a scalable architecture which could be used to simulate interesting physical models. This has been demonstrated by extensive numerical experiments, in which we have simulated the time evolution induced by target spin and fermionic Hamiltonians, obtaining a very good agreement with the exact dynamics.

The next step would be the experimental demonstration of the performance of the proposed platforms. This is challenging, but within reach of current technology. As far as molecular qubits are concerned, manipulating them with global magnetic pulses requires a two-frequency EPR spectrometer. These are necessary to induce transitions within each molecular ring (single-qubit rotations), as well as to excite/de-excite the switch for two-qubit entangling gates. Moreover, nanomagnets should be diluted in a diamagnetic matrix, to reduce the harmful effect of dipolar interactions, and their coherence time should be enhanced as far as possible by chemical engineering. Global readout could be performed by magnetization measurements.

Conversely, the redox-active setup requires grafting single molecules on a surface and then addressing them with a tip at an appropriate potential, thus inducing the tunneling of a single electron on a timescale < 1 ns. Readout could be achieved by means of nano-SQUID devices (acting at the molecular scale).

In the field of circuit Quantum-Electrodynamics a high level of control has been reached, both on superconducting qubits and on coplanar resonators. The implementation of our scheme requires the storage of a single photon within each resonator and the ability to fast tuning its frequency, without loosing the high quality factor of the resonator. Spin ensembles consisting of high-spin units (such as molecular nanomagnets) would increase the coupling with the resonator, hence the coherence of the system. A future, challenging perspective is the magnetic coupling of the resonator with a single molecule. This requires to increase the intensity of the vacuum field radiation by means of proper constrictions and to choose the best spin system.

In the end, the physical implementation of a quantum computer is one of the major goal of current research. While building a general purpose quantum computer means nowadays nurturing a dream, the realization of a quantum simulator, able to outperform a classical device in predicting the behaviour of systems at the nano-scale, seems within reach of present technology. The here-proposed spin-based schemes for quantum information processing could immediately involve experimental groups for their practical realization. This requires an intense partnership between scientists belonging to different fields (Physics, Chemistry, Engineering), who can share their knowledge to win this challenging race.

Appendices

Density Functional Theory

APPENDIX

A

Here we state the *many-electron* problem and provide an overview on density functional theory. Differently from chemical approaches, based on developments of Hartree-Fock theory, whose aim is to attack the many-electron problem by approximating as better as possible the exact ground-state many-electron wave-function, in the density functional theory the emphasis shifts from the ground-state wave-function to the much more manageable ground-state one-body electron density $n(\mathbf{r})$. The density functional theory shows that the ground-state energy of a many-particle system can be expressed as a functional of the one-body density; minimization of this functional allows in principle the determination of the actual ground-state density [219]. The success of the theory is also to provide a reasonable approximation of the functional to be minimized. The peculiarity of the density functional approach to the many-body theory is to attain rigorously a one-electron Schrödinger equation with a local effective potential in the study of the ground-state properties of the many-electron systems.

A.1 The Many-electron problem

Essentially all of condensed matter physics is described (neglecting Relativistic effects) by the Schrödinger equation $i\hbar\frac{\partial|\psi\rangle}{\partial t} = \hat{H}\,|\psi\rangle$, with the Hamiltonian

$$\begin{aligned}\hat{H} = &-\frac{\hbar^2}{2m}\sum_{i=1}^{N_e}\nabla_i{}^2 - \sum_{I=1}^{P}\frac{\hbar^2\nabla_I^2}{2M_I} + \frac{e^2}{2}\sum_{I=1}^{P}\sum_{J\neq I}^{P}\frac{Z_I Z_J}{|\mathbf{R}_I - \mathbf{R}_J|}\\ &+\frac{e^2}{2}\sum_{i=1}^{N_e}\sum_{j\neq i}^{N_e}\frac{1}{|\mathbf{r}_i - \mathbf{r}_j|} - e^2\sum_{I=1}^{P}\sum_{i=1}^{N_e}\frac{Z_I}{|\mathbf{R}_I - \mathbf{r}_i|}\end{aligned} \tag{A.1}$$

where $\mathbf{R}_I$ is a set of P nuclear coordinates, $\mathbf{r}_i$ is a set of N_e electronic coordinates, Z_I and M_I are the nuclear charges and masses, respectively. Born-Oppenheimer approximation allows us to separate the motion of the electrons and of the nuclei: as the former are smaller and faster, they see the potential generated by the nuclei as fixed. Even if solving this equation is all we have to do in order to accurately describe materials, a brute-force approach to the many-body Schrödinger equation is unfeasible. Hence, we need to find a reasonable approximation of Eq. A.1, which captures all the essential physical properties of the examined system, while being still solvable on our computers.

One of the first problems we have to face in quantum many-body theory is to find the ground state of an inhomogeneous system composed of N_e interacting electrons [220]. This can be cast in terms of a variational principle for the energy, differently from the excited states. The ground state energy is given by:

$$E = \left\langle \Phi \left| \hat{T} + \hat{V}_{ext} + \hat{V}_{ee} \right| \Phi \right\rangle , \tag{A.2}$$

where $|\Phi\rangle$ is the N_e-electron ground state wave-function, $\hat{T}$ is the kinetic operator, $\hat{V}_{ext}$ is the interaction with external fields - a generalization of the electron-nuclear interaction - and $\hat{V}_{ee}$ is the electron-electron interaction. This many body wave-function must include correlation among electrons. It is useful to define the one- and two-body density matrices, which are related to the process of creating and annihilating one or two electrons at different points in space. The one-body and two-body density matrices expressed in real space are defined by

$$n_1(\mathbf{r},\mathbf{r}') = N_e \int d\mathbf{r}_2 ... \int d\mathbf{r}_{N_e} \Phi(\mathbf{r},\mathbf{r}_2,...,\mathbf{r}_{N_e})\Phi^*(\mathbf{r}',\mathbf{r}_2,...,\mathbf{r}_{N_e}) \tag{A.3a}$$

$$n_2(\mathbf{r},\mathbf{r}') = N_e(N_e-1)\sum_{\sigma,\sigma'}\int d\mathbf{r}_3 ... \int d\mathbf{r}_{N_e} \left|\Phi(\mathbf{r},\mathbf{r}',\mathbf{r}_3,...,\mathbf{r}_{N_e})\right|^2 \tag{A.3b}$$

If it is confusing that there are two different quantities depending on two particle coordinates, note that the one-particle reduced density matrix depends on two **r** arguments of the same particle, while the two-particle density depends on the positions of two different particles. We can now define the two-body direct correlation function $g(\mathbf{r},\mathbf{r}')$ as follows:

$$n_2(\mathbf{r},\mathbf{r}') = \frac{1}{2} n_1(\mathbf{r},\mathbf{r}) n_1(\mathbf{r}',\mathbf{r}') g(\mathbf{r},\mathbf{r}'), \tag{A.4}$$

where $n_1(\mathbf{r},\mathbf{r}')$ is the one-body density matrix, and its diagonal elements $n(\mathbf{r}) = n_1(\mathbf{r},\mathbf{r})$ represent the electronic density.

Using the above notation the expectation value of kinetic operator $\hat{T}$, of the external field operator $\hat{V}_{ext}$ and of the electron-electron operator $\hat{V}_{ee}$ can be written as:

$$\begin{aligned}
T &= \left\langle \Phi \left| \hat{T} \right| \Phi \right\rangle = -\frac{\hbar^2}{2m}\sum_{i=1}^{N_e}\left\langle \Phi \left| \nabla_i{}^2 \right| \Phi \right\rangle = -\frac{\hbar^2}{2m}\int \left[\nabla_{\mathbf{r}}{}^2 n_1(\mathbf{r},\mathbf{r}')\right]_{\mathbf{r}'=\mathbf{r}} d\mathbf{r} \\
V_{ext} &= \left\langle \Phi \left| \hat{V}_{ext} \right| \Phi \right\rangle = \left\langle \Phi \left| \sum_{i=1}^{N_e} v_{ext}(\mathbf{r}_i) \right| \Phi \right\rangle = \int n(\mathbf{r}) v_{ext}(\mathbf{r}) d\mathbf{r} \\
V_{ee} &= \left\langle \Phi \left| \hat{V}_{ee} \right| \Phi \right\rangle = \frac{1}{2}\sum_{i=1}^{N_e}\sum_{j\neq i}^{N_e}\left\langle \Phi \left| \frac{1}{|\mathbf{r}_i - \mathbf{r}_j|} \right| \Phi \right\rangle = \int\int \frac{n_2(\mathbf{r},\mathbf{r}')}{|\mathbf{r}-\mathbf{r}'|} d\mathbf{r} d\mathbf{r}'
\end{aligned} \tag{A.5}$$

Using definition (A.4) and the fact that $g(\mathbf{r},\mathbf{r}')$ is different from one only when **r** is sufficiently close to **r**′, it is natural to separate the energetic contributions to the electron-

electron interaction into two terms:

$$V_{ee} = \frac{1}{2}\int\int \frac{n(\mathbf{r})n(\mathbf{r}')}{|\mathbf{r}-\mathbf{r}'|} d\mathbf{r}d\mathbf{r}' + \frac{1}{2}\int\int \frac{n(\mathbf{r})n(\mathbf{r}')}{|\mathbf{r}-\mathbf{r}'|}\left[g(\mathbf{r},\mathbf{r}')-1\right] d\mathbf{r}d\mathbf{r}' \tag{A.6}$$

the first term ignores correlation altogether, as if $g(\mathbf{r},\mathbf{r}') = 1$ everywhere and it is the classical electrostatic interaction energy, corresponding to a charge distribution $n(\mathbf{r})$. The second term corrects the first one by taking into account the departure of $g(\mathbf{r},\mathbf{r}')$ from 1. It contains both local (on-site) and non local contributions and includes both exchange and correlation effects: $g(\mathbf{r},\mathbf{r}')$ takes into account the fact that the presence of an electron at **r** discourages a second electron from being located at a position $\mathbf{r}'$ very close to **r**, because of the Coulomb repulsion. In more precise terms, the probability of finding two electrons close is reduced with respect to the probability of finding them at infinite distance. For any potential that is repulsive at short range, the classical pair correlation function exhibits a region of very low (or zero) probability. In quantum mechanics, the classical pair correlation function is modified in such a way as to interpolate between a finite value at the origin and one at long distances. The finite value at the origin arises because now the particles are represented by probabilistic distributions instead of being perfectly localized. In addition, due to Pauli's exclusion principle, the above probability is further reduced if the electrons have the same spin projection.

The simplest possible approximation is to neglect the second term in Eq. A.6 altogether, which is equivalent to assuming $g(\mathbf{r},\mathbf{r}') = 1$ everywhere. This corresponds to a completely uncorrelated system and it is referred to as the Hartree approximation. The next step is to introduce the exchange interaction: let us imagine that there is a spin ↑ electron at the origin and we look at the density of the other $N_e - 1$ electrons. Pauli's principle forbids the presence of electrons with spin ↑ at the origin, but says nothing about electrons with spin ↓, which can perfectly well be located there; therefore, the exchange-only part of the pair correlation function verifies

$$lim_{\mathbf{r}\to\mathbf{r}'} g_X(\mathbf{r},\mathbf{r}') = 1/2. \tag{A.7}$$

If this is the only contribution considered, i.e. if we neglect correlation, this is equivalent to postulating a many-body wave-function of Slater determinant form, which ensures that Pauli's principle is verified. In that case we are within the *Hartee-Fock* theory, where the electron-electron interaction becomes

$$\begin{aligned} V_{ee}^{HF} =& \frac{1}{2}\int\int \frac{n^{HF}(\mathbf{r})n^{HF}(\mathbf{r}')}{|\mathbf{r}-\mathbf{r}'|} d\mathbf{r}d\mathbf{r}' + \\ & \frac{1}{2}\int\int \frac{n^{HF}(\mathbf{r})n^{HF}(\mathbf{r}')}{|\mathbf{r}-\mathbf{r}'|}\left[g_X(\mathbf{r},\mathbf{r}')-1\right] d\mathbf{r}d\mathbf{r}', \end{aligned} \tag{A.8}$$

with

$$g_X(\mathbf{r},\mathbf{r}') = 1 - \frac{\sum_\sigma \left|n_\sigma^{HF}(\mathbf{r},\mathbf{r}')\right|}{n^{HF}(\mathbf{r})n^{HF}(\mathbf{r}')}, \tag{A.9}$$

with the sum running over the spin projections. The density and the density matrix are calculated from the ground state Slater determinant.

The calculation of the electronic hole, i.e. the remaining part of the correlation function, once exchange has been taken into account, is the major problem in many-body theory. Up to the present time this has been an open problem in the general case of an inhomogeneus electron gas.

A.2 The Hohenberg-Kohn theorem

Consider a system of N_e electrons, described by the standard many-body Hamiltonian

$$\hat{H}_e = \hat{H}_{int} + \hat{V}_{ext} = \hat{T} + \hat{V}_{ee} + \sum_i v_{ext}(\mathbf{r}_i). \tag{A.10}$$

in which we have separated the ”internal” part (kinetic energy of the electrons plus electron-electron Coulomb interactions) from the ”external” part (here the electronic-nuclear interactions). For simplicity, we suppose that the many-body ground-state $|\Psi_G\rangle$ is non-degenerate (in principle, any degeneracy can be removed by an arbitrary small perturbation that appropriately lowers the symmetry of the system). Let us consider as the only variable of the many-electron problem the external potential $v_{ext}(\mathbf{r})$; the mass of the electrons, their charge, their number N_e and the form of the internal interactions are known and fixed. The Hohenberg-Kohn theorem states that there is a one-to-one correspondence between the ground-state density of a N_e-electron system and the external potential acting on it; hence the ground-state electron density becomes the variable of interest.
In other words, there exists a functional that links $n(\mathbf{r})$ and $v_{ext}(\mathbf{r})$, and we write

$$n(\mathbf{r}) = F[v_{ext}(\mathbf{r})]. \tag{A.11}$$

which can be demonstrated straightforwardly [219]. We note that two external potentials, which differ by a constant in the whole space, lead to the same $n(\mathbf{r})$.
The great novelty of the Hohenberg-Kohn theorem is that the functional relation (A.11) can be inverted in the form

$$v_{ext}(\mathbf{r}) = G[n(\mathbf{r})], \tag{A.12}$$

which means that from the knowledge of the ground-state density $n(\mathbf{r})$ we can determine uniquely the external potential (to within a non-essential additive constant) and thus the Hamiltonian of the system. In order to prove A.12, we have to show that for any given pair of external potentials $v_{ext}(\mathbf{r}) \neq \overline{v}_{ext}(\mathbf{r})$ we have $n(\mathbf{r}) \neq \overline{n}(\mathbf{r})$. This follows from the minimum property of the ground-state energy. See [219] for a detailed proof. The most important consequence of the Hohenberg-Kohn theorem is the formulation of a variational principle for the ground-state density of a system. Following Hohenberg and Kohn, we consider the functional

$$E^{HK}[n(\mathbf{r}), v_{ext}(\mathbf{r})] = \langle \Psi_G[n] | \hat{T} + \hat{V}_{ee} + \hat{V}_{ext} | \Psi_G[n] \rangle \,, \tag{A.13}$$

where $v_{ext}(\mathbf{r})$ is taken fixed, $n(\mathbf{r})$ is allowed to vary, and $\Psi_G[n]$ is the ground-state of the system with ground-state density $n(\mathbf{r})$. The absolute minimum of the energy functional A.13 is found when $\Psi_G[n]$ is the ground-state of the operator $\hat{T} + \hat{V}_{ee} + \hat{V}_{ext}$, i.e. when $n(\mathbf{r})$ is the exact electron density of the system. The properties of the Hohenberg-Kohn energy functional A.13 can be summarized as follows:

- The energy functional $E^{HK}[n(\mathbf{r}), v_{ext}(\mathbf{r})]$, which exists and is unique, is minimal at the exact ground-state density, and its minimum gives the exact ground-state energy of the many-electron system.

- The functional $F[n] = T[n] + V_{ee}[n]$ is universal, i.e. it does not depend on $v_{ext}(\mathbf{r})$. However $F[n]$ is not known explicitly, and must be appropriately approximated.

A.3 The Kohn-Sham equations

The Kohn-Sham equations are obtained by minimizing the functional A.13 with respect to $n(\mathbf{r})$. The variational procedure can be carried out explicitly if we decompose the ground-state density $n(\mathbf{r})$ of an interacting electron system into the sum of N independent orbital contributions as follows

$$n(\mathbf{r}) = \sum_i \phi_i^*(\mathbf{r})\phi_i(\mathbf{r}), \tag{A.14}$$

where $\{\phi_i(\mathbf{r})\}\,(i = 1, 2, \ldots, N)$ are orthonormal orbitals. This decomposition is exact and unique for any chosen density $n(\mathbf{r})$. Indeed, we can always imagine a fictitious (reference) system of non-interacting electrons, whose ground-state density satisfies $n_0(\mathbf{r}) = n(\mathbf{r})$. For the reference system of density $n_0(\mathbf{r})$, the Hohenberg-Kohn theorem guarantees that an external potential $v^0_{ext}(\mathbf{r})$, producing the ground-state density $n_0(\mathbf{r})$, exists and is unique. Being $\{\phi_i(\mathbf{r})\}\,(i = 1, 2, \ldots, N)$ the N orbitals of lowest energy of the reference system, the ground-state wave-function is given by the Slater determinant obtained from these orbitals and the electron density is $n_0(\mathbf{r}) = \sum_i \phi_i^*(\mathbf{r})\phi_i(\mathbf{r})$. Since we have taken $n_0(\mathbf{r}) = n(\mathbf{r})$, the decomposition A.14 is also justified for the interacting electrons, even if the exact ground-state of an interacting electron system is not the Slater determinant obtained with the orbitals contributing to $n(\mathbf{r})$. In order to proceed with the variational approach, we introduce some useful quantities, namely the inter-electron Coulomb interaction $V_H[n]$ (called Hartree potential)

$$V_H[n] = \frac{1}{2}\sum_{ij}\left\langle \phi_i\phi_j \left| \frac{e^2}{r_{12}} \right| \phi_i\phi_j \right\rangle \tag{A.15}$$

and the kinetic energy $T_0[n]$ (of a system of non-interacting electrons with the same density):

$$T_0[n] = \sum_i \left\langle \phi_i \left| -\frac{\hbar^2\nabla^2}{2m} \right| \phi_i \right\rangle. \tag{A.16}$$

The Hohenberg-Kohn functional A.13 can be recast as

$$E^{HK}[n(\mathbf{r}), v_{ext}(\mathbf{r})] = T_0[n] + V_H[n] + \int n(\mathbf{r})v_{ext}(\mathbf{r})d\mathbf{r} + E_{XC}[n]. \tag{A.17}$$

Here we have defined the *exchange-correlation* functional $E_{XC}[n]$ as

$$E_{XC}[n] = T[n] - T_0[n] + V_{ee}[n] - V_H[n]. \tag{A.18}$$

The functional A.17 can be rewritten in the form

$$\begin{aligned} E^{HK}[n(\mathbf{r}), v_{ext}(\mathbf{r})] =& \sum_i \left\langle \phi_i \left| \frac{-\hbar^2\nabla^2}{2m} + v_{ext} \right| \phi_i \right\rangle \\ &+ \frac{1}{2}\sum_{ij}\left\langle \phi_i\phi_j \left| \frac{e^2}{r_{12}} \right| \phi_i\phi_j \right\rangle + E_{XC}[n]. \end{aligned} \tag{A.19}$$

Following the standard variational procedure, we vary the N contributing orbitals $\{\phi_i(\mathbf{r})\}$ $(i = 1, 2, \ldots, N)$ in order to minimize the energy functional A.19, with the constraint of orthonormalization of the single-electron wave-functions $\{\phi_i(\mathbf{r})\}$. Notice that we define the variation of the functional $E_{XC}[n]$ as

$$\delta E_{XC}[n] = \int V_{XC}(\mathbf{r})\delta n(\mathbf{r})d\mathbf{r}, \tag{A.20}$$

and accordingly

$$V_{XC}(\mathbf{r}) = \frac{\delta E_{XC}[n]}{\delta n(\mathbf{r})}. \tag{A.21}$$

By carrying out the variational calculation of A.19 one finds the *Kohn-Sham equations*:

$$\left[-\frac{\hbar^2\nabla^2}{2m} + V_{nucl}(\mathbf{r}) + V_H(\mathbf{r}) + V_{XC}(\mathbf{r})\right]\phi_i(\mathbf{r}) = \epsilon_i\phi_i(\mathbf{r}), \tag{A.22}$$

where $V_H(\mathbf{r})$ is the Hartree potential, $V_{XC}(\mathbf{r})$ represents the functional derivative of $E_{XC}[n]$ and $V_{nucl}(\mathbf{r})$ denotes the external potential in consideration. The exact total ground-state energy (A.19) of the electronic system

$$\begin{aligned} E^{HK}[n(\mathbf{r}), v_{ext}(\mathbf{r})] = \sum_i \epsilon_i - \frac{1}{2}\sum_{ij}\left\langle \phi_i\phi_j \left| \frac{e^2}{r_{12}} \right| \phi_i\phi_j \right\rangle \\ + E_{XC}[n] - \int V_{XC}(\mathbf{r})n(\mathbf{r})d\mathbf{r}. \end{aligned} \tag{A.23}$$

can be easily obtained once we have determined the Kohn-Sham orbitals $\phi_i(\mathbf{r})$ and energies ϵ_i. We notice that the Kohn-Sham equations are standard differential equations with a local effective potential $V_{eff}(\mathbf{r}) = V_{nucl}(\mathbf{r}) + V_H(\mathbf{r}) + V_{XC}(\mathbf{r})$. The effective potential depends on the solutions of the one-electron Schrödinger equation (the Kohn-Sham orbitals) through the electron density; therefore, this equation must be solved in a self-consistent way. Remarkably, any difficulty in the procedure has been confined to a reasonable guess of the exchange-correlation functional $E_{XC}[n]$ (which is known only in principle).

Conceptually, the Kohn-Sham equations determine exactly the electron density and the electronic energy of the ground-state. The orbital energies ϵ_i appearing in Eq. A.22 are usually interpreted as one-particle energies (even if formally they are purely Lagrange multipliers). Experience shows that the calculations, performed with different choices for the exchange-correlation functional, generally understimate the energy band gap in semiconductor and insulators; however, the trend of the dispersion curves of the bands is often represented to reasonably accuracy. Our approach to many-body problems exploits DFT-based calculations to build a one-electron basis for a Hubbard description of magnetic molecules: the Kohn-Sham eigenstates are a good approximation for delocalized $s-$ and $p-$ electrons. This is not the case for strongly-correlated $d-$ electrons, but correlations are explicitely treated via the generalized Hubbard model introduced in Section 1.1.

A.4 Local density approximation

In order to make the formal definition of the exchange-correlation functional $E_{XC}[n]$ useful, one needs to find good approximations for it. The exchange contribution to $E_{XC}[n]$, although well known from Hartree-Fock theory as a function of the single-particle orbitals, involves the calculation of computationally expensive integrals. In addition, up

to now there is no approximation available where the correlation energy is treated at a comparable level of accurancy. Therefore one usually considers as the really meaningful quantity the sum of the two terms (exchange+correlation) in $E_{XC}[n]$.
One of the natural starting point is the homogeneous electron gas, which is a simplified model for metallic systems. This many-body system is constituted by interacting electrons embedded in a uniform neutralizing background of positive charges (jellium model). Being a prototype many-body system, it has been studied in great detail and excellent approximations for correlation are available.
The main idea behind the local density approximation (LDA), is to consider a general inhomogeneous electron system as locally homogeneous. In practice, energy terms local in the density are calculated by integrating over the volume of the system the corresponding energy density calculated at the values that the electronic density assumes at every point **r** in the volume. In other words, the exchange-correlation functional A.18 is obtained from the integral:

$$E_{XC}^{LDA}[n(\mathbf{r})] = \int \epsilon_{XC}[n(\mathbf{r})]n(\mathbf{r})d\mathbf{r}, \tag{A.24}$$

where $\epsilon_{XC}(n(\mathbf{r}))$ is the many-body exchange-correlation energy per electron of a uniform gas of interacting electrons of density $n(\mathbf{r})$. The corresponding exchange-correlation potential becomes

$$V_{XC}^{LDA}(\mathbf{r}) = \frac{\delta E_{XC}^{LDA}[n(\mathbf{r})]}{\delta n(\mathbf{r})} = \epsilon_{XC}(n(\mathbf{r})) + n(\mathbf{r})\frac{d\epsilon_{XC}(n(\mathbf{r}))}{dn(\mathbf{r})}. \tag{A.25}$$

In the LDA, the total ground-state energy E_0^{LDA} takes the form

$$\begin{aligned} E_0^{LDA} = \sum_i \epsilon_i - \frac{1}{2}\int\int n(\mathbf{r})\frac{e^2}{|\mathbf{r}-\mathbf{r}'|}n(\mathbf{r}')d\mathbf{r}d\mathbf{r}' \\ - \int n(\mathbf{r})\frac{d\epsilon_{XC}(n(\mathbf{r}))}{dn(\mathbf{r})}n(\mathbf{r})d\mathbf{r}. \end{aligned} \tag{A.26}$$

A.5 Performance of the LDA

There are a number of features of LDA that are rather general and well-established:

- It favours electron densities that are more homogeneous than the exact ones.
- As a consequence, it tends to overstimate the binding energy of molecules and the cohesive energy of solids. This trend is opposite to Hartree-Fock, which understimates binding energies.
- Geometries of systems involving strong bonds (covalent, ionic or metallic) are remarkably good within the LDA. Bond strenghts, bond angles and vibrational frequencies reproduce experimental values within a few percent. In general LDA tends to understimates bond lengths.
- For weakly bond systems that involve hydrogen bonds or van der Waals closed-shell interactions, bond lengths are too short (over-binding).
- Chemical trends as a function of the atomic number of atomic quantities, such as ionization potential, are usually correct.

- Electronic densities of atoms in the core region, where the electrons are quite localized, are poor. The reason is that LDA fails to cancel the self interaction, which is important for strongly localized states. The electronic density in the valence region of atoms is much better reproduced. Hartree-Fock, where the self-interaction is exactly canceled by the exchange term, gives much better results for atoms than the LDA.

Irreducible Tensor Operators

APPENDIX B

The formalism of irreducible tensor operators (ITOs) [66, 221] is a powerful tool to calculate matrix elements of spin operators. Indeed, as shown in Sec. 1.2, any term appearing in the spin Hamiltonian can be written in terms of ITOs. Moreover, Wigner-Eckart theorem simplifies this task and allows us to immediately classify the examined systems, depending on their symmetry properties.

B.1 Definition

The concept of tensor operator is a generalization of that of vector operator. As it is well known, a vector in physics is a quantity with three components which transforms under a rotation as $V_i \to \sum_j R_{ij} V_j$. It is reasonable to demand that the expectation value of a vector operator $\hat{\mathbf{V}}$ in quantum mechanics be transformed like a classical vector under rotation. Therefore, if the ket is changed under rotation according to $|\alpha\rangle \to \hat{\mathcal{D}}(R)|\alpha\rangle$, the operator equation

$$\hat{\mathcal{D}}^\dagger(R)\hat{V}_i\hat{\mathcal{D}}(R) = \sum_j R_{ij}\hat{V}_j \tag{B.1}$$

must hold, where R_{ij} is the 3×3 matrix corresponding to the rotation $\hat{\mathcal{D}}(R)$. By considering infinitesimal rotations along cartesian axes (see Ref. [221]), we find that $\hat{\mathbf{V}}$ must satisfy the commutation relations

$$\left[\hat{V}_i, \hat{J}_j\right] = i\epsilon_{ijk}\hbar\hat{V}_k, \tag{B.2}$$

where $\hat{J}_i$ are the components of the total angular momentum. We can use B.2 as an alternative definition of vector operator.

In perfect analogy, in classical physics it is customary to define a tensor $T_{ijk\ldots}$ as the quantity which transforms as

$$T_{ijk\ldots} \to \sum_{i'}\sum_{j'}\sum_{k'}\cdots R_{ii'}R_{jj'}\ldots T_{i'j'k'\ldots} \tag{B.3}$$

under a rotation specified by the 3×3 orthogonal matrix R. The number of indices is the *rank* of the *Cartesian* tensor. The simplest example of classical tensor of rank 2 is a dyadic formed out of two vectors **U** and **V**: $T_{ij} \equiv U_i V_j$. The trouble with such a Cartesian tensor is that it is reducible, i.e. it can be decomposed into objects that transform differently under rotations:

$$U_i V_j = \frac{\mathbf{U} \cdot \mathbf{V}}{3} \delta_{ij} + \frac{U_i V_j - U_j V_i}{2} + \left(\frac{U_i V_j + U_j V_i}{2} - \frac{\mathbf{U} \cdot \mathbf{V}}{3} \delta_{ij} \right). \tag{B.4}$$

Here the first term is a scalar product, invariant under rotation. The second is an antisymmetric tensor with 3 independent components, that can be written as vector product $\epsilon_{ijk}(\mathbf{U} \times \mathbf{V})_k$. The last is a 3×3 symmetric traceless tensor with 5 independent components. These numbers $(1, 3, 5)$ are the multiplicities of objects with angular momentum $l = 0$, $l = 1$, and $l = 2$, respectively. This suggests that the dyadic has been decomposed into tensors that can transform like spherical harmonics with $l = 0, 1, 2$. In fact, this is the simplest nontrivial example to illustrate the reduction of a Cartesian tensor into irreducible spherical tensors.

More formally, we define an $n-$component tensor as an element of a vector space $\mathcal{E}_n$ which transforms linearly under rotations in a vector belonging to the same space. If n operators transform under rotation like n linearly independent vectors belonging to $\mathcal{E}_n$, these are the components of a tensor operator of rank n. A tensor is irreducible if the space $\mathcal{E}_n$ in which it is defined is irreducible with respect to rotations.

Similarly to vector operators, also tensor operators are unambiguously defined by the law of transformation under rotation of its components in a given representation. By definition, the $(2k+1)$ operators $\hat{T}_q^{(k)}$ $(q = -k, -k+1, \ldots, +k)$ are the standard components of an irreducible tensor operator of rank k, $\hat{T}^{(k)}$, if they transform under rotation as

$$\hat{R}\, \hat{T}_q^{(k)} \hat{R}^{-1} = \sum_{q'} \hat{T}_{q'}^{(k)} \hat{R}_{q'q}^{(k)}. \tag{B.5}$$

This transformation law is the same as the one for basis vectors $|kq\rangle$ of a standard representation for a $(2k+1)-$dimensional space irreducible with respect to rotations: $\hat{R}|kq\rangle = \sum_{q'} |kq'\rangle \hat{R}_{q'q}^{(k)}$. Here $\hat{R}_{q'q}^{(k)}$ is the rotation operator:

$$\hat{R}_{MM'}^{(J)}(\alpha, \beta, \gamma) \equiv \langle JM| e^{-i\alpha \hat{J}_z} e^{-i\beta \hat{J}_y} e^{-i\gamma \hat{J}_z} |JM'\rangle.$$

Starting from the expression of $\hat{R}$ valid for an infinitesimal rotation, it is easy to obtain the following commutation relations with the total angular momentum $\hat{\mathbf{J}}$:

$$\begin{aligned} \left[\hat{J}_\pm, \hat{T}_q^{(k)}\right] &= \sqrt{k(k+1) - q(q \pm 1)}\, \hat{T}_{q\pm1}^{(k)} \\ \left[\hat{J}_z, \hat{T}_q^{(k)}\right] &= q\hat{T}_q^{(k)}, \end{aligned} \tag{B.6}$$

which provide an equivalent definition of the $q-$th component of a tensor operator of rank k. If Eqs. B.5-B.6 are satisfied for any infinitesimal rotations, they will hold for any rotation whatsoever. In order to represent physical quantities, the $\hat{T}_q^{(k)}$ are necessary invariant in a rotation through 2π and k is therefore integer. We shall consider only tensor operator of integer rank.

Scalars are irreducible tensor operators of rank 0. Vector operators are irreducible tensor operators of rank 1: if $\hat{\mathbf{s}}_x$, $\hat{\mathbf{s}}_y$ and $\hat{\mathbf{s}}_z$ are the Cartesian components of a spin operator, its standard components are:

$$\hat{T}^{(1)}_1 = -\frac{1}{\sqrt{2}}(\hat{\mathbf{s}}_x + i\hat{\mathbf{s}}_y), \qquad \hat{T}^{(1)}_0 = \hat{\mathbf{s}}_z, \qquad \hat{T}^{(1)}_{-1} = \frac{1}{\sqrt{2}}(\hat{\mathbf{s}}_x - i\hat{\mathbf{s}}_y) \tag{B.7}$$

The $(2k+1)$ spherical harmonics Y^q_k are the standard components of an irreducible tensor operator of rank k.

B.2 Representation: Wigner-Eckart theorem

The most important property of irreducible tensor operators is given by the *Wigner-Eckart theorem*:

Theorem B.1. *The matrix elements of irreducible tensor operators with respect to angular-momentum eigenstates $|\alpha JM\rangle$ can be expressed as*

$$\langle \alpha JM|\hat{T}^{(k)}_q|\alpha' J'M'\rangle = \frac{1}{\sqrt{2J+1}}\langle J'kM'q|JM\rangle\langle \alpha J||\hat{T}^{(k)}||\alpha' J'\rangle. \tag{B.8}$$

Wigner-Eckart theorem states that the matrix element of a tensor operator in the total angular momentum basis is the product of two terms. The first is a Clebsch-Gordan coefficient $\langle J'kM'q|JM\rangle$ for adding angular momenta J and k to get J'. It depends only on the geometry of the system, that is, the way it is oriented with respect to the $z-$axis. There is no reference whatsoever to the particular nature of the tensor operator. The second factor is the reduced matrix element, which is independent of M, M' and q. It depends on the dynamics, but not on the specific orientation of the system. To evaluate $\langle \alpha JM|\hat{T}^{(k)}_q|\alpha' J'M'\rangle$ with various combinations of M, M' and q it is sufficient to know just one of them; all others can be related geometrically via the Clebsch-Gordan coefficients, which are tabulated. Eq. B.8 can be rewritten by replacing the Clebsch-Gordan coefficient with a $3j$ symbol (see Appendix C):

$$\langle \alpha JM|\hat{T}^{(k)}_q|\alpha' J'M'\rangle = (-1)^{J-M}\begin{pmatrix} J & k & J' \\ -M & q & M' \end{pmatrix}\langle \alpha J||\hat{T}^{(k)}||\alpha' J'\rangle. \tag{B.9}$$

Important selection rules follow from Wigner-Eckart theorem: indeed, the $3j-$symbol is nonzero only if

$$\begin{gathered} q = M - M' \\ |J - J'| \leq k \leq J + J'. \end{gathered} \tag{B.10}$$

B.3 Compound tensor operators

Compound tensor operators are obtained as a tensor product of irreducible tensor operators: $\hat{V}^{(K)} \equiv \hat{T}^{(k_1)} \otimes \hat{U}^{(k_2)}$ is an irreducible tensor operator of rank K, whose components are given by:

$$\hat{V}^{(K)}_Q \equiv \left\{\hat{T}^{(k_1)} \otimes \hat{U}^{(k_2)}\right\}^{(K)}_Q = \sum_{q_1,q_2}\langle k_1k_2q_1q_2|KQ\rangle\hat{T}^{(k_1)}_{q_1}\hat{U}^{(k_2)}_{q_2}. \tag{B.11}$$

By varying K, satisfying $|k_1 - k_2| \leq K \leq k_1 + k_2$, we get a set of $(2k_1 + 1)(2k_2 + 1)$ operators.

In a quantum system consisting of two subsystems with respective angular momenta $\hat{\mathbf{j}}_1$ and $\hat{\mathbf{j}}_2$, with $\hat{\mathbf{J}} = \hat{\mathbf{j}}_1 + \hat{\mathbf{j}}_2$ and basis vectors $|j_1 m_1\rangle$ and $|j_2 m_2\rangle$, let $\hat{T}^{(k_1)}$ and $\hat{U}^{(k_2)}$ be tensor operators acting on subsystem 1 and 2, respectively. In the standard basis of the total angular momentum $\{|j_1 j_2 J M\rangle\}$, the reduced matrix elements of $\hat{V}^{(K)} \equiv \hat{T}^{(k_1)} \otimes \hat{U}^{(k_2)}$ are given by:

$$\begin{aligned}\langle j_1 j_2 J || \hat{V}^{(K)} || j_1' j_2' J' \rangle &= \sqrt{(2J+1)(2K+1)(2J'+1)} \\ &\left\{ \begin{array}{ccc} K & J & J' \\ k_1 & j_1 & j_1' \\ k_2 & j_2 & j_2' \end{array} \right\} \langle j_1 || \hat{T}^{(k_1)} || j_1' \rangle \langle j_2 || \hat{U}^{(k_2)} || j_2' \rangle. \qquad \text{(B.12)}\end{aligned}$$

This procedure (known as *recoupling technique*, see Sec. 1.2) can be applied iteratively to decompose a compound tensor operator acting on several subsystems into the product of $9j-$symbols and reduced matrix elements acting on each single subsystem.

Wigner nj symbols

APPENDIX C

C.1 $3j$ symbols

Given a quantum system with two angular momenta $\hat{\mathbf{j}}_1$ and $\hat{\mathbf{j}}_2$, let $\hat{\mathbf{J}} = \hat{\mathbf{j}}_1 + \hat{\mathbf{j}}_2$, be the total angular momentum. It is always possible to pass from the product basis $|j_1 j_2 m_1 m_2\rangle \equiv |j_1 m_1\rangle |j_2 m_2\rangle$, to the basis of the total angular momentum $|j_1 j_2 JM\rangle$ (with $|j_1 - j_2| \leq J \leq j_1 + j_2$, $M = -J, -J+1, \ldots, J$). The change of basis is expressed by the Clebsch-Gordan coefficients:

$$|j_1 j_2 JM\rangle = \sum_{m_1, m_2} |j_1 j_2 m_1 m_2\rangle \langle j_1 j_2 m_1 m_2 | j_1 j_2 JM\rangle. \tag{C.1}$$

The Clebsch-Gordan coefficients $\langle j_1 j_2 m_1 m_2 | j_1 j_2 JM\rangle$ can be recast in terms of the Wigner-$3j$ symbols:

$$\begin{pmatrix} j_1 & j_2 & J \\ m_1 & m_2 & -M \end{pmatrix} = \frac{(-1)^{j_1 - j_2 + M}}{2J+1} \langle j_1 j_2 m_1 m_2 | j_1 j_2 JM\rangle. \tag{C.2}$$

The following selection rules holds:

$$\begin{aligned} M &= m_1 + m_2 \\ |j_1 - j_2| \leq J &\leq j_1 + j_2 \end{aligned} \tag{C.3}$$

Moreover, $3j$ symbols satisfy the symmetry relations:

- invariance in a circular permutation of the three columns
- are multiplied by $(-1)^{j_1 + j_2 + J}$ in a permutation of two columns
- are multiplied by $(-1)^{j_1 + j_2 + J}$ if m_1, m_2 and M change sign simultaneously.

C.2 $6j$ and $9j$ symbols

$6j$ and $9j$ symbols are obtained analogously to $3j$ symbols in the unitary transformation which connects two different coupling schemes of 3 and 4 angular momenta, respectively [66].

In this last case, let $\hat{\mathbf{J}} = \hat{\mathbf{j}}_1 + \hat{\mathbf{j}}_2 + \hat{\mathbf{j}}_3 + \hat{\mathbf{j}}_4$ be the total angular momentum and imagine to pass from the representation in which first we sum momenta 1-2 and 3-4

$$\begin{array}{ccc} \hat{\mathbf{J}}_{12} = \hat{\mathbf{j}}_1 + \hat{\mathbf{j}}_2 & & \hat{\mathbf{J}}_{34} = \hat{\mathbf{j}}_3 + \hat{\mathbf{j}}_4 \\ & \Downarrow & \\ \hat{\mathbf{J}} & = & \hat{\mathbf{J}}_{12} + \hat{\mathbf{J}}_{34} \end{array} \tag{C.4}$$

to another in which we first sum momenta 1-3 and 2-4

$$\begin{array}{ccc} \hat{\mathbf{J}}_{13} = \hat{\mathbf{j}}_1 + \hat{\mathbf{j}}_3 & & \hat{\mathbf{J}}_{24} = \hat{\mathbf{j}}_2 + \hat{\mathbf{j}}_4 \\ & \Downarrow & \\ \hat{\mathbf{J}} & = & \hat{\mathbf{J}}_{13} + \hat{\mathbf{J}}_{24} \end{array} \tag{C.5}$$

In the change of basis we get a 3 rows × 3 columns object known as $9j$ symbol:

$$\begin{gathered} \langle (j_1 j_2) J_{12} (j_3 j_4) J_{34}; JM | (j_1 j_3) J_{13} (j_2 j_4) J_{24}; J'M' \rangle = \delta_{JJ'} \delta_{MM'} \\ \sqrt{(2J_{12}+1)(2J_{34}+1)(2J_{13}+1)(2J_{24}+1)} \left\{ \begin{array}{ccc} j_1 & j_2 & J_{12} \\ j_3 & j_4 & J_{34} \\ J_{13} & J_{24} & J \end{array} \right\}. \end{gathered} \tag{C.6}$$

Among the most important symmetry properties of $9j$ symbols, we recall that a $9j$ symbol coincides with its transpose and is non-zero only if triangle inequalities are satisfied on each row and each column. The computation of $9j$ symbols can be done by recasting them in terms of $3j$ symbols, which are tabulated. Moreover, several routines can be found to calculate them numerically.

Linear Response Theory

APPENDIX D

Linear response theory provides a general framework to study the dynamical properties of quantum systems close to thermal equilibrium. This appendix reports some useful definitions and results; for a more detailed mathematical treatment and for the derivation of the main results, we refer to [76]. A response function for a macroscopic system relates the change of an ensemble-averaged physical observable $\langle \hat{B}(t) \rangle$ to an external force $f(t)$. We consider a system at thermal equilibrium, described at time t by the density operator $\hat{\rho}(t)$ and characterized by a weak external perturbation $f(t)$, which gives rise to a time dependent term in the system Hamiltonian:

$$\hat{H}_1 = -\hat{A} f(t). \tag{D.1}$$

To this perturbation is associated a change of the ensemble average of the operator $\hat{B}$, which at time t takes the form $\langle \hat{B}(t) \rangle = \mathrm{tr}[\hat{\rho}(t)\hat{B}]$. The linear relation between this quantity and the external force can be written as:

$$\langle \hat{B}(t) \rangle - \langle \hat{B} \rangle = \int_{-\infty}^{t} \phi_{BA}(t - t') f(t') dt' \tag{D.2}$$

This means that the differential change of $\langle \hat{B}(t) \rangle$ is proportional to the external disturbance and the duration of the perturbation, and that disturbances at different times act independently of each other. This last condition is formalized by the requirement that the response function ϕ_{BA} only depends on $t - t'$. Moreover, the response is independent of any future perturbations, i.e. $\phi_{BA}(t - t') = 0$ for $t' > t$. Then we can consider the Laplace transform of $\phi_{BA}(t)$

$$\chi_{BA}(z) = \int_{0}^{\infty} \phi_{BA}(t) e^{izt} dt, \tag{D.3}$$

where z is a complex variable and χ_{BA} an analytic function defined for $\mathrm{Im}z > 0$, if we ensure that $\int_0^\infty |\phi_{BA}(t)| e^{-\epsilon t} dt$ is finite in the limit $\epsilon \to 0^+$. To ensure that the evolution of the system is uniquely determined by $\hat{\rho}_0 = \hat{\rho}(-\infty)$ and $f(t)$, it is necessary that the external perturbation be switched on in a smooth, adiabatic way. This may be accomplished by replacing $f(t')$ in Eq. D.2 by $f(t')e^{-\epsilon t'}$, with $\epsilon > 0$. This choice leads to a force vanishing for $t \to -\infty$, and any unwanted higher effect can be removed by taking $\epsilon \to 0^+$. Then we define

$$\langle \hat{B}(\omega) \rangle = \lim_{\epsilon \to 0^+} \int_{-\infty}^{\infty} \Big(\langle \hat{B}(t) \rangle - \langle \hat{B} \rangle \Big) e^{i\omega t} e^{-\epsilon t} dt \tag{D.4}$$

and Eq. D.2 is transformed into

$$\langle \hat{B}(\omega) \rangle = \chi_{BA}(\omega) f(\omega). \tag{D.5}$$

Here $\chi_{BA}(\omega) \equiv \lim_{\epsilon \to 0^+} \chi_{BA}(z = \omega + i\epsilon)$ is the frequency-dependent or *generalized susceptibility*. The above mathematical requirements ensure that the physical system is causal and stable against small perturbations [76].

The *Kubo formula* gives an expression of the response function ϕ_{BA} in terms of the operators $\hat{A}$, $\hat{B}$ and of the unperturbed Hamiltonian $\hat{H}_0$:

$$\phi_{BA}(t - t') = \frac{i}{\hbar} \theta(t - t') \left\langle \left[\hat{B}(t), \hat{A}(t') \right] \right\rangle, \tag{D.6}$$

where $\theta(t)$ is the Heaviside step function: $\theta(t) = 1$ for $t > 0$ and $\theta(t) = 0$ elsewhere. We stress that both the variations with time and the ensemble average are thermal-equilibrium values determined by $\hat{H}_0$, and are unaffected by the external perturbation. It is also useful to introduce

$$K_{BA}(t) = \frac{i}{\hbar} \left\langle \left[\hat{B}(t), \hat{A} \right] \right\rangle = \frac{i}{\hbar} \left\langle \left[\hat{B}, \hat{A}(-t) \right] \right\rangle. \tag{D.7}$$

The generalized susceptibility is divided into the reactive (real) and absorptive (imaginary) part:

$$\chi_{BA}(\omega) = \chi'_{BA}(\omega) + i\chi''_{BA}(\omega), \tag{D.8}$$

related by the Kramers-Kroning relation. It is easy to show that the Laplace transform of $K_{BA}(t)$, $K_{BA}(\omega)$, is proportional to the imaginary part of the susceptibility: $K_{BA}(\omega) = 2i\chi''_{BA}(\omega)$.

Then we introduce the *dynamic correlation function*, also known as *scattering function*, defined as:

$$S_{BA}(t) \equiv \langle \hat{B}(t)\hat{A} \rangle - \langle \hat{B} \rangle \langle \hat{A} \rangle. \tag{D.9}$$

Its Fourier transform is connected to the imaginary susceptibility by the *fluctuation-dissipation theorem*:

$$S_{BA}(\omega) = 2\hbar \frac{\chi''_{BA}(\omega)}{1 - e^{-\beta\hbar\omega}}, \tag{D.10}$$

having fulfilled the *condition of detailed balance*: $S_{BA}(\omega) = e^{\beta\hbar\omega} S_{AB}(-\omega)$.

We now calculate the energy transferred to the system by the external perturbation $\hat{H}_1 = -\hat{A}f(t)$. The energy absorption can be expressed in terms of $\chi_{AA}(\omega)$ and, without loss of generality, $\hat{A}$ may be assumed Hermitian. The part of the response which is in phase with the external force is proportional to $\chi'_{AA}(\omega)$, which justifies the name of reactive component. Conversely, the rate of energy absorption due to the field is

$$Q = \frac{d}{dt} \langle \hat{H} \rangle = \langle \partial \hat{H} / \partial t \rangle = -\langle \hat{A}(t) \rangle \partial f / \partial t, \tag{D.11}$$

[77] which leads to a mean absorption rate determined by the out-of-phase response proportional to $\chi''_{BA}(\omega)$.
If the eigenvalues E_α and eigenvectors $|\alpha\rangle$ of the unperturbed Hamiltonian $\hat{H}_0$ are known, it is possible to derive an explicit expression for $\chi_{BA}(\omega)$, which is given by:

$$\chi_{BA}(\omega) = \lim_{\epsilon \to 0^+} \sum_{\alpha,\alpha'} \frac{\langle\alpha|\hat{B}|\alpha'\rangle\langle\alpha'|\hat{A}|\alpha\rangle}{E_{\alpha'} - E_\alpha - \hbar\omega - i\hbar\epsilon} (n_\alpha - n_{\alpha'}) \,. \tag{D.12}$$

where $n_\alpha = e^{-\beta E_\alpha}/Z$ and Z is the partition function, $Z = \sum_{\alpha'} e^{-\beta E_{\alpha'}}$. This expression can be separated into the absorptive

$$\chi''_{BA}(\omega) = \pi \sum_{\alpha\alpha'} \langle\alpha|\hat{B}|\alpha'\rangle\langle\alpha'|\hat{A}|\alpha\rangle \, (n_\alpha - n_{\alpha'}) \, \delta\left(\hbar\omega - (E_{\alpha'} - E_\alpha)\right) \tag{D.13}$$

and reactive

$$\chi'_{BA}(\omega) = \sum_{\alpha,\alpha'}^{E_\alpha \neq E_{\alpha'}} \frac{\langle\alpha|\hat{B}|\alpha'\rangle\langle\alpha'|\hat{A}|\alpha\rangle}{E_{\alpha'} - E_\alpha - \hbar\omega} (n_\alpha - n_{\alpha'}) + \chi'_{BA}(el)\delta_{\omega 0} \tag{D.14}$$

components. Here the elastic term $\chi'_{BA}(el)\delta_{\omega 0}$ only contributes in the static limit. These results show that, if the eigenstates of the Hamiltonian are discrete and the matrix-elements are well-defined, the poles of $\chi_{BA}(\omega)$ all lie on the real axis. Hence, $\chi''_{BA}(\omega)$ is a sum of δ-functions and no spontaneous transitions occur. In a real macroscopic system, the distribution of states is continuous, and only the ground state may be considered as a well-defined discrete state. At non-zero temperatures, the parameters of the system are subject to fluctuations in space and time. A non-zero probability for a spontaneous transition between the states $|\alpha\rangle$ and $|\alpha'\rangle$ can be included in a phenomenological way by replacing the energy difference $E_{\alpha'} - E_\alpha$ with $E_{\alpha'} - E_\alpha + i\Gamma(\omega)$. In practice, δ functions are broadened and spectra are interpreted by employing other peak functions such as Gaussians or Lorentzians.

Dynamics of Open Quantum systems

APPENDIX E

The quantum dynamics of an open system cannot, in general, be represented by means of a unitary time evolution, in contrast to the case of a closed system. It is often found to be useful to formulate, instead, the dynamics of an open system in terms of an appropriate equation of motion for its density matrix, a quantum master equation. In this appendix we introduce the Lindblad master equation, which provides a Markovian treatment of the dynamics of open quantum systems [222, 223].

E.1 Liouville-von Neumann equation

We first focus on the dynamics of a closed quantum system. Let's assume that the system under consideration is in a mixed state. Then, the corresponding statistical ensemble is described by the density operator:

$$\hat{\rho}(t_0) = \sum_{\alpha} w_\alpha |\psi_\alpha(t_0)\rangle\langle\psi_\alpha(t_0)| \tag{E.1}$$

at some initial time t_0. Here w_α are positive weights and $|\psi_\alpha(t_0)\rangle$ are normalized state vectors, which evolve according to the Schrödinger equation $i\hbar\frac{d|\psi_\alpha(t)\rangle}{dt} = \hat{H}(t)|\psi_\alpha(t)\rangle$. The Hamiltonian operator might be time-dependent. Therefore, the density operator at time t will be given by:

$$\hat{\rho}(t) = \sum_{\alpha} w_\alpha \hat{U}(t,t_0)|\psi_\alpha(t_0)\rangle\langle\psi_\alpha(t_0)|\hat{U}^\dagger(t,t_0) = \hat{U}(t,t_0)\hat{\rho}(t_0)\hat{U}^\dagger(t,t_0) \tag{E.2}$$

where $\hat{U}(t,t_0) = \hat{T}_{\leftarrow}\left[e^{-\frac{i}{\hbar}\int_{t_0}^{t}\hat{H}(s)ds}\right]$ is the time-evolution operator and $\hat{T}_{\leftarrow}$ is the chronological time-ordering operator. Since we are considering the evolution of a closed quantum system, $\hat{U}(t,t_0)$ is unitary. Differentiating Eq. E.2 with respect to time we get the equation of motion for the density matrix:

$$\frac{d}{dt}\hat{\rho}(t) = -\frac{i}{\hbar}\left[\hat{H}(t),\hat{\rho}(t)\right], \tag{E.3}$$

which is known as the *Liouville-von Neumann* equation. This can also be rewritten in form analogous to the classical Liouville equation:

$$\frac{d}{dt}\hat{\rho}(t) = \mathcal{L}(t)\hat{\rho}(t), \tag{E.4}$$

where $\mathcal{L}(t)$ is the *Liouville* super-operator.

E.2 Open quantum systems

An open quantum system is a quantum system S coupled to another quantum system B called environment. It thus represents a subsystem of the combined total $S+B$ system, which is assumed to be closed and to follow Hamiltonian dynamics. However, the state of the subsystem S evolves as a consequence of both internal dynamics and interaction with the environment. This interaction leads, in general, to $S-B$ entanglement, such that the resulting dynamics of S can be no longer described by a unitary evolution.
The total system+environment Hamiltonian takes the form

$$\hat{H}_{tot}(t) = \hat{H}_S \otimes \hat{I}_B + \hat{I}_S \otimes \hat{H}_B + \hat{V}(t), \tag{E.5}$$

where $\hat{H}_S$ is the open system Hamiltonian acting on the system subspace, $\hat{H}_B$ is the free Hamiltonian of the environment acting on the B subspace and the system-environment interaction is modeled by $\hat{V}$. Of course, one may also include time-dependent terms into $\hat{H}_S$. In many cases of physical interest, the environment includes infinitely many degrees of freedom and computing the evolution of the whole $S+B$ system is unaffordable. Moreover, often the modes of the environment are neither known exactly, nor controllable. Hence, we develop a simpler description in the reduced Hilbert space spanned by the system S, relying on the assumption that all observations of interest refer to this subsystem. These are represented by operators of the form $\hat{A} \otimes \hat{I}_B$. If the state of the total system is described by the density matrix $\hat{\rho}$, the expectation values of all observables acting on the open system's Hilbert space are determined by

$$\langle \hat{A} \rangle = \mathrm{tr}_S \left\{ \hat{A}\hat{\rho}_S \right\} \tag{E.6}$$

where

$$\hat{\rho}_S = \mathrm{tr}_B \hat{\rho} \tag{E.7}$$

is the reduced density matrix of the open quantum system S. Here tr_S (tr_B) denotes the partial trace over the S (B) Hilbert space. The reduced density matrix $\hat{\rho}_S(t)$ at time t is obtained from the density matrix $\hat{\rho}(t)$ of the total system by taking the partial trace over the degrees of freedom of the environment. Thus, we find the equation of motion for the reduced density matrix:

$$\frac{d}{dt}\hat{\rho}_S(t) = -\frac{i}{\hbar}\mathrm{tr}_B \left[\hat{H}_{tot}(t), \hat{\rho}(t)\right]. \tag{E.8}$$

E.3 Lindblad equation

In general the dynamics of the reduced system described by Eq. E.8 will be pretty complex. However, in case of short environmental correlation times (Markov approximation) we can neglect memory effects and formulate the reduced system dynamics in

terms of a quantum dynamical semigroup [222].
Suppose to initialize the total $S + B$ system in the uncorrelated product state $\hat{\rho}(0) = \hat{\rho}_S(0) \otimes \hat{\rho}_B$, where the environment is in an equilibrium state. Then, there exist a transformation $W(t)$ describing the evolution of the reduced system state from $t = 0$ to any $t > 0$ of the form

$$\hat{\rho}_S(t) = W(t)\hat{\rho}_S(0) \equiv \text{tr}_B \left\{ \hat{U}(t,0) \left[\hat{\rho}_S(0) \otimes \hat{\rho}_B\right] \hat{U}^\dagger(t,0) \right\}. \tag{E.9}$$

This relation defines a map from the space of the reduced density matrices of the system S into itself and is called a *dynamical map*. It can be shown that $W(t)$ is a convex-linear completely positive and trace-preserving quantum operation [222]. A quantum *dynamical semigroup* is a continuous, one-parameter family of dynamical maps satisfying the semigroup property $W(t_1)W(t_2) = W(t_1 + t_2)$ for any $t_1,\ t_2 \geq 0$; this is the case for $W(t)$, under the Markovian approximation.
Given a quantum dynamical semigroup there exist a linear map $\mathcal{L}$, the generator of the semigroup, which allows us to represent the semigroup in exponential form:

$$W(t) = e^{\mathcal{L}t}. \tag{E.10}$$

This representation yields a first-order differential equation for the open system density matrix: $\dot{\hat{\rho}}_S = \mathcal{L}\hat{\rho}_S$, the Markovian quantum master equation. It is the generalization of the Liouville-von Neumann equation for closed systems. We now construct the most general form of the generator $\mathcal{L}$ of a quantum dynamical semigroup. To this end, we consider a finite dimensional Hilbert space with dimension N. The corresponding Liouville space is a complex space of dimension N^2, spanned by the complete basis of orthonormal operators $\hat{F}_i$, $i = 1, 2, ..., N^2$. It can be shown [222] that the standard form of the generator is:

$$\mathcal{L}[\hat{\rho}_S] = -i\left[\hat{H}, \hat{\rho}_S\right] + \sum_{i,j=1}^{N^2-1} a_{ij} \left(\hat{F}_i \hat{\rho}_S \hat{F}_j^\dagger - \frac{1}{2}\hat{F}_j^\dagger \hat{F}_i \hat{\rho}_S - \frac{1}{2}\hat{\rho}_S \hat{F}_j^\dagger \hat{F}_i \right). \tag{E.11}$$

The coefficient positive matrix a_{ij} can be diagonalized via the unitary transformation u, leading to non-negative eigenvalues γ_i. Introducing a new set of operators $\hat{A}_k$ related to $\hat{F}_i$ through $\hat{F}_i = \sum_{k=1}^{N^2-1} u_{ki}\hat{A}_k$, we obtain the *diagonal* form of the generator:

$$\mathcal{L}[\hat{\rho}_S] = -i\left[\hat{H}, \hat{\rho}_S\right] + \sum_{k=1}^{N^2-1} \gamma_k \left(\hat{A}_k \hat{\rho}_S \hat{A}_k^\dagger - \frac{1}{2}\hat{A}_k^\dagger \hat{A}_k \hat{\rho}_S - \frac{1}{2}\hat{\rho}_S \hat{A}_k^\dagger \hat{A}_k \right). \tag{E.12}$$

This is the most general form for the generator of a quantum dynamical semigroup. The first term of the generator represents the unitary part of the dynamics generated by the Hamiltonian $\hat{H}$. The operators $\hat{A}_k$ are usually referred to as Lindblad operators and the corresponding density matrix equation is called the Lindblad equation. We note that the non-negative quantities γ_k have the dimension of an inverse time provided the $\hat{A}_k$ are taken to be dimensionless.
It is sometimes convenient to introduce the *dissipator*

$$\mathcal{D}[\hat{\rho}_S] = \sum_{k=1}^{N^2-1} \gamma_k \left(\hat{A}_k \hat{\rho}_S \hat{A}_k^\dagger - \frac{1}{2}\hat{A}_k^\dagger \hat{A}_k \hat{\rho}_S - \frac{1}{2}\hat{\rho}_S \hat{A}_k^\dagger \hat{A}_k \right) \tag{E.13}$$

and to write the quantum master equation in the form

$$\frac{d}{dt}\hat{\rho}_S(t) = -i\left[\hat{H}, \hat{\rho}_S(t)\right] + \mathcal{D}[\hat{\rho}_S]. \tag{E.14}$$

We note that the generator does note uniquely fix the form of the Hamiltonian and of the Lindblad operators. In fact, it is invariant under unitary transformations of the Lindblad operators.
The open system may be subject to an external time-dependent field. The description of such an open system requires the help of time-dependent generators and can be found in Ref. [222].

E.4 Microscopic derivation

In this section we derive a microscopic form of the Lindbald equation, adopting some general approximations to get the dynamical semigroup form of Eq. E.12. These assumptions will be summarized in the last part of this appendix. Since we are generally interested in situations such that $\hat{V}$ is a small time-dependent perturbation with respect to $\hat{H}_0 = \hat{H}_S + \hat{H}_B$, we can eliminate fast oscillating terms (secular approximation) and work in interaction picture. Then the equation of motion for the system-environment density matrix becomes

$$i\hbar\frac{d}{dt}\hat{\rho}_I = \left[\hat{V}_I(t), \hat{\rho}_I(t)\right], \tag{E.15}$$

where both $\hat{V}_I$ and $\hat{\rho}_I$ must be intended in interaction picture, $\hat{\rho}_I(t) = e^{i\hat{H}_0 t/\hbar}\hat{\rho}(t)e^{-i\hat{H}_0 t/\hbar}$. This equation can be formally integrated [223], obtaining:

$$\hat{\rho}_I(t) = \hat{\rho}_I(t_0) - \frac{i}{\hbar}\int_{t_0}^{t}\left[\hat{V}_I(s), \hat{\rho}_I(s)\right] ds. \tag{E.16}$$

On substituting $\hat{\rho}_I(t)$ back into E.15 we find:

$$\frac{d}{dt}\hat{\rho}_I = -\frac{i}{\hbar}\left[\hat{V}_I(t), \hat{\rho}_I(t_0)\right] - \frac{1}{\hbar^2}\int_{t_0}^{t}\left[\hat{V}_I(t), \left[\hat{V}_I(s), \hat{\rho}_I(s)\right]\right] ds. \tag{E.17}$$

If $\hat{V}_I = 0$, system and environment are independent and $\hat{\rho}_I$ would factor as a direct product $\hat{\rho}_I(t) = \hat{\rho}_{S_I}(t) \otimes \hat{\rho}_{B_I}(t_0)$, where we have assumed the environment at equilibrium. Since $\hat{V}_I$ is small (*Born* approximation), we look for solutions of the form $\hat{\rho}_I(t) = \hat{\rho}_{S_I}(t) \otimes \hat{\rho}_{B_I}(t_0) + \hat{\rho}_c(t)$, where $\hat{\rho}_c$ is of higher order in $\hat{V}$. To satisfy E.7, we require $\mathrm{tr}_B\hat{\rho}_c = 0$. If we now substitute $\hat{\rho}_I(t)$ into E.17 and retain terms up to quadratic order in $\hat{V}$, we get

$$\begin{aligned}\dot{\hat{\rho}}_S = & -\frac{i}{\hbar}\mathrm{tr}_B\left[\hat{V}(t), \hat{\rho}_S(t_0) \otimes \hat{\rho}_B(t_0)\right] + \\ & -\frac{1}{\hbar^2}\mathrm{tr}_B\int_{t_0}^{t}\left[\hat{V}(t), \left[\hat{V}(s), \hat{\rho}_S(s) \otimes \hat{\rho}_B(t_0)\right]\right] ds.\end{aligned} \tag{E.18}$$

From now on we drop the subscripts I, implying that operators are intended in interaction picture. We see that, since $\hat{\rho}_S(s)$ appears in the integrand, the reduced density operator, which determines the statistical properties of the system, depends on its past history from $t = t_0$ to $t = s$. However, the environment is usually a reservoir containing many degrees of freedom. Moreover, the huge number of reservoir degrees of freedom leads to a $\delta(t-s)$ function, which allows us to replace $\hat{\rho}_S(s)$ with $\hat{\rho}_S(t)$ in the integrand. In this case the process looses memory of its past and is said to be *Markovian*. This is generally a reasonable assumption.

E.4.1 Atom decay

We now consider a simple example to derive the explicit form of the master equation. We consider an atom coupled to a reservoir of simple harmonic oscillators. This describes the radiative decay of the atom, damped by the bath of oscillators. However the same picture can be applied to many other interesting situations, such as the decay of a radiation field inside a cavity. In the interaction picture and the rotating-wave approximation, the Hamiltonian is simply given by

$$\hat{V}(t) = \hbar \sum_{\mathbf{k}} g_{\mathbf{k}} \left[\hat{b}^\dagger_{\mathbf{k}} \hat{\sigma}_- e^{-i(\omega-\nu_k)t} + \text{h.c.} \right], \tag{E.19}$$

where $\hat{b}_{\mathbf{k}}$ ($\hat{b}^\dagger_{\mathbf{k}}$) are annihilation (creation) operator of the bath modes, with density distributed frequencies $\nu_k = ck$ and $\hat{\sigma}_\pm$ are excitation/de-excitation operators acting on the atom (treated as a two-level system), with transition frequency ω. On inserting E.19 into the equation of motion E.18 we obtain

$$\begin{aligned}
\dot{\hat{\rho}}_S =& -i \sum_{\mathbf{k}} g_{\mathbf{k}} \langle \hat{b}^\dagger_{\mathbf{k}} \rangle \left[\hat{\sigma}_-, \hat{\rho}_S(t_0) \right] e^{-i(\omega-\nu_k)t} - \int_{t_0}^{t} ds \sum_{\mathbf{k},\mathbf{k}'} g_{\mathbf{k}} g_{\mathbf{k}'} \\
& \times \Bigg\{ \Big(\hat{\sigma}_- \hat{\sigma}_- \hat{\rho}_S(s) - 2\hat{\sigma}_- \hat{\rho}_S(s) \hat{\sigma}_- + \hat{\rho}_S(s) \hat{\sigma}_- \hat{\sigma}_- \Big) e^{-i(\omega-\nu_k)t - i(\omega-\nu_{k'})s} \langle \hat{b}^\dagger_{\mathbf{k}} \hat{b}^\dagger_{\mathbf{k}'} \rangle \\
& + \Big(\hat{\sigma}_- \hat{\sigma}_+ \hat{\rho}_S(s) - \hat{\sigma}_+ \hat{\rho}_S(s) \hat{\sigma}_- \Big) e^{-i(\omega-\nu_k)t + i(\omega-\nu_{k'})s} \langle \hat{b}^\dagger_{\mathbf{k}} \hat{b}_{\mathbf{k}'} \rangle \\
& + \Big(\hat{\sigma}_+ \hat{\sigma}_- \hat{\rho}_S(s) - \hat{\sigma}_- \hat{\rho}_S(s) \hat{\sigma}_+ \Big) e^{i(\omega-\nu_k)t - i(\omega-\nu_{k'})s} \langle \hat{b}_{\mathbf{k}} \hat{b}^\dagger_{\mathbf{k}'} \rangle \Bigg\} + \text{h.c.}
\end{aligned} \tag{E.20}$$

where the expectation values must be taken with respect to the initial state of the reservoir and hence depend on the choice of the particular model for the state of the reservoir. For instance, let's consider a reservoir whose variables are distributed in the uncorrelated thermal equilibrium mixture of states. The reservoir reduced density matrix operator is thus the multi-mode extension of the thermal operator, namely:

$$\hat{\rho}_B = \prod_{\mathbf{k}} \left[1 - \exp\left(-\frac{\hbar \nu_k}{k_B T} \right) \right] \exp\left(-\frac{\hbar \nu_k \hat{b}^\dagger_{\mathbf{k}} \hat{b}_{\mathbf{k}}}{k_B T} \right), \tag{E.21}$$

where T is the temperature and k_B is the Boltzmann constant. It can be shown that

$$\begin{aligned}
\langle \hat{b}_{\mathbf{k}} \rangle =& \langle \hat{b}^\dagger_{\mathbf{k}} \rangle = 0 \\
\langle \hat{b}^\dagger_{\mathbf{k}} \hat{b}_{\mathbf{k}'} \rangle =& \bar{n}_{\mathbf{k}} \delta_{\mathbf{k}\mathbf{k}'} \\
\langle \hat{b}_{\mathbf{k}} \hat{b}^\dagger_{\mathbf{k}'} \rangle =& (\bar{n}_{\mathbf{k}} + 1) \delta_{\mathbf{k}\mathbf{k}'} \\
\langle \hat{b}_{\mathbf{k}} \hat{b}_{\mathbf{k}'} \rangle =& \langle \hat{b}^\dagger_{\mathbf{k}} \hat{b}^\dagger_{\mathbf{k}'} \rangle = 0,
\end{aligned} \tag{E.22}$$

where $\bar{n}_{\mathbf{k}} = \left[\exp\left(\frac{\hbar\nu_k}{k_B T}\right) - 1\right]^{-1}$ is the thermal average boson number. If then we replace the sum over **k** with an integral and carry out the usual Weissekopf-Wigner approximation ($\nu_k \sim \omega$), we find for the reduced density operator of the two-level system:

$$\begin{aligned}\dot{\hat{\rho}}_S(t) =& -\bar{n}_{th}\frac{\Gamma}{2}\left[\hat{\sigma}_-\hat{\sigma}_+\hat{\rho}_S(t) - \hat{\sigma}_+\hat{\rho}_S(t)\hat{\sigma}_-\right] \\ & -(\bar{n}_{th}+1)\frac{\Gamma}{2}\left[\hat{\sigma}_+\hat{\sigma}_-\hat{\rho}_S(t) - \hat{\sigma}_-\hat{\rho}_S(t)\hat{\sigma}_+\right] + \text{h.c.}\end{aligned} \tag{E.23}$$

where $\bar{n}_{th} \equiv \bar{n}_{k_0}$ ($k_0 = \omega/c$) and Γ is the atomic decay rate, which can be derived by evaluating the integrals above (or assumed as a parameter of the model). Notice that here we have focused only on the incoherent part of the evolution, neglecting the first term of E.20, which leads to an Hamiltonian dynamics.

E.4.2 Cavity field damping

An analogous expression can be obtained for the damping of an electromagnetic field into a cavity. We simply need to replace the atomic $\hat{\sigma}_\pm$ operators with the bosonic operators $\hat{a}$, $\hat{a}^\dagger$ describing the photon. Then the equation of motion for the photon interacting with a bath in thermal equilibrium is:

$$\begin{aligned}\dot{\hat{\rho}}_S =& -\bar{n}_{th}\frac{\Gamma}{2}\left(\hat{a}\hat{a}^\dagger\hat{\rho}_S - 2\hat{a}^\dagger\hat{\rho}_S\hat{a} + \hat{\rho}_S\hat{a}\hat{a}^\dagger\right) \\ & -(\bar{n}_{th}+1)\frac{\Gamma}{2}\left(\hat{a}^\dagger\hat{a}\hat{\rho}_S - 2\hat{a}\hat{\rho}_S\hat{a}^\dagger + \hat{\rho}_S\hat{a}^\dagger\hat{a}\right).\end{aligned} \tag{E.24}$$

Here again Γ is the damping rate and $\bar{n}_{th}$ is the mean number of quanta at the frequency of the cavity field in the thermal bath. In particular, at zero temperature ($\bar{n}_{th} = 0$),

$$\dot{\hat{\rho}}_S = \frac{\Gamma}{2}\left(2\hat{a}\hat{\rho}_S\hat{a}^\dagger - \hat{a}^\dagger\hat{a}\hat{\rho}_S - \hat{\rho}_S\hat{a}^\dagger\hat{a}\right). \tag{E.25}$$

We notice that in the simple case of a two-level atomic system or of a cavity-field initialized with a single-photon at zero-temperature, Eq. E.25 yields a decay of the diagonal component of the density matrix (representing the state with a single photon) with damping time $T_1 = \frac{1}{\Gamma}$ and of the coherence (off-diagonal component) with characteristic dephasing time $T_2 = \frac{2}{\Gamma}$. Diagonal and off-diagonal component of $\hat{\rho}_S$ evolve independently, due to the secular approximation.

E.4.3 Pure dephasing

Beyond the damping term introduced in the previous subsection, many quantum systems of interest (in particular spin systems) are subject to pure dephasing. Hence, their characteristic dephasing time T_2 is not simply the one deriving from damping terms in the dissipator (which, for a two-level system, leads to $T_2 = 2T_1$), but it is much shorter. This can be modeled with a pure-dephasing term in the Lindblad equation. For a bosonic system, the pure-dephasing dissipator takes the form:

$$\mathcal{D}_{deph}[\hat{\rho}] = \gamma\left[\hat{a}^\dagger\hat{a}\hat{\rho}\,\hat{a}^\dagger\hat{a} - \frac{1}{2}\left(\hat{a}^\dagger\hat{a}\,\hat{a}^\dagger\hat{a}\hat{\rho} + \hat{\rho}\,\hat{a}^\dagger\hat{a}\,\hat{a}^\dagger\hat{a}\right)\right]$$

where $\gamma = 1/T_2$ is the pure dephasing rate and $\hat{a}$ ($\hat{a}^\dagger$) are annihilation (creation) operators of the boson field.
To incorporate both damping and pure dephasing in a single expression, throughout the text, we refer to the Lindblad dissipator for an arbitrary operator, $\hat{x}$, given by

$$\mathcal{D}_{\hat{x}}[\hat{\rho}] = -\frac{1}{2}\left(\hat{x}^\dagger \hat{x}\hat{\rho} + \hat{\rho}\,\hat{x}^\dagger \hat{x}\right) + \hat{x}\hat{\rho}\,\hat{x}^\dagger. \tag{E.26}$$

If the operator $\hat{x}_\mu$ destroys an excitation in the system, terms like $\mathcal{D}_{\hat{x}_\mu}[\hat{\rho}]$ account for energy losses, while pure dephasing processes are described by $\mathcal{D}_{\hat{x}^\dagger_\mu \hat{x}_\mu}[\hat{\rho}]$.

E.4.4 Summary of assumptions

In order to guarantee that the equation derived by means of the microscopic approach defines the generator of a dynamical semigroup, the following approximations have been applied:

- Large reservoir: the degrees of freedom in the reservoir are infinitely many, if compared to the system degrees of freedom.
- Markov: no memory effects. It is justified if the time scale over which the state of the system varies appreciably is large compared to the time scale over which the reservoir correlation functions decay.
- Born: in order to eliminate $\hat{\rho}_B(t)$ from the equation of motion we assume that the coupling between the system and the reservoir is weak, such that the influence of the system on the reservoir is small (weak-coupling approximation). Thus, the density matrix of the reservoir $\hat{\rho}_B(t)$ is only negligibly affected by the interaction and the state of the total system at time t may be approximately characterized by a tensor product $\hat{\rho}_B(t) \approx \hat{\rho}_S(t) \otimes \hat{\rho}_B$. We emphasize that this does not imply that there are no excitations in the reservoir caused by the reduced system. The Markovian approximation provides a description on a coarse-grained time scale and the assumption is that environmental excitations decay over times which are not resolved.
- Secular approximation: it involves an averaging over the rapidly oscillating terms in the master equation and it is also known as the rotating-wave approximation. It allows us to separate the time evolution of the diagonal terms of the density matrix from the off-diagonal ones, provided that the inverse frequency differences involved in the problem are small compared to the relaxation time of the system.

Bibliography

[1] S. Haroche and J. M. Raimond, *Exploring the Quantum* (Oxford University Press (New York), 2006).

[2] T. Ladd, F. Jelezko, R. Laflamme, Y. Nakamura, C. Monroe, and J. O'Brien, "Quantum Computers," Nature **464**, 45 (2012).

[3] D. Loss and D. P. DiVincenzo, "Quantum computation with quantum dots," Phys. Rev. A **57**, 120 (1998).

[4] P. Santini, S. Carretta, and G. Amoretti, *Magnetic molecules as spin-qubits* (in press, 2016).

[5] F. Meier, J. Levy, and D. Loss, "Quantum computing with antiferromagnetic spin clusters," Phys. Rev. B **68**, 134417 (2003).

[6] F. Troiani, A. Ghirri, M. Affronte, S. Carretta, P. Santini, G. Amoretti, S. Piligkos, G. Timco, and R. E. P. Winpenny, "Molecular engineering of antiferromagnetic rings for quantum computation," Phys. Rev. Lett. **94**, 207208 (2005).

[7] J. Lehmann, A. Gaita-Arino, E. Coronado, and D. Loss, "Spin qubits with electrically gated polyoxometalate molecules," Nature Nanotech. **2**, 312 (2007).

[8] M. Trif, F. Troiani, D. Stepanenko, and D. Loss, "Spin-Electric coupling in molecular magnets," Phys. Rev. Lett. **101**, 217201 (2008).

[9] G. A. Timco, S. Carretta, F. Troiani, F. Tuna, R. J. Pritchard, C. A. Muryn, E. J. L. McInnes, A. Ghirri, A. Candini, P. Santini, G. Amoretti, M. Affronte, and R. E. P. Winpenny, "Engineering the coupling between molecular spin qubits by coordination chemistry," Nature Nanotech. **4**, 173 (2009).

[10] D. P. DiVincenzo, "The Physical Implementation of Quantum Computation," arXiv:quant-ph/0002077v3 (2000).

[11] M. A. Nielsen and I. L. Chuang, *Quantum Computation and Quantum Information* (Cambridge University Press, Cambridge, UK, 2000).

[12] J. Fei, D. Zhou, Y.-P. Shim, S. Oh, X. Hu, and M. Friesen, "Mediated gates between spin qubits," Phys. Rev. A **86**, 062328 (2012).

[13] W. K. Wootters, "Entanglement of formation of an arbitrary state of two qubits," Phys. Rev. Lett. **80**, 2245 (1998).

[14] R. P. Feynman, "Simulating Physics with Computers," Int. J. Theor. Phys. **21**, 467 (1982).

[15] I. M. Georgescu, S. Ashab, and F. Nori, "Quantum Simulation," Rev. Mod. Phys. **86**, 153 (2014).

[16] S. Lloyd, "Universal Quantum Simulators," Int. J. Theor. Phys. **273**, 1073 (1996).

[17] P. Santini, S. Carretta, F. Troiani, and G. Amoretti, "Molecular nanomagnets as quantum simulators," Phys. Rev. Lett. **107**, 230502 (2011).

[18] L. Lamata, A. Mezzacapo, J. Casanova, and E. Solano, "Efficient quantum simulation of fermionic and bosonic models in trapped ions," EPJ Quantum Technology **1**, 9 (2014).

[19] B. Lanyon, C. Hempel, D. Nigg, M. Müller, R. Gerritsma, F. Zähringer, P. Schindler, J. Barreiro, M. Rambach, G. Kirchmair, M. Hennrich, P. Zoller, R. Blatt, and C. F. Roos, "Universal digital quantum simulation with trapped ions," Science **334**, 57 (2011).

[20] D. Gatteschi, R. Sessoli, and J. Villain, *Molecular Nanomagnets* (Oxford University Press, Oxford, UK, 2006).

[21] S. Sanvito, "Molecular spintronics," Chem. Soc. Rev. **40**, 3336 (2011).

[22] J. M. Clemente-Juan, E. Coronado, and A. Gaita-Arino, "Magnetic polyoxometalates: from molecular magnetism to molecular spintronics and quantum computing," Chem. Soc. Rev. **41**, 7464 (2012).

[23] R. Vincent, S. Klyatskaya, M. Ruben, W. Wernsdorfer, and B. F., "Electronic readout of a single nuclear spin using a molecular spin transistor," Nature **488**, 357 (2012).

[24] M. J. Martínez-Pérez, S. Cardona-Serra, C. Schlegel, F. Moro, P. J. Alonso, H. Prima-García, J. M. Clemente-Juan, M. Evangelisti, A. Gaita-Arino, J. Sesé, J. van Slageren, E. Coronado, and F. Luis, "Gd-based single-ion magnets with tunable magnetic anisotropy: Molecular design of spin qubits," Phys. Rev. Lett. **108**, 247213 (2012).

[25] A. Cornia, A. C. Fabretti, P. Garrisi, C. Mortaló, D. Bonacchi, D. Gatteschi, R. Sessoli, L. Sorace, W. Wernsdorfer, and A.-L. Barra, "Energy Barrier Enhancement by Ligand Substitution in Tetrairon(III) Single-Molecule Magnets," Angew. Chem. Int. Ed. **43**, 1136 (2004).

[26] E. Garlatti, S. Carretta, J. Schnack, G. Amoretti, and P. Santini, "Theoretical design of molecular nanomagnets for magnetic refrigeration," Appl. Phys. Lett. **103**, 202410 (2013).

[27] F. Troiani, M. Affronte, S. Carretta, P. Santini, and G. Amoretti, "Quantum gates in permanently coupled antiferromagnetic spin rings without need of local fields," Phys. Rev. Lett. **94**, 190501 (2005).

[28] J. van Slageren, R. Sessoli, D. Gatteschi, A. Smith, M. Helliwell, R. E. P. Winpenny, A. Cornia, A. L. Barra, A. G. M. Jansen, E. Rentschler, and G. Timco, "Magnetic anisotropy of the antiferromagnetic ring [$Cr_8F_8Piv_{16}$]," Chem. Eur. J. **8**, 277 (2002).

[29] F. K. Larsen, E. J. L. McInnes, H. E. Mkami, J. Overgaard, S. Piligkos, G. Rajaraman, E. Rentschler, A. A. Smith, G. M. Smith, V. Boote, M. Jennings, G. A. Timco, and R. E. P. Winpenny, "Synthesis and characterization of heterometallic Cr_7M wheels," Angew. Chem. Int. Ed. **42**, 101 (2003).

[30] C. J. Wedge, G. A. Timco, E. T. Spielberg, R. E. George, F. Tuna, S. Rigby, E. J. L. McInnes, R. E. P. Winpenny, S. J. Blundell, and A. Ardavan, "Chemical engineering of molecular qubits," Phys. Rev. Lett. **108**, 107204 (2012).

[31] S. Bertaina, S. Gambarelli, T. Mitra, B. Tsukerblat, A. Müller, and B. Barbara, "Quantum oscillations in a molecular magnet," Nature **453**, 203 (2008).

[32] F. Moro, D. Kaminski, F. Tuna, G. F. S. Whitehead, G. A. Timco, D. Collison, R. E. P. Winpenny, A. Ardavanb, and E. J. L. McInnes, "Coherent electron spin manipulation in a dilute oriented ensemble of molecular nanomagnets: pulsed EPR on doped single crystals," Chem. Comm. **50**, 91 (2014).

[33] C. Schlegel, J. van Slageren, M. Manoli, E. K. Brechin, and M. Dressel, "Direct observation of Quantum Coherence in Single-Molecule Magnets," Phys. Rev. Lett. **101**, 147203 (2008).

[34] M. Mannini, F. Pineider, C. Danieli, F. Totti, L. Sorace, P. Sainctavit, M. Arrio, E. Otero, L. Joly, J. C. Cezar, A. Cornia, and R. Sessoli, "Quantum tunnelling of the magnetization in a monolayer of oriented single-molecule magnets," Nature **468**, 417 (2010).

[35] V. Corradini, A. Ghirri, E. Garlatti, R. Biagi, V. De Renzi, U. del Pennino, V. Bellini, S. Carretta, P. Santini, G. Timco, R. Winpenny, and M. Affronte, "Magnetic anisotropy of Cr_7Ni spin clusters on surfaces," Adv. Funct. Mat. **22**, 3706 (2012).

[36] S. Carretta, P. Santini, G. Amoretti, F. Troiani, and M. Affronte, "Spin triangles as optimal units for molecule-based quantum gates," Phys. Rev. B **76**, 024408 (2007).

[37] A. Blais, R.-S. Huang, A. Wallraff, S. M. Girvin, and R. J. Schoelkopf, "Cavity quantum electrodynamics for superconducting electrical circuits: An architecture for quantum computation," Phys. Rev. A **69**, 062320 (2004).

[38] A. Wallraff, D. I. Schuster, A. Blais, L. Frunzio, R. S. Huang, J. Majer, S. Kumar, S. M. Girvin, and R. J. Schoelkopf, "Strong coupling of a single photon to a superconducting qubit using circuit quantum electrodynamics," Nature (London) **431**, 162 (2004).

[39] S. Schmidt and J. Koch, "Circuit QED lattices," Ann. Phys. **6**, 395 (2013).

[40] A. A. Houck, H. E. Türeci, and J. Koch, "On-chip quantum simulation with superconducting circuits," Nat. Physics **8**, 292 (2012).

[41] J. Majer, J. M. Chow, J. M. Gambetta, J. Koch, B. R. Johnson, J. A. Schreier, L. Frunzio, D. I. Schuster, A. A. Houck, A. Wallraff, A. Blais, M. H. Devoret, S. M. Girvin, and S. R. J., "Coupling superconducting qubits via a cavity bus," Nature (London) **449**, 443 (2007).

[42] M. Mariantoni, H. Wang, T. Yamamoto, M. Neeley, R. C. Bialczak, Y. Chen, M. Lenander, E. Lucero, A. D. O'Connell, D. Sank, M. Weides, J. Wenner, Y. Yin, J. Zhao, A. N. Korotkov, A. N. Cleland, and J. M. Martinis, "Implementing the quantum von Neumann architecture with superconducting circuits," Science **334**, 61 (2011).

[43] Y. Makhlin, G. Schön, and A. Shnirman, "Josephson-junction qubits with controlled couplings," Nature **398**, 305 (1999).

[44] J. Koch, T. M. Yu, J. Gambetta, A. A. Houck, D. I. Schuster, J. Majer, A. Blais, M. H. Devoret, S. M. Girvin, and R. J. Schoelkopf, "Charge insensitive qubit design derived from Cooper pair box," Phys. Rev. A **76**, 042319 (2007).

[45] Y. Kubo, C. Grezes, A. Dewes, T. Umeda, J. Isoya, H. Sumiya, N. Morishita, H. Abe, S. Onoda, T. Ohshima, V. Jacques, A. Dréau, J.-F. Roch, I. Diniz, A. Auffeves, D. Vion, D. Esteve, and P. Bertet, "Hybrid quantum circuit with a superconducting qubit coupled to a spin ensemble," Phys. Rev. Lett. **107**, 220501 (2011).

[46] D. I. Schuster, A. P. Sears, E. Ginossar, L. DiCarlo, L. Frunzio, J. J. L. Morton, H. Wu, G. A. D. Briggs, B. B. Buckley, D. D. Awschalom, and R. J. Schoelkopf, "High-Cooperativity Coupling of Electron-Spin Ensembles to Superconducting Cavities," Phys. Rev. Lett. **105**, 140501 (2010).

[47] A. Chiesa, S. Carretta, P. Santini, G. Amoretti, and E. Pavarini, "Many-Body Models for Molecular Nanomagnets," Phys. Rev. Lett. **110**, 157204 (2013).

[48] J. Kortus, C. S. Hellberg, and M. R. Pederson, "Hamiltonian of the V_{15} spin system from first-principles Density-Functional Calculations," Phys. Rev. Lett. **86**, 3400

(2001).

[49] K. Park and M. R. Pederson, "Effect of extra electrons on the exchange and magnetic anisotropy in the anionic single-molecule magnet Mn_{12}," Phys. Rev. B **70**, 054414 (2004).

[50] J. Cano, R. Costa, S. Alvarez, and E. Ruiz, "Theoretical study of the magnetic properties of an Mn_{12} Single-Molecule Magnet with a loop structure: The role of the next-nearest neighbor interactions," J. Chem. Theory Comput. **3**, 782 (2007).

[51] D. M. Tomecka, V. Bellini, F. Troiani, F. Manghi, G. Kamieniarz, and M. Affronte, "Propagation of spin information at the supramolecular scale through heteroaromatic linkers," Phys. Rev. B **77**, 224401 (2008).

[52] E. Cremades, J. Cano, E. Ruiz, G. Rajamaran, C. J. Milios, and E. K. Brechin, "Theoretical methods enlighten magnetic properties of a family of Mn_6 single-molecule magnets," Inorg. Chem. **48**, 8012 (2009).

[53] V. Bellini, G. Lorusso, A. Candini, W. Wernsdorfer, T. B. Faust, G. A. Timco, R. E. P. Winpenny, and M. Affronte, "Propagation of spin information at the supramolecular scale through heteroaromatic linkers," Phys. Rev. Lett. **106**, 227205 (2011).

[54] D. Boukhvalov, A. I. Lichtenstein, V. Dobrovitski, M. I. Katsnelson, B. N. Harmon, V. Mazurenko, and V. I. Anisimov, "Effect of local coulomb interactions on the electronic structure and exchange interactions in Mn_{12} magnetic molecules," Phys. Rev. B **65**, 184435 (2002).

[55] D. Boukhvalov, V. V. Dobrovitski, M. Katsnelson, A. Lichtenstein, B. Harmon, and P. Kögerler, "Electronic structure and exchange interactions in V_{15} magnetic molecules: LDA+U results," Phys. Rev. B **70**, 054417 (2004).

[56] S. F. Boys, "Construction of some molecular orbitals to be approximately invariant for changes from one molecule to another," Rev. Mod. Phys. **32**, 296 (1960).

[57] O. Gunnarsson, O. Andersen, O. Jepsen, and J. Zaanen, "Density-functional calculation of the parameters in the Anderson model: Application to Mn in CdTe," Phys. Rev. B **39**, 1708 (1989).

[58] A. MacDonald, S. Girvin, and D. Yoshioka, "t/U expansion for the Hubbard model," Phys. Rev. B **37**, 9753 (1988).

[59] E. Pavarini, E. Koch, and A. Lichtenstein, "Mechanism for orbital ordering in $KCuF_3$," Phys. Rev. Lett. **101**, 266405 (2008).

[60] E. Pavarini, *"The LDA Approach", in* The LDA+DMFT Approach to strongly correlated materials (Verlag des Forschungszentrum Jülich, eds. E. Pavarini, E. Koch, A. Lichtenstein, D. Vollhardt, 2011).

[61] M. Valiev, E. Bylaska, N. Govind, K. Kowalski, T. Straatsma, H. van Dam, D. Wang, J. Nieplocha, E. Apra, T. Windus, and W. de Jong, "Orbital-order melting in rare-earth manganites: Role of superexchange," Comput. Phys. Commun. **181**, 1477 (2010).

[62] A. Szabo and N. S. Ostlund, *Modern Quantum Chemistry* (Dover publications, INC., New York, 1996).

[63] S. Faas, J. Snijdcrs, J. H. van Lenthe, E. van Lenthe, and E. Baerends, "The ZORA formalism applied to the dirac-fock equation," Chem. Phys. Lett. **246**, 632 (1995).

[64] A. Abragam and B. Bleaney, *Electron Paramagnetic Resonance of Transition Metal Ions* (Clarendon Press, Oxford, 1970).

[65] G. Amoretti, *Formulazione Microscopica delle Interazioni Fondamentali nel Magnetismo, dispense presentate al XXII corso del G.N.S.M.* (L'Aquila, 1990).

[66] A. Messiah, *Quantum Mechanics, vol. 2* (North-Holland Publishing Company (Am-

sterdam), 1961).

[67] A. Bencini and D. Gatteschi, *EPR of Exchange Coupled Systems* (Springer Verlag, Berlin, 1990).

[68] J. J. Borrás-Almenar, J. M. Clemente-Juan, E. Coronado, and B. S. Tsukerblat, "High-nuclearity magnetic clusters: Generalized spin hamiltonian and its use for the calculation of the energy levels, bulk magnetic properties, and inelastic neutron scattering spectra," Inorg. Chem. **38**, 6081 (1999).

[69] E. Liviotti, S. Carretta, and G. Amoretti, "S-mixing contributions to the high-order anisotropy terms in the effective spin hamiltonian for magnetic clusters," J. Chem. Phys. **117**, 3361 (2002).

[70] E. Garlatti, "Quantum effects in molecular nanomagnets: from theory to applications," PhD Thesis (2013).

[71] A. Lascialfari, Z. H. Jang, F. Borsa, D. Gatteschi, A. Cornia, D. Rovai, A. Caneschi, and P. Carretta, "Magnetic and structural properties of an octanuclear Cu(II) $s = 1/2$ mesoscopic ring; susceptibility and NMR measurements," Phys. Rev. B **61**, 6839 (2000).

[72] A. Cornia, M. Affronte, A. Jansen, D. Gatteschi, A. Caneschi, and R. Sessoli, "Magnetic anisotropy of Mn_{12}-acetate nanomagnets from high-field torque magnetometry," Chem. Phys. Lett. **322**, 477 (2000).

[73] S. Carretta, P. Santini, G. Amoretti, M. Affronte, A. Ghirri, I. Sheikin, S. Piligkos, G. Timco, and R. E. P. Winpenny, "Topology and spin dynamics in magnetic molecules," Phys. Rev. B **72**, 060403(R) (2005).

[74] O. Waldmann, S. Carretta, P. Santini, R. Koch, A. G. M. Jansen, G. Amoretti, R. Caciuffo, L. Zhao, and L. K. Thompson, "Quantum magneto-oscillations in a supramolecular Mn(II)-[3x3] grid," Phys. Rev. Lett. **92**, 096403 (2004).

[75] F. E. Mabbs and D. Collison, *Electron Paramagnetic Resonance of d Transition Metal Compounds* (Elsevier (Amsterdam), 1992).

[76] J. Jensen and A. R. Mackintosh, *Rare Earth Magnetism* (Clarendon Press, Oxford, 1991).

[77] G. Morin and D. Bonnin, "Modeling EPR powder spectra using numerical diagonalization of the spin hamiltonian," J. Magn. Reson. **136**, 176 (1999).

[78] E. Wasserman, L. C. Snyder, and W. A. Yager, "ESR of the triplet states of randomly oriented molecules," J. Chem. Phys. **41**, 1763 (1964).

[79] J. W. Orton, *Electron Paramagnetic Resonance* (London Iliffe Books LTD (London), 1968).

[80] R. Caciuffo, G. Amoretti, A. Murani, R. Sessoli, A. Caneschi, and D. Gatteschi, "Neutron spectroscopy for the magnetic anisotropy of molecular clusters," J. Chem. Phys. **21**, 4744 (1998).

[81] M. L. Baker, T. Guidi, S. Carretta, J. Ollivier, H. Mutka, H. U. Güdel, G. A. Timco, E. J. L. McInnes, G. Amoretti, R. E. P. Winpenny, and P. Santini, "Spin dynamics of molecular nanomagnets unravelled at atomic scale by four-dimensional inelastic neutron scattering," Nat. Phys. **8**, 906 (2012).

[82] O. Waldmann, "Q dependence of the inelastic neutron scattering cross section for molecular spin clusters with high molecular symmetry," Phys. Rev. B **68**, 174406 (2003).

[83] R. Caciuffo, T. Guidi, G. Amoretti, S. Carretta, E. Liviotti, P. Santini, G. Timco, C. A. Muryn, and R. E. P. Winpenny, "Spin dynamics of heterometallic Cr_7M wheels (M=Mn, Zn, Ni) probed by inelastic neutron scattering," Phys. Rev. B **71**, 174407

(2005).

[84] A. Chiesa, G. F. S. Whitehead, S. Carretta, L. Carthy, G. A. Timco, S. J. Teat, G. Amoretti, E. Pavarini, R. E. P. Winpenny, and P. Santini, "Molecular Nanomagnets with switchable coupling for quantum simulation," Sci. Rep. **4**, 7423 (2014).

[85] S. Bertaina, S. Gambarelli, T. Mitra, B. Tsukerblat, A. Mueller, and B. Barbara, "Quantum oscillations in a molecular magnet," Nature **453**, 203 (2008).

[86] J. Yang, Y. Wang, Z. Wang, X. Rong, C.-K. Duan, J.-H. Su, and J. Du, "Observing quantum oscillation of ground states in single molecular magnet," Phys. Rev. Lett. **108**, 230501 (2012).

[87] S. Carretta, P. Santini, G. Amoretti, T. Guidi, J. Copley, Y. Qiu, R. Caciuffo, G. Timco, and R. Winpenny, "Quantum oscillations of the total spin in a heterometallic antiferromagnetic ring: Evidence from neutron spectroscopy," Phys. Rev. Lett. **98**, 167401 (2007).

[88] S. Nakazawa, S. Nishida, T. Ise, T. Yoshino, N. Mori, R. Rahimi, K. Sato, Y. Morita, K. Toyota, D. Shiomi, M. Kitagawa, H. Hara, P. Carl, P. Höfer, and T. Takui, "A synthetic two-spin quantum bit: g-engineered exchange-coupled biradical designed for controlled-NOT gate operations," Agew. Chem. Int. Ed. **51**, 9860 (2012).

[89] D. Aguilá, L. Barrios, V. Velasco, O. Roubeau, A. Repollés, P. Alonso, J. Sesé, S. Teat, F. Luis, and G. Aromí, "Heterodimetallic [LnLn′] lanthanide complexes: Toward a chemical design of two-qubit molecular spin quantum gates," J. Am. Chem. Soc. **136**, 14215 (2014).

[90] A. Ardavan, A. M. Bowen, A. Fernandez, A. J. Fielding, D. Kaminski, F. Moro, C. A. Muryn, M. D. Wise, A. Ruggi, E. J. L. McInnes, K. Severin, G. A. Timco, C. R. Timmel, F. Tuna, G. F. S. Whitehead, and R. E. P. Winpenny, "Engineering coherent interactions in molecular nanomagnet dimers," npj Quantum Information **1**, 15012 (2015).

[91] S. C. Benjamin, "Quantum computing without local control of qubit-qubit interactions," Phys. Rev. Lett. **88**, 017904 (2001).

[92] J. F. Nossa, M. F. Islam, C. M. Canali, and M. R. Pederson, "First-principles studies of spin-orbit and Dzyaloshinskii-Moriya interactions in the Cu_3 single-molecule magnet," Phys. Rev. B **85**, 085427 (2012).

[93] R. E. P. W. et al., "private communication," .

[94] J. Jing and X. Hu, "Scaling of decoherence for a system of uncoupled spin qubits," Sci. Rep. **5**, 17013 (2015).

[95] U. Las Heras, A. Mezzacapo, L. Lamata, S. Filipp, A. Wallraff, and E. Solano, "Digital quantum simulation of spin systems in superconducting circuits," Phys. Rev. Lett. **112**, 200501 (2014).

[96] G. A. Timco, E. J. L. McInnes, R. G. Pritchard, F. Tuna, and R. E. P. Winpenny, "Heterometallic rings made from chromium stick together easily," Angew. Chem., Int. Ed. **47**, 9681 (2008).

[97] R. H. Laye, F. K. Larsen, J. Overgaard, C. A. Muryn, E. J. L. McInnes, E. Rentschler, V. Sanchez, S. J. Teat, H. U. Güdel, O. Waldmann, G. A. Timco, and R. E. P. Winpenny, "A family of heterometallic wheels containing potentially fourteen hundred siblings," Chem. Commun. , 1125 (2005).

[98] E. Garlatti, M. A. Albring, M. L. Baker, R. J. Docherty, H. Mutka, T. Guidi, V. G. Sakai, G. F. S. Whitehead, R. G. Pritchard, G. A. Timco, F. Tuna, G. Amoretti, S. Carretta, P. Santini, G. Lorusso, M. Affronte, E. J. L. McInnes, D. Collison, and R. E. P. Winpenny, "A detailed study of the magnetism of chiral Cr_7M rings: An investi-

gation into parametrization and transferability of parameters," J. Am. Chem. Soc. **136**, 9763 (2014).

[99] M. L. Baker, G. A. Timco, S. Piligkos, J. S. Mathieson, H. Mutka, F. Tuna, P. K. owski, M. Antkowiak, T. Guidi, T. Gupta, H. Rath, R. J. Woolfson, G. Kamieniarz, R. G. Pritchard, H. Weihe, L. Cronin, G. Rajaraman, D. Collison, E. J. L. McInnes, and R. E. P. Winpenny, "A classification of spin frustration in molecular magnets from a physical study of large odd-numbered-metal, odd electron rings," PNAS **109**, 19113 (2012).

[100] V. Bellini and M. Affronte, "A density-functional study of heterometallic cr-based molecular rings," J. Phys. Chem. B **114**, 14797 (2010).

[101] F. Adelnia, A. Chiesa, S. Bordignon, S. Carretta, A. Ghirri, A. Candini, C. Cervetti, M. Evangelisti, M. Affronte, I. Sheikin, R. E. P. Winpenny, G. Timco, F. Borsa, and A. Lascialfari, "Low temperature magnetic properties and spin dynamics in single crystals of Cr_8Zn antiferromagnetic molecular rings," J. Chem. Phys. **143**, 244321 (2015).

[102] A. Ghirri, A. Chiesa, S. Carretta, F. Troiani, J. van Tol, S. Hill, I. Vitorica-Yrezabal, G. A. Timco, R. E. P. Winpenny, and M. Affronte, "Coherent spin dynamics in molecular Cr_8Zn wheels," J. Phys. Chem. Lett. **6**, 5062 (2015).

[103] S. Takahashi, J. van Tol, C. C. Beedle, D. N. Hendrickson, L.-C. Brunel, and M. S. Sherwin, "Coherent manipulation and decoherence of $s = 10$ Single-Molecule Magnets," Phys. Rev. Lett. **102**, 087603 (2009).

[104] S. Takahashi, I. S. Tupitsyn, J. van Tol, C. C. Beedle, D. N. Hendrickson, and P. C. E. Stamp, "Decoherence in crystals of quantum molecular magnets," Nature **476**, 76 (2011).

[105] A. Ardavan, O. Rival, J. J. L. Morton, S. J. Blundell, A. M. Tyryshkin, T. G. A., and R. E. P. Winpenny, "Will spin-relaxation times in molecular magnets permit quantum information processing?" Phys. Rev. Lett. **77**, 054428 (2007).

[106] F. Troiani, V. Bellini, and M. Affronte, "Decoherence induced by hyperfine interactions with nuclear spins in antiferromagnetic molecular rings," Phys. Rev. B **77**, 054428 (2008).

[107] K. Bader, D. Dengler, S. Lenz, B. Endeward, S.-D. Jiang, P. Neugebauer, and J. van Slageren, "Room temperature quantum coherence in a potential molecular qubit," Nat. Commun. **5**, 5304 (2014).

[108] M. J. Graham, J. M. Zadrozny, M. Shiddiq, J. S. Anderson, M. S. Fataftah, S. Hill, and D. E. Freedman, "Influence of electronic spin and spin–orbit coupling on decoherence in mononuclear transition metal complexes," J. Am. Chem. Soc. **136**, 7623 (2014).

[109] J. M. Zadrozny, J. Niklas, O. G. Poluektov, and D. E. Freedman, "Multiple quantum coherences from hyperfine transitions in a Vanadium(IV) complex," J. Am. Chem. Soc. **136**, 15841 (2014).

[110] M. Warner, S. Din, I. S. Tupitsyn, G. W. Morley, A. M. Stoneham, J. A. Gardener, Z. Wu, A. J. Fisher, S. Heutz, C. W. M. Kay, and G. Aeppli, "Potential for spin-based information processing in a thin-film molecular semiconductor," Nature **503**, 504 (2013).

[111] L. Vergnani, A.-L. Barra, P. Neugebauer, M. J. Rodriguez-Douton, R. Sessoli, L. Sorace, W. Wernsdorfer, and A. Cornia, "Magnetic bistability of isolated giant-spin centers in a diamagnetic crystalline matrix," Chem. Eur. J. **18**, 3390 (2012).

[112] M. Affronte, S. Carretta, G. A. Timco, and R. E. P. Winpenny, "A ring cycle: studies of heterometallic wheels," Chem. Commun. , 1789 (2007).

[113] A. Ghirri, A. Candini, M. Evangelisti, M. Affronte, S. Carretta, P. Santini, G. Amoretti, R. S. G. Davies, G. Timco, and R. E. P. Winpenny, "Elementary excitations in antiferromagnetic Heisenberg spin segments," Phys. Rev. B **76**, 214405 (2007).

[114] Y. Furukawa, K. Kiuchi, K. i. Kumagai, Y. Ajiro, Y. Narumi, M. Iwaki, K. Kindo, A. Bianchi, S. Carretta, G. A. Timco, and R. E. P. Winpenny, "Topological effects on the magnetic properties of closed and open ring-shaped Cr-based antiferromagnetic nanomagnets," Phys. Rev. B **78**, 092402 (2008).

[115] T. Guidi, B. Gillon, S. A. Mason, E. Garlatti, S. Carretta, P. Santini, A. Stunault, R. Caciuffo, J. van Slageren, B. Klemke, A. Cousson, G. A. Timco, and R. E. P. Winpenny, "Direct observation of finite size effects in chains of antiferromagnetically coupled spins," Nat. Commun. **6**, 7061 (2015).

[116] A. Bianchi, S. Carretta, P. Santini, G. Amoretti, T. Guidi, Y. Qiu, J. R. D. Copley, G. Timco, C. Muryn, and R. E. P. Winpenny, "Rotational bands in open antiferromagnetic rings: A neutron spectroscopy study of Cr_8Zn," Phys. Rev. B **79**, 144422 (2009).

[117] F. Cinti, M. Affronte, and A. Jansen, "Effects of antisymmetric interactions in molecular iron rings," Eur. Phys. J. B **30**, 461 (2002).

[118] T. Moriya, "Anisotropic superexchange interaction and weak ferromagnetism," Phys. Rev. **120**, 91 (1960).

[119] P. Santini, S. Carretta, E. Liviotti, G. Amoretti, P. Carretta, M. Filibian, A. Lascialfari, and E. Micotti, "NMR as a probe of the relaxation of the magnetization in magnetic molecules," Phys. Rev. Lett. **94**, 077203 (2005).

[120] E. Garlatti, S. Carretta, P. Santini, G. Amoretti, M. Mariani, A. Lascialfari, S. Sanna, K. Mason, J. Chang, P. Tasker, and E. K. Brechin, "Relaxation dynamics in a fe_7 nanomagnet," Phys. Rev. B **87**, 054409 (2013).

[121] E. Micotti, A. Lascialfari, F. Borsa, M. H. Julien, C. Berthier, M. Horvatic, J. van Slageren, and D. Gatteschi, "Spin dynamics at the level crossing in the molecular antiferromagnetic ring $[Cr_8F_8Piv_{16}]$ from proton NMR," Phys. Rev. B **72**, 020405(R) (2005).

[122] F. Borsa, Y. Furukawa, and A. Lascialfari, *New Developments in Magnetic Resonance* (Springer Verlag, 2006).

[123] A. Bianchi, S. Carretta, P. Santini, G. Amoretti, J. Lago, M. Corti, A. Lascialfari, P. Arosio, G. Timco, and R. E. P. Winpenny, "Phonon-induced relaxation in the Cr_7Ni magnetic molecule probed by NMR," Phys. Rev. B **82**, 134403 (2010).

[124] C. Kutter, H. P. Moll, J. van Tol, H. Zuckermann, J. C. Maan, and P. Wyder, "Electron-spin echoes at 604 Ghz using far infrared lasers," Phys. Rev. Lett. **74**, 2925 (1995).

[125] E. Garlatti, S. Carretta, M. Affronte, E. C. Sanudo, G. Amoretti, and P. Santini, "Magnetic properties and relaxation dynamics of a frustrated Ni_7 molecular nanomagnet," J. Phys.: Condens. Matter **24**, 104006 (2012).

[126] J. Schnack, "Effects of frustration on magnetic molecules: a survey from Olivier Kahn until today," Dalton Trans. **39**, 4677 (2010).

[127] E. H. Lieb, T. Schultz, and D. C. Mattis, "Two soluble models of an antiferromagnetic chain," Ann. Phys. **16**, 407 (1961).

[128] O. Cador, D. Gatteschi, R. Sessoli, F. K. Larsen, J. Overgaard, A.-L. Barra, S. J. Teat, G. A. Timco, and R. E. P. Winpenny, "The magnetic Möbius strip: Synthesis, structure, and magnetic studies of odd-numbered antiferromagnetically coupled

wheels," Angew. Chem. Int. Ed. **43**, 5196 (2004).

[129] Y. Furukawa, K. Kiuchi, K. i. Kumagai, Y. Ajiro, Y. Narumi, M. Iwaki, K. Kindo, A. Bianchi, S. Carretta, P. Santini, F. Borsa, G. A. Timco, and R. E. P. Winpenny, "Evidence of spin singlet ground state in the frustrated antiferromagnetic ring $\mathrm{Cr_8Ni}$," Phys. Rev. B **79**, 134416 (2009).

[130] M. L. Baker, O. Waldmann, S. Piligkos, R. Bircher, O. Cador, S. Carretta, D. Collison, F. Fernandez-Alonso, E. J. L. McInnes, H. Mutka, A. Podlesnyak, F. Tuna, S. Ochsenbein, R. Sessoli, A. Sieber, G. A. Timco, H. Weihe, H. U. Güdel, and R. E. P. Winpenny, "Inelastic neutron scattering studies on the odd-membered antiferromagnetic wheel $\mathrm{Cr_8Ni}$," Phys. Rev. B **86**, 064405 (2012).

[131] P. A. Angaridis, P. Baran, R. Boca, F. Cervantes-Lee, W. Haase, G. Mezei, R. G. Raptis, and R. Werner, "Synthesis and structural characterization of trinuclear Cu^{II}pyrazolato complexes containing μ_3-OH, μ_3-o, and μ_3-Cl ligands. Magnetic Susceptibility study of $[\mathrm{PPN}]_2[(\mu_3\text{-O})\mathrm{Cu}_3(\mu\text{-pz})_3\mathrm{Cl}_3]$," Inorg. Chem. **41**, 2219 (2002).

[132] K.-Y. Choi, Y. H. Matsuda, H. Nojiri, U. Kortz, F. Hussain, A. C. Stowe, C. Ramsey, and N. S. Dalal, "Observation of a half step magnetization in the $\mathrm{Cu_3}$-type triangular spin ring," Phys. Rev. Lett. **96**, 107202 (2006).

[133] N. Hoshino, M. Nakano, H. Nojiri, W. Wernsdorfer, and H. Oshio, "Templating Odd Numbered Magnetic Rings: Oxovanadium Heptagons Sandwiched by β-Cyclodextrins," J. Am. Chem. Soc. **131**, 15100 (2009).

[134] H.-C. Yao, J.-J. Wang, Y.-S. Ma, O. Waldmann, W.-X. Du, Y. Song, Y.-Z. Li, L.-M. Zheng, S. Decurtins, and X.-Q. Xin, "An iron(III) phosphonate cluster containing a nonanuclear ring," Chem. Comm. .

[135] M. Antkowiak, P. K. owski, G. Kamieniarz, G. A. Timco, F. Tuna, and R. E. P. Winpenny, "Detection of ground states in frustrated molecular rings by in-field local magnetization profiles," Phys. Rev. B **87**, 184430 (2013).

[136] G. Kamieniarz, W. Florek, and M. Antkowiak, "Universal sequence of ground states validating the classification of frustration in antiferromagnetic rings with a single bond defect," Phys. Rev. B **92**, 140411(R) (2015).

[137] P. Kozlowski, "Frustration and quantum entanglement in odd-membered ring-shaped chromium nanomagnets," Phys. Rev. B **91**, 174432 (2015).

[138] M. L. Baker, T. Lancaster, A. Chiesa, G. Amoretti, P. J. Baker, C. Barker, S. J. Blundell, S. Carretta, D. Collison, H. U. Güdel, T. Guidi, E. J. L. McInnes, J. S. Möller, H. Mutka, J. Ollivier, F. L. Pratt, P. Santini, F. Tuna, P. L. W. Tregenna-Piggott, I. J. Vitorica-Yrezabal, G. A. Timco, and R. E. P. Winpenny, "Studies of a Large Odd-Numbered Odd-Electron Metal Ring: Inelastic Neutron Scattering and Muon Spin Relaxation Spectroscopy of $\mathrm{Cr_8Mn}$," Chem. Eur. J. **22**, 1779 (2016).

[139] V. Simonet, M. Loire, and R. Ballou, "Magnetic chirality as probed by neutron scattering," The European Physical Journal Special Topics **213**, 5 (2012).

[140] C. G. Windsor, *Pulsed Neutron Scattering* (Taylor and Francis, 1981).

[141] N. K. Langford, "Circuit QED — Lecture Notes," arXiv:1310.1897v1 (2013).

[142] L. Bishop, "Circuit Quantum Electrodynamics," PhD Thesis , arXiv:1007.3520v1 (2010).

[143] M. H. Devoret, *"Quantum fluctuations in electrical circuits", in Quantum Fluctuations: Les Houches Session LXIII* (North-Holland/Elsevier, Amsterdam, 1997).

[144] G. Burkard, R. H. Koch, and D. P. DiVincenzo, "Multilevel quantum description of decoherence in superconducting qubits," Phys. Rev. B **69**, 064503 (2004).

[145] M. Wallquist, V. S. Shumeiko, and G. Wendin, "Selective coupling of superconducting qubits via tunable stripline cavity," Phys. Rev. B **74**, 224506 (2006).

[146] M. Sandberg, C. M. Wilson, F. Persson, T. Bauch, G. Johansson, V. Shumeiko, T. Duty, and P. Delsing, "Tuning the field in a microwave resonator faster than the photon lifetime," Applied Physics Letters **92**, 203501 (2008).

[147] A. Palacios-Laloy, F. Nguyen, F. Mallet, P. Bertet, D. Vion, and D. Esteve, "Tunable resonators for quantum circuits," J. Low Temp. Phys. **151**, 1034 (2008).

[148] J. H. Wesenberg, A. Ardavan, G. A. D. Briggs, J. J. L. Morton, R. J. Schoelkopf, D. I. Schuster, and K. Mølmer, "Quantum computing with an electron spin ensemble," Phys. Rev. Lett. **103**, 070502 (2009).

[149] J. M. Martinis, S. Nam, J. Aumentado, and C. Urbina, "Rabi oscillations in a large Josephson-junction qubit," Phys. Rev. Lett. **89**, 117901 (2002).

[150] J. R. Friedman, V. Patel, W. Chen, S. K. Tolpygo, and J. E. Lukens, "Quantum superposition of distinct macroscopic states," Nature **406**, 43 (2000).

[151] C. H. van der Wal, A. C. J. ter Haar, F. K. Wilhelm, R. N. Schouten, C. J. P. M. Harmans, T. P. Orlando, S. Lloyd, and J. E.Mooij, "Quantum superposition of macroscopic persistent-current states," Science **290**, 773 (2000).

[152] Y. Nakamura, Y. A. Pashkin, and J. S. Tsai, "Coherent control of macroscopic quantum states in a single-Cooper-pair box," Nature **398**, 786 (1999).

[153] J. Clarke and F. K. Wilhelm, "Superconducting quantum bits," Nature **453**, 1031 (2008).

[154] I. Chiorescu, Y. Nakamura, C. J. P. M. Harmans, and J. E. Mooij, "Coherent quantum dynamics of a superconducting flux qubit," Science **299**, 1869 (2003).

[155] T. P. Orlando, J. E.Mooij, L. Tain, C. H. van der Wal, L. S. Levitov, S. Lloyd, and J. J. Mazo, "Superconducting persistent-current qubit," Phys. Rev. B **60**, 15398 (1999).

[156] D. Marcos, M. Wubs, J. M. Taylor, R. Aguado, M. D. Lukin, and A. S. Sø rensen, "Coupling nitrogen-vacancy centers in diamond to superconducting flux qubits," Phys. Rev. Lett. **105**, 210501 (2010).

[157] M. Jenkins, T. Hümmer, M. J. Martinez-Perez, J. Garcia-Ripoll, D. Zueco, and F. Luis, "Coupling single-molecule magnets to quantum circuits," New Journal of Physics **15**, 095007 (2013).

[158] A. Megrant, C. Neill, R. Barends, B. Chiaro, Y. Chen, L. Feigl, J. Kelly, E. Lucero, M. Mariantoni, P. J. J. O'Malley, D. Sank, A. Vainsencher, J. Wenner, T. C. White, Y. Yin, J. Zhao, C. J. Palmstrom, J. M. Martinis, and A. N. Cleland, "Planar superconducting resonators with internal quality factors above one million," Appl. Phys. Lett. **100**, 113510 (2012).

[159] Z. L. Wang, Y. P. Zhong, L. J. He, H. Wang, J. M. Martinis, A. N. Cleland, and Q. W. Xie, "Quantum state characterization of a fast tunable superconducting resonator," Applied Physics Letters **102**, 163503 (2013).

[160] Y. Kubo, I. Diniz, A. Dewes, V. Jacques, A. Dréau, J.-F. Roch, A. Auffèves, D. Vion, D. Esteve, and P. Bertet, "Storage and retrieval of a microwave field in a spin ensemble," Phys. Rev. A **85**, 012333 (2012).

[161] M. Sandberg, F. Persson, I. C. Hoi, C. M. Wilson, , and P. Delsing, "Exploring circuit quantum electrodynamics using a widely tunable superconducting resonator," Phys. Scr. **T137**, 014018 (2009).

[162] A. Ghirri, C. Bonizzoni, D. Gerace, S. Sanna, A. Cassinese, and M. Affronte, "$YBa_2Cu_3O_7$ microwave resonators for strong collective coupling with spin ensembles," Appl. Phys. Lett. **106**, 184101 (2015).

[163] M. H. Devoret and R. J. Schoelkopf, “Superconducting circuits for quantum information: An outlook,” Science **339**, 1169 (2013).

[164] F. W. Strauch, P. R. Johnson, A. Dragt, C. Lobb, J. R. Anderson, and F. C. Wellstood, “Quantum Logic Gates for Coupled Superconducting Phase Qubits,” Phy. Rev. Lett. **91**, 167005 (2003).

[165] L. DiCarlo, J. Chow, J. Gambetta, L. S. Bishop, B. Johnson, D. Schuster, J. Majer, A. Blais, L. Frunzio, S. Girvin, and R. Schoelkopf, “Demonstration of two-qubit algorithms with a superconducting quantum processor,” Nature **460**, 240 (2009).

[166] R. Barends, J. Kelly, A. Megrant, A. Veitia, D. Sank, E. Jeffrey, T. C. White, J. Mutus, A. G. Fowler, B. Campbell, Y. Chen, Z. Chen, B. Chiaro, A. Dunsworth, C. Neill, P. O’Malley, P. Roushan, A. Vainsencher, J. Wenner, A. N. Korotkov, A. N. Cleland, and J. M. Martinis, “Superconducting quantum circuits at the surface code threshold for fault tolerance,” Nature **500**, 508 (2014).

[167] T. Larsen, K. D. Petersson, F. Kuemmeth, T. S. Jespersen, P. Krogstrup, J. Nygard, and C. M. Marcus, “Semiconductor-nanowire-based superconducting qubit,” Phys. Rev. Lett. **115**, 127001 (2015).

[168] H. Paik, D. I. Schuster, L. S. Bishop, G. Kirchmair, G. Catelani, A. P. Sears, B. R. Johnson, M. J. Reagor, L. Frunzio, L. I. Glazman, S. M. Girvin, M. H. Devoret, and R. J. Schoelkopf, “Observation of high coherence in Josephson junction qubits measured in a three-dimensional circuit QED architecture,” Phys. Rev. Lett. **107**, 240501 (2011).

[169] C. Rigetti, J. M. Gambetta, S. Poletto, B. L. T. Plourde, J. M. Chow, A. D. C’orcoles, J. A. Smolin, S. T. Merkel, J. R. Rozen, G. A. Keefe, M. B. Rothwell, M. B. Ketchen, and M. Steffen, “Superconducting qubit in a waveguide cavity with a coherence time approaching 0.1 ms,” Phys. Rev. B **86**, 100506(R) (2012).

[170] P. Campagne-Ibarcq, E. Flurin, N. Roch, D. Darson, P. Morfin, M. Mirrahimi, M. H. Devoret, F. Mallet, and B. Huard, “Persistent control of a superconducting qubit by stroboscopic measurement feedback,” Phys. Rev. X **3**, 021008 (2013).

[171] S. Carretta, A. Chiesa, F. Troiani, D. Gerace, G. Amoretti, and P. Santini, “Quantum information processing with hybrid spin-photon qubits,” Phys. Rev. Lett. **111**, 110501 (2013).

[172] A. Chiesa, D. Gerace, F. Troiani, G. Amoretti, P. Santini, and S. Carretta, “Robustness of quantum gates with hybrid spin-photon qubits in superconducting resonators,” Phys. Rev. A **89**, 052308 (2014).

[173] J. Ghosh, A. Galiautdinov, Z. Zhou, A. N. Korotkov, J. M. Martinis, and M. R. Geller, “High-fidelity controlled-σ^z gate for resonator-based superconducting quantum computers,” Phys. Rev. A **87**, 022309 (2013).

[174] P. Rabl, D. DeMille, J. Doyle, M. Lukin, R. Schoelkopf, and P. Zoller, “Hybrid Quantum Processors: Molecular Ensembles as Quantum Memory for Solid State Circuits,” Phy. Rev. Lett. **97**, 033003 (2006).

[175] A. Imamoglu, “Cavity QED based on collective magnetic dipole coupling: Spin ensembles as hybrid two-level systems,” Phy. Rev. Lett. **102**, 083602 (2009).

[176] J. Verdu, H. Zoubi, C. Koller, J. Majer, H. Ritsch, and J. Schmiedmayer, “Strong magnetic coupling of an ultracold gas to a superconducting waveguide cavity,” Phy. Rev. Lett. **103**, 043603 (2009).

[177] Z.-L. Xiang, S. Ashhab, J. Q. You, and F. Nori, “Hybrid quantum circuits: Superconducting circuits interacting with other quantum systems,” Rev. Mod. Phys. **85**, 623 (2013).

[178] Y. Ping, E. Gauger, and S. Benjamin, "Measurement-based quantum computing with a spin ensemble coupled to a stripline cavity," New Journal of Physics **14**, 013030 (2012).

[179] Y. Kubo, F. R. Ong, P. Bertet, D. Vion, V. Jacques, D. Zheng, A. Dréau, J.-F. Roch, A. Auffeves, F. Jelezko, J. Wrachtrup, M. F. Barthe, P. Bergonzo, and D. Esteve, "Strong coupling of a spin ensemble to a superconducting resonator," Phys. Rev. Lett. **105**, 140502 (2010).

[180] J.-Q. Liao, Z. Gong, L. Zhou, Y.-X. Liu, C. Sun, and F. Nori, "Controlling the transport of single photons by tuning the frequency of either one or two cavities in an array of coupled cavities," Phys. Rev. A **81**, 042304 (2010).

[181] G. Haack, F. Helmer, M. Mariantoni, F. Marquardt, and E. Solano, "Resonant quantum gates in circuit quantum electrodynamics," Phys. Rev. B **82**, 024514 (2010).

[182] D. L. Underwood, W. E. Shanks, J. Koch, and A. A. Houck, "Low-disorder microwave cavity lattices for quantum simulation with photons," Phys. Rev. A **86**, 023837 (2012).

[183] H. Wang, M. Hofheinz, M. Ansmann, R. C. Bialczak, E. Lucero, M. Neeley, A. D. O'Connell, D. Sank, J. Wenner, A. N. Cleland, and J. M. Martinis, "Measurement of the decay of Fock states in a superconducting quantum circuit," Phys. Rev. Lett. **101**, 240401 (2008).

[184] J. E. Healey, T. Lindstrom, M. S. Colclough, C. M. Muirhead, and A. Y. Tzalenchuk, "Magnetic field tuning of coplanar waveguide resonators," Appl. Phys. Lett. **93**, 043513 (2008).

[185] J. Q. You and F. Nori, "Superconducting Circuits and Quantum Information," Physics Today **58**, 42 (2005).

[186] R. E. George, J. P. Edwards, , and A. Ardavan, "Chemical engineering of molecular qubits," Phys. Rev. Lett. **110**, 027601 (2013).

[187] S. D. Liberato, D. Gerace, I. Carusotto, and C. Ciuti, "Extracavity quantum vacuum radiation from a single qubit," Phys. Rev. A **80**, 053810 (2009).

[188] I. Diniz, S. Portolan, R. Ferreira, J. M. Gerard, P. Bertet, and A. Auffèves, "Strongly coupling a cavity to inhomogeneous ensembles of emitters: Potential for long-lived solid-state quantum memories," Phys. Rev. A **84**, 063810 (2011).

[189] Z. Kurucz, J. H. Wesenberg, and K. Mølmer, "Spectroscopic properties of inhomogeneously broadened spin ensembles in a cavity," Phys. Rev. A **83**, 053852 (2011).

[190] T. C. Ralph and J. G. Pryde, Progress in Optics **54**, 209 (2010).

[191] P. Kok, W. J. Munro, K. Nemoto, T. C. Ralph, J. P. Dowling, and G. J. Milburn, "Linear optical quantum computing with photonic qubits," Rev. Mod. Phys. **79**, 135 (2007).

[192] M. Silva, M. Rötteler, and C. Zalka, "Thresholds for linear optics quantum computing with photon loss at the detectors," Phys. Rev. A **72**, 032307 (2005).

[193] D. S. F. Troiani and D. Loss, "Hyperfine-induced decoherence in triangular spin-cluster qubits," Phys. Rev. B **86**, 161409(R) (2012).

[194] A. Mezzacapo, U. Las Heras, J. S. Pedernales, L. DiCarlo, E. Solano, and L. Lamata, "Digital quantum Rabi and Dicke models in superconducting circuits," Sci. Rep. **4**, 7482 (2014).

[195] U. Las Heras, L. Garcia-Alvarez, A. Mezzacapo, E. Solano, and L. Lamata, "Fermionic models with superconducting circuits," EPJ Quantum Technology **2**, 8 (2015).

[196] R. Barends, L. Lamata, J. Kelly, L. García-Álvarez, A. G. Fowler, A. Megrant, E. Jef-

frey, T. C. White, D. Sank, J. Y. Mutus, B. Campbell, Y. Chen, Z. Chen, B. Chiaro, A. Dunsworth, I.-C. Hoi, C. Neill, P. J. J. O'Malley, C. Quintana, P. Roushan, A. Vainsencher, J. Wenner, E. Solano, and J. M. Martinis, "Digital quantum simulation of fermionic models with a superconducting circuit," Nat. Commun. **6**, 7654 (2015).

[197] Y. Salathé, M. Mondal, M. Oppliger, J. Heinsoo, P. Kurpiers, A. Potočnik, A. Mezzacapo, U. Las Heras, L. Lamata, E. Solano, S. Filipp, and A. Wallraff, "Digital quantum simulation of spin models with circuit quantum electrodynamics," Phys. Rev. X **5**, 021027 (2015).

[198] S. Probst, A. Tkalčec, H. Rotzinger, D. Rieger, J.-M. Le Floch, M. Goryachev, M. E. Tobar, A. V. Ustinov, and P. A. Bushev, "Three-dimensional cavity quantum electrodynamics with a rare-earth spin ensemble," Phys. Rev. B. **90**, 100404(R) (2014).

[199] C. Grezes, B. Julsgaard, Y. Kubo, M. Stern, T. Umeda, J. Isoya, H. Sumiya, H. Abe, S. Onoda, T. Ohshima, V. Jacques, J. Esteve, D. Vion, D. Esteve, K. Mølmer, and P. Bertet, "Multimode storage and retrieval of microwave fields in a spin ensemble," Phys. Rev. X **4**, 021049 (2014).

[200] A. Chiesa, P. Santini, D. Gerace, J. Raftery, A. A. Houck, and S. Carretta, "Digital quantum simulators in a scalable architecture of hybrid spin-photon qubits," Sci. Rep. **5**, 16036 (2015).

[201] M. Troyer and U. J. Wiese, "Computational complexity and fundamental limitations to fermionic quantum Monte Carlo simulations," Phys. Rev. Lett. **94**, 170201 (2005).

[202] E. Fradkin, "Jordan-Wigner transformation for quantum-spin systems in two dimensions and fractional statistics," Phys. Rev. Lett. **63**, 332 (1989).

[203] W. Shaofeng, "Jordan-Wigner transformation in a higher-dimensional lattice," Phys. Rev. E **51**, 1004 (1995).

[204] B. Bock and M. Azzouz, "Generalization of the Jordan-Wigner transformation in three dimensions and its application to the Heisenberg bilayer antiferromagnet," Phys. Rev. B **64**, 054410 (2001).

[205] D. Abrams and S. Lloyd, "Simulation of many-body Fermi systems on a universal quantum computer," Phys. Rev. Lett. **79**, 2586 (1997).

[206] G. Ortiz, J. E. Gubernatis, E. Knill, and R. Laflamme, "Quantum algorithms for fermionic simulations," Phys. Rev. A **64**, 022319 (2001).

[207] R. Somma, G. Ortiz, J. E. Gubernatis, E. Knill, and R. Laflamme, "Simulating physical phenomena by quantum networks," Phys. Rev. A **65**, 042323 (2002).

[208] R. A. Bari, "Classical linear-chain Hubbard model: Metal-insulator transition," Phys. Rev. B **7**, 4318 (1973).

[209] L. DiCarlo, J. M. Chow, J. M. Gambetta, L. S. Bishop, B. R. Johnson, D. I. Schuster, J. Majer, A. Blais, L. Frunzio, S. M. Girvin, and R. J. Schoelkopf, "Demonstration of two-qubit algorithms with a superconducting quantum processor," Nature **460**, 240 (2009).

[210] Z. Chen, A. Megrant, J. Kelly, R. Barends, J. Bochmann, Y. Chen, B. Chiaro, A. Dunsworth, E. Jeffrey, J. Y. Mutus, P. J. J. O'Malley, C. Neill, P. Roushan, D. Sank, A. Vainsencher, J. Wenner, T. C. White, A. N. Cleland, and J. M. Martinis, "Fabrication and characterization of aluminum airbridges for superconducting microwave circuits," Appl. Phys. Lett. **104**, 052602 (2014).

[211] S. Putz, D. O. Krimer, R. Amsüss, A. Valookaran, T. Nöbauer, J. Schmiedmayer, S. Rotter, and J. Majer, "Protecting a spin ensemble against decoherence in the

strong-coupling regime of cavity QED," Nat. Physics **10**, 720 (2014).

[212] H. Wu, R. E. George, J. H. Wesenberg, K. Mølmer, D. I. Schuster, R. J. Schoelkopf, K. M. Itoh, A. Ardavan, J. J. L. Morton, and G. A. D. Briggs, "Storage of multiple coherent microwave excitations in an electron spin ensemble," Phys. Rev. Lett. **105**, 140503 (2010).

[213] B. Julsgaard, C. Grezes, P. Bertet, and K. Mølmer, "Quantum memory for microwave photons in an inhomogeneously broadened spin ensemble," Phys. Rev. Lett. **110**, 250503 (2013).

[214] W. C. Holton, J. Schneider, and T. L. Estle, "Electron paramagnetic resonance of photosensitive iron transition group impurities in ZnS and ZnO," Phys. Rev. **133**, A1638 (1964).

[215] A. Rauber and J. Schneider, Z. Naturforsch. **17a**, 266 (1962).

[216] E. R. Feher, "Effect of uniaxial stresses on the paramagnetic spectra of Mn^{3+} and Fe^{3+} in MgO," Phys. Rev. **136**, A145 (1964).

[217] A. M. Tyryshkin, S. A. Lyon, A. V. Astashkin, and A. M. Raitsimring, "Electron spin relaxation times of phosphorus donors in silicon," Phys. Rev. B **68**, 193207 (2003).

[218] W. G. Farr, D. L. Creedon, M. Goryachev, K. Benmessai, and M. E. Tobar, "Ultrasensitive microwave spectroscopy of paramagnetic impurities in sapphire crystals at millikelvin temperatures," Phys. Rev. B **88**, 224426 (2013).

[219] G. Grosso and G. P. Parravicini, *Solid State Physics* (Academic Press, San Diego, 2000).

[220] J. Kohanoff, *Electronic Structure Calculations for solids and molecules* (Cambridge University Press, 2006).

[221] J. J. Sakurai, *Modern Quantum Mechanics* (Addison-Wesley Publishing Company, 1994).

[222] H. P. Breuer and F. Petruccione, *The theory of open quantum systems* (Oxford University Press, 2002).

[223] M. O. Scully and M. S. Zubairy, *Quantum Optics* (Cambridge University Press, Cambridge, UK, 1997).

List of Publications

Refereed publications

1. A. Chiesa, S. Carretta, P. Santini, G. Amoretti and E. Pavarini, *Many-Body Models for Molecular Nanomagnets*, Phys. Rev. Lett. **110**, 157204 (2013).
2. S. Carretta, A. Chiesa, F. Troiani, D. Gerace, G. Amoretti and P. Santini, *Quantum Information Processing with Hybrid Spin-Photon Qubit Encoding*, Phys. Rev. Lett. **111**, 110501 (2013).
3. A. Chiesa, D. Gerace F. Troiani G. Amoretti P. Santini and S. Carretta, *Robustness of quantum gates with hybrid spin-photon qubits in superconducting resonators*, Phys. Rev. A **89**, 052308 (2104).
4. A. Chiesa, G. F. S. Whitehead, S. Carretta, L. Carthy, G. A. Timco, S. J. Teat, G. Amoretti, E. Pavarini, R. E. P. Winpenny and P. Santini, *Molecular nanomagnets with switchable coupling for quantum simulation*, NPG Sci. Rep. **4**, 7423 (2014).
5. A. Chiesa, P. Santini, D. Gerace, J. Raftery, A. A. Houck and S. Carretta, *Digital quantum simulators in a scalable architecture of hybrid spin-photon qubits*, NPG Sci. Rep. **5**, 16036 (2015).
6. A. Ghirri, A. Chiesa, S. Carretta, F. Troiani, J. van Tol, S. Hill, I. Vitorica-Yrezabal, G. A. Timco, R. E. P. Winpenny and M. Affronte, *Coherent spin dynamics in molecular* Cr_8Zn *wheels*, J. Phys. Chem. Lett. **6**, 5062 (2015).
7. F. Adelnia , A. Chiesa, S. Bordignon, S. Carretta, A. Ghirri, A. Candini, C. Cervetti, M. Evangelisti, M. Affronte, I. Sheikin, R. Winpenny, G. A. Timco, F. Borsa and A. Lascialfari, *Low temperature magnetic properties and spin dynamics in single crystals of* Cr_8Zn *antiferromagnetic molecular rings*, J. Chem. Phys. 143, 244321 (2015).
8. M. L. Baker, T. Lancaster, A. Chiesa, G. Amoretti, P. J. Baker, C. Barker, S. J. Blundell, S. Carretta, D. Collison, H. U. Güdel, T. Guidi, E. J. L. McInnes, J. S. Möller, H. Mutka, J. Ollivier, F. L. Pratt, P. Santini, F. Tuna, P. L. W. Tregenna-Piggott, I. J. Vitorica-Yrezabal, G. A. Timco and R. E. P. Winpenny, *Studies of a Large Odd-Numbered Odd-Electron Metal Ring: Inelastic Neutron Scattering and Muon Spin Relaxation Spectroscopy of* Cr_8Mn, Chem. Eur. J. **22**, 1779 (2016).

Publications under review

1. A. Chiesa, P. Santini, D. Gerace, and S. Carretta, *Long-lasting quantum information processing in a cavity-protection regime*.
2. J. Ferrando-Soria, E. M. Pineda, A. Chiesa, A. Fernandez, S. Magee, S. Carretta, P. Santini, I. Vitorica-Yrzebal, F. Tuna, G. A. Timco, E. J. L. McInnes and R. E. P. Winpenny, *A modular design of molecular qubits to implement universal quantum gates*.

Publications in preparation

1. R. J. Woolfson, G. A. Timco, A. Chiesa, I. J. Vitorica-Yrezabal, F. Tuna, T. Guidi, P. Santini, S. Carretta and R. E.P. Winpenny, *Physical Studies of a Homometallic Odd-Number Odd-Electron Ring*
2. J. Ferrando-Soria, S. A. Magee, A. Chiesa, S. Carretta, P. Santini, I. J. Vitorica-Yrezabal, F. Tuna, S. Sproules, K. M. Lancaster, A.-L. Barra, G. A. Timco, E. J. L. McInnes and Richard E. P. Winpenny, *Redox-Switchable Electron Exchange Interaction in Molecular Double Qubits: Towards the Physical Implementation of Quantum Information Processing*
3. A. Chiesa, *Many-Body models for Anti-ferromagnetic* Cr_7M *Rings: a first principle study*

Ringraziamenti

Scrivo questa parte nella lingua in cui posso meglio esprimere il mio grazie a tutti coloro che mi hanno sostenuto, incoraggiato ed hanno collaborato con me in questi tre anni di dottorato. Sono convinto che la vita di ciascuno sia segnata dalle persone che il Signore mette sulla sua strada. Sono dunque grato a Dio di avermi arricchito attraverso l'incontro con ciascuno di voi. Questi tre anni sono stati come un lungo giro in bicicletta. Il mio ringraziamento va a tutti quelli che hanno condiviso con me un tratto di strada, più o meno lungo. A chi ha tirato e a chi si è messo a ruota, a chi mi ha fatto da gregario e a chi, spronandomi ad andare più forte, ha sfruttato la mia scia. Ma soprattutto a chi ha creduto in me e mi ha motivato sempre, come coach dall'ammiraglia o come tifoso a bordo strada.

In primis un grazie sentito, caloroso ed accorato va al mio supervisore, professor Stefano Carretta, che mi ha guidato con la sua estrema competenza ed accompagnato con l'affetto di un fratello maggiore, sopportando i miei errori ed esultando con me per i comuni successi. Spero di aver preso almeno una goccia della sua correttezza, del suo altruismo e del suo amore per la ricerca. Oltre, ovviamente, ad un briciolo del suo sapere, che continuamente ed assiduamente ha cercato di trasmettermi. Grazie a lui e a tutto il gruppo di ricerca di Magnetismo Molecolare del Dipartimento di Fisica e Scienze della Terra dell'Università degli Studi di Parma, per aver creduto in me fin dai tempi della mia Laurea Triennale. Da allora la mia stima nei vostri confronti non fa che aumentare, sia sul piano dell'estrema competenza e brillantezza in campo scientifico, sia sul piano dei rapporti umani.

Con Stefano ringrazio il mio co-supervisore, professor Paolo Santini, per il suo sguardo lucido sulla realtà ed i suoi suggerimenti mai banali. La sua capacità di individuare il cuore dei problemi ed il suo intuito fisico sono sempre stati per me un modello da seguire.

Sarò eternamente grato al professor Giuseppe Amoretti, che per primo mi ha introdotto al fascino del magnetismo ed al gusto della ricerca. La sua attenzione ed il suo amorevole sostegno mi hanno accompagnato sempre, nel corso di questi anni. Grazie per avermi trasmesso le sue vastissime conoscenze e per non avermi mai negato un sorriso.

Un ringraziamento anche alla dottoressa Elena Garlatti, che ha chiarito pazientemente i miei dubbi e condiviso le mie perplessità, senza mai negarmi il suo aiuto. Con lei grazie anche a tutti i colleghi dottorandi del Dipartimento di Fisica e Scienze della Terra, con particolare riguardo per chi ha condiviso con me l'Area 51: oltre a Elena, Sara, con cui ho avuto modo di collaborare, Mattia, Tiziano, Pietro, Matteo, Francesco, Serena, Daniela, Giacomo, che si sono avvicendati nel corso degli anni.

Desidero inoltre ringraziare tutti coloro che hanno collaborato con il nostro gruppo ed interagito con me. In particolare il professor Dario Gerace, dell'Università di Pavia, che mi ha formato ed accolto come un caro amico in occasione delle mie visite. Poi la professoressa Eva Pavarini, che mi ha aperto le porte del Forschungszentrum di Jülich, all'avanguardia per l'High Performance Computing, fin dalla mia Laurea Magistrale e con cui continuo a lavorare. Grazie anche per la collaborazione al professor Marco Affronte, dell'Università e del CNR di Modena, e al suo gruppo, con particolare riferimento al dottor Alberto Ghirri e al dottor Filippo Troiani; e poi a chi mi ha assistito negli esperimenti di scattering di neutroni: in primis alla dottoressa Tatiana Guidi, della facility ISIS, insieme al dottor Hannu Mutka, al dottor Jacques Ollivier (Institute Laue-Langevin, Grenoble) e al dottor Mike Baker (Stanford University); al professor Lascialfari e a Fatemeh, dell'Università di Milano, che hanno arricchito i nostri studi con misure NMR. Infine un doveroso ringraziamento al professor Winpenny, dell'Università di Manchester, il cui gruppo ha sintetizzato tutte le molecole riportate in questa tesi. Ricordo in particolare Jesus Ferrando-Soria e Robert Woolfson, con i quali ho interagito maggiormente.

Poi un dolcissimo ringraziamento sgorga dal profondo del mio cuore verso i miei sostenitori più sfegatati: i miei genitori, Mariateresa e Bruno, mia zia Cristina e la donna con cui spero di condividere il resto della mia vita, Luisa. Il loro amore e la loro stima sono state la mia forza ogni giorno. A Luisa prometto che non parlerò soltanto di Fisica. A volte anche di bicicletta.

A tal proposito, non poteva mancare un ringraziamento al mio antistress per eccellenza: la mia bici, sempre disponibile ad una sgambata in qualsiasi ritaglio di tempo. Per insegnarmi che il ciclismo, come la vita, non regala nulla. Serve uno sforzo costante, una estrema tenacia ed una grande forza di volontà. Meglio se con il fedelissimo compagno di mille pedalate (forse di più), Gabry, che ringrazio per aver sopportato la mia esuberanza (cercando, senza successo, di frenarla) e, a volte, anche i miei discorsi strampalati sui qubit. Credo che sia la persona con lo sguardo più positivo sul mondo che abbia mai incontrato. Grazie per avermi trasmesso il tuo sorriso.

Infine un affettuoso grazie a tutti i fucini del gruppo di Parma (e non solo) con cui ho condiviso il mio percorso universitario ed, in parte, anche gli anni del dottorato. Con loro e con il Centro Universitario Cattolico, che ringrazio per il supporto e l'amicizia, ho potuto intraprendere in questi anni un importante percorso di servizio e crescita spirituale.

Copyright Permissions

- Figure 2.1 reproduced with permission from:
  A. Cornia, M. Affronte, A.G.M. Jansen, D. Gatteschi, A. Caneschi and R. Sessoli, Chem. Phys. Lett. **322**, 477 (2000).
  Copyright (2000) by Elsevier Limited.

- Figures 6.8, 6.10 and 6.11 reproduced with permission from:
  A. Ghirri, A. Chiesa, S. Carretta, F. Troiani, J. van Tol, S. Hill, I. Vitorica-Yrezabal, G. A. Timco, R. E. P. Winpenny and M. Affronte, J. Phys. Chem. Lett. **6**, 5062 (2015).
  Copyright (2015) by the American Chemical Society.

- Figures 7.1, 7.2, 7.4 and 7.7 reproduced with permission from:
  M. L. Baker, T. Lancaster, A. Chiesa, G. Amoretti, P. J. Baker, C. Barker, S. J. Blundell, S. Carretta, D. Collison, H. U. Güdel, T. Guidi, E. J. L. McInnes, J. S. Möller, H. Mutka, J. Ollivier, F. L. Pratt, P. Santini, F. Tuna, P. L. W. Tregenna-Piggott, I. J. Vitorica-Yrezabal, G. A. Timco and Richard E. P. Winpenny, Chem. Eur. J. **22**, 1779 (2016).
  Copyright (2016) by John Wiley and Sons.

- Figure 8.5 reproduced with permission from:
  J. Koch, T. M. Yu, J. Gambetta, A. A. Houck, D. I. Schuster, J. Majer, A. Blais, M. H. Devoret, S. M. Girvin, and R. J. Schoelkopf, Phys. Rev. A **76**, 042319 (2007).
  Copyright (2007) by the American Physical Society.

- Figures 9.1 and 9.3 reproduced with permission from:
  S. Carretta, A. Chiesa, F. Troiani, D. Gerace, G. Amoretti and P. Santini, *Quantum Information Processing with Hybrid Spin-Photon Qubit Encoding*, Phys. Rev. Lett. **111**, 110501 (2013).
  Copyright (2013) by the American Physical Society.

- Figures 9.6 and 9.9 reproduced with permission from:
  A. Chiesa, D. Gerace F. Troiani G. Amoretti P. Santini and S. Carretta, *Robustness of quantum gates with hybrid spin-photon qubits in superconducting resonators*, Phys. Rev. A **89**, 052308 (2104).
  Copyright (2014) by the American Physical Society.